UNIVERSITY OF CAPE TOWN
IYUNIVESITHI YASEKAPA • UNIVERSITEIT VAN KAAPSTAD

Response of plates subjected to air-blast and buried explosions.

Candidate: Richard Curry

Supervisor: Prof Genevieve Langdon

Blast Impact and Survivability Research Center

Thesis submitted for the degree of:
DOCTOR OF PHILOSOPHY
in the Department of
Mechanical Engineering
UNIVERSITY OF CAPE TOWN
June 2017

Declaration

I hereby grant the University of Cape Town free license to reproduce for the purpose of research either the whole or any portion of the contents in any manner whatsoever of the above dissertation.

I know the meaning of plagiarism and declare that all the work in this document, save for that which is properly acknowledged, is my own. I also declare that this material has not been submitted for any purpose or examination to any other Department or University.

Signed on the 12th of June 2017

.....

Richard Curry

Abstract

Explosive threats have become more prevalent in both military and terrorist theatres of conflict, showing up largely in the form of Improvised Explosive Devices (IED) which are often buried in soil to conceal them and increase their effectiveness. The response of a structure subjected to a blast load is influenced by many factors, namely stand off distance, mass of explosive, degrees of confinement and medium surrounding the charge. This study focuses on characterizing the transient deformation of test plates which have been exposed to different explosive loading conditions including free air blasts (AIR), backed charge (VBP) and buried charge (SBP) configurations.

In the three loading configurations, four charge masses are considered, utilizing 10g, 15g, 20g and 25g masses of PE4 plastic explosive which were moulded into cylindrical charges of a constant 38mm diameter.

The transient deformation of the test plates was captured using high speed Digital Image Correlation (DIC), which utilized two high speed cameras to record the experiments. Extensive modifications to the blast pendulum to incorporate the cameras was necessary to adapt this technique in a different method to that used in previous literature. The mounting method proposed allowed the cameras to record the experiment while capturing the impulse imparted on a test plate using a blast pendulum.

The experimental plates exhibited only Mode I failure, which is plastic deformation, enabling the effect of different loading configurations on the transient and final plate deformation profiles to be identified.

Numerical simulations of the experiments were developed to further the understanding of the load arising from the three configurations and the deformation mechanisms involved. The experimental results are used to validate the numerical models, which allow for a better understanding of the evolution of the deformation and strains across the plate. The transient data for the numerical simulation and the experiments were found to match closely.

This work clearly shows the effect that the different loading conditions have on the tests plates, specifically the impulse distributions and transient strain in the plates.

It was observed in this study that the impulse imparted on a test plate increases with the addition of sand while keeping other test conditions constant. The impulse recorded was observed to increase by 490-540% and 19-100% when compared to AIR and VBP 50mm SOD tests respectively. The loading profile acting on the test plate as a result of the specific impulse changes significantly with the inclusion of sand. The midpoint deflection increases with a decrease in stand off distance, increase in charge mass, increase in level of confinement or the inclusion of an overburden of sand. The observed increase in midpoint deflection of between 90-160% and 30-40% when compared to AIR and VBP 50mm SOD tests respectively was reported. The transient plate profile does not match the final deformation profile.

Acknowledgements

It is a pleasure to recognise those who made this thesis possible.

First and foremost I would like to thank my supervisor, Professor Langdon, for her support, advice and encouragement. I honestly would not have been able to accomplish this research without your assistance. To Professor Nurick, who has always featured as a sounding board, always willing to share your experience and knowledge with the next generation of students, your are and always will be an example of how to teach people.

My sincere thanks go to the Mechanical Engineering workshop staff especially Glen Newins, Pierre Smith and Dillon Jacobs who were the machinists I had the pleasure of working with. To Mr Hubert Tomlinson who was responsible for running the laboratories in Mechanical Engineering, you taught me more than I think you realised, we were all sad the day you retired.

Financial support from the National Research Foundation (NRF), David and Elain Potter foundation and Oppenheimer Trust without whom this work would never have been possible.

To the Staff in the Centre for Materials Engineering, thank you to each of you for your support and assistance during this project.

The the other staff and students in BISRU who created the unique working environment which allowed us to learn so much from one another.

To my friends and flat mate who saw me through the hard times even when you didn't understand what I was talking about.

To my family who have always been an unwavering source support and encouragement. For the many cups of tea and meals we had over the years. I would particularly like to mention my grand parents who are no longer with us, my two grandfathers who were both engineers and encouraged me so much with my studies and my grand mother who all graduated from UCT, I am proud to have followed in your footsteps.

Contents

List of Figures

List of Tables

Chapter 1

Introduction

1.1 Background and Motivation

The threat of an explosive event is foremost in the minds of an increasing number of people. Much work has gone into the detection of explosives prior to detonation and the prevention of detonation, however if explosives are detonated in close proximity to people, prevention of injury or loss of life becomes a critical objective.

The design of protective measures in the event of a detonation requires a sound understanding of the mechanisms involved in the evolution of a detonation. In order to design effective means of protection, the blast itself needs to be better understood. The differences between free air blasts and buried charge explosions, and the mechanisms which result in damage need to be investigated. When assessing protection, a better understanding of the mechanisms and phenomena of free air blasts and buried charge explosions on plated structures will reduce injury and mortality.

Landmines are a prevalent problem throughout the world. According to the Landmine Monitor Report [1], more than 64 geographic areas around the world are mine-affected. Landmines have a lasting effect, putting civilians and demining forces at risk. Improvised Explosive Devices (IED) have become a more prominent threat in the battle field and also in civilian settings. Many of these improvised devices are buried in order to avoid detection. The US army has reported a decrease in military casualties as a result of IED's, down form 368 in 2010 [2], to only two in 2016 according to the database maintained on the Operation Enduring Freedom (OEF) website [3]. The UN mission to Afghanistan reports that 713 civilians were killed as a result of IED's in

2015 [4], with the landmine monitor report stating that 1672 civilians were killed in 2015 in all monitored areas around the world [1]. In order to develop effective counter measures to these threats a better understanding of buried charges and the resulting mechanisms are needed.

Due to the small volume of reliable data available in open literature from actual landmine blasts, deformable plates are often used in laboratory scale experimental configurations to ascertain information about the blast. There is little full-scale explosion test data available as these tests are often classified by the military or are prohibitively expensive and time consuming to perform. Small scale testing offers a number of advantages such as being able to increase the number of tests performed by reducing the expense of the experimental work. The test process can be better controlled with regards to:

- accurate measurement of explosive size
- accurate positioning of the explosive
- easier to shape the explosive in different configurations (spherical, disc shaped of various diameter to height ratios)
- stand-off distance from soil level to target structure, and
- calibrated and controlled measurement of the impulse

The link between the small scale experimental and the full scale testing is being able to scale the work. Some work on scaling the response of plates [5, 6] has been performed and showed promising results. Most available studies [5–7] have focused on the permanent deformation response of structures, as transient response has been difficult to measure. Difficulties include the extreme environment (high temperature and pressure), the speed of the response and the cost of accurate measurement equipment suitable for these environments. Transient test data would greatly improve the validation of the numerical models and provide useful insights into the deformation and failure processes that cannot be inferred from post-test plate measurements.

1.2 Thesis Objective

The aim of this thesis is to compare the transient response of laboratory scale test plates subjected to explosive loading from air blasts and buried charge explosions with a shallow depth of burial. This comparison will fill a gap in the literature which allows the effect of the sand to be identified, with the aim of eventually being able to improve experimental scaling between full size and laboratory experiments. The three loading configurations used to assess this are:

1. Free air blast (referred to as AIR)
2. Metal-backed charge (referred to as VBP)
3. Buried charge (referred to as SBP)

The objective of the thesis is to capture and evaluate the transient response of mild steel test plates subjected to the effects of sand and metal back plate charge explosive loading.

1.3 Scope and limitations

Small scale explosive charge detonations were performed to assess the transient and permanent deformation response of the test plates to the AIR, VBP and SBP loading conditions. Material characterisation of the test plates was performed to provide data for use in the numerical simulations. Numerical simulations were performed using LS Dyna to investigate the loading and response of the test plates. The numerical simulations results were compared to the corresponding experiments. Once validated, aspects of the numerical model results which could not be directly measured in the experiments were used to provide further insight into the differences between free air and buried charge explosions.

This investigation is limited to explosive charges manufactured from Plastic Explosive number 4 (PE4) with a maximum allowable charge mass of 75g. The blast test plates were manufactured from thin sheets of Domex 355MC steel with an overall size of 400x400mm with a 300mm diameter exposed circular area. The sand used for the buried sand charges was common builders sand, locally available in South Africa.

Three configurations (AIR, VBP and SBP) are used to examine the effect of blast media (such as air and sand) and metal backing on deformable test plates. PE4 charges of varying quantities were detonated at fixed stand off distances (SOD), and the response of the test plates measured by means of high speed imaging and digital image correlation.

1.4 Thesis Development

Chapter 2 contains a literature review, which covers the background to explosive loading of structures, air blasts, buried charge explosions and numerical modelling. A brief background on experimental measurement techniques which have been used in the literature, such as Digital Image Correlation (DIC) and pressure measurement devices, is given for blast loading.

Chapter 3 describes the experimental method, where the AIR, VBP and SBP loading conditions are defined. The development of the experimental equipment and the measurement techniques are explained.

Chapter 4 contains the experimental results. The results are grouped by the individual loading conditions and simple descriptions of the results are presented.

Chapter 5 covers the characterisation of the test plate material, with specific emphasis placed on the characterisation of the steel parameters required in the numerical model. The quasistatic and dynamic material tests are presented together with the material optimisation scheme used to define the final material model used in the numerical simulations.

Chapter 6 describes the three numerical models that were constructed to represent the three loading conditions. The boundary conditions in each model represented that found in the experimental arrangement, while keeping common elements such as the test plate material and equations of state for the individual elements unchanged. The summary results from the simulations are presented at the end of Chapter 6 for each of the simulated loading conditions.

Chapter 7 covers the discussion of the experimental and numerical results, and the

comparison of the three loading conditions. The differences in the loading conditions are highlighted and reasons for them are discussed.

In Chapters 8 and 9 the conclusions and recommendations respectively are presented.

Chapter 2

Literature review

This literature review starts with a brief outline of the basics of free air blasts, followed by the fundamentals of buried charge explosions. The response of deformable plates subjected to these loads is then reported, followed by the effect of clamping along the boundary. Numerical modelling options and possible experimental tools and techniques available are explored and reviewed.

2.1 Explosions in air

The rapid release of energy in an explosion generates a blast wave which propagates through the medium in which the blast occurs [8, 9]. In air, the blast wave is a region of highly compressed air which travels outwards and interacts with any objects in its path. This interaction imposes dynamic or impulsive loads on objects which can cause deformation and failure. In reality, the pressure history of a blast load is extremely complex, but is often generalised to the form shown in Figure 2.1, which represents the idealised pressure-time history resulting from a free-air far field explosion.

In air, the peak over-pressure is followed by an under pressure, which is smaller in magnitude but has a longer duration than the positive phase. The under-pressure, also know as the negative phase, is often neglected but could be of importance in some cases, such as glazing. The pressure profile has often been simplified as a triangular or rectangular pulse for modelling purposes. Examples of the pressure-time history simplifications are shown in Figure 2.2

The magnitude of the generated overpressure will differ with explosive type, detonation point and stand off distance [8–11]. The blast wave will travel radially

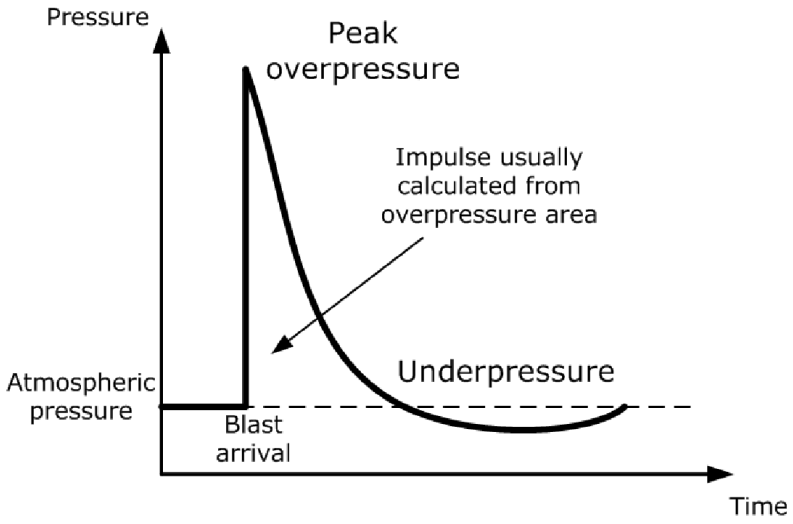

Figure 2.1: Typical free air blast pressure profile [8, 9]

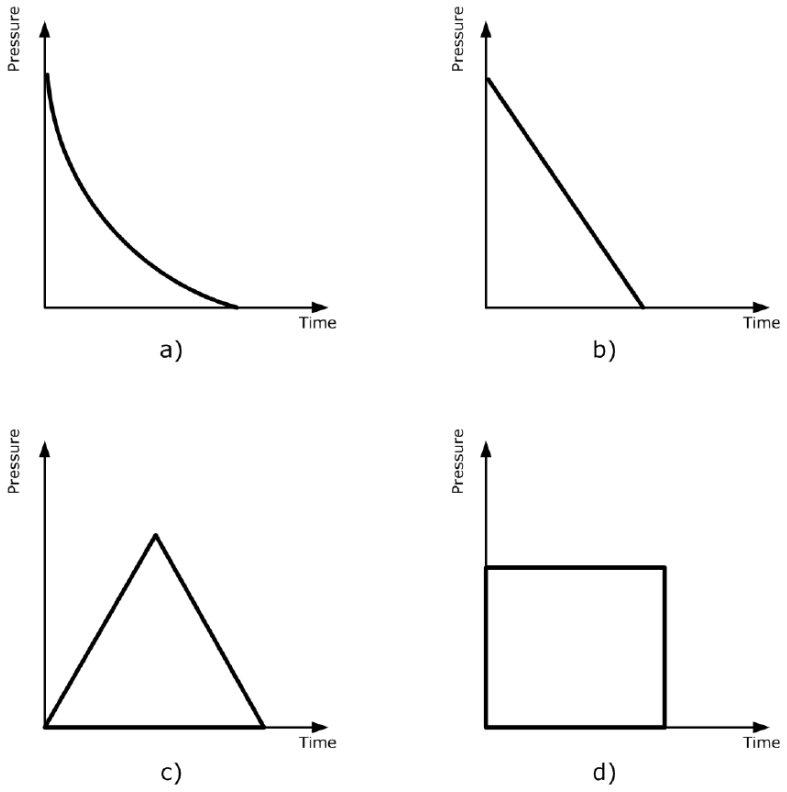

Figure 2.2: The different representations of the pressure profile for air blasts.

outward and interact with surrounding structures transferring energy to them during this interaction. Baker [12] defined an impulsive load as one where the product of the loading duration $\boldsymbol{t_d}$ and natural frequency of the structure $\boldsymbol{\omega}$ is less then $\mathbf{0.4}$.

When investigating explosive detonations, the shape and density of the produced overpressure front will vary with charge geometry and the detonation point, resulting in a detonation front moving through the explosive [9, 13]. Kennedy [13] reported that the axial impulse component from a cylindrical charge detonation has a limit linked to the ratio of the charge height and diameter. This effective charge mass, in the case of a cylinder, is a 60°cone seen in Figure 2.3 radiating inwards from the target face of the charge. The remaining portion of the charge is said to contribute to "side losses" which do not increase the axial component but rather expand the impulse profile radially.

Further work on this subject can be found in references [14, 15] where a thorough explanation of the effects of charge geometry and detonation point on the development of the blast wave are given.

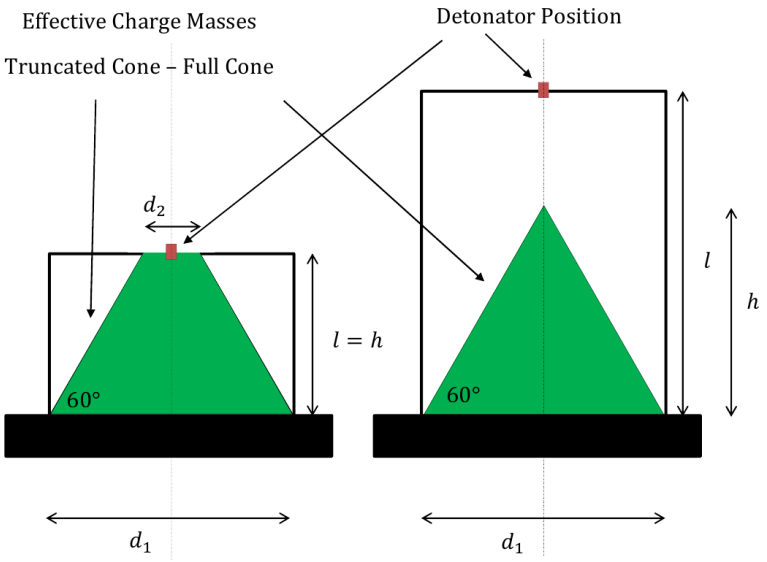

Figure 2.3: The conical portion of a cylindrical charge (shown in green) which contributes to the axial impulse as reported by Kennedy [13], taken from [16].

2.2 Buried explosions

Interest in the effects of buried charge explosions stems largely from their use against vehicles in the form of landmines or buried IED's. The NATO Stanag 4569 AEP-55 Vol 2 [17] standard provides a reference guide for the standardised testing of vehicles subjected to simulated mine detonation. Two key approaches are specified for simulating a mine; a buried charge in a sandpit, and on a metal plate shown in Figure 2.4 [17].

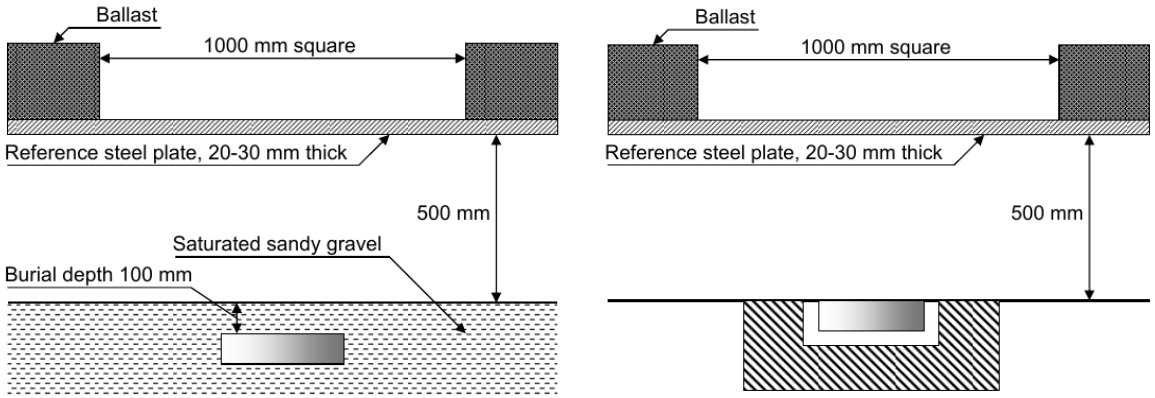

(a) buried charge (b) steel pot

Figure 2.4: The proposed configuration from the NATO AEP-55 [17] standard specifying the two methods for simulating a mine blast on a vehicle with (a) charge buried in sand and (b) mounted on a metal plate called a steel pot.

Explosions in, or on, the ground transmit energy to their surroundings, i.e., to the ground, the air and nearby structures. This energy release takes many forms, including heat, air and soil kinetic energy, soil deformation and work done by expanding gaseous products. Several factors affect the energy partition. For example, when an explosion occurs far under the surface of the ground, the energy is totally absorbed by soil deformation, mechanical losses and thermal losses [18]. This kind of explosion is called a camouflet, since the detonation products are completely contained in the ground and no air shock is generated. While this is of little interest to the current work, it does represent the lower limit of a buried charge output. At the other extreme is a surface detonation on frozen soil (similar to Figure 2.4b), where very little energy is transmitted

to the ground and the air shock and impingement of the detonation products do the majority of the work on nearby structures. The area of interest lies between these limiting cases where the explosion occurs in a shallow layer of soil near the surface.

Bergeron *et al* [18] described the detonation of an explosive buried in soil. The work produced data from X-ray diffraction showing the transient evolution of a buried charge shown in Figure 2.5. A key aspect of the work by Bergeron [18] was the identification of three temporal phases in a buried charge explosion:

Phase I: the detonation of the explosive and the ensuing soil interaction

Phase II: expansion of the gaseous detonation products

Phase III: the development of soil ejecta.

Phase I: The detonation produces a shock wave in the surrounding soil [18,19]. When this shock (traveling through the soil) reaches the soil-air interface, it largely reflects as an expansion wave. Only a small fraction of the incident shock is transmitted into air. The large difference in acoustic impedance between soil and air causes the resultant air shock to have minimal influence on the target structure [20]. Consequently, in buried charge explosions, the primary loading of the structure is caused by impact of soil ejecta and gaseous expansion, associated with phases II and III.

Phase II: When the compressive wave reaches the soil-air interface, it is partly transmitted to air as a shock, but mostly reflected back toward the centre as a tensile wave. The tensile wave combines with the expanding high-pressure detonation products, to hemispherically expand the soil into the surrounding air (seen in the first 5 frames of Figure 2.5), which eventually results in ejection of a soil cap. This process occurs within the first millisecond.

Phase III: The high-pressure gas in the soil continues to do work on the walls of the cavity created by the explosion. Soil continues to be eroded and ejected at high speed for tens (sometimes hundreds) of milliseconds. The trajectory of the associated ejecta is generally in the upward direction, within an inverse cone having included angle (between 60 and 90 degrees) that increases with either decreasing depth of burial or looser soil [18].

In Figure 2.5 the X-Ray diffraction images captured by Bergeron *et al* [18] show the progression from phase II to phase III in the last frame shown. It should be noted that

in the last image of Figure 2.5 the explosive products appear to have broken out from the buried camouflet indicating that the explosive products may play some part in the loading of the structure together with the impulsive loading of the sand ejecta. This is contentious issue currently being dealt with in the literature and has implications on the most appropriate methods for modelling a buried charge.

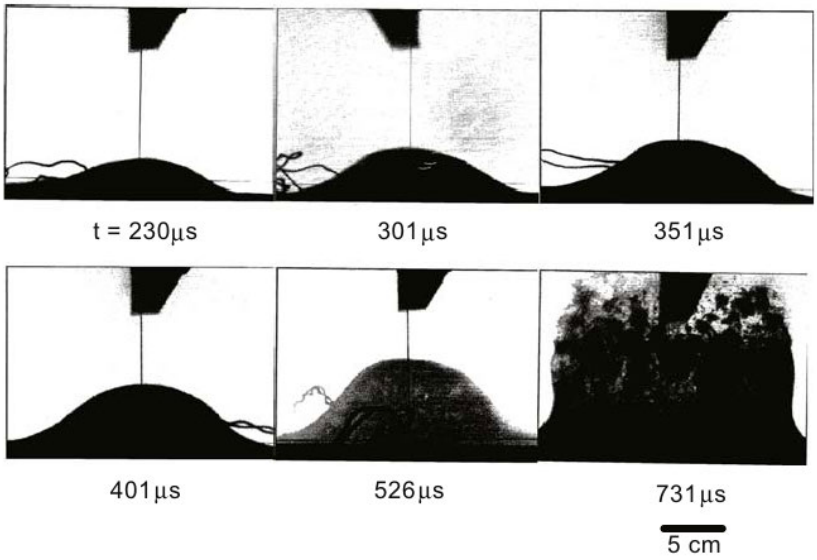

Figure 2.5: The X-RAY diffraction images captured by Bergeron *et al* [18] of a buried charge explosion.

The effect of buried charges on structures has been extensively reported on in references [20–28]. The effects of different blast conditions has been experimentally researched with many researchers focusing on localised response of test plates as a primary metric, then further developing techniques to capture and report impulse by different methods. One significant weakness in the literature is the reporting and quantification of the soil type and conditions in these tests.

Recent work by Clark and co-workers [27, 29–31] attempted to describe and fully characterise the geo-technical conditions under which the buried charge explosion tests were performed. The work was a direct comparison to previous work done by Dynamics Effects Laboratory at the University of Maryland, USA [32–34], except that a different sand was used. Tests often measure pressure on a rigid plate with pressure transducers or Hopkinson bar arrangements because it is not always possible to measure the pressure on a deformable plate. The results reported by [31] are shown in Figure 2.6, which compared the pressure data recorded on a rigid plate with Hopkinson bars at different

radial distances from the plate centre. The two trends are similar with peak central pressure of approximately 250 MPa, decreasing to about 50 MPa at a radius of 100mm.

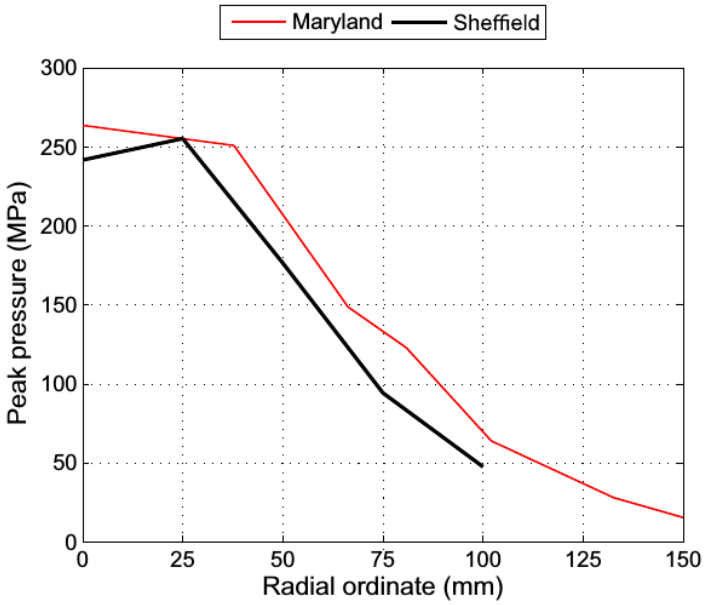

Figure 2.6: Discrete pressure measurements at radial gauge points comparing two sand types under the same experimental conditions, from [31]

Leiste [34] reported the pressure profiles for different buried charges in saturated sand using a Hopkinson bar array. Figure 2.7 shows the pressure measured at different gauge points from the centre of the plate. The pressure profile was sometimes irregular and often contained discontinuities such as those displayed in Figure 2.7. The peak pressure was at the plate centre, while at 0.57in from the centre, the pressure is only slightly lower. There was a significant decrease in pressure at an intermediate gauge point (0.4in). The profiles varied through the tests and often included discontinuities in the pressure loading reported leading to specific impulse profiles shown in Figure 2.8.

The impulsive loading profile on a test plate is clearly described by Figure 2.9 [31] which shows an example loading broken down into distinct phases:

- pre-curser shoulder
- "shock" pressure

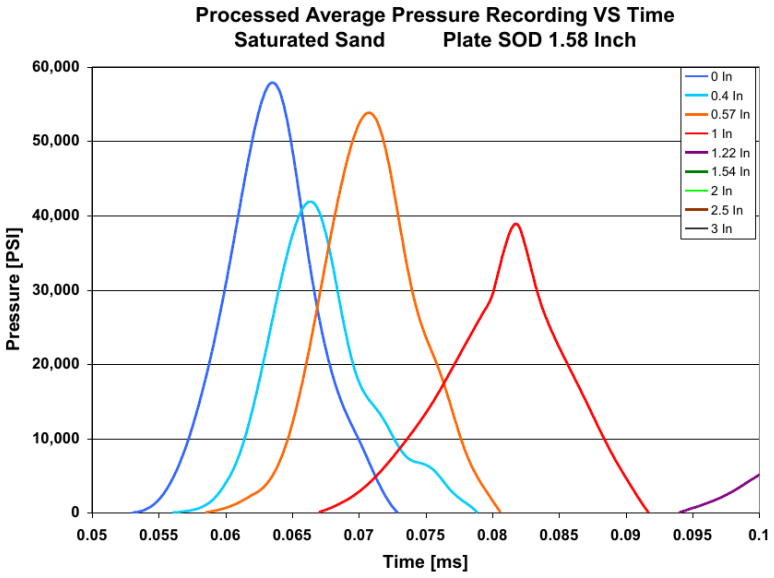

Figure 2.7: Pressure measured at discrete gauge points from the centre of a buried charge test in saturated sand [34]

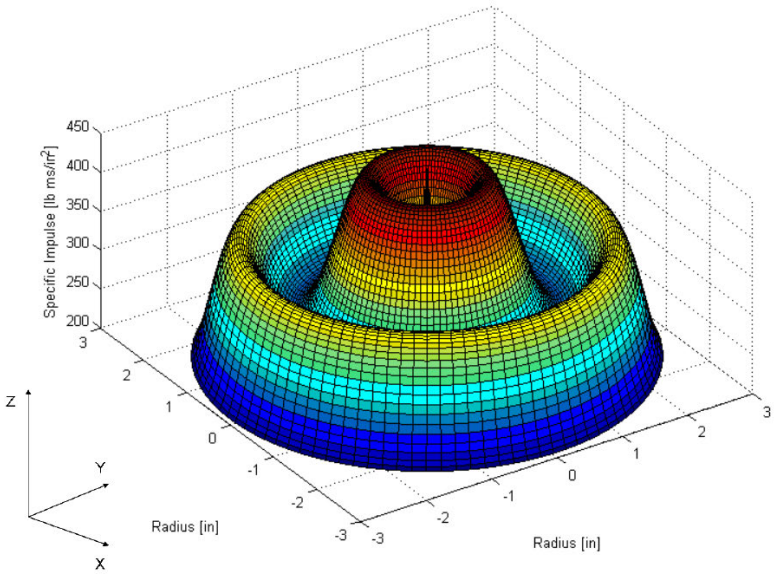

Figure 2.8: Profile of specific impulse for a test performed by Leiste [34] on a 3 inch diameter area.

- post peak shoulder
- long term loading 1MPa

The durations of these phases are reported to change with scaling, but were evident in experimental work considered. The long term loading is reported to effect the overall peak displacement of numerical simulations in the work, as well as the predicted numerical impulses.

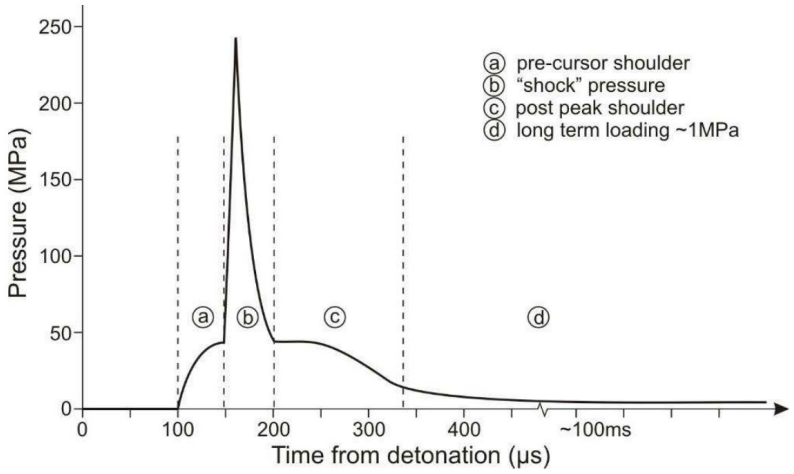

Figure 2.9: The typical loading profile experienced by a plate subjected to a buried charge explosion [31] (Durations dependent on scale)

2.3 Response of circular plates to air blast loading

Extensive experimental studies have been carried out to understand the large permanent ductile deformation and rupture of plates, beams and shells due to blast loading conditions in air. Jones [35] and Nurick and Martin [36, 37] present overviews of theoretical and experimental studies of plates that are uniformly loaded over the entire plate area. Further studies have been carried out to investigate different boundary conditions (clamped or built-in) [38, 39] and loading conditions (localised loading) [40–42]. This work [5, 6, 18, 20, 36–39, 43, 44] was for impulsively loaded plates and specifically examined the permanent deformation of the structures.

Menkes and Opat [43] were the first to define three modes of failure for blast loaded clamped beams. The three modes were observed as the applied uniform impulse was increased. The three modes were classified as:

Mode I: large inelastic deformation

Mode II: large inelastic deformation with tensile tearing at the supports

Mode III: transverse shear failure at supports

Similar modes of failure, for uniformly loaded plates, were reported by Teeling-Smith and Nurick [45] for fully clamped circular plates and by Olson, Fagnan and Nurick [46] for fully clamped square plates. Nurick, Gelman and Marshall [47] identified other modes of failure within Mode I, defined as:

Mode I large inelastic deformation: no necking

- **Mode Ia** large inelastic deformation: necking at places on the boundary
- **Mode Ib** large inelastic deformation: necking around entire boundary

Some additions to Mode II were defined by Nurick and Shave [48]:

Mode II* partial tearing at the boundary

- **Mode IIa** complete tearing with increasing midpoint deflection
- **Mode IIb** complete tearing with decreasing midpoint deflection

It should be noted that the above descriptions are limited to elastic-plastic solids such as metals and are not applicable to all materials.

2.4 Influence of clamping

Limited work has been published on the influence of clamping and boundary conditions. Bonorchis *et al* [38] performed a thorough experimental study looking at the effects of different boundary conditions on the failure mechanisms of plates. It was clearly noted that the clamped configuration had the highest failure threshold due to pull-in occurring within the clamped region which reduced the edge constraint. It is important to have identical boundary conditions in all experiments as they influence the failure mechanism. Photographs of the four different boundary conditions used by Bonorchis [38] are shown in Figure 2.10.

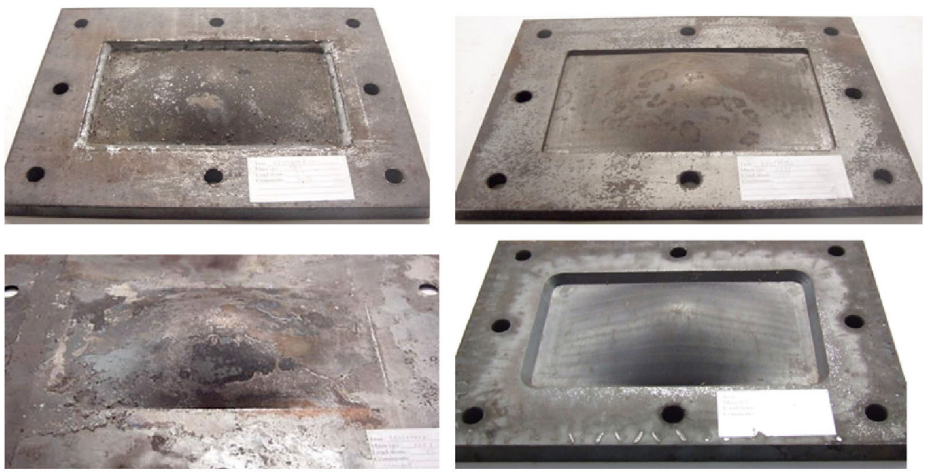

Figure 2.10: Photographs of the various boundary conditions. Top left proceeding clockwise: welded, straight machined, chamfer machined and clamped. [39]

Bonorchis and Nurick [49] also reported the differences between modelling rigid and deformable boundary conditions and the effect on rectangular deformable plates exposed to localised blast loading. The influence of clamp height (the perpendicular distance from the deformable plate surface) was also investigated. All the results presented are from Autodyn simulations of the experimental arrangement representing a 15 + 1 g PE4 detonation. The three cases that were examined are:

- No clamps (where there is no clamped boundary)
- One clamp height

- Two clamps (Doubling the clamp height)

Increasing the clamp height created some confinement at the boundary which increased the gas pressure as the pressure front reached the boundary. This is evident in the impulse density graph shown in Figure 2.11, where the pressure increase is observed at the plate periphery.

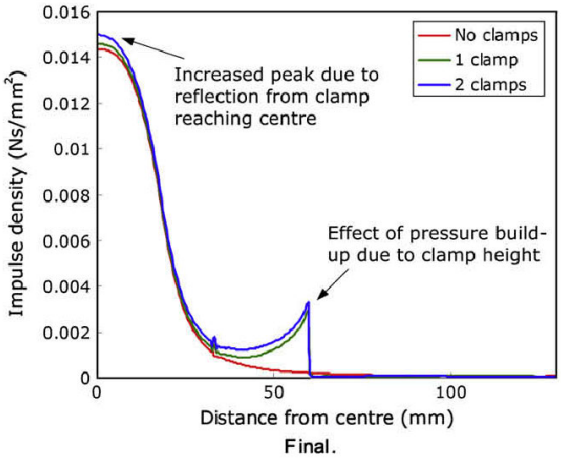

Figure 2.11: The simulated impulse density reported by Bonorchis [49] due to clamp boundary effects.

2.5 Scaling response to explosion

Scaling of explosive events has a long history dating back to Hopkinson [50] and Cranz [51] who studied how scaling could be employed for quantifying the effects of different spherical air blast waves. When studying a specific physical property, Hopkinson [50] and Cranz [51] showed that the distance from the centre of the explosion and the time at which it is evaluated are proportional to the diameter of the spherical charge. Advances in instrumentation have led to many new studies to try and quantify these scaling effects.

The work reported by Jacob *et al* [52] was performed on rectangular plates of varying length to width ratio and different thickness. The effects of varying both the loading conditions and the plate geometries on the deformation are discussed. A modified dimensionless number was presented for quadrangular plate displacement when subjected to localised blast loading. In addition, numerical predictions were performed and compared with experiments for a limited selection of plate geometries.

Sutton *et al* [7] provide a very good overview of scaling effects in sand blasts, using dimensional analysis to show the main terms for scaling. Sutton [7] also gave an example of an experimental arrangement and recommended using a 3D Digital Image Correlation (DIC) system to capture the out of plane displacement history of a plate along a radial line seen in Figure 2.12. Later work by Zhao and Sutton [53] expanded on collected DIC data from [7] and performed dimensional analysis to scale the two results. The work [53] proposed that scaling can be performed, for scaling factors up to 1.56 by employing the Buckingham π dimensional analysis method, seen in Figure 2.13, for very small charges in the range of 0.5 - 2.0g.

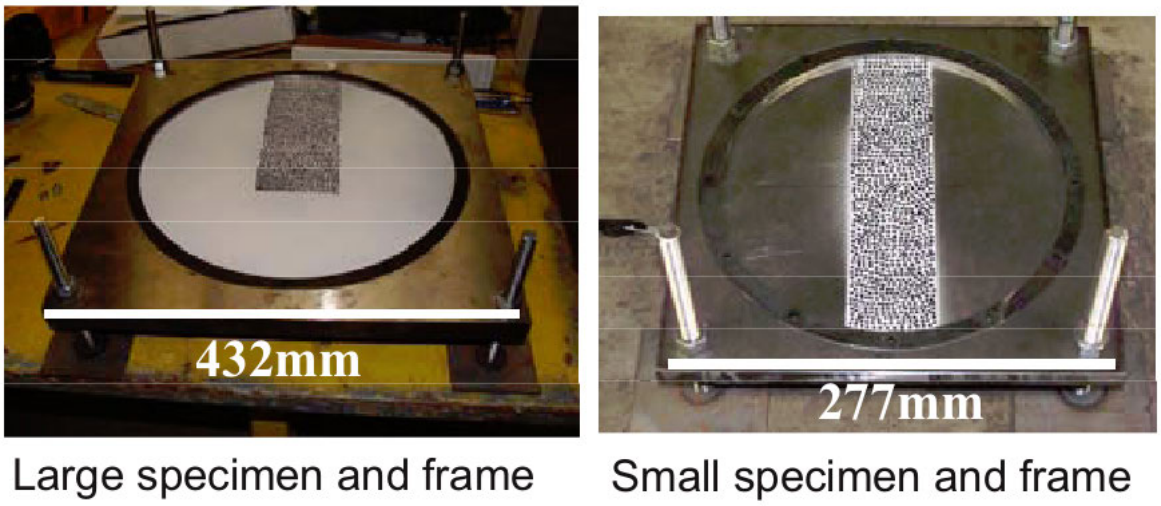

Figure 2.12: The small and large plates used by Sutton *et al* showing the radial line the authors suggest capturing using 3D DIC. [7]

Fourney et al [22] investigates a very extreme limit of scaling using charge masses up to 3.3 g of explosive which comprise RP83 detonators. The work attempted to compare very small scale detonations with experiments conducted at the Aberdeen proving grounds where the charge masses were up to 4.54 kg. A high speed camera was used to ascertain the initial velocity of the tested plates. This was possible for the first few frames of footage but measurements became erratic as the plates started to rotate. While the results left unanswered questions about the experimental methodology, an interesting experimental arrangement for investigating the effect of confinement on a buried charge was implemented. In Figure 2.14, the experimental arrangement is shown where the volume between the buried charge and the test plate was confined in a tube.

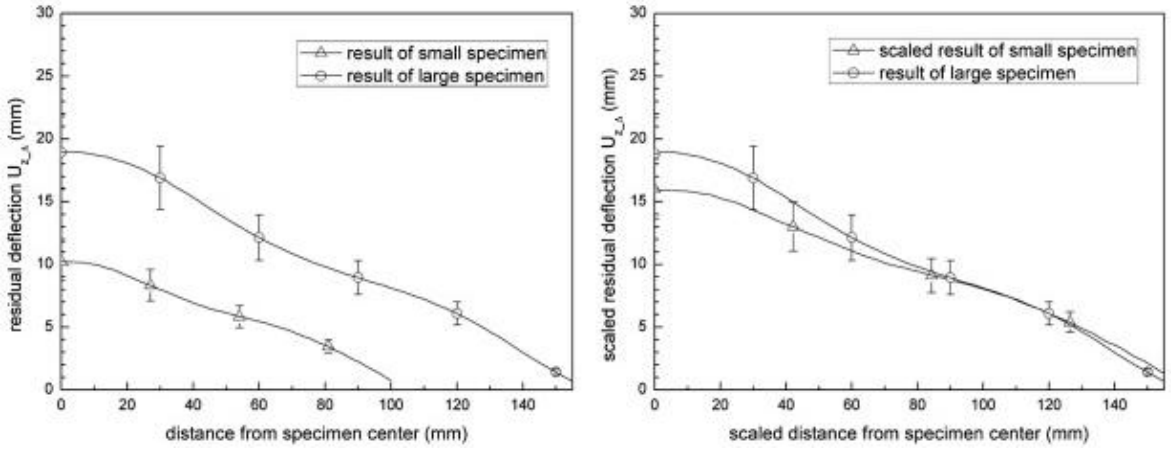

Figure 2.13: Scaling of plate deformation proposed by Zhao *et al* [53], performed on the plates seen in Figure 2.12.

Little data is reported but it is determined that the confined tests do experience a higher impulse than the unconfined tests which suspended the plate above the charge.

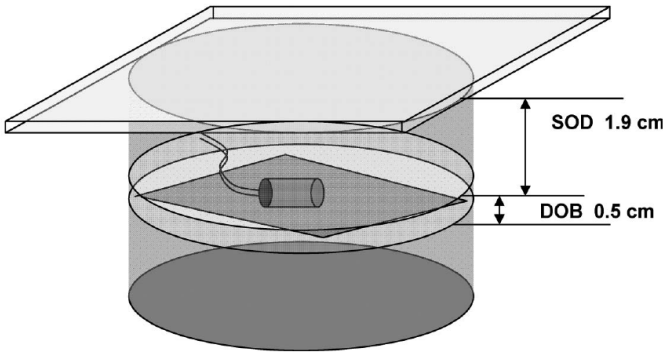

Figure 2.14: The confined experimental setup used by Fourney *et al* [22]

Neuberger et al [5,6] investigated the response of fully clamped circular plates to air blast and flush buried charge explosions with charge masses in the range of 0.4 - 8.75 kg of TNT. The test arrangement for investigating the air-blast response of the plates is shown in Figure 2.15. The spherical charge was suspended above the plate from its detonator wire. The clamp frame had a chamfer at the plate boundary, which reduced

the pressure confinement effect at the boundary, similar to Bonorchis [38].

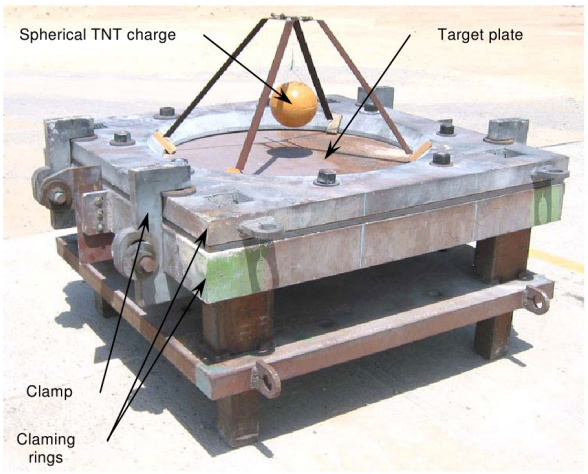

Figure 2.15: The Expermental setup used by Neuberger *et al* [5] in the air blasts.

In Neuberger *et al* [6], results from experiments involving a flush buried charge, shown in Figure 2.16, were reported. A spherical charge of TNT was buried flush with the surface and the stand-off distance between the soil and the target plate was varied. The clamp frame shown in Figure 2.15 was re-oriented to face the buried charge, and a metal measuring comb was placed on a bridge above the centre of the test plate. The metal comb was used to capture the difference between the elastic rebound and the permanent deformation of the centre of the test plate.

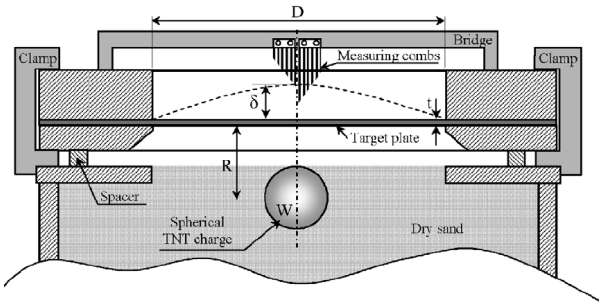

Figure 2.16: The Buried charge experimental setup used by Neuberger *et al* [6] in the buried charge experiments.

Although it was possible to scale these experiments with good agreement, the buried charge work only included one depth of burial limiting the scope of this observation in

a similar way to the work by Zhao [53].

2.6 Numerical Modelling

One distinctive characteristic of a spherical blast wave is a moving shock wave accompanied by expansion waves. The intensity of a blast wave always decays with time and distance during propagation due to its three-dimensional expansion. The propagation can be measured experimentally and compared to analytical predictions to verify them under simple conditions. Hydrocodes are able to numerically model the detonation of explosives and the resulting blast front, enabling more complicated arrangements to be analysed. The permanent deformation (Mode I) that results from the blast loading interacting with the plate is measured and commonly compared to the predicted results of the numerical models for validation purposes. Once the failure mode moves toward tearing, simple numerical models are no longer able to capture the full behaviour of a plate and more complex models are needed which include material models that can predict failure.

2.6.1 Air blasted plates

There are many authors in the literature who have reported different methods to numerically model the deformation of a plate subjected to blast loading such as [54–61] and the references contained therein.

Chung Kim Yuen *et al* [57] and Langdon *et al* [56] conducted experimental and numerical investigations into the blast loading response of quadrangular stiffened plates.The air-blast was approximated as a uniform pressure loading applied over the whole plate [57] or just the central portion [56]. The blast loading was considered impulsive due to the very small stand off distance of 13mm. The experimental observations compared favourably with their numerical simulations, indicating that the simplified loading conditions had successfully replicated the experimental conditions. Examples of the results are shown in Figures 2.17 and 2.18. It was concluded in [56, 57] that spatial distribution of the blast loading had a significant influence on the deformation profiles of the plates. This work shows that it is possible to approximate the impulsive localised blast load imparted on these plates as a uniform load applied over the central portion of the plate. Making use of this approach would have significant benefits in computational speed when compared to more complex methods that model the explosive detonation and gas products. Similarly a more uniform blast load could be approximated by applying an impulsive uniform pressure loading to the entire plate.

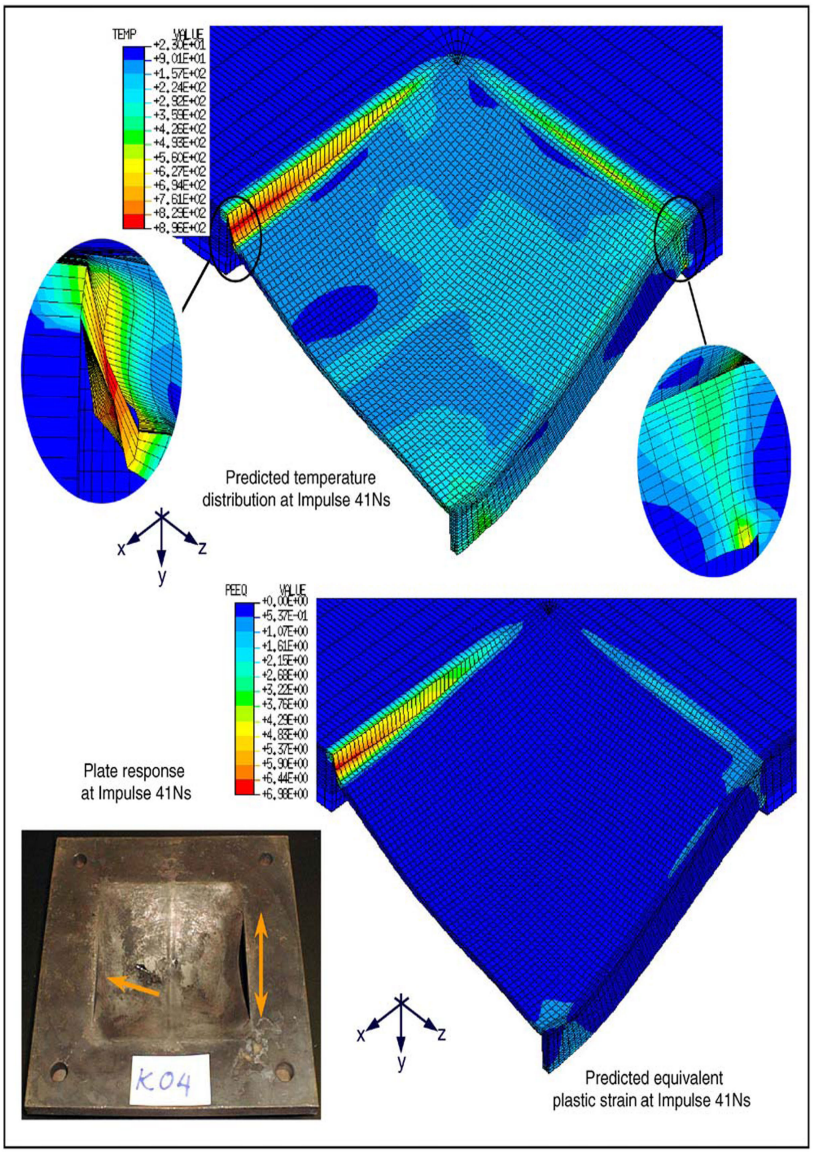

Figure 2.17: Comparison of predicted Mode II* response of a Square plate with stiffener size 4x7mm subjected to a uniformly distributed blast loading at 41Ns impulse. [57]

Balden and Nurick [54] investigated the post-failure motion of blast loaded plates and were able to simulate the failure of the plate with a 200% failure strain criteria. The results shown in Figure 2.19 illustrate how the plates failed on the boundary which closely resembled the experimental results obtained.

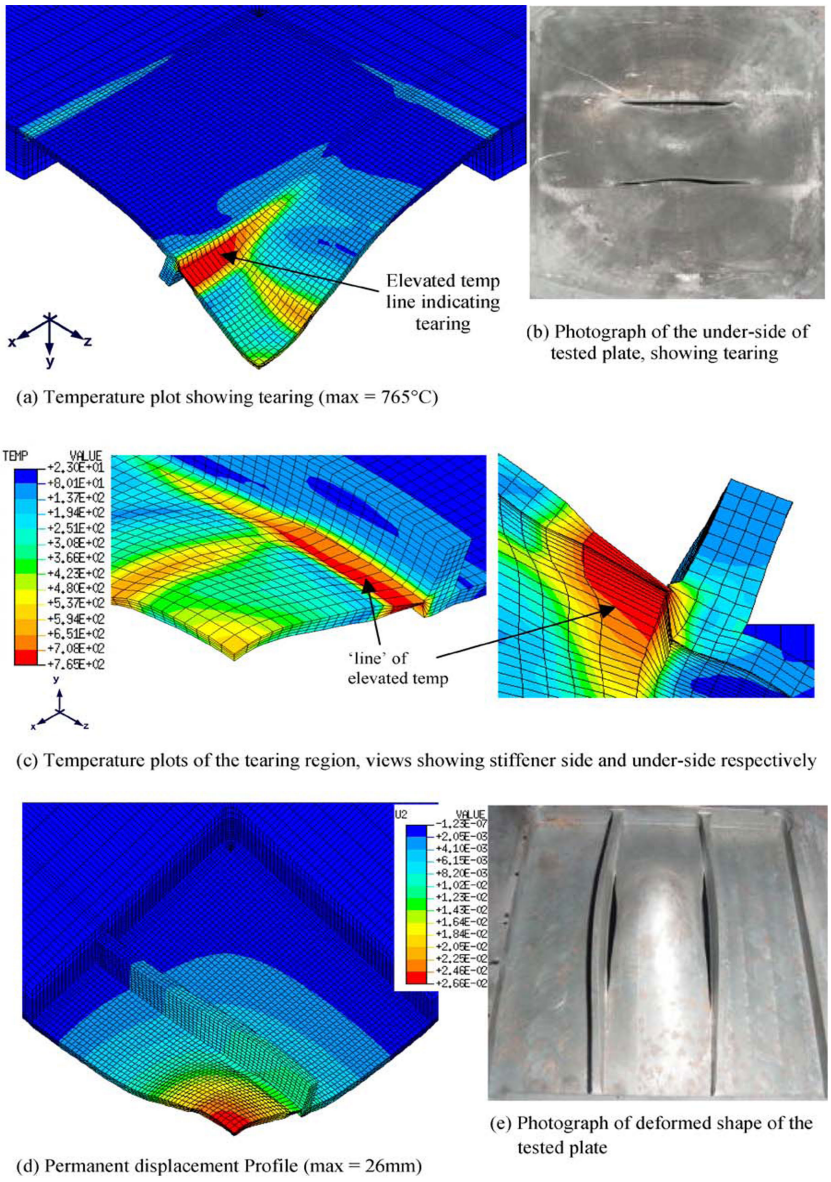

Figure 2.18: FE results showing contour plots of temperature and displacement for a double stiffened 3x7mm plate subjected to localised blast loading of 9.5 Ns impulse: (a) temperature plot showing tearing (Max = 765 ℃), (b) photograph of the underside of the tested plate showing the tearing, (c) temperature plots of the tearing region, (d) Permanent displacement profile (max = 26mm), and (e) Photograph of the deformed shape of the tested plate [56]

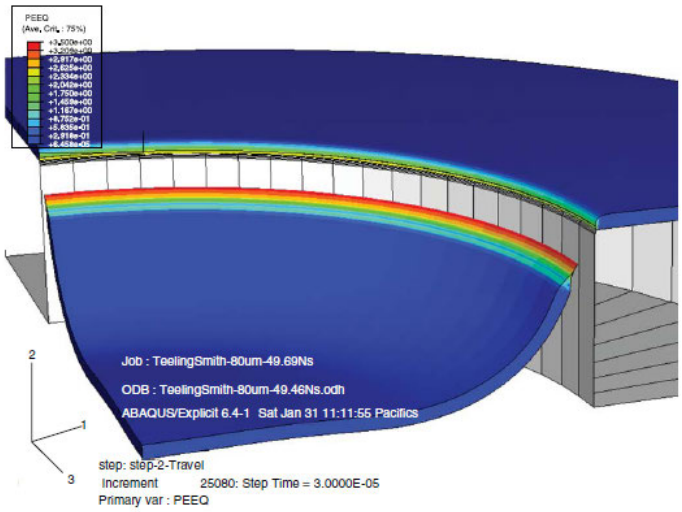

Figure 2.19: Numerical simulation results for a uniform blast impulse of 49.46 Ns showing the contour plot of equivalent plastic strain and clear Mode III failure at the support [54].

One of the most relevant damage models for the response of metals to high intensity dynamic loading is the model developed by Johnson and Cook [62] and implemented by Anderson [63] in which the equivalent plastic strain at the onset of damage $\bar{\varepsilon}_D^{pl}$, is assumed to be of the form

$$\bar{\varepsilon}_D^{pl} = [d_1 + d_2 exp(-d_3\eta)] \left[1 + d_4 ln\left(\frac{\dot{\bar{\varepsilon}}^{pl}}{\dot{\varepsilon}_0}\right)\right] (1 + d_5\hat{\theta}) \tag{2.1}$$

Where $d_1 - d_5$ are failure parameters and $\dot{\varepsilon}_0$ is the reference strain rate. $\hat{\theta}$ is the non-dimensional temperature defined as

$$\hat{\theta} = \begin{cases} 0 & \text{for } \theta < \theta_{trans}, \\ (\theta - \Theta_{trans})/(\theta_{melt} - \theta_{trans}) & \text{for } \theta_{trans} \leq \theta \leq \theta_{melt}, \\ 1 & \text{for } \theta > \theta_{melt} \end{cases} \tag{2.2}$$

where θ is the current temperature,θ_{melt} is the melting temperature, and θ_{trans} is the transition temperature defined as the temperature at or below which there is no temperature dependence on the expression of the yield stress. The material parameters

must be measured at or below the transition temperature.

Material parameters for numerical models are traditionally derived from standard material tests such as tensile, compression, bend and charpy. Spranghers *et al* [60, 64] use an inverse approach to determine the appropriate parameters for the Johnson-Cook numerical model; utilising the information from their experimental DIC results to optimise material parameters. The authors report this approach uses the full field of DIC information, yielding more accurate results shown in Figure 2.20. A similar inverse approach was followed by Bretall [65], who only managed to use a 50x50mm section of the plate for DIC and additionally made use of quasistatic tests to validate the simulated loading on the numerical plate. While these approaches are valid their reliability could be called into question as the model could be trained to synthetically give the correct answer by using non-meaningful parameters. Readers are directed to the book written by Meuwissen [66] which fully describes the inverse modelling approach specifically for modelling of metals where a very thorough overview of the field is given. Other authors such as [67–69] have successfully made use of an inverse modelling approach in their work and it has widely become accepted as an acceptable method when the calibrated models are validated with other experimental data.

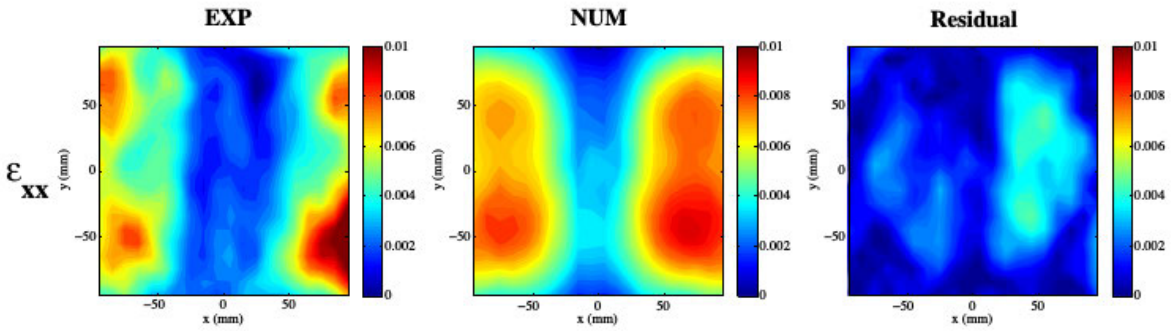

Figure 2.20: The final strain fields reported by Spranghers [60, 64] from the experimental and numerical results and the residual shown on the right. Numerical model parameters were optimised with an inverse approach. (areas of red indicate higher displacement of the test plate)

The choice of numerical method used to model a blast load varies in the literature

[42,54,55,70–73], with many authors comparing different techniques and using the most accurate, such as that shown in the work by Børvik *et al* [55], where the authors contrast the use of different Conwep models against Eulerian approaches for large stand off distances.

2.6.2 Sand blasts

In addition to the affects of changing charge mass and stand off distance, buried charge explosions are effected by the moisture content of the soil, grain size and the compaction. Hlady [21] presented a cursory investigation, varying different soil parameters and the effect these have on the impulse transferred to a "plunger like" vertical pendulum seen in Figure 2.21. It was found in [21] that loading resulting from the detonation of a landmine buried in a high moisture content, silty-clay, is significantly greater than the loading resulting from the detonation of a landmine detonated in dry sand. Rimoli [74] confirmed this finding in a series of experiments using spherical charges with varying degrees of sand saturation at a constant stand off distance.

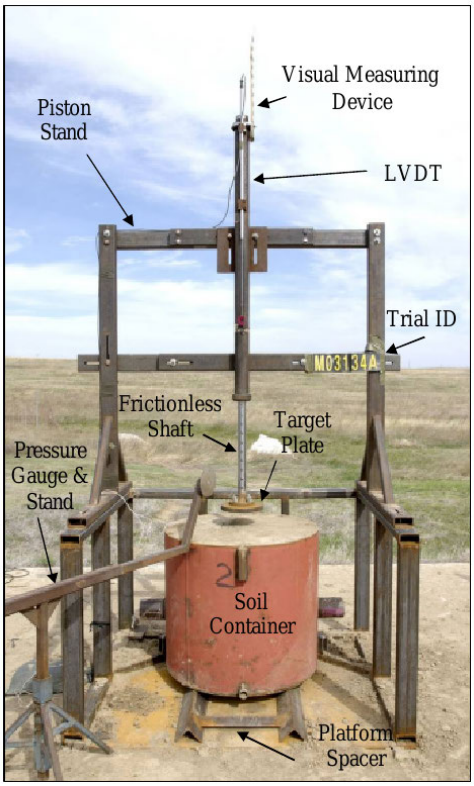

Figure 2.21: Photograph of the plunger like vertical pendulum used by Hlady [21].

Development of a robust numerical description of sand under blast loading conditions is ongoing. The work presented by Laine and Sandvik [75] presents an equation of state description for dry sand. The Sjobo sand, as it is referred to in the publication, is specifically noted to contain **6%** water and have a density of $\mathbf{1574 kg/m^3}$. The

characterisation resulted from multiple tests being performed and overlaid to describe the consolidation pressure as seen in Figure 2.22. These were used to describe the pressure over a wide range of volumetric strains. One criticism of this work is that the range of pressures for which the sand was characterised does not extend into the GPa range which is the upper end of the pressures reportedly experienced in the literature in real sand [76].

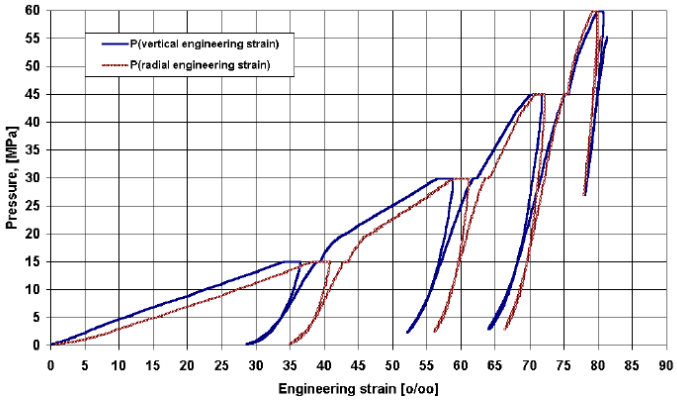

Figure 2.22: Graph of Pressure versus engineering strain used to describe the consolidation pressure of dry sand by Laine and Sandvik [75].

Grujicic [70, 71, 77–80] has investigated the different issues of sand modelling from a numerical perspective. The model developed by Laine and Sandvik [75] has been implemented in the commercial simulation suite by LS Dyna. The disadvantage of the Laine and Sandvik material model is that it is only appropriate for the sand type that it was calibrated against (dry builders sand). Grujicic [80] proposed a new sand model that allows sand type, moisture content and compaction to be accounted for. Due to a reported lack of published data on clay soil, the developed model was reportedly calibrated against the work conducted by Froedinger *et al* [81].

Barsotti and Sammarco [82] provided a more specific look at implementations of sand models in LS Dyna. The authors specifically looked at the Arbitrary Lagrange Eulerian (ALE), Finite Element Method (FEM), Smooth Particle Hydrodynamic (SPH) and Discrete Element Method (DEM) approaches that could be applied. The majority of sand properties were extracted from the work by Laine and Sandvik [75], but comparisons are also made to the work by Kerley [83–85]. According to the work by Kerley [83–85], the Laine and Sandvik model [75] can be adapted for different sand

conditions by altering the density of the sand in the model. Modifications to account for different levels of saturation in the sand are proposed, based on the three-spring model seen in Figure 2.23. Different stiffnesses for the air void fraction, water and sand fractions were proposed.

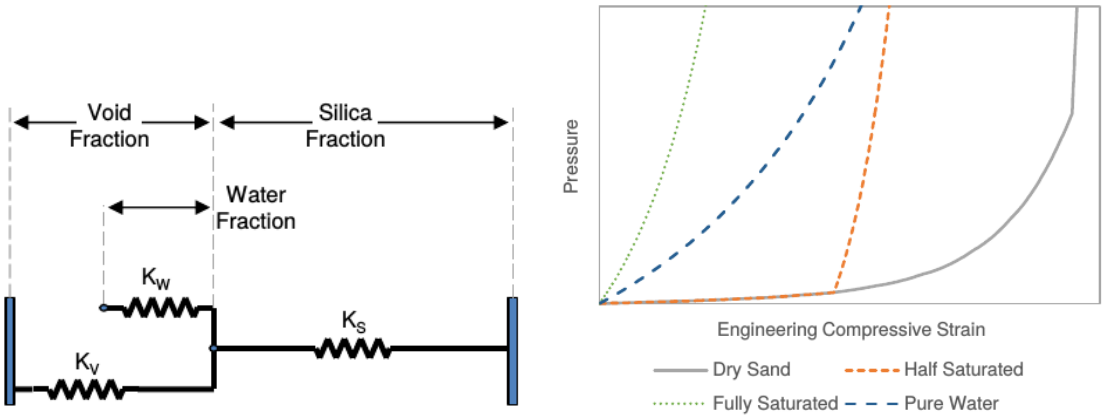

(a) The three-spring model

(b) Different soil conditions

Figure 2.23: The Three-Spring compaction model proposed by Barsotti [82] with the relative effect of soil composition.

The four approaches (namely ALE, FEM, SPH and DEM) investigated by Barsotti and Sammarco [82] were compared to the previous work by Bergeron [20], as seen in Figure 2.24. The evolution of the camouflet of sand produced by the expansion of the explosive products from the different models on the right of the image is compared to the original images captured by Bergeron [20]on the left. The ALE approach, shown in Figure 2.24, reliably reproduces the geometry of the sand as well as the impulses transferred to the plates. While methods such as DEM might be able to more precisely capture the deformation of the sand at a much higher computation cost, other approaches such as ALE have been shown to be able to sufficiently reproduce the impulse transfer to the structure which is of greater concern in an investigation.

Extensive work has gone into numerically characterising sand, for example, Grujicic [70, 71, 77–80], Børvik *et al* [86], and Barr [76, 87] reported experimental results used to calibrate their numerical models. This work is extensive, but at present is only applicable to specific models which are calibrated to individual sands.

In a technical report by Schwer and Rigby [88], the experimental work conducted

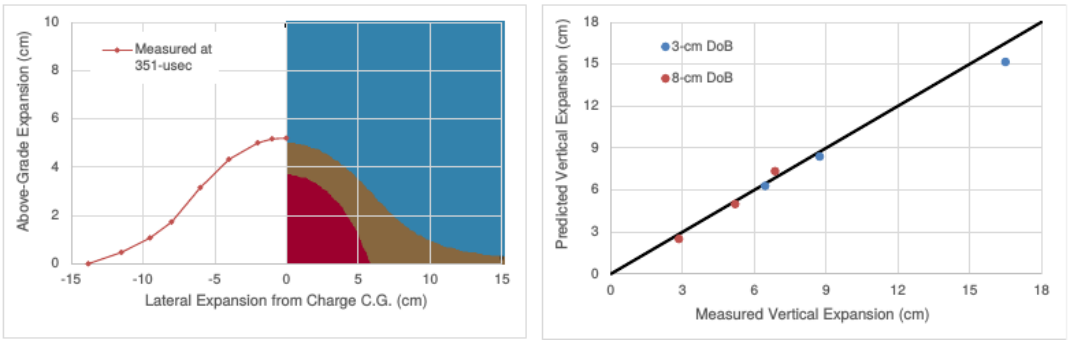

(a) ALE model

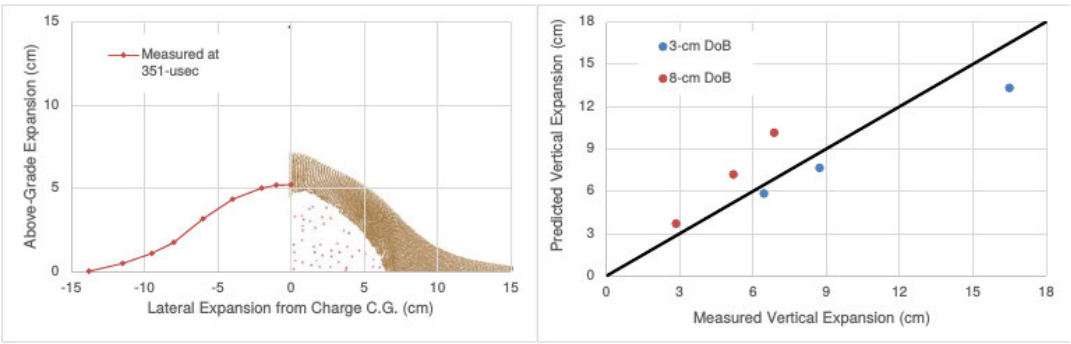

(b) SPH model

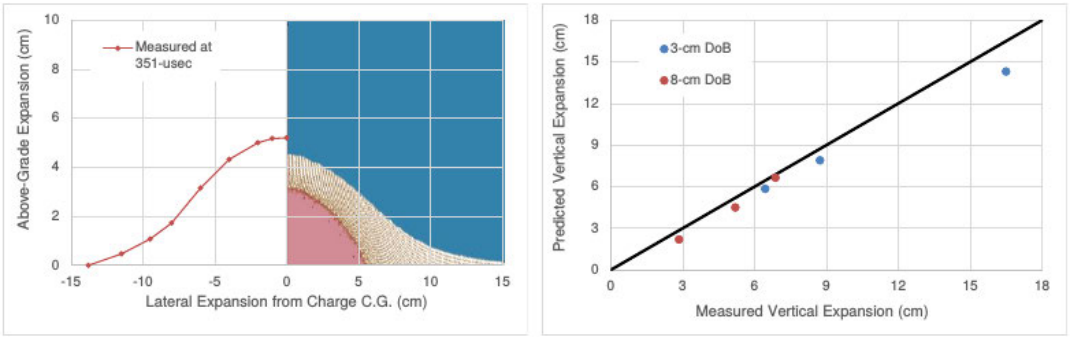

(c) Hybrid ALE-SPH

Figure 2.24: The results of different modelling approaches shown on the right replicating the experimental data shown on the left [82].

by Clarke *et al* [31], was numerically modelled to compare the pressures obtained in the simulations with the results from the Hopkinson bars in the original experimental work [31]. Schwer and Rigby [88] developed an axisymmetric model of the experimental configuration with the cylindrical charge buried in sand and placed tracer points in the simulation at the same position as the Hopkinson bars, seen in Figure 2.25. Typical

numerical model results are shown in Figure 2.26. The pressures reported at these tracer points exhibited huge variation, with some models reporting pressures two or three times that measured experimentally. By integrating the pressure readings at these pressure points, a specific impulse was obtained and compared to the results from the experimental work, as shown in Figure 2.27 for a typical test. Both the numerical (dashed) and experimental (solid) specific impulses seen in Figure 2.27 exhibit the same general shapes, however there is mismatch in the magnitudes of the specific impulses and generally the numerical results lag the experimental visibly. At the point closest to the plate centre (green), the numerical result roughly tracks the experimental result at a slightly lower value, however the next point over (black), the numerical result is reporting about one third of the impulse observed experimentally. These mismatches indicate that there is still much work to be done in the area of numerical modelling of sand.

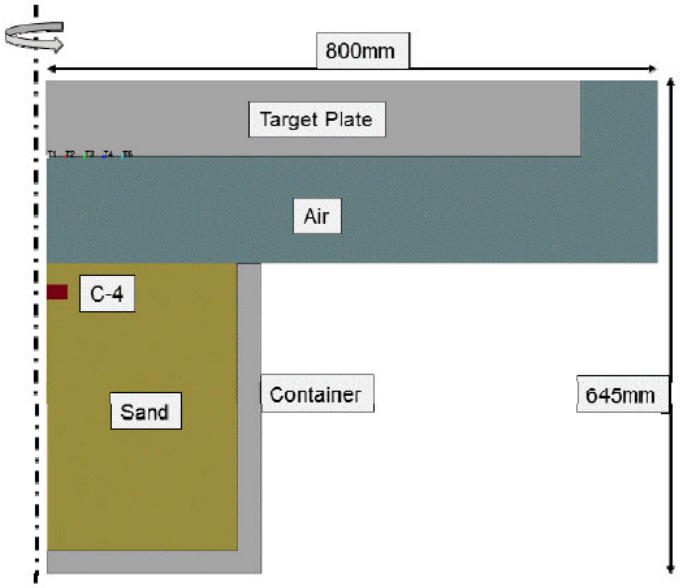

Figure 2.25: The Axis symmetric numerical model devolved by Schwer to replicate the experimental results by Rigby at the University of Sheffield [88]

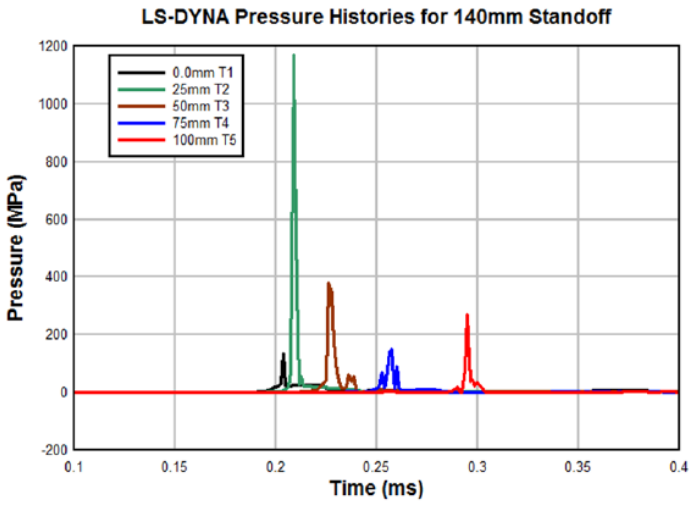

Figure 2.26: The pressure recorded in the simulations by Schwer [88] at the tracer points T1 - T5.

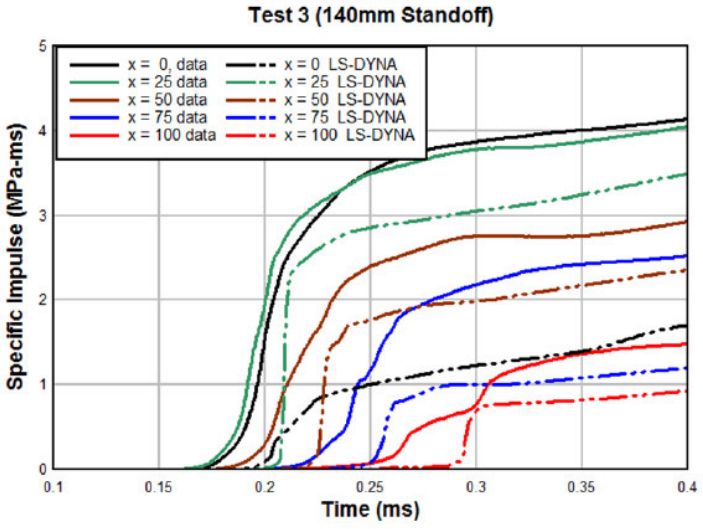

Figure 2.27: The specific impulse comparison between the experimental and simulation results from the two works [88].

2.7 Digital Image Correlation

2.7.1 General application

Digital Image Correlation (DIC) has become a more commonly used technique in experimental work with the advances in digital image capture and image analysis techniques. A comprehensive review of DIC, its history and evolution of the technique is provided by Sutton *et al* [89]. The technique can be widely used as a non-contact measurement, either replacing or augmenting existing systems.

DIC has been widely used in areas such as simple displacement measurements [90], modal analysis [91–93], 2D analysis of tensile specimens [94, 94, 95] and micro tensile specimens [96–99]. In 2D DIC, only one camera is required to analyse the planar field of interest, however deviation from the initial planer field induce small errors which were characterised by Sutton [100]. 3D DIC utilises two cameras to better characterise the out of plane motion; an example is shown in Figure 2.28 where Grytten [95] reports the out of plane displacements in polymeric tensile specimens. Yu and Pan [101] propose a method using an image splitter, allowing for a single camera to be used to capture the images of a subject from two different angles, mimicking the effect of having two cameras. In theory more than two cameras could be used with an overlap between the images to cover a larger area or shapes where regions might not be visible with only two cameras. The error associated with this technique was assessed by Chen [102], who found that significant artefacts were visible in the areas where the images overlapped, indicating that caution should be exercised when using more than two cameras.

The information obtained from DIC can prove particularly useful as it produces a field of data as opposed to discrete points from other measurement methods. In the work by Gerbig *et al* [103], the DIC displacement field is used to calibrate a numerical material model using an optimisation technique which was developed. The difference between the numerical and experimental displacement fields is shown in Figure 2.29 (c) for the initial stages of the optimisation. Once the material had been optimised, the displacement field reported by the FEM analysis, seen in Figure 2.29 (i), is less than 0.05mm. It should be noted that this technique should primarily be used on one set of data which trains the model and independently applied to a separate set of data for validation. If the same set of data used for training the model were used for validation this would be problematic.

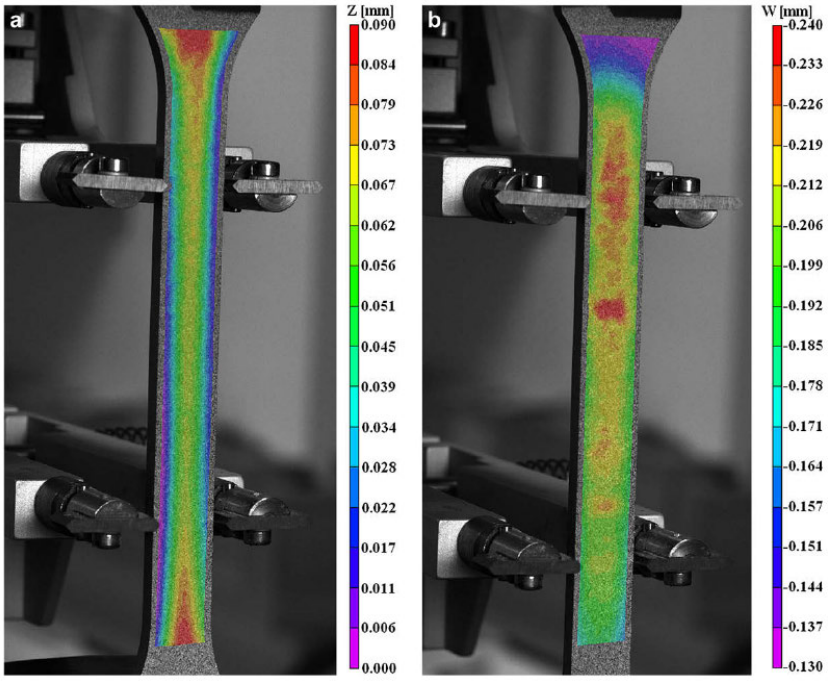

Figure 2.28: DIC being used to track the normal displacement in polymeric tensile specimens manufactured by Grytten *et al* [95]

The DIC technique is well suited as a non-contact measurement technique for blast loading of structures, where conventional measurement such as strain gauges and LVDT's would be damaged by the exposed loading. The error associated with this measurement has been well characterised at low and high speed [100, 104, 105]. Luo *et al* [104] fully characterised the error associated with the use of a stereo camera system and DIC, reporting that errors as little as 14 microns were capable in laboratory conditions. Tiwari *et al* [105] evaluated the error associated with high speed CMOS camera sensors and found it to be minimal, reporting that the system was able to accurately measure under quasistatic and dynamic conditions, eliminating uncertainty associated with the camera sensors. Park *et al* [106] characterised the effect of the speckle pattern size and subset selection on DIC, reporting that a medium density (majority of pixels have a grey value of between 100-200 on the grey scale) speckle functioned best. An example of the speckle and the grey value distributions in the image are shown in Figure 2.30

Reu and Miller [107] provide an introduction to the important technical concepts of

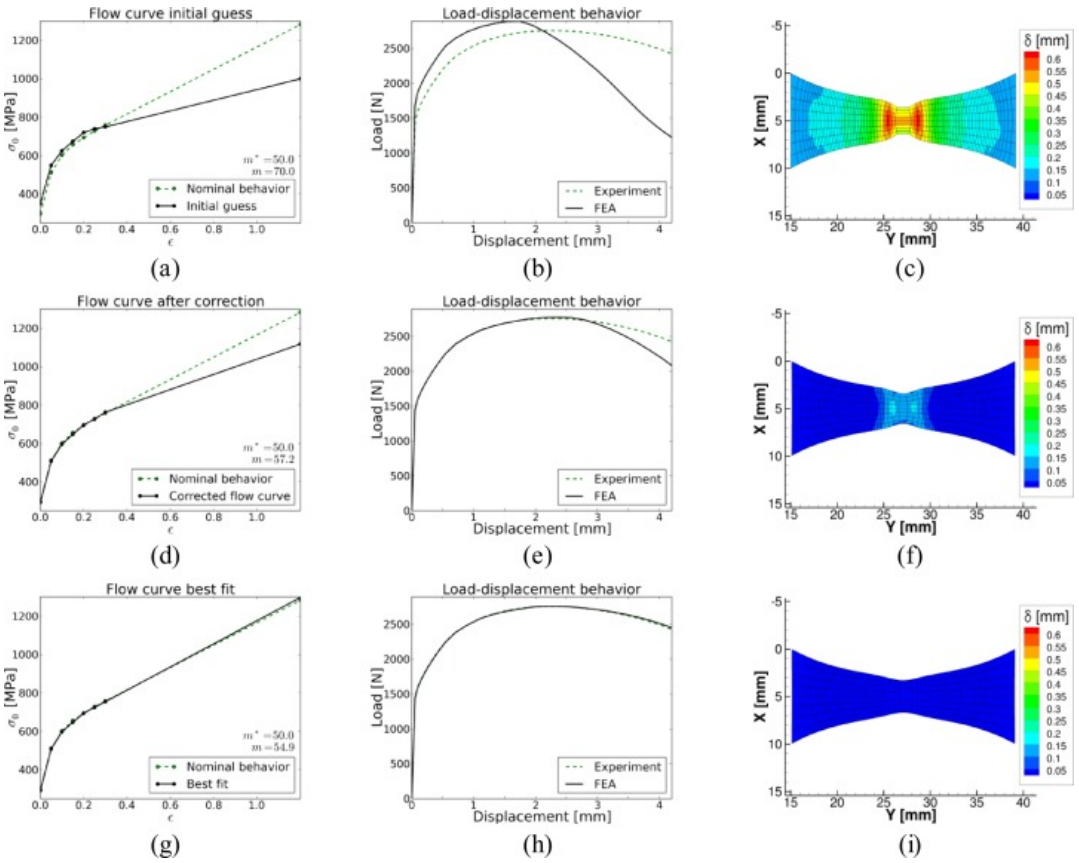

Figure 2.29: DIC being used to calibrate a material mode in a FEM analysis using an optimisation scheme devised by Gerbig [103]. Experimental values are shown on the left side with the reported difference between the numerical simulation and the DIC result shown on the right in Figure (c),(f) and (i) (areas of red show significant deviation from the experimental value)

DIC and its applications; issues such as camera choice, lens selection, speckle patterns, lighting and software analysis are discussed.

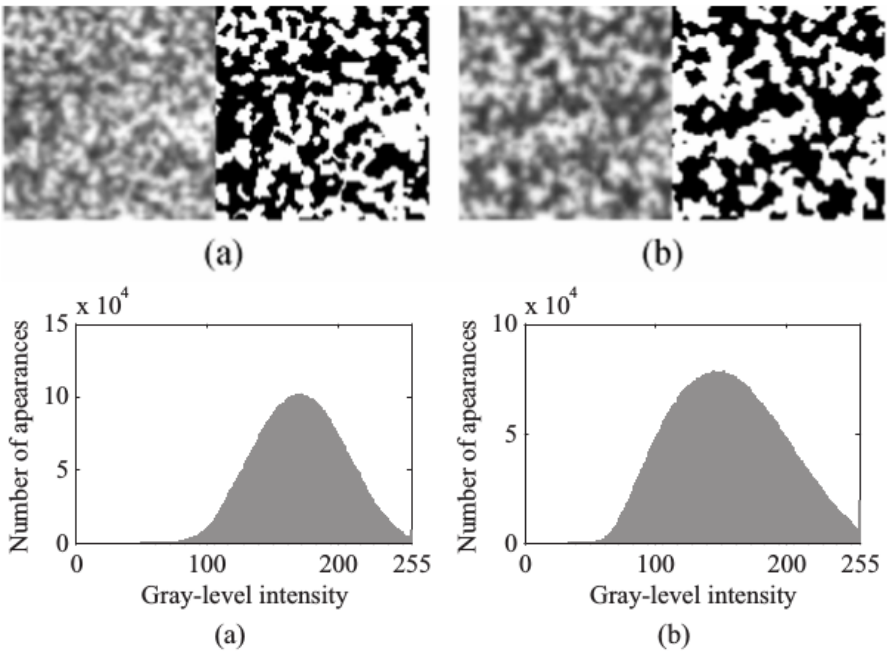

Figure 2.30: (a) Fine and (b)medium speckle pattern proposed by Park [106] for a 100x100 pixel image to work best with DIC.

2.7.2 Impulsive loading

DIC is not restricted by the duration of an event, but rather by the ability of the selected camera system to successfully record the event of interest. Short duration events such as impulsive loading or blast events must make use of high speed cameras to capture images for use with DIC. Holmen *et al* [108] used DIC to measure the transient deformation of thin steel plates subjected to low velocity impact with different shaped projectiles. The experiments were filmed with two cameras at a frame rate of 16 000 fps; the impactor velocity was in the region of 10m/s.

Pan *et al* [101] made use of an image splitter and a single camera to record images of specimens impacted with spherical projectiles, as shown in Figure 2.31. It is noted that movement of the mirrors and camera during the experiment were a concern. The thermal expansion of the camera affected the results meaning the system had to be warmed up for two hours before the experiment could be performed.

Later work by Yu [110], seen in Figure 2.32, proposed using a single colour camera and the individual color channels on the camera sensor, combined with band pass filters

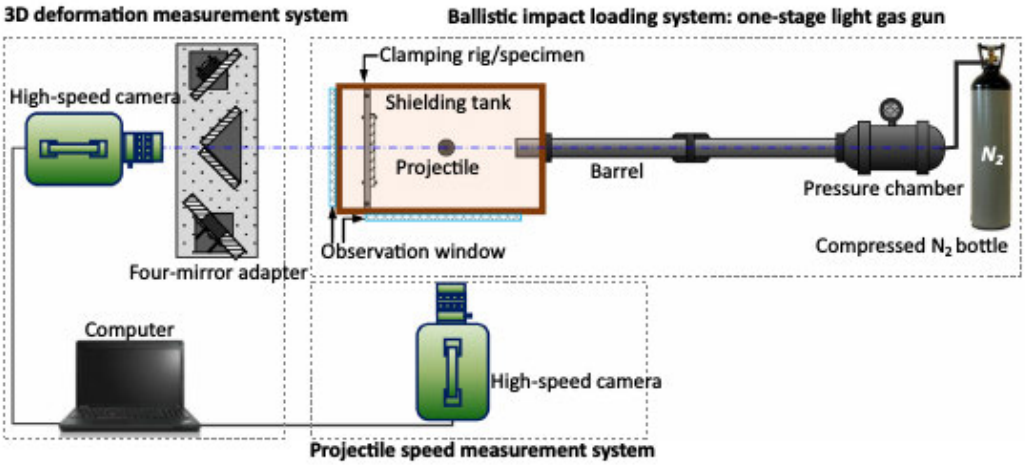

Figure 2.31: DIC technique applied to impulsive loading of plates by Pan [109]. The image splitter is clearly shown here enabling 3D DIC to be achieved with only one camera.

and a mirror system, to replace the need for a second camera.

An alternate method of image splitting such as that described by Rijensky and Rittel [111], makes use of a commercially available lens splitter, which divides the image down the centre of the sensor. This has the advantage of being a commercially available product, but significantly reduces the frame rate or the available resolution for image capture by using half the pixels for each image. Rijensky *et al* were only able to record 180 frames through the experiment and used frame rates of 50 000 - 200 000 fps. This technique was used on plates subjected to loading from a shock tube.

Aune *et al* [73] make use of stereo cameras which are used to film the deformation of structures in a blast simulator.

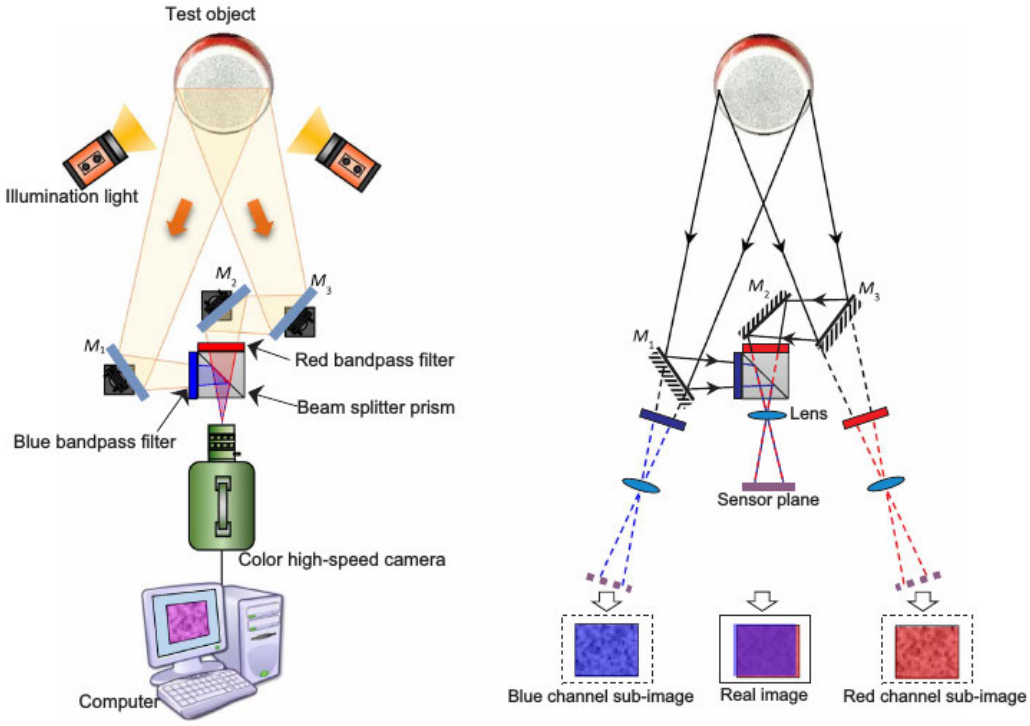

Figure 2.32: DIC technique utilising one color camera and band pass filters to create a stereo DIC image for analysis [110].

2.7.3 Blast loading

Large stand off distance

Dear and co-workers [112–114], have utilised DIC to record the response of blast loaded plates in experiments where the stand off distance between the charge and the plate was greater than 250mm. The responses resembled those found in uniform blast loading of structures, indicating that the loading was uniform.

Spranghers *et al* [59, 115] utilised 40g spherical charge masses of PE4 explosive at stand off distances of 250mm, on square 3mm thick aluminium plates with an exposed area of 300x300mm shown in Figure 2.33.The response was captured using cameras placed 2.5m away at 25000 fps. Difficulties with lighting and camera movement were reported, and a resolution of 1 pixel = 1mm was achieved.

Louar *et al* [116] extended the work performed by Spranghers *et al* [59,115] to include the plate response with an explosively driven shock tube, recording the experiments

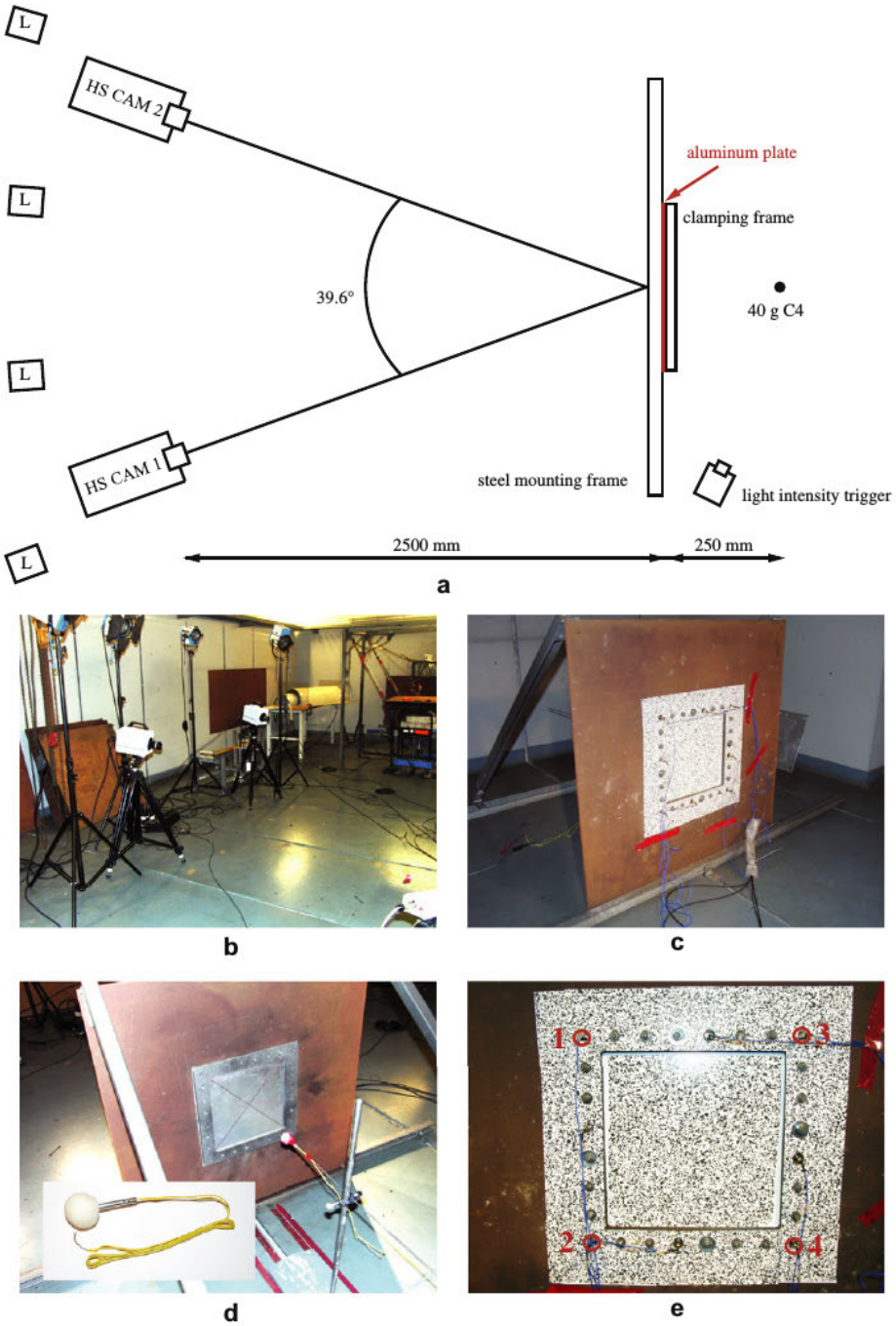

Figure 2.33: Experimental setup proposed by Spranghers [59] using 40g spherical charge masses of PE4 explosive at stand off distances of 250mm. The central 200x200mm of the test plate was captured and processed using DIC.

using the same method as Spranghers [59]. A much more uniform loading condition was achieved with the free air blast than with the explosively driven shock tube.

Localised blast loading

Fourney [22] used a 3D DIC system to measure the transient response of test plates. Both the velocity and acceleration profiles of the plates are reported. Figure 2.34 shows the experimental arrangement used. The camera system successfully recorded data at a rate between 25000 - 62500 frames per second, which was processed using DIC.

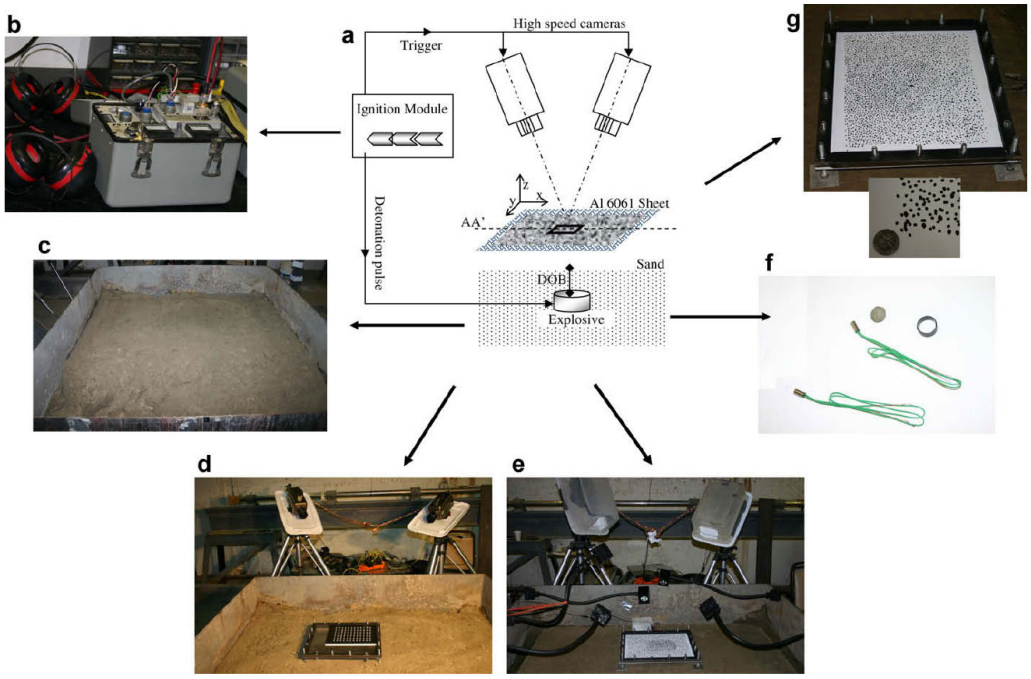

Figure 2.34: The 3D DIC system used by Fourney *et al* [22]. **(a)** A schematic of the experimental arrangement. **(b)** The ignition and camera synchronization module. **(c)** The sand pit where experiments were performed. **(d)** Camera arrangement with calibration target in place. **(e)** Camera and light arrangement just before detonation. **(f)** The detonators used. **(g)** The speckle pattern used on the test plates.

This was one of the first papers to attempt to record a transient response from a buried charge using a 3D DIC system. The results of the displacement field are shown

in Figure 2.35. In this test, the camera frame rate was set to 62500 fps and the framed area of 50x50mm was filmed at a resolution of 128x128 pixels indicating that a ratio of 0.5mm to 1 pixel. The remainder of the tests were performed at a much lower frame rate of 25000 fps and a resolution of 256x256 pixels with similarly results in a ratio of 0.5mm to 1 pixel.

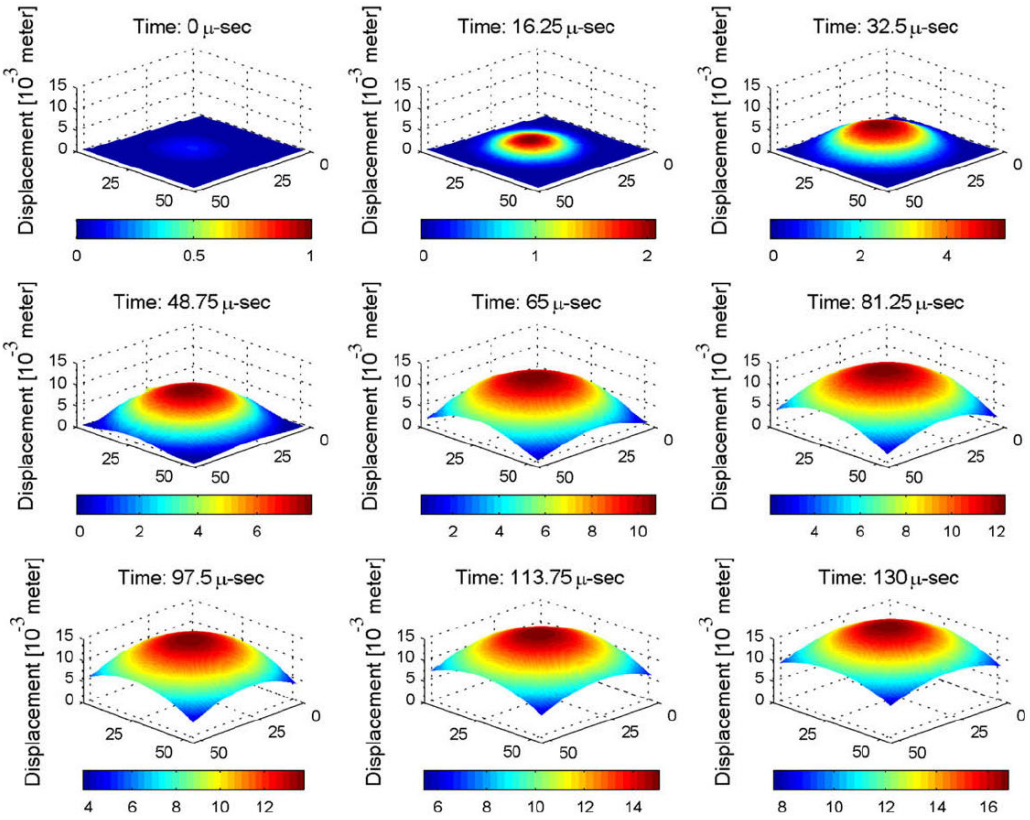

Figure 2.35: Full-field transient sheet displacement profile of shallow (7.6 mm) buried test, representing the out-of-plane deformation in the initial part of the impact. [22]

In more recent work, Aune *et al* [117] was successfully able to track the deformation of thin aluminium plates subjected to blast loading. The work makes use of stereo vision high speed cameras placed in the blast chamber with the experiment, recording at 21 000 frames a second. Issues highlighted in this work are the motion blur during the high speed deformation and the flaking of paint, leading to DIC data not being available in areas of the test plates.

2.8 Summary

Empirical formula and analytical models have been developed to predict the propagation of the blast front resulting from an unconfined explosion in air. Numerical modelling of air-blast loaded plates has been successfully performed for both localised and uniformly loaded plates, up to the tearing failure threshold of response. These models have been validated, in the majority of cases, using post-test deformation profile data as transient measurements are difficult to obtain during explosions.

There is limited literature available on buried charge explosions with systematic and complete experimental data to allow trends to be predicted. There is specifically limited experimental data available in the buried charge regime, which investigates the influence of soil content, depth of burial and stand off distance. No literature was found to investigate the structural response and transient measurements to free air blasts, metal backed charges (or flush buried) and buried charges in a comparable configuration.

Numerical modelling of buried charge experiments has progressed due to the improvements in computational hardware, there are still however a lot of room for improvement in the material models used to predict the response of different sand types.

Attempts have been made to make use of a 3D DIC system to capture the response of plates to both air-blasts and buried charge explosions, but not in the same experimental configuration to date. Hence, there is no systematic comparison of the transient deformation and evolution of plates subjected to air-blast and buried charge explosions.

Chapter 3

Experimental Method

The development of the experimental method is explained in this chapter. The experimental method comprises three distinct areas:

- Blast-impulse pendulum and modifications to the conventional test arrangement
- Loading conditions
- Transient response measurement

3.1 Blast Pendula

Two pendula were used in this work, namely the horizontal and vertical. For the air blast tests, the familiar horizontal blast pendulum was used [36,37,118]. For all the tests with the charge on the metal backing plate and those with buried charges, the vertical pendulum was used. Two pendula were used for both the horizontal and vertical systems. The first pendulum was a bare metal pendulum with no cameras and the second was a pendulum specifically designed to accommodate the high speed camera system. This was done so that initial testing could be performed on plates where the fracture limit could easily be found without endangering the expensive cameras, lights and electronics. The oscillation theories of the vertical and horizontal pendulum system were used to determine the impulse imparted on the system. In each system, a laser displacement sensor was used to measure the displacement of each pendulum which was recorded on an oscilloscope and then post processed on a computer to calculate the impulse.

3.1.1 Horizontal Pendulum

The conventional pendulum can be seen in Figure 3.1 inside the blast chamber. The conventional pendulum consists of an I-beam with the test plate and clamp frames bolted to the front and counter masses to balance the pendulum on the back. It was hung from 4 steel cables inside the blast chamber at the Blast Impact and Survivability Research Unit (BISRU) at the University of Cape Town. Turnbuckles at the end of each wire cable allow for the pendulum to be levelled and balanced so that the tension in each cable is equal. This allowed the pendulum to swing in a straight line when the impulsive load from the explosive detonation is applied to the test plate. A new design was required in order to accommodate the cameras needed for the high speed imaging which requires mounting and lighting. A new pendulum was designed and built which incorporated these modifications and housed the lights and high speed cameras.

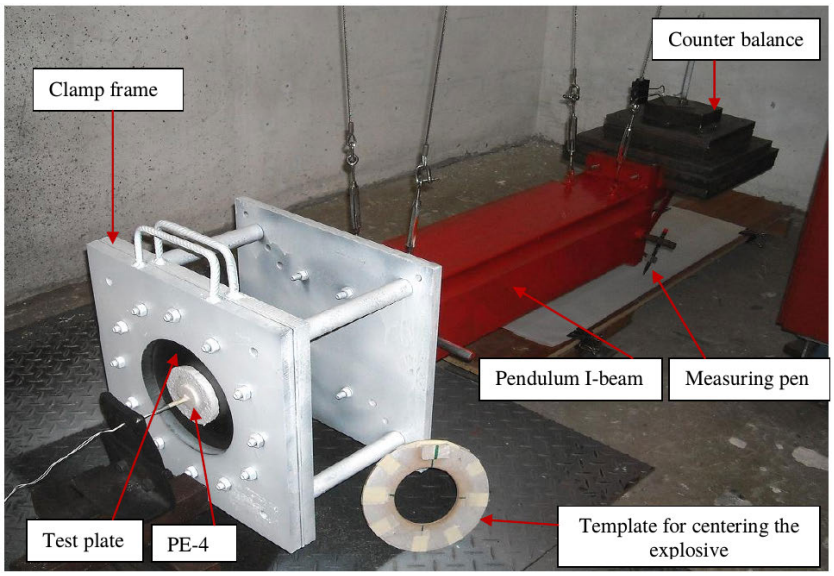

Figure 3.1: The horizontal pendulum hanging in the blast chamber as reported Ahmad [119].

3.1.2 Horizontal Impulse Measurement

Simple pendulum theory is applied to the motion of the horizontal pendulum. Figure 3.2 depicts the schematic layout of the pendulum and the different measurements needed for the calculation. The equation of motion assuming viscous damping can be written as:

$$\ddot{X} + 2\beta\dot{X} + \omega_n^2 X = 0 \tag{3.1}$$

where $\beta = \frac{C}{2M_p}$, $\omega_n = \frac{2\pi}{T}$ and $\omega_d = \sqrt{\omega_n^2 - \beta^2}$. C is the damping coefficient, M_p is the total mass of the pendulum, experimental rig and T is the natural period of the pendulum motion.

Since the pendulum is at rest at its lowest position prior to the explosion, the maximum forward displacement, X_1 will occur at $t = \frac{T}{4}$ and the maximum backwards displacement X_2, will occur at $t = \frac{3T}{4}$ as seen in Figure 3.2, where t is the time.

Therefore:

$$X_1 = \frac{T\dot{X}_0}{2\pi} e^{-\frac{\beta T}{4}} \tag{3.2}$$

$$X_2 = -\frac{T\dot{X}_0}{2\pi} e^{-\frac{3\beta T}{4}} \tag{3.3}$$

Relating X_1 and X_2 to solve for β produces:

$$\beta = \frac{2}{T} ln \frac{X_1}{X_2} \tag{3.4}$$

Now that β can be determined, the initial velocity, $\dot{X}_0$, can be determined from:

$$\dot{X}_0 = \frac{2\pi}{T} x_1 e^{\frac{\beta T}{4}} \tag{3.5}$$

Multiplying the total loaded mass of the pendulum, M_p, with the initial velocity of the pendulum, $\dot{X}_0$, gives the Impulse, I, imparted onto the test plate by the explosive charge. It should be noted that this impulse calculation assumes that the impulse transfer is instantaneous which is not actually the case, however the short duration of loading when compared to the long period of oscillation of the pendulum makes this a safe assumption.

$$I = M_p \dot{X}_0 \tag{3.6}$$

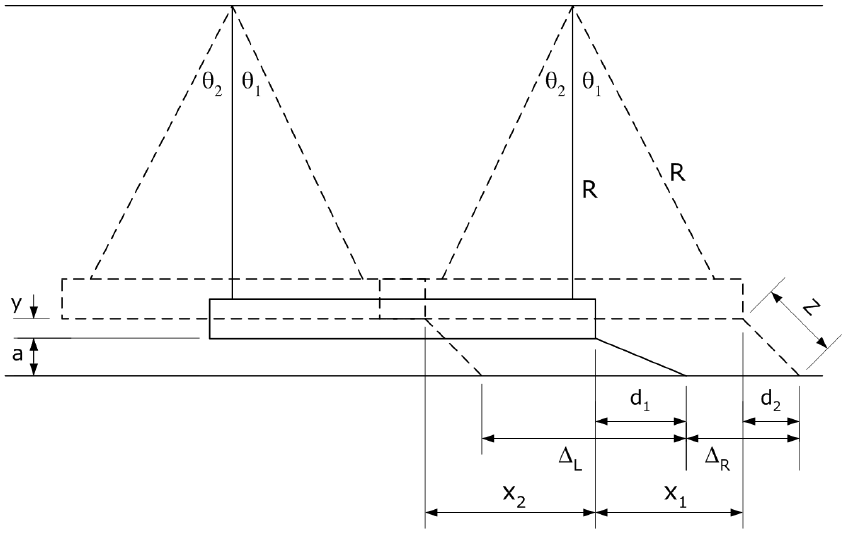

Figure 3.2: Schematic of the horizontal pendulum geometry

3.1.3 Vertical Pendulum

The vertical pendulum, as seen in Figure 3.3, was suspended from the roof of the blast chamber on a spring which allowed the pendulum to oscillate vertically. A set of guide rails mounted to the wall behind the pendulum kept it aligned and prevented it from rotating during oscillation. The pendulum was suspended over a steel plate which formed the backing plate for both the vertical back-plate (VBP) and buried charge series of experiments. The mass of the pendulum for each series was calibrated to limit the total magnitude of oscillation to 300mm which was the maximum range of the sensor. The standoff distance between the charge and the test plate was adjusted by varying the height of the hanging pendulum using an electric hoist.

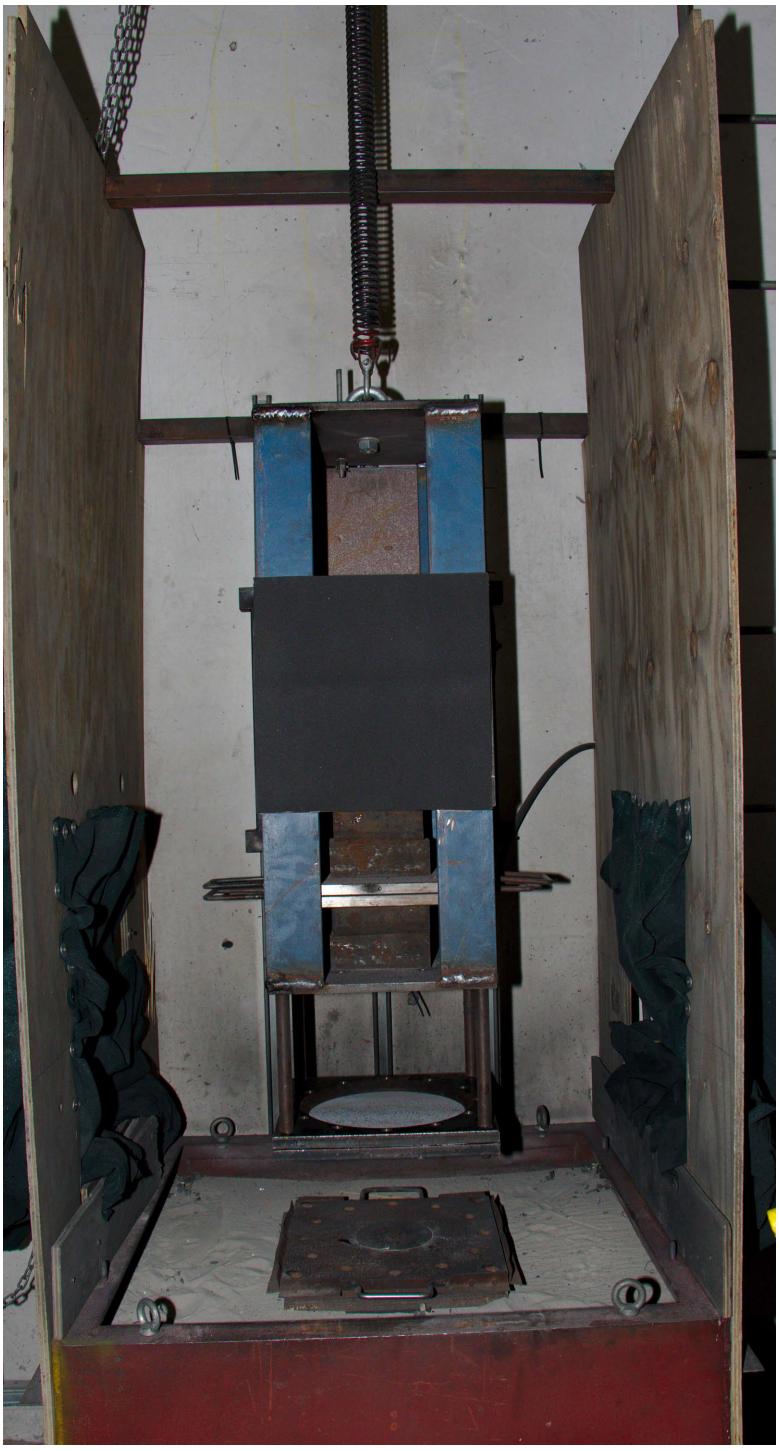

Figure 3.3: Photograph of the vertical pendulum shown hanging in the blast chamber, above the metal back plate.

3.1.4 Vertical Impulse Measurement

Considering the dynamic forces acting on the vertical pendulum with mass $\boldsymbol{M_p}$ and spring stiffness $\boldsymbol{k}$, it can be modeled as a single degree of freedom system as shown below in Figure 3.4. The gravitational forces acting on the pendulum are constant and accounted for by the pre-detonation deflection of the spring.

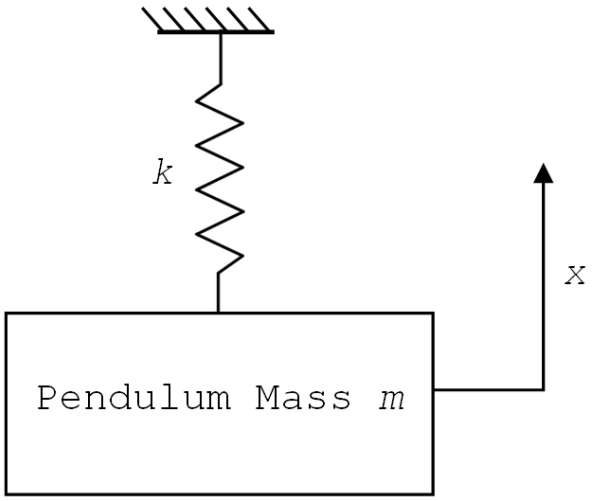

Figure 3.4: Schematic showing SDOF model used to describe the motion of the vertical pendulum.

This results in a simple second order differential equation of motion

$$\boldsymbol{M_p\ddot{X} = -kX} \tag{3.7}$$

which after noting equation (3.8) can be rewritten as:

$$\boldsymbol{\omega_n} = \sqrt{\frac{\boldsymbol{k}}{\boldsymbol{M_p}}} \tag{3.8}$$

$$\boldsymbol{\ddot{X}} = \boldsymbol{-\omega_n^2 X} \tag{3.9}$$

Equation (3.9) has the standard form solution of:

$$\boldsymbol{X\,(t) = A \times \sin\left(\omega_n t + \phi\right)} \tag{3.10}$$

where $\boldsymbol{A}$ and $\boldsymbol{\phi}$ shift the vibrations amplitude and phase respectively, and $\boldsymbol{t}$ is the time. Noting the initial zero position of the displacement and that the maximum deflection

will occur when:

$$\boldsymbol{t = \frac{T}{4}} \tag{3.11}$$

(3.12)

where

$$\boldsymbol{\omega_n = \frac{2\pi}{T}} \tag{3.13}$$

gives

$$\boldsymbol{X\,(t) = A \times \sin\,(\omega_n t)} \tag{3.14}$$

with $\boldsymbol{A}$ therefore equal to the maximum upward displacement of the pendulum.

The impulse imparted onto the pendulum can be determined from momentum-impulse theory (provided the impulsive loading can be deemed instantaneous), that is:

$$\boldsymbol{I = M_p \Delta \dot{X}} \tag{3.15}$$

but since the pendulum displaces from rest, i.e. zero velocity, and we assume instantaneous velocity transfer,

$$\boldsymbol{\Delta(\dot{X}) = \dot{X}\,(0)} \tag{3.16}$$

Differentiating equation (3.14) gives

$$\boldsymbol{\dot{X}\,(t) = A\omega_n \cos\,(\omega_n t)} \tag{3.17}$$

$$\boldsymbol{\dot{X}\,(0) = A\omega_n} \tag{3.18}$$

Solving for impulse by substituting equation (3.18) into equation (3.15) (and again noting the relation given by equation (3.8)) results in

$$\boldsymbol{I_v = A\sqrt{kM_p}} \tag{3.19}$$

The spring the pendulum hangs on was carefully calibrated in order to determine the spring stiffness $\boldsymbol{k = 5654 N/m}$. The spring was pulled in a Zwick 1484 200kN quasistatic load from and the load-displacement curve was obtained to calculate the stiffness.The resulting force-displacement curve is plotted in Figure 3.5 together with a line fitted through the data used to calculate the stiffness.

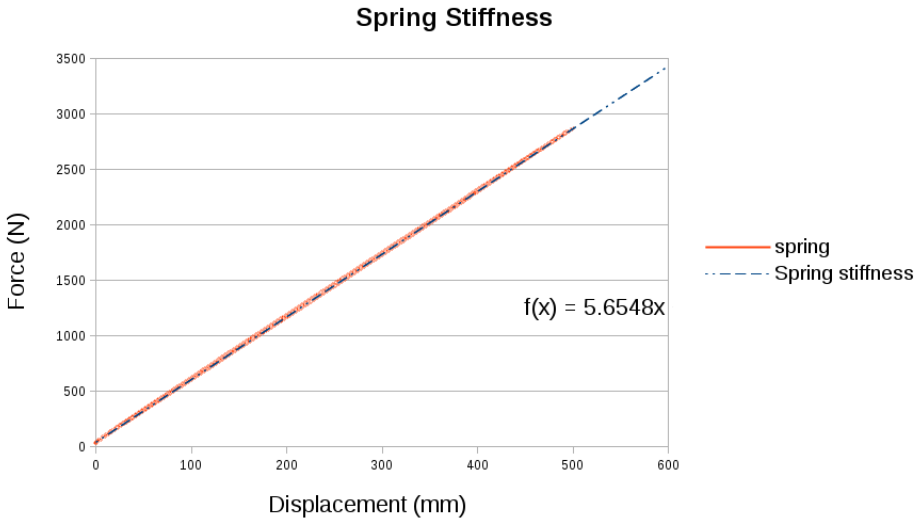

Figure 3.5: The force-displacement curve obtained from the spring calibration test.

3.1.5 Displacement Sensor Post-processing

The swing of the pendulum was recorded using a laser displacement sensor (CP35MHT80) during each test, and the impulse was determined using the pendulum swing recorded by an oscilloscope. The laser displacement sensor was mounted to the wall behind the horizontal pendulum, and measured the change in distance between the wall and the pendulum. A plate was added to the back of the horizontal pendulum to ensure the sensor had a flat vertical surface which the laser light could reflect on. A typical output from the displacement sensor is shown in Figure 3.6 for the horizontal pendulum.

This data was processed to determine values for $\boldsymbol{X_1}$ and $\boldsymbol{X_2}$ of the swing of the pendulum and then used to calculate the impulse of the pendulum.

On the vertical pendulum a laser displacement sensor was built into the wall mounted guide to prevent the pendulum from rotating. The location of the sensor was adjustable and measured the change in vertical displacement of the pendulum as it was displaced upwards by the blast, in a similar was to the horizontal pendulum.

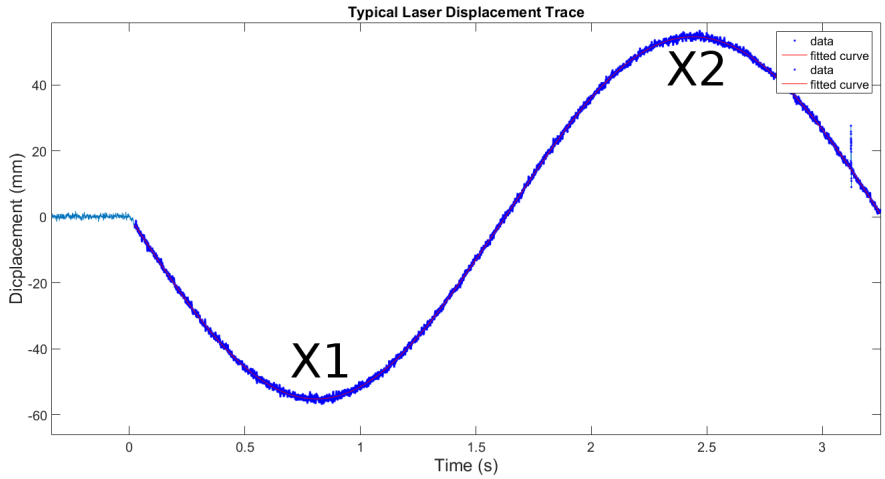

Figure 3.6: Typical displacement versus time output from the displacement sensor.

3.2 Experimental Arrangement

Experiments were performed at the blast chamber located in the Blast Impact and Survivability Research Unit (BISRU) at the University of Cape Town. The hypothesis of this investigation requires the comparison of loading conditions arising from free air blasts to those of buried charge explosions.

The three loading conditions used in the investigation are shown in Figure 3.7, and are defined as:

- Air blast (AIR)- Explosive charge was detonated in air with no confinement.
- Vertical back plate air blast (VBP) - Explosive charge was mounted on a metal back plate (20mm thick) and detonated in air.
- Sand back plate blast (SBP) - Explosive charge was surrounded with sand and detonated on a metal back plate with a 10mm overburden of sand above the charge.

The AIR tests employed a horizontal pendulum to capture the impulse while the VBP and SBP tests used a vertical pendulum arrangement. Impulse measurement is described in Section 3.1.

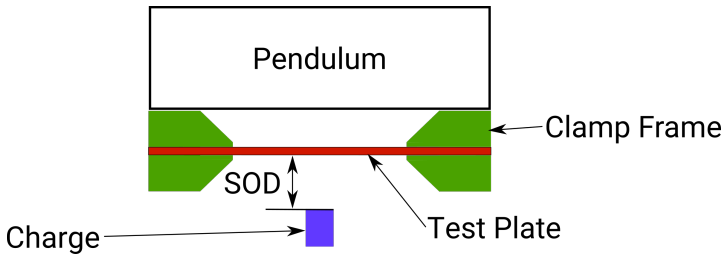

(a) AIR configuration

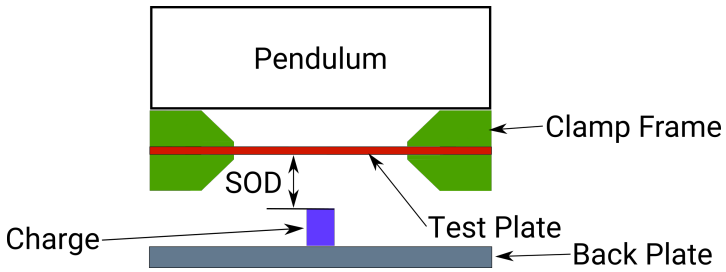

(b) VBP configuration

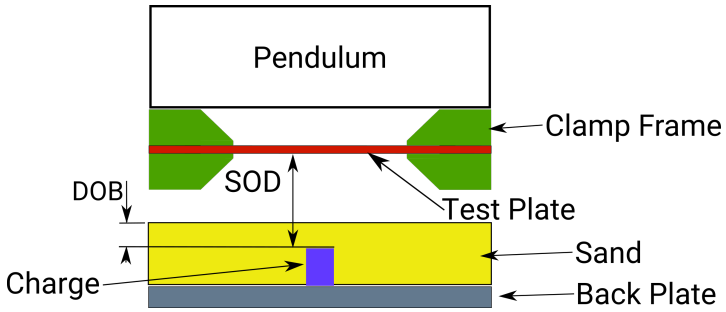

(c) SBP configuration

Figure 3.7: Schematics showing section views of the three experimental configurations.

3.2.1 Blast test specimens

Each test plate was bolted into a clamp frame with 12 bolts evenly spaced around the periphery of the circular exposed area at a pitch circle diameter of 350 mm. The test plates were made from 3mm thick Domex 355MC [120], a high strength hot rolled low alloy steel. The plates were square with a side length of 400 mm. When placed in the clamp frame, the plates had a exposed circular area with a diameter of 300 mm, as shown in Figures 3.8, 3.9 and 3.10.

Domex 355MC was chosen because it is a very ductile steel with a yield strength of 430 MPa under quasistatic conditions. It also has a particularly high engineering plastic strain at failure of around 20% [120]. Full material characterisation is discussed in Chapter 5. The plates were all cut from the same sheets originating from a single batch of Domex 355MC. Figure 3.8 shows the full dimensions of a test plate.

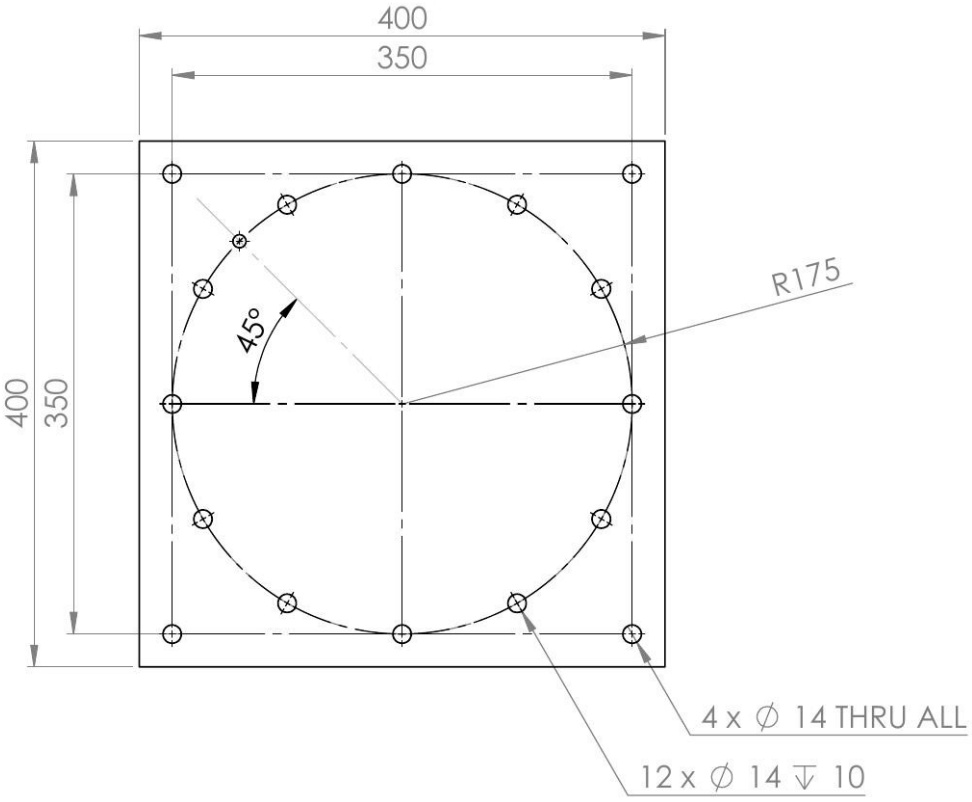

Figure 3.8: Drawing of a test plate which was laser cut from the material.

The clamp frame was manufactured from 20mm thick mild steel. The inside edge

was chamfered at a 45°angle around the edge of the plate to reduce pressure build up and recirculation [38, 49]. Figure 3.9 shows the drawing and CAD representation of the clamp frame.

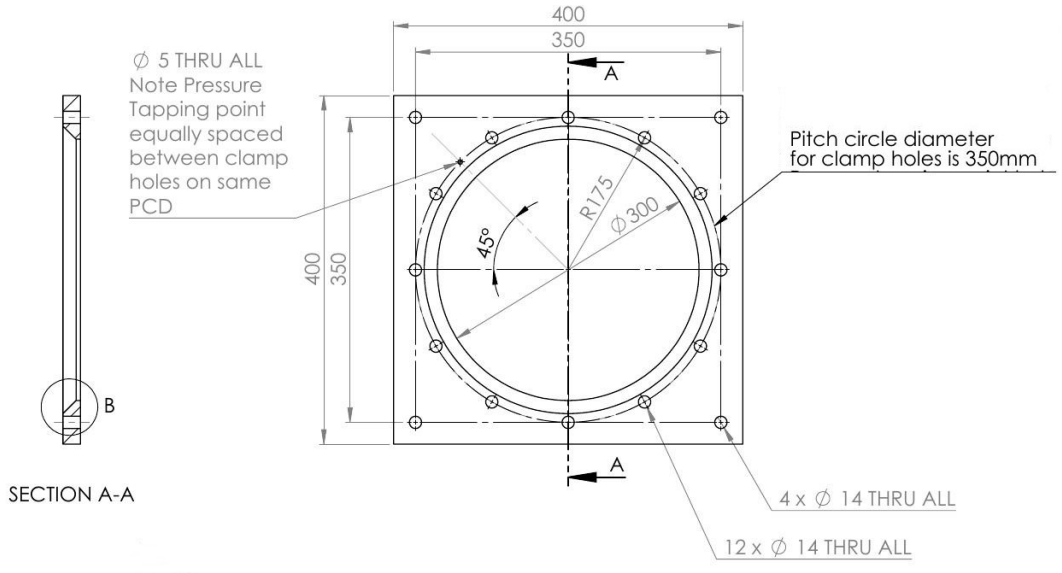

Figure 3.9: Drawing of clamp frame which was used to restrain the test plate and mount it onto the blast pendulum.

The clamp frames and test plates were bolted together as shown in Figure 3.7 and mounted to a blast pendulum. The horizontal experimental arrangement is shown in Figure 3.11 and 3.10.

3.2.2 New pendulum system to incorporate high speed imaging

The horizontal pendulum used at BISRU for many years [37, 49, 52, 57] consisted of an I-beam suspended from four cables with a mounting frame at the front and a counterbalance mass at the rear. It was not possible to mount the cameras to this pendulum as it would have provided no protection from the intense light burst during an explosion, or the ensuing blast wave. The light would have saturated the camera sensor, making it impossible capture images of the deformation response, and the blast wave would have caused considerable damage to the camera body, lenses, electronic systems and cabling. The design of the pendulum is covered in the publication by the author [121] in the International Journal of Impact Engineering.

In order to protect the camera system, a new pendulum was constructed with a shroud around it. The shroud isolated the cameras from the blast loading and protected the cameras from the intense light emissions that could saturate the camera sensor. The new pendulum is shown in Figures 3.10 and 3.11. Figure 3.10 is a photograph of the pendulum prior to a test, showing the steel shrouding in place. Figure 3.11 is a schematic drawing of the pendulum, shown without the shroud to allow viewing of the internal arrangement. Part of the web was removed in order to give the cameras a direct line of sight to the rear surface of the test specimens and also provide space to mount a lighting system, as shown in Figure 3.12. The cameras were mounted on a rail system to isolate them from vibration and positioned appropriately for the focal distance of the lenses selected, as shown in Figure 3.12. The vibration mounts consisted of natural nylon blocks which were found to isolate sufficient high frequency vibration between the camera rail and the pendulum. The mass of the modified pendulum increased to 308 kg due to the changes (the previous pendulum was less than 30kg when unladen).

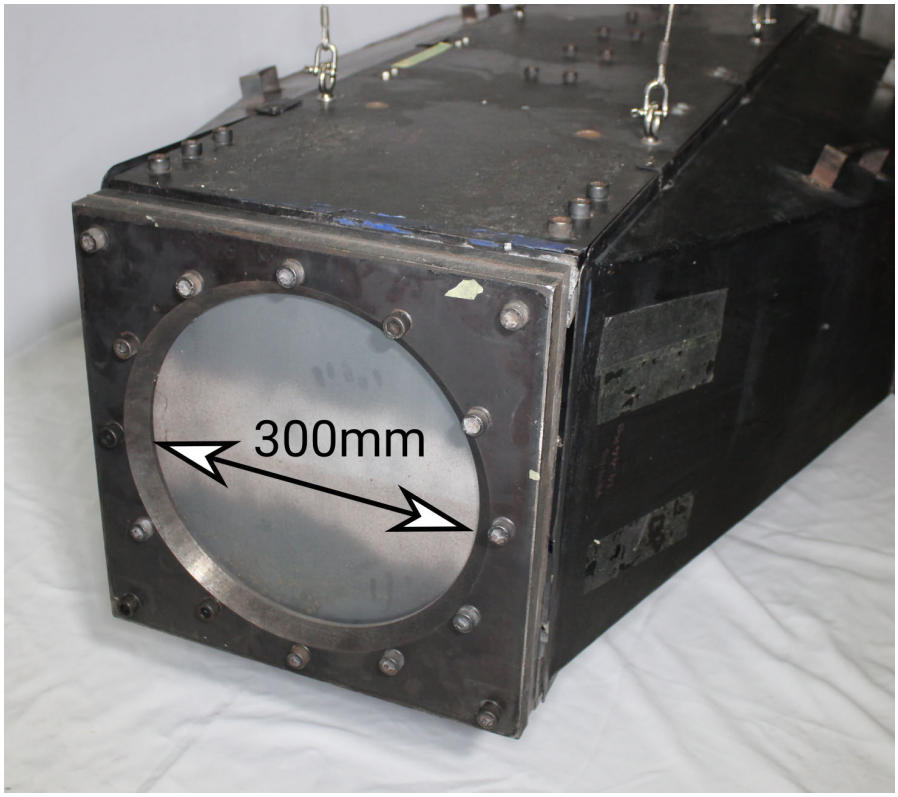

Figure 3.10: Photograph of the new pendulum hanging in blast chamber, with a test plate with a 300mm circular exposed area.

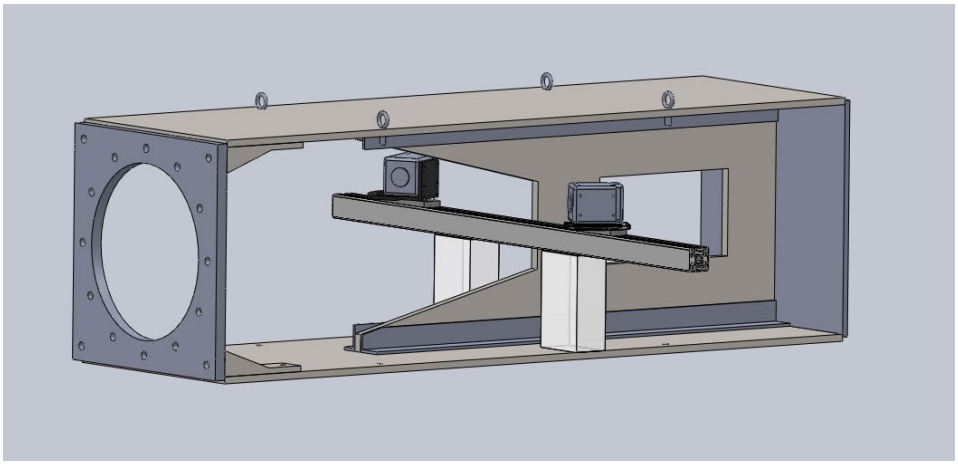

Figure 3.11: Schematic drawing of modified pendulum, showing internal arrangement (shroud removed for clarity)

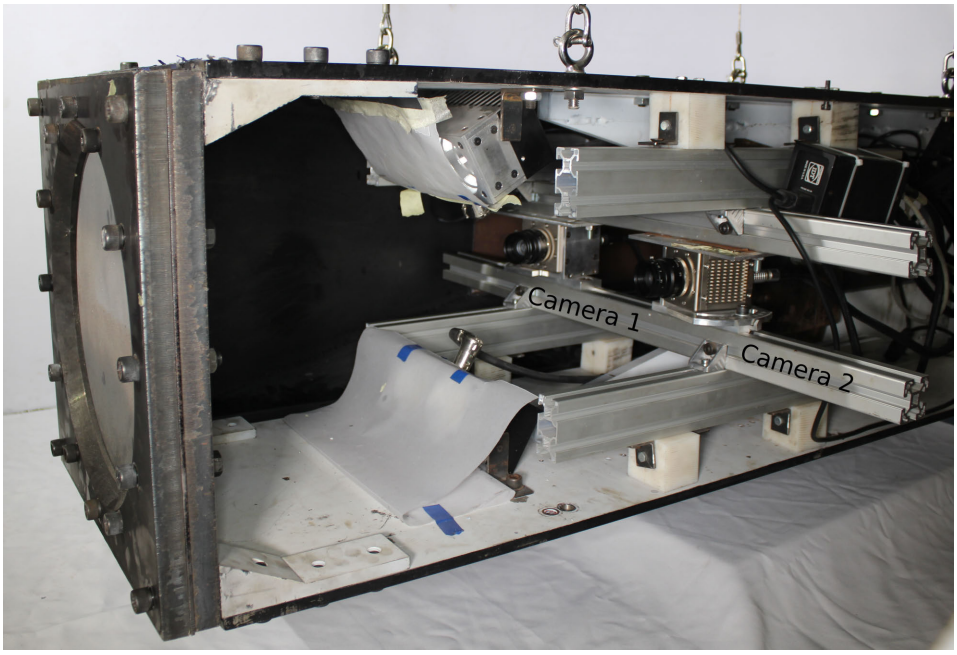

Figure 3.12: The new pendulum with shrouds removed to show the inside

The pendulum was constructed such that it could be hung as either as a horizontal or vertical pendulum. The hoist attachment point and guide rails for the vertical pendulum were designed that they could be easily bolted on to the new pendulum.

This facilitated easy switching between experimental configurations by changing the attachment method with the cameras internal mounting and adjustment remaining unchanged. The pendulum is show in the vertical position in Figure 3.13.

Figure 3.13: The new pendulum with attachments added and hanging as a vertical pendulum

3.2.3 Loading conditions

In all three loading conditions, small cylinders of 38 mm diameter PE4 plastic explosive were detonated in the centre of the back face using instantaneous electrical detonators (type M2A3). The charge mass in these experiments varied from 10-25g.

AIR - Air charge

Cylinders of PE4 were mounted at two stand off distances, 40mm and 50mm, where the stand-off distance was determined by placing the charge on a polystyrene bridge, and adjusting the length of the bridge legs as shown in Figure 3.14a. A template was used to mark the position of the polystyrene bridge to ensure that the centres of the plate and the explosive charge were co-axial.

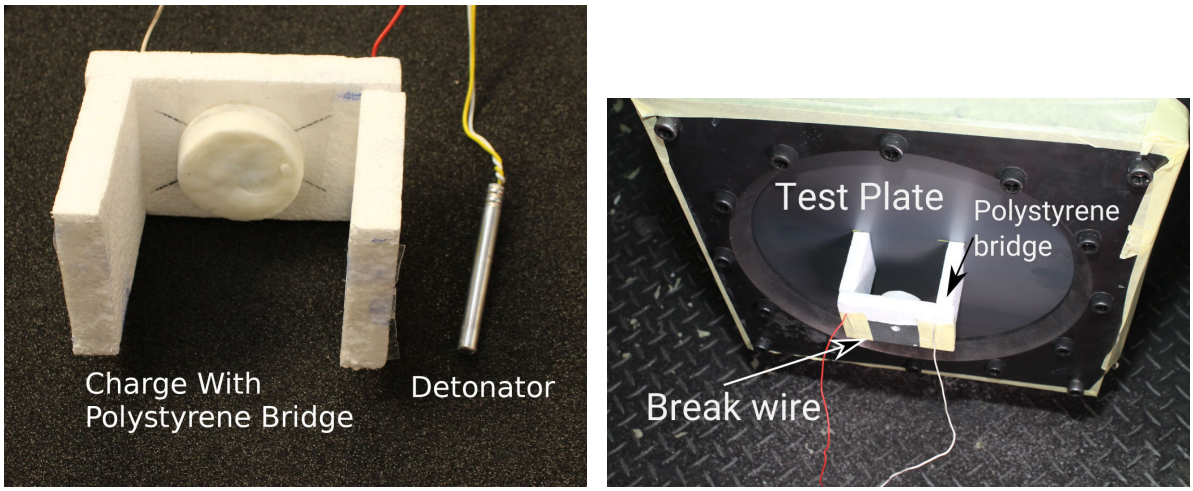

(a) Detonator and the polystyrene bridge

(b) The charge mounted on the bridge positioned on the test plate

Figure 3.14: Photograph showing charge configuration

VBP - Vertical back plate air charge

Cylinders of PE4 were mounted in the centre of the metal back plate, as shown in Figure 3.15b. The detonator was inserted through a hole drilled in the centre of the back plate and positioned such that the face was flush with the surface of the back plate. The charge was placed centrally on the detonator and detonator wires were gently secured with adhesive tape. Once the charge had been positioned the pendulum with the test plate attached was then lowered with the electric hoist until the stand off distance between the top of the charge and the plate reached the required SOD of either 40mm or 50mm. Air was the medium between the charge and the test plate.

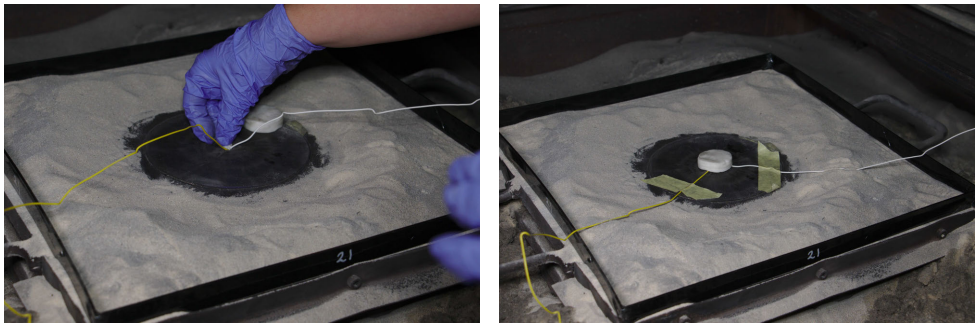

(a) Detonator being placed through the back plate

(b) The charge mounted on top of the detonator

Figure 3.15: Charge configuration for the vertical back plate charge configuration

SBP - Buried sand charge

The charges were positioned on the back plate in the same manner as the vertical back plate experiments. Once the charge had been positioned a HDPE frame was positioned around the metal back plate as seen in Figure 3.16. The height of the HDPE frame was carefully cut to ensure that a depth of burial of 10mm would be achieved if the frame were filled level with sand as seen in Figure 3.16

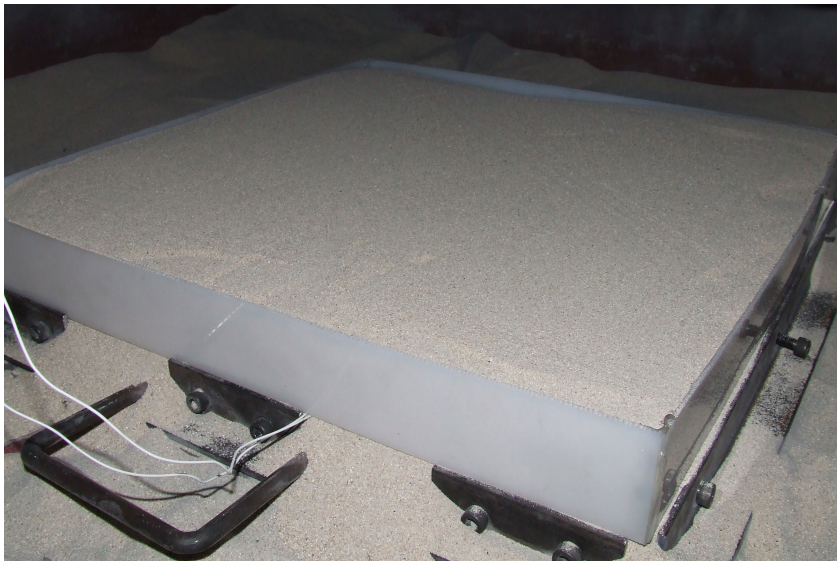

Figure 3.16: HDPE frame filled with sand to create the desired depth of burial

3.3 Transient response measurement

3.3.1 Specimen preparation

The rear surface of each test plate used with DIC was painted with a random speckle pattern to enable the DIC procedure to determine the spatial deformation of the plate. Prior to applying the speckle pattern, the plates were thoroughly cleaned and abraded to ensure that the paint remained adhered to the plate during testing. The surface was degreased with acetone and then painted with a thin layer of white primer before a black speckle pattern was added. The surface preparation procedure is illustrated in Figure 3.17.

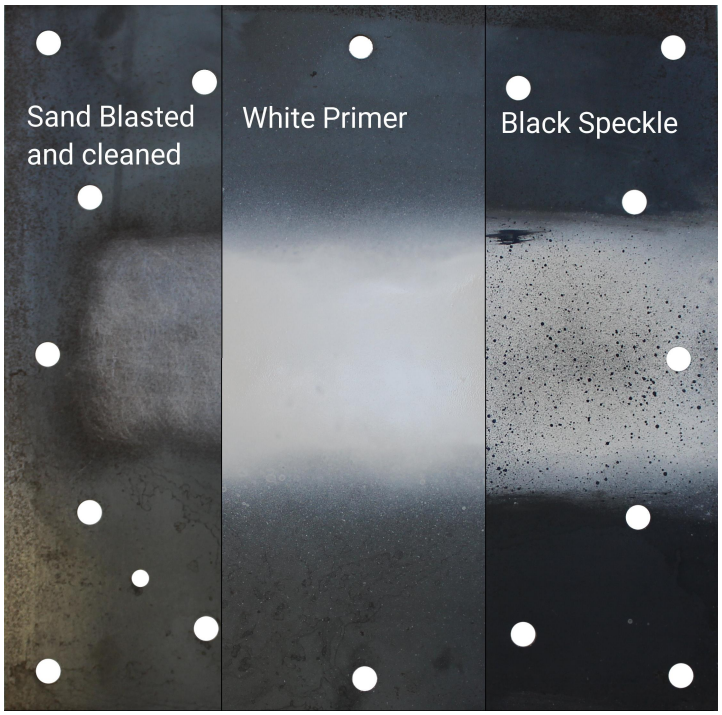

Figure 3.17: The 400mm x 400mm test plate used, showing the the bolt holes with the preparation steps to create the DIC speckle pattern.

3.3.2 High speed imaging

Two IDT vision NR4 S3 high speed cameras shown in Figure 3.18 were mounted to a vibration isolated aluminium rail system and installed in the new pendulum, as described in section 3.2.2. This mounting method, shown in Figure 3.12, ensured that the two cameras did not move independently during the test (independent camera movement would have invalidated the calibration of the DIC system before the test). This movement became more challenging to prevent as the charge mass increased. The two cameras were separated and make an approximate 30°included angle. A two camera system was used to the increase the resolution achieved with the existing hardware. Alternate methods of image splitting such as those described by Rijensky and Rittel [111] would have significantly reduced the frame rate or the available resolution for image capture. This also has the benefit of increasing the achievable DIC resolution by increasing the pixel density in the acquired images.

These cameras were rated to operate in high acceleration environments (up to 200G) and feature an all metal housing which acted as a heatsink for heat dissipation.

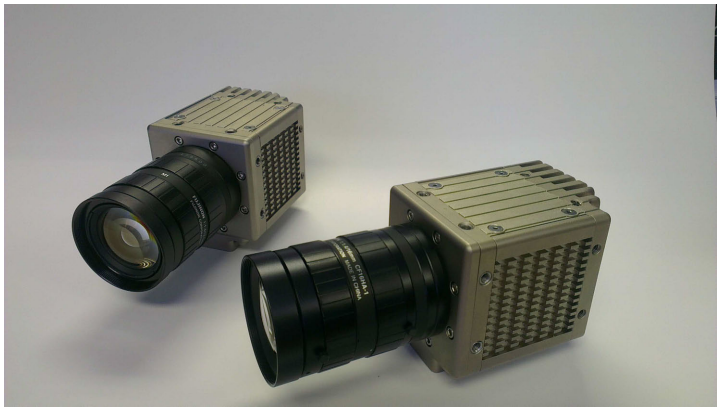

Figure 3.18: Photograph of the two IDT NRS4 cameras that were built into the pendulum to capture the images used for DIC.

The images from the two cameras were synchronised by means of a synchronising cable that connected the two camera control boxes. The cameras were triggered with a custom built TTL trigger circuit that was activated by the detonation of the charge.

Each camera used 25mm fixed focus lenses and the views were set at 1024x76 pixels. This allowed a full width strip along the mid-line of each plate to be filmed by both

cameras (25x300mm). The frame rate was set at 30 000 Fps with the exposure set at 31 $\boldsymbol{\mu}$ Sec (which was limited by the available light). At this short exposure a lot of extra illumination was required on the specimen and two custom built LED lights were focused on the test plate during testing. It was found that diffusers were needed for the lighting to ensure uniform specimen illumination and prevent "hot spots" or localised regions of over exposure along the plate width.

3.4 Processing DIC data

The camera images were post processed using the Dantec Dynamics Istra 4D DIC software package, to calculate the displacement field for the camera views. Prior to testing, calibration was required and used as an input to the post-processing analysis. The calibration steps were performed prior to each test to account for any movement that may have occurred between experiments.

The process identifies object points in the images of the two cameras by applying the correlation algorithm and finding homologous points. The imaging parameters were used to calculate the contour of the object and the displacements.

3.4.1 Calibration of DIC system

Prior to testing, the projection parameters (intrinsic and extrinsic imaging parameters) were determined from the calibration process. Multiple images of the calibration target were captured in different positions using the cameras set in their respective positions. The calibration target had a known accurate pattern which was recorded with both cameras simultaneously.

The software then processed these images to locate the target markers from the sequence of images at different positions. From the located target markers, the projection parameter of the whole system, with additional distortion parameters, were calculated based on the pinhole model [122]. A bundle-adjustment algorithm within the software calculated the intrinsic parameters (focal length, principal point, distortion parameter) for each camera, their respective orientation and the extrinsic parameters (translation vector and rotation matrix). The intrinsic and extrinsic calibration values for the system were stored in a calibration file and imported into the analysis. The quality of the measurement was directly related to the accuracy of the projection parameters. The simple calibration process in the software allowed more accurate

measurements through feedback of the projection parameters. Typically eight images were sufficient to calculate all calibration parameters accurately.

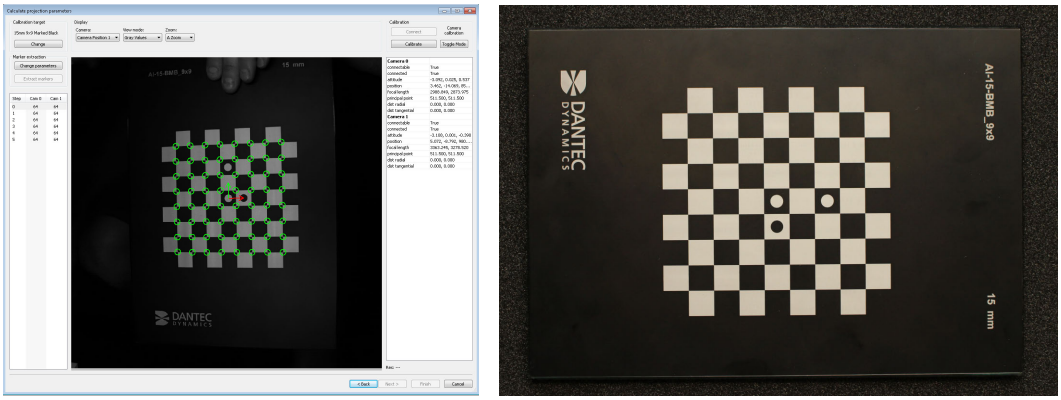

(a) The calibration in the software (b) The calibration target used in the calibration

Figure 3.19: The calibration target shown together with the software identified markers

3.4.2 Correlation method

The correlation algorithm of the commercial software was based on tracking of the grey value pattern in small local neighbourhood facets seen in Figure 3.20. A transformation matrix for each of the subsets, G(x,y) is calculated from this information in each of the two camera images, at each time step.

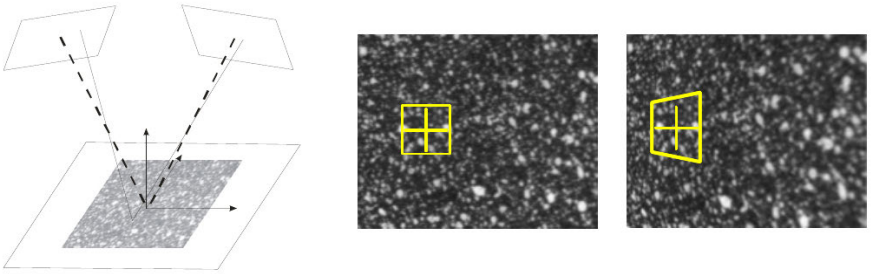

Figure 3.20: The DIC stereo subsets

As the test plate deforms, the speckle pattern deforms with it, resulting in a new position for each subset of pixels. Within the correlation algorithm the difference of these patterns was automatically minimized. Effectively meaning that the intrinsic

variables that control the amount of movement of a subset could be optimised to account for the differences between consecutive images. The software automatically varies the illumination parameters and the parameters of the affine transformation, resulting in a matching accuracy of better than 0.08 pixels, but this varied (up to 5 pixels) during the deformation of the test plates in the worst case example during this experimental set. This effectively means that the software determined accuracy under good conditions was 0.08 pixels under optimal conditions and 5 pixels as an upper bound. For this set of tests, an equivalence of 1 pixel = 0.3mm meant that the worst uncertainty in the DIC data would give an equivalent error of less than 1.5mm in the deformation data. Subset sizes were fixed at 19 pixels with a grid spacing of 5 pixels to ensure overlap in the subsets. An example of the displacement field which is extracted from the correlation is shown in Figure 3.21. Once this displacement field has been calculated for the area of interest, other information such as the strain field, velocity and acceleration field could be calculated based on the displacement field. It should be noted that due to subsets being bigger than a single pixel the technique of correlation reduces the displacement value of a subset to the centre point of each subset. To minimise this, high resolution cameras and fine speckle pattern were used. All data presented here in is the raw and unfiltered data as exported from the correlation software.

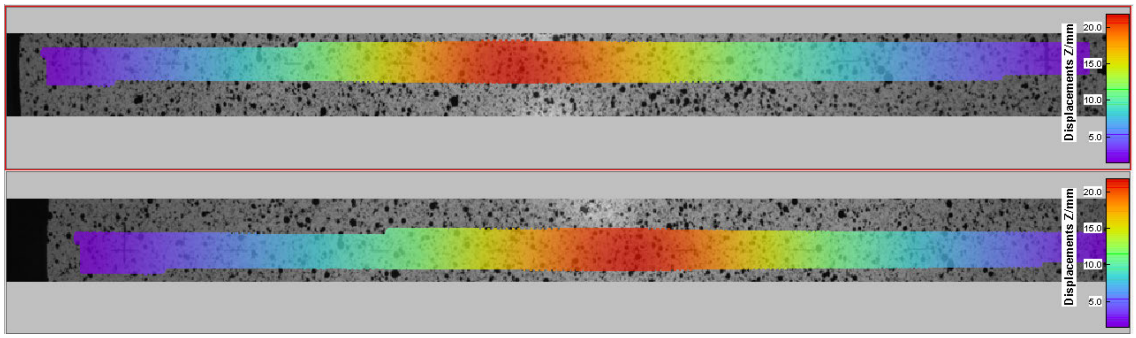

Figure 3.21: The Z Displacement field obtained from the correlation seen overlayed on the left(top) and right (bottom) images shortly after detonation

3.4.3 Gauge points and lines

Data was extracted from two separate gauge points on each test plate so that easily comparable analysis was possible. To ensure the centre line of each plate was measured,

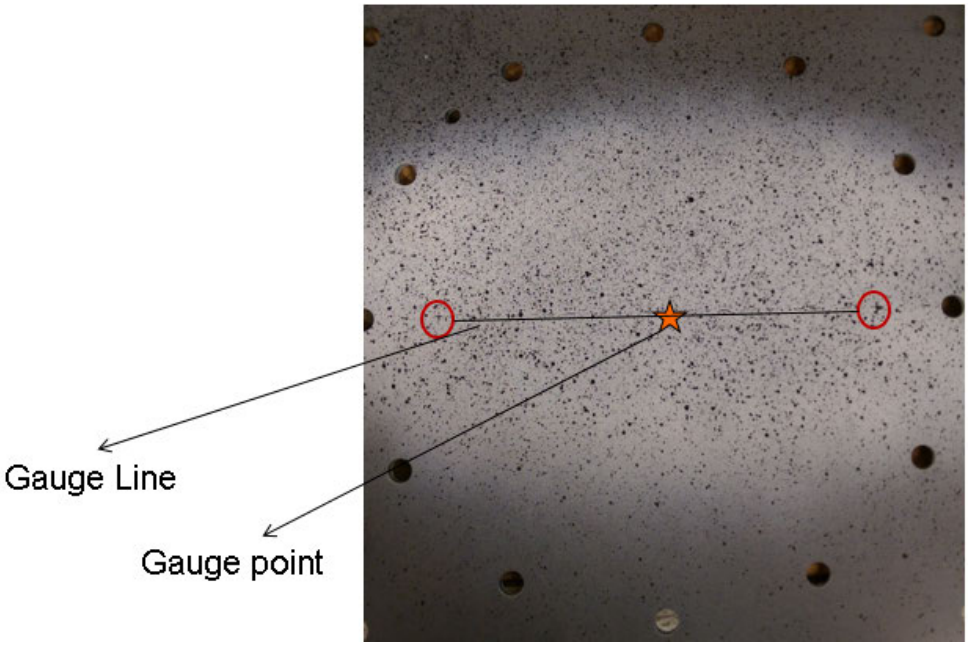

Figure 3.22: The gauge point and line extracted in the DIC

small markers (in form of a small cross) were placed 20mm from the clamp frame on the centre line of each test plate. These small markers were then used in the DIC analysis to define a gauge line across the centre of each plate as shown in Figure 3.22. The gauge point for the plate midpoint, was defined as the midpoint of this centre line. It was found that marker size was important; markers that were too large interfered with the DIC analysis. Information such as displacement and strain were extracted at discrete points along the line. Each data point in the field is representative of a facet and any irregularities in the pixels of that facet (associated with motion blur for example), may cause variations in the readings at that point. The extracted displacement information was post processed using a custom Python script to align and plot the information together with the 3D scans of the plates.

From the displacement field, an engineering strain field was generated with reference to the undeformed plate as seen in Figure 3.23. This strain field represents the strain observed in individual subsets of the correlation. The strain data exhibited more noise than the displacement field due to the small subset size and the fact that it is a derivative of the displacement field, effectively accentuating any noise which might have been present in the displacement field.

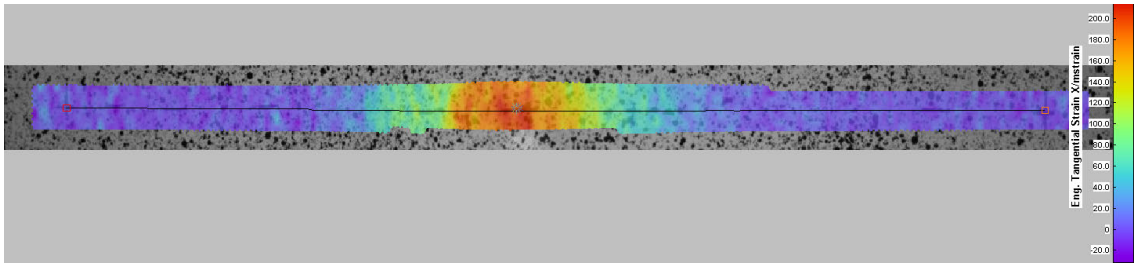

Figure 3.23: Typical example of the engineering strain field in the radial plate direction extracted from the DIC

Chapter 4

Experimental Results

The results of the blast tests performed are presented in this chapter grouped by loading condition (AIR, VBP and SBP). The results are summarised in a table and graphical forms. The permanent mid-line profile of the test plates are extracted from 3D scans of the rear side of the plates. The transient information from the tests are presented in three ways:

- The transient plate profiles through the mid-line of the test plate obtained from the Digital Image Correlation are presented for each experiment at discrete time intervals.
- The midpoint transient deflection for the experimental series is presented grouped by stand off distance (SOD).
- Transient engineering strain results are presented along the mid-line.

Finally the results are compared and the observed differences are noted.

The DIC data is presented in two different ways. Firstly the evolution of the plate profile can be seen by looking at the Z-displacement (out of plane) of the plate. This is shown at discrete points in time together with the observed final deformation profile of the each plate shown in black in the transient deformation section for each series. The transient deformation time histories of the midpoint of the plate are shown for each of the four charge masses (10, 15, 20 and 25g) which shows the mid-point deformation-time response for these different charge masses.

As the deformation of the plate was tracked using the images captured by the high speed camera, it is important to keep note that the frame rate was limited to 30 000 fps due to the amount of light needed to illuminate the specimen, and that this means each

frame was captured at 33 $\boldsymbol{\mu s}$ intervals and the exposure time was 31 $\boldsymbol{\mu s}$. Motion blur was evident in regions of high plate velocity, causing irregularities in the DIC data. In frames affected by the motion blur, the profile of the plate may be partially captured resulting in displacement profiles which are irregular or exhibit artificial discontinuities.

The results from the AIR tests have already been published in the open literature by the author [121] and can be found in the International Journal of Impact Engineering.

Readers are directed to Section 7.1.1 for a discussion on the validation of the different measurement techniques.

4.1 AIR - Air charge

4.1.1 AIR Test Summary

The results of the 26 air-blast experiments are summarised in Table 4.1. A graph of impulse versus charge mass is shown in Figure 4.1. The results of tests at two SODs (40 and 50mm) are indicated in two series for a charge mass range of 10-50g. The results presented in Figure 4.2 show an approximately linear trend of increasing deflection with increasing charge mass, although there is some scatter in the 20g detonations at a 50 mm SOD. The impulses obtained from the 50 mm SOD were consistently lower than the 40 mm SOD impulses which correlates with previous experimental work by Teeling-Smith and Nurick [45].

The post-test inspection revealed that all plates exhibited Mode I (that is, large plastic deformation) failure without any indication of tearing or shearing failures. Membrane action and shear stresses would be present as deformation increases in the plate section but there was no evidence of rupture due to these internal forces.

A graph of permanent mid-point displacement versus impulse for this experimental series is shown in Figure 4.2. The results show the expected trend of increasing displacement with increasing impulse, and also show that the permanent midpoint displacements exhibited by plates tested at 40 mm SOD were larger than those exhibited by plates tested at a SOD of 50 mm. The differences in displacement shown in Figure 4.2 are greater than the small differences observed in the global impulse transfer at the two SODs. This is attributed to the significant variation in the spatial distribution of the loading at the two SODs.

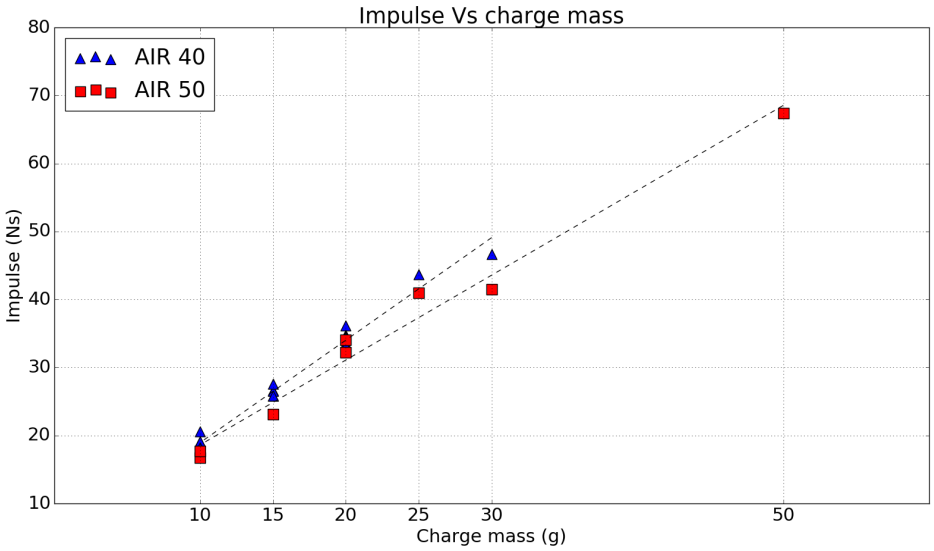

Figure 4.1: Graph of impulse Vs charge mass for all AIR tests.

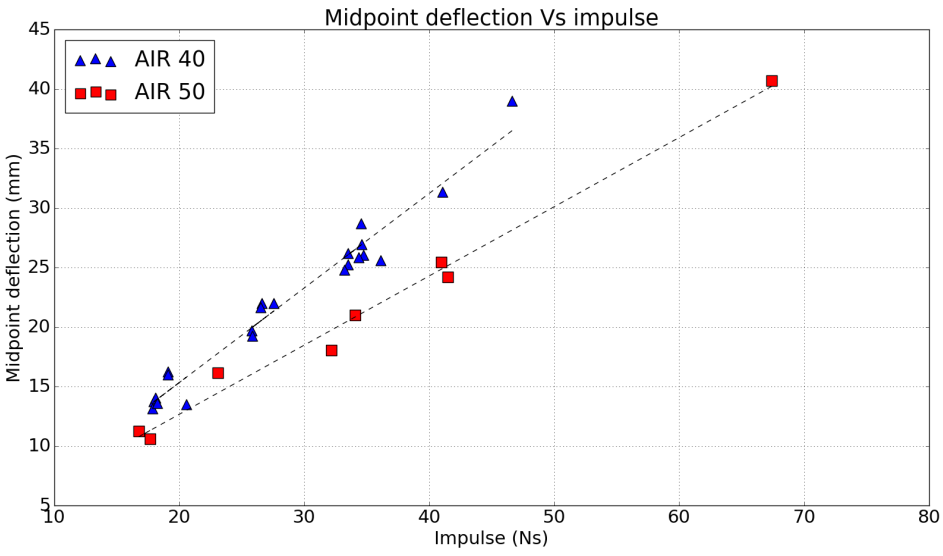

Figure 4.2: Graph of permanent mid-point deflection Vs impulse for all AIR tests.

Date	**DIC data available**	**Charge Mass (g)**	**SOD (mm)**	**Impulse (Ns)**	**δPerm (mm)**	**δPeak (mm)**
2015-09-14		30	40	46.6	39.00	
2016-02-18	Yes	25	40	40.0	31.34	36.27
2015-11-11		20	40	34.5	28.72	
2015-10-05	Yes	20	40	34.7	26.04	31.10
2015-11-11		20	40	34.4	25.87	
2015-09-17		20	40	36.1	25.60	
2016-02-18	Yes	20	40	33.5	25.25	30.67
2016-02-18	Yes	20	40	33.2	24.78	30.24
2015-11-11		15	40	26.6	22.00	
2015-10-01		15	40	27.5	21.98	
2015-10-01		15	40	26.5	21.64	
2016-02-17	Yes	15	40	25.8	19.24	25.28
2016-02-12	Yes	10	40	19.1	16.24	22.02
2015-11-11		10	40	19.1	16.01	
2015-10-02		10	40	18.1	14.05	
2015-10-01		10	40	18.0	13.76	
2015-11-11		10	40	18.2	13.60	
2015-09-14		10	40	17.8	13.15	
2015-09-14		50	50	67.4	40.68	
2015-09-11		30	50	41.5	24.19	
2016-02-18	Yes	25	50	41.0	25.46	30.46
2016-02-18	Yes	20	50	34.1	20.99	26.16
2016-02-18	Yes	20	50	32.2	18.06	23.16
2016-02-17	Yes	15	50	23.1	16.13	21.74
2016-02-17	Yes	10	50	16.7	11.26	16.84
2015-09-14		10	50	17.6	10.61	

Table 4.1: Table of AIR experimental results

4.1.2 Final Deformation profiles of the AIR Specimens

The rear surfaces of the blasted plates were 3D scanned and processed to extract the cross-sectional deformation profile. The permanent displacements along the mid-line of the blasted plates are plotted in Figures 4.3a and Figure 4.3b, for SODs of 40 mm and 50 mm respectively. The plates are stacked in order of increasing charge mass from bottom

to top with charge mass indicated on the left hand side. As expected, the larger charges masses produced larger permanent deformations. It is also evident from Figure 4.3a that the 10g, 15g and 20g tests gave very repeatable profiles shown by the overlapping curves of the repeated tests. The 10g repeat test at 50 mm SOD, shown in Figure 4.3b, also gave excellent repeatability. This indicated that the applied loading and response of the system was repeatable.

An inspection of the permanent displacement profiles in Figures 4.3a and 4.3b shows that the deformation at the 40 mm (closer) SOD was larger in the plate centre, indicating that the blast loading was more localised. This is consistent with observations by Jacob et al [52], who noted a change in plate response from localised to more uniformly distributed with increasing SOD. This is more evident in Figure 4.3c, which shows the deformation profiles for the 40mm and 50mm SOD 20g detonations. The profiles are similar at the centre region of the plate, but the 40mm SOD test shows a higher deflection in the central third of the profile. Similar changes were evident for the remaining charge masses.

The general plate deformation profiles are observed to be similar at the different charge mass between the 40 and 50mm SOD, with the main deviation happening locally under the charge in a 100mm diameter of the centre of the plate. The deformation of the 50mm SOD was always found to be lower than the deformation of the 40mm SOD tests.

Figure 4.4 shows the overlaid representative plate profiles at each SOD for the charge masses; the progressive increase in midpoint deflection and general plate deformation with an increase in charge mass can be seen.

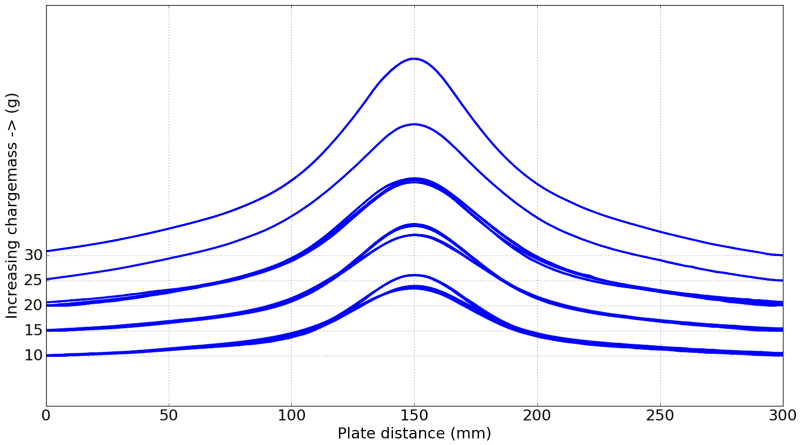

(a) AIR 40mm SOD

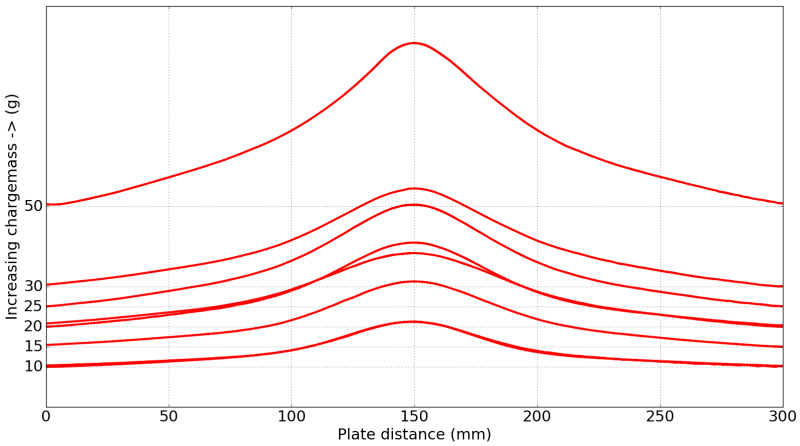

(b) AIR 50mm SOD

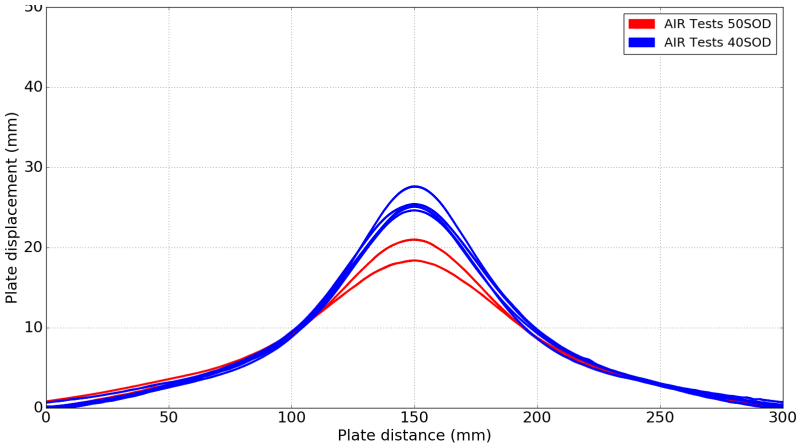

(c) Comparison of 40mm (blue) and 50mm (red) SOD for 20g charge mass.

Figure 4.3: Permanent deformation profiles along the centre line of the blasted plates obtained by 3D scanning.

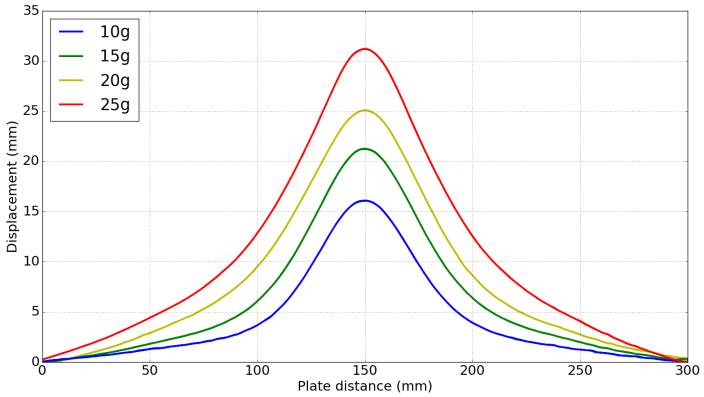

(a) AIR 40mm SOD

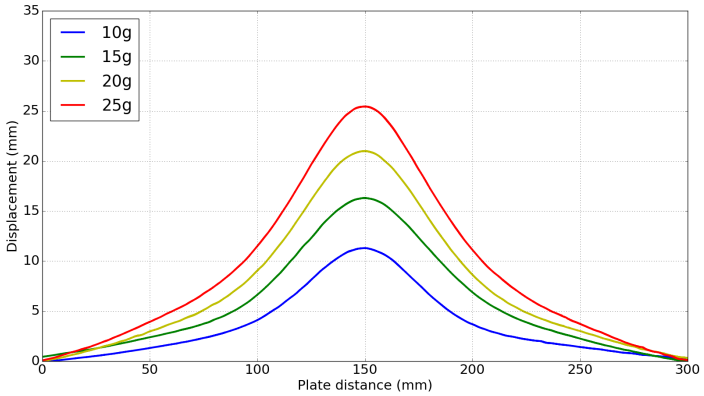

(b) AIR 50mm SOD

Figure 4.4: The final deformed profile of the AIR (a) 40mm and (b) 50mm SOD experiments

4.1.3 Transient Deformation Response AIR

The transient deformation profiles at discrete times are compared in Figures 4.5 - 4.8. From the transient profiles it was observed that, at 66 μs (blue curve), the deformation was consistently more localised in the 40mm SOD series. These profiles are also the most irregular due to motion blur. The deformation appears to be localised to a 100mm diameter plastic hinge in the centre of the plate for both SODs with a higher mid-point deflection in the 40mm SOD series. Similar observations with regard to the radially expanding deformation are mentioned by Tiwari et al [123] looking at a much smaller area of test plate. At 165 μs the plastic hinge had moved out towards the clamp frame

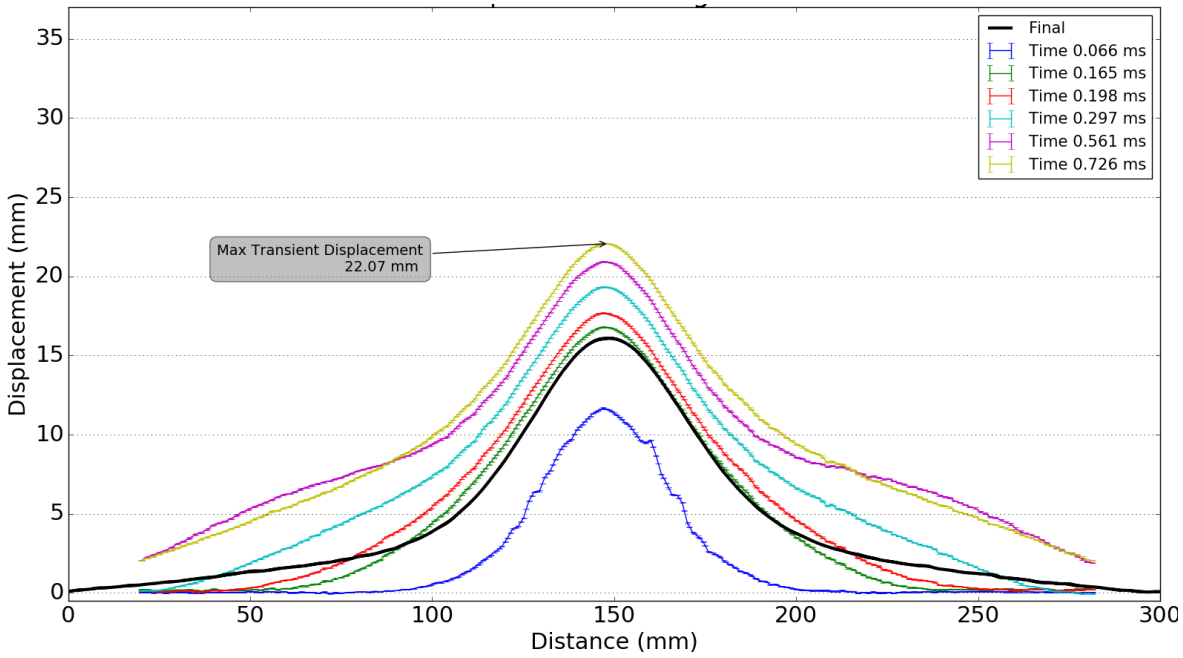

(a) AIR 10g 40mm SOD

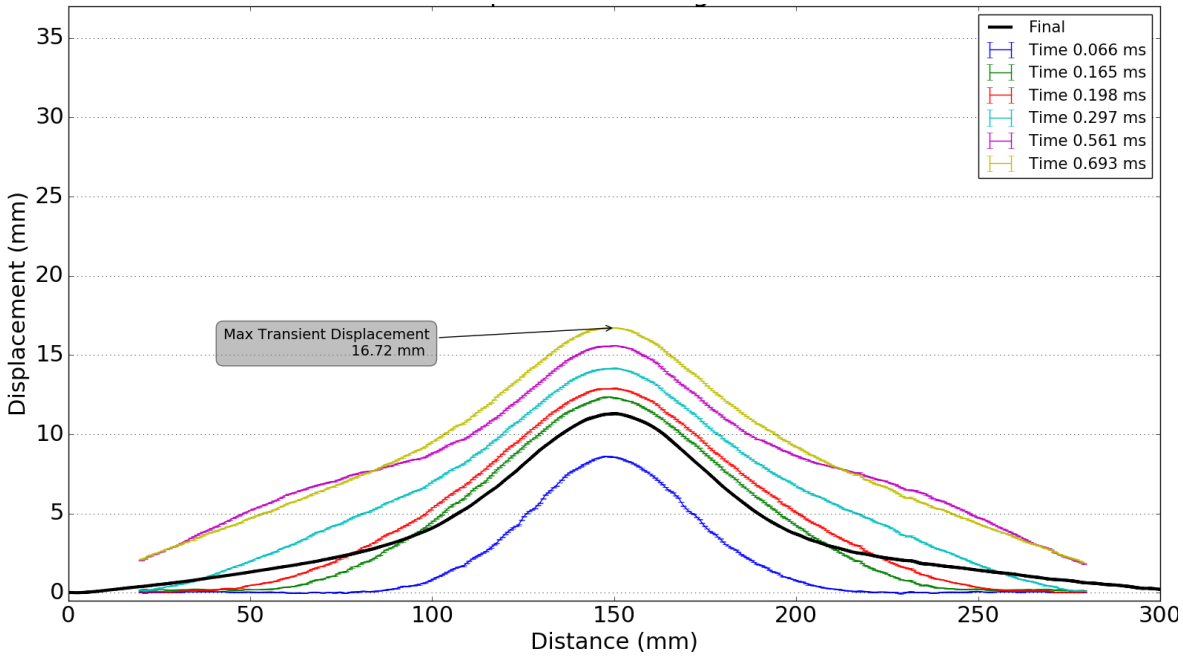

(b) AIR 10g 50mm SOD

Figure 4.5: Transient plate deformation data from DIC for 10g charge detonations

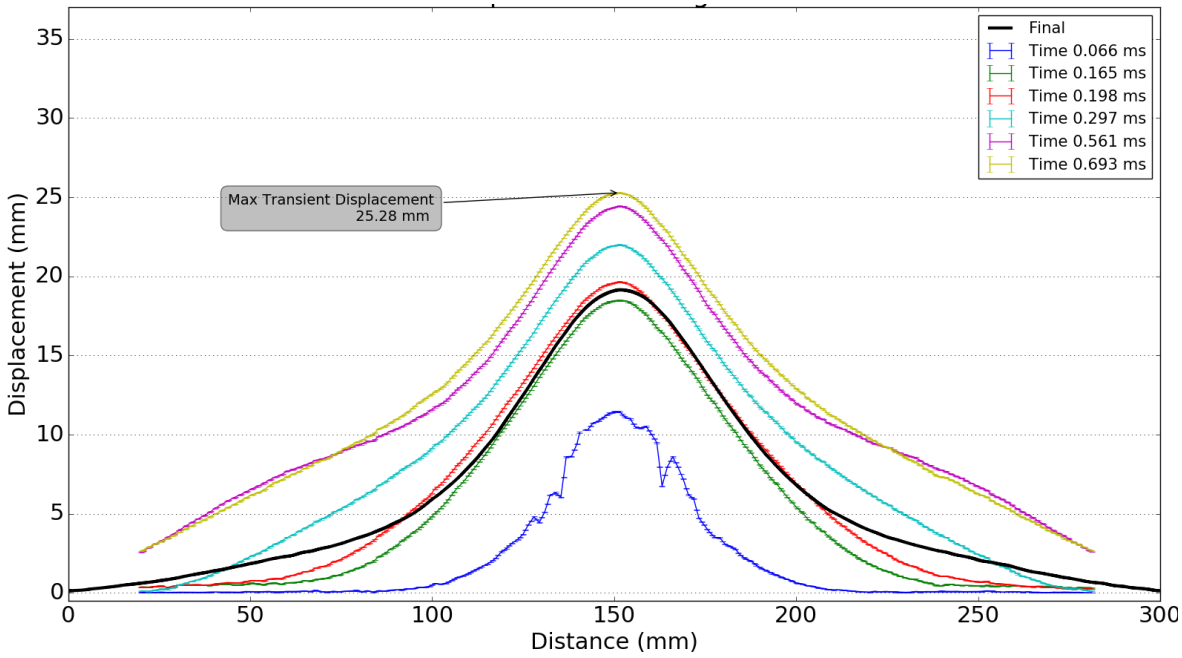

(a) AIR 15g 40mm SOD

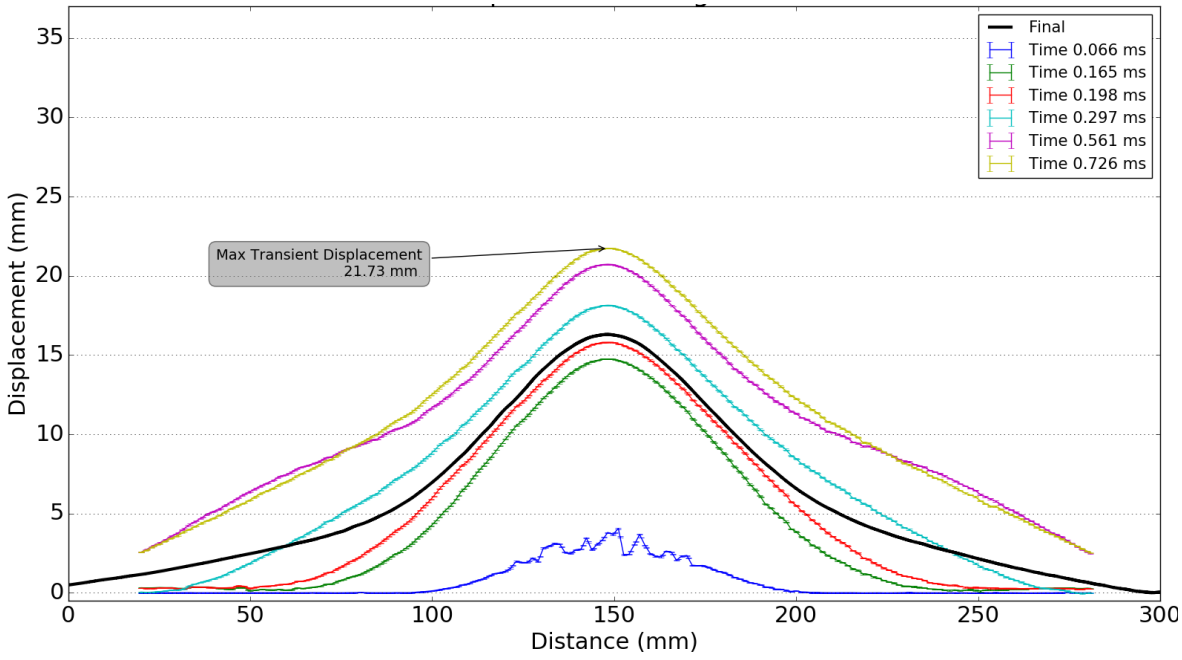

(b) AIR 15g 50mm SOD

Figure 4.6: Transient plate deformation data from DIC for 15g charge detonations

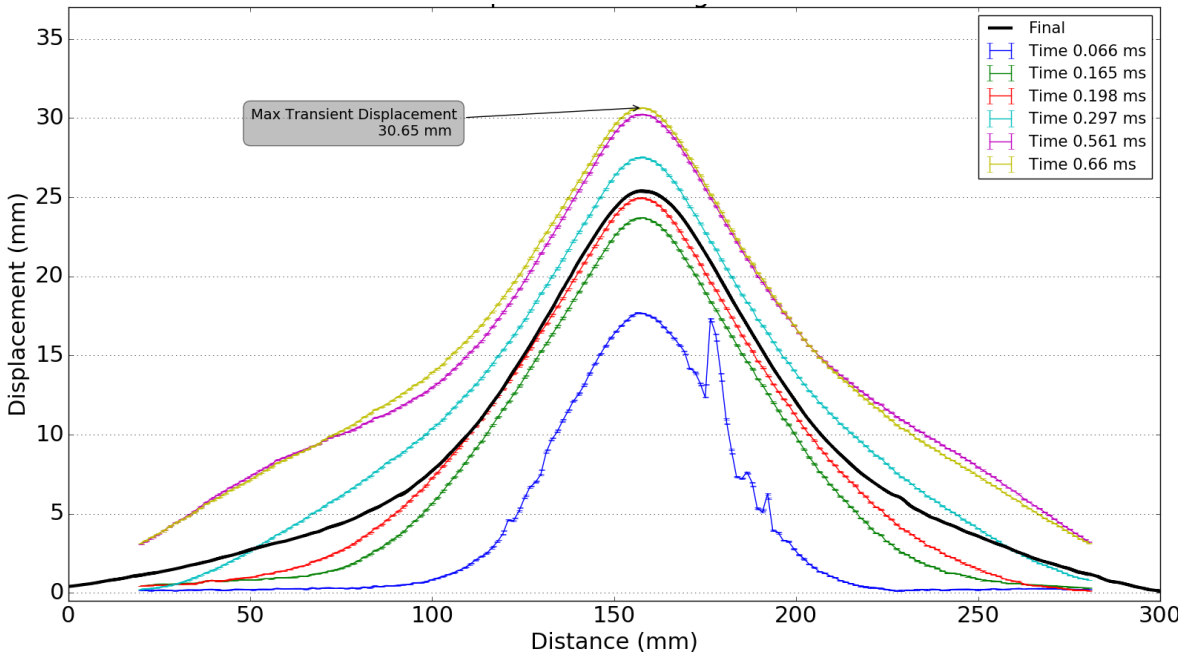

(a) AIR 20g 40mm SOD

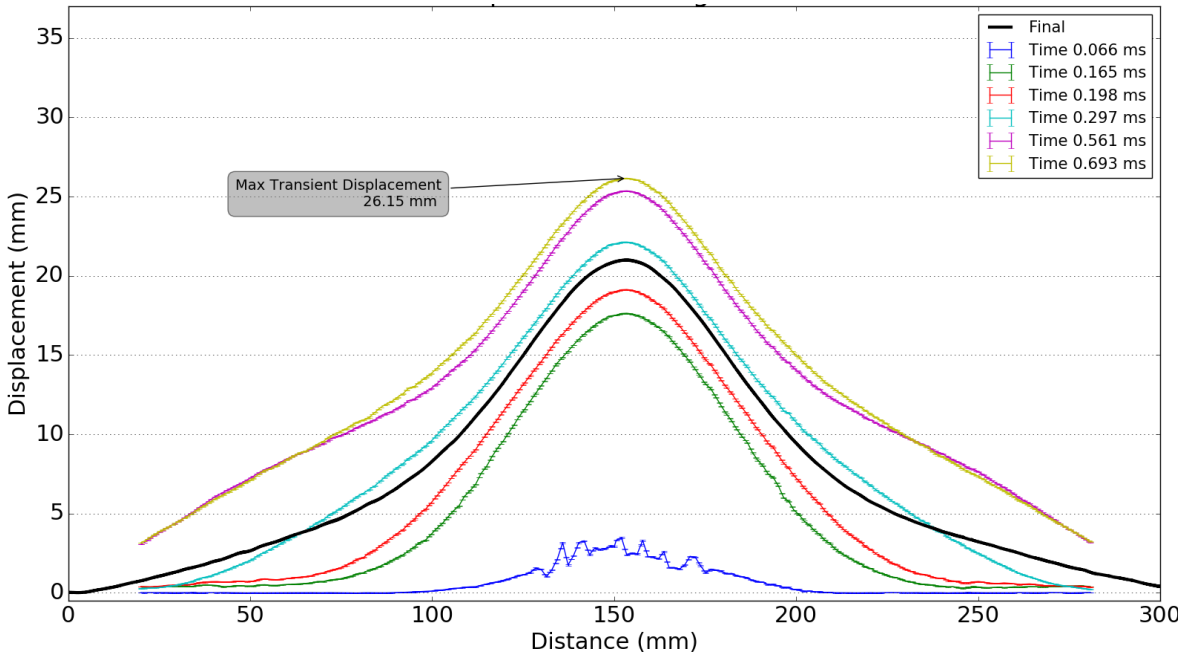

(b) AIR 20g 50mm SOD

Figure 4.7: Transient plate deformation data from DIC for 20g charge detonations

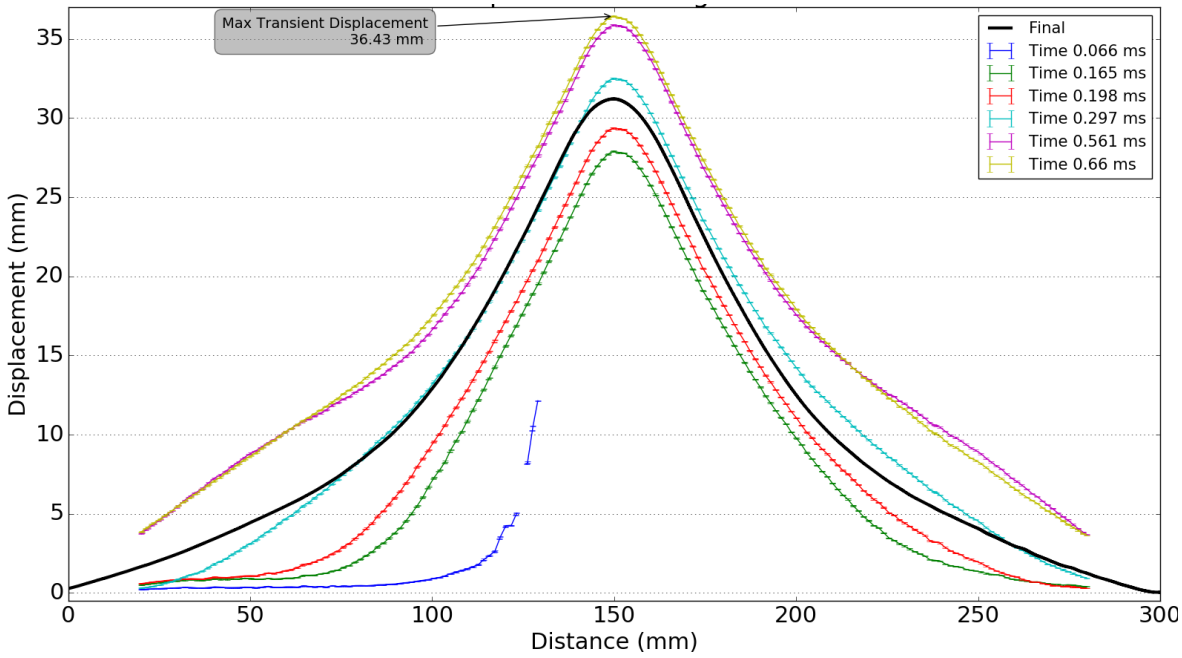

(a) AIR 25g 40mm SOD

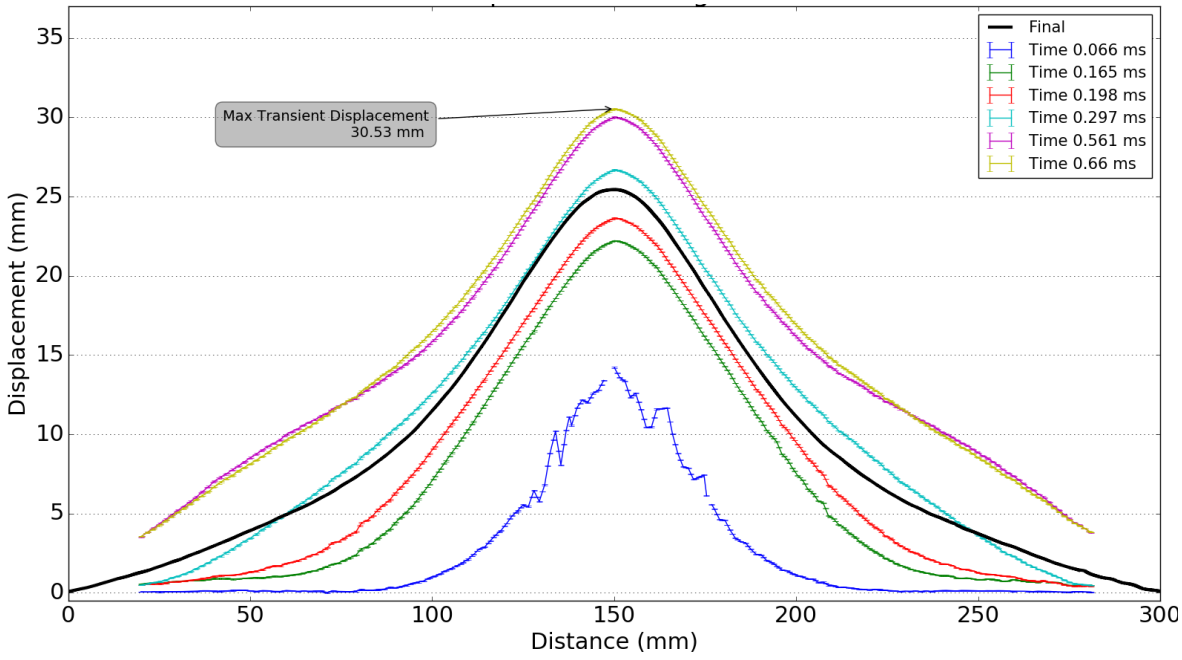

(b) AIR 25g 50mm SOD

Figure 4.8: Transient plate deformation data from DIC for 25g charge detonations

and seemed to be positioned at a diameter of approximately 150mm, and the shape of the deformed section was conical between the midpoint and the plastic hinge. By 297 $\boldsymbol{\mu s}$, the plastic hinge has reached a diameter of approximately 250mm. The profile was bell-shaped with a point of inflection at approximately 100mm diameter.

This point of inflection becomes more noticeable just before the plate reaches its maximum transient deformation and was the most pronounced after 561 $\boldsymbol{\mu s}$. After the plates reach their maximum transient deformation, the point of inflection becomes less significant and was almost undetectable by the time the plate reaches its final shape.

The transient midpoint deflection time histories for the 10-25g charges are shown in Figure 4.9. There was a sharp linear increase in the midpoint displacement which becomes non-linear as the central plate velocity decreased to zero at the peak maximum transient deflection. After this point, elastic recovery of the plate was observed and the midpoint oscillated around the mean permanent deflection point. It is observed that there is a consistent time to reach peak transient deflection of 0.7 ms. The post-peak transient displacements oscillated about the permanent in a similar way, for all charge masses, with a period of 2.82 ms. The final displacement is represented by the dashed lines and was defined as the average of three post-test displacement measurements, obtained using a vernier height gauge. Figure 4.9 also shows very good repeatability of the form of the transient midpoint displacement history at different charge masses. The displacement histories throughout the AIR charge configuration produced very similar profiles.

The difference in the transient mid point deflection and final mid point deflection, seen in Table 4.1 for both SODs, was fairly constant, being 5-6mm (less than two plate thicknesses).A similar decrease due to elastic rebound was also present in the midpoint deflection data reported by Neurberger *et al* [124].

It is further noted that up to the point of maximum transient midpoint displacement the shape of the general plate profile does not match the final deformed profile shape at any point. This implies that any measurements extracted from numerical simulations or DIC measurements are unlikely to match the final deformation profile until the plate has been allowed to settle.

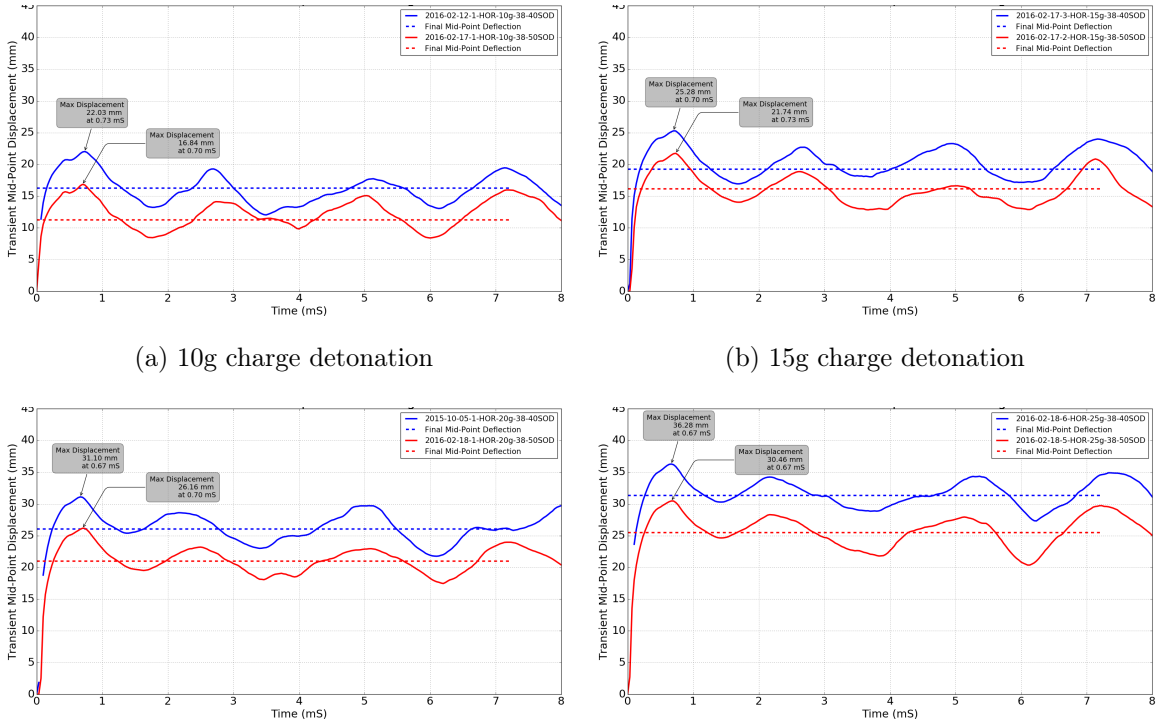

(a) 10g charge detonation

(b) 15g charge detonation

(c) 20g charge detonation

(d) 25g charge detonation

Figure 4.9: Mid-point transient deflection - time histories for various charge masses

4.1.4 Transient strain for AIR charges

The radial plastic strain along the centre line of the plates (at the point of maximum transient deflection) is shown in Figure 4.10. It is observed from Figure 4.10 that the strain along the mid line was localised at the plate centre. The strain peaked at the centre and decayed to nominally zero at approximately a 100mm diameter around the centre. The location where the strain appears to have nominally reached zero, appears to coincide with the point of inflection in the permanent deflection profile seen in Figure 4.3. The maximum strain increased with a decrease in SOD and an increase in charge mass. Representative values of the maximum central strain value along the centre line of the plates are shown in Table 4.2, grouped by SOD. Full plots of the respective strains, at the same time points seen in displacement plots shown in Figure 4.5 - 4.8, are shown in Appendix A.1.

	Maximum central strain value (mstrain)	
Charge Mass (g)	**40 SOD**	**50 SOD**
10	154	65
15	145	83
20	177	99
25	210	140

Table 4.2: The AIR maximum centre point strain along the centre line of the test plates.

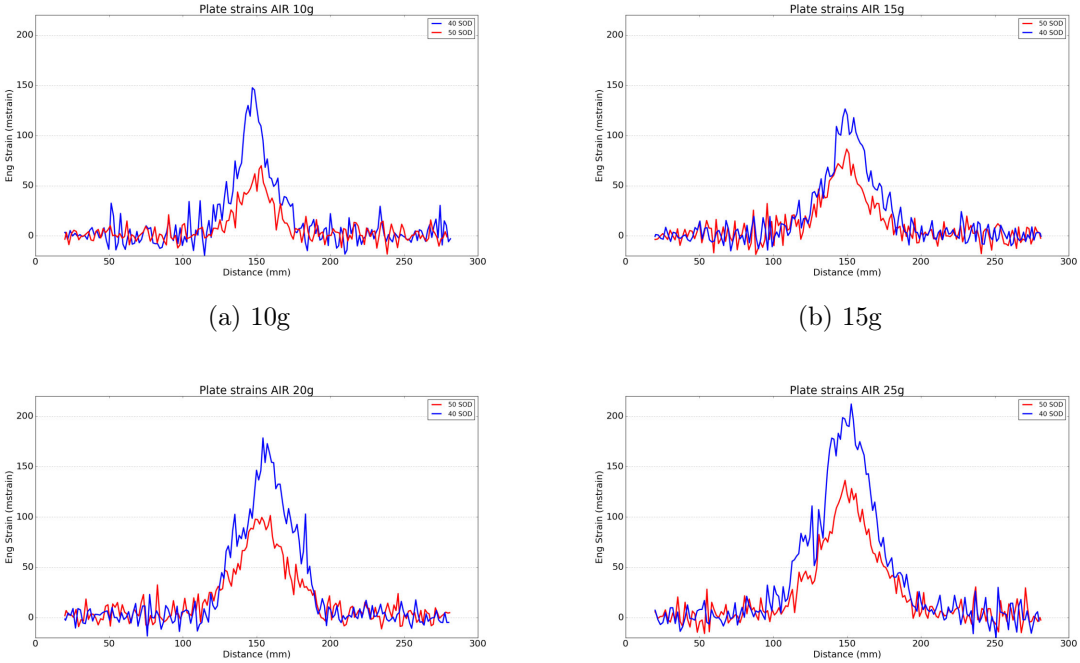

(a) 10g (b) 15g

(c) 20g (d) 25g

Figure 4.10: Typical radial plastic strain through the AIR plate centres at 0.7 ms (point of maximum transient deflection) for various charge mass detonations.

4.2 VBP - Vertical back plate air charge

4.2.1 VBP Test Summary

The results of 22 VBP tests are summarised in Table 4.3. As with the AIR series, two SODs, 40mm and 50mm, were used and are compared here.

The post-test inspection revealed that all the VBP plates exhibited Mode I (that is, large plastic deformation) failure without any indication of tearing or shearing failures.

Date	**DIC data available**	**Charge Mass (g)**	**SOD (mm)**	**Impulse (Ns)**	**δPerm (mm)**	**δPeak (mm)**
2016-02-10	Yes	25	40	126.94	38.37	42.73
2016-01-22	Yes	20	40	131.71	35.55	40.76
2015-12-18		20	40	118.86	33.34	
2015-12-22		15	40	111.67	29.56	
2015-12-21		15	40	106.19	28.01	
2015-12-21		15	40	115.64	31.80	
2016-01-19	Yes	15	40	110.24	31.47	37.19
2016-01-14	Yes	15	40	117.22	28.16	33.42
2015-12-22		10	40	92.08	21.90	
2015-12-21		10	40	95.00	21.65	
2016-02-05	Yes	10	40	93.06	25.98	31.84
2016-02-09	Yes	25	50	120.15	34.41	36.32
2016-01-27	Yes	20	50	110.57	29.95	37.11
2015-12-23		20	50	117.22	29.73	
2015-12-22		20	50	106.70	26.01	
2015-12-23		15	50	106.29	23.68	
2015-12-23		15	50	103.96	23.63	
2016-02-05	Yes	15	50	90.70	24.31	29.79
2016-01-26	Yes	10	50	88.00	21.85	28.25
2016-01-25	Yes	10	50	89.00	22.33	28.23
2015-12-23		10	50	80.00	20.56	
2015-12-23		10	50	88.00	21.22	

Table 4.3: Table of VBP experimental results

Figure 4.11 shows the impulse versus charge mass for the two SOD's. The impulse

was noted to increase with charge mass in a linear fashion for each SOD. A graph of permanent mid-point displacement versus impulse is shown in Figure 4.12 and displays the expected trend of linearly increasing displacement with increasing impulse. The permanent midpoint displacements for plates tested at 40 mm SOD were larger than the displacements of plates tested at a 50 mm SOD. The differences in displacements due to SOD are smaller in the VBP tests compared to the air backed charge (AIR) tests.

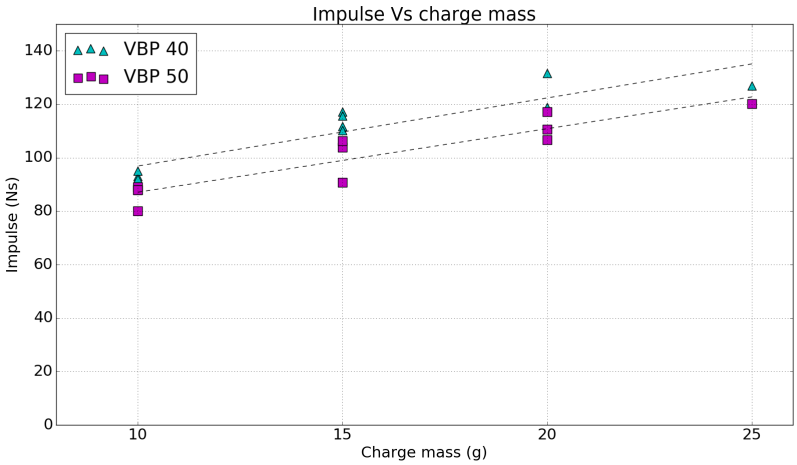

Figure 4.11: Graph of impulse versus charge mass for the VBP tests

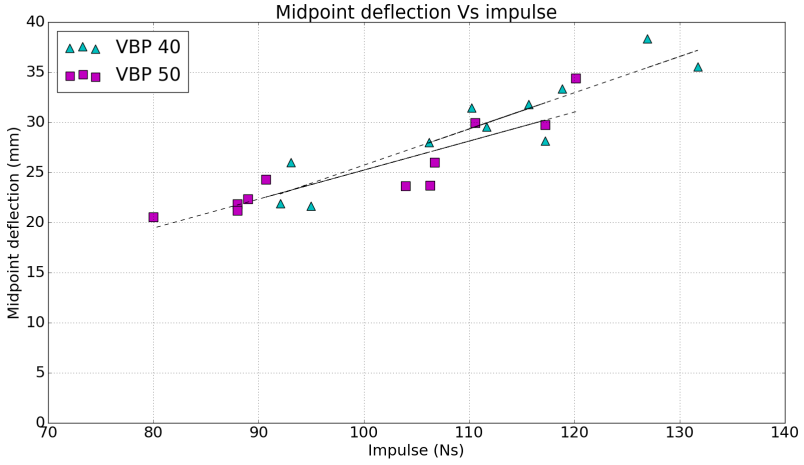

Figure 4.12: Graph of permanent mid-point deflection versus impulse

4.2.2 Final Deformation profiles of the VBP Specimens

The permanent displacements along the mid-line of the blasted plates were obtained from 3D scanning and are shown in Figures 4.13a and 4.13b, for SODs of 40 mm and 50 mm respectively. The plates are stacked in order of increasing charge mass from bottom to top with charge mass indicated on the left hand side. As expected, the larger charges masses produced larger permanent deformation in the plates. It is also evident from Figures 4.13a and 4.13b that the 10g, 15g and 20g tests gave very repeatable profiles shown by the overlapping curves of the repeated tests. The permanent midpoint deflection of the plates at repeated charge masses varied by no more than 1 plate thickness. This indicated that the applied loading and response of the system was repeatable.

An inspection of the permanent displacement profiles of the plates in Figures 4.13a and 4.13b shows that the deformation at the 40 mm (closer) SOD was larger in the plate centre, indicating that the blast loading was more locally applied. This was also observed in the AIR plates where it was noted that the 40mm S experiments displayed a more localised deformation response. Figure 4.13c shows the overlaid tests performed with 15g charge mass clearly showing a similar response to that reported by Jacob *et al* [52], who noted a change in plate response from localised to more uniformly distributed with increasing SOD and is clearly seen in Figure 4.13c.

The general plate deformation profiles are observed to be similar at the different charge mass between the 40 and 50mm SOD, with the main deviation happening locally under the charge in a 100mm diameter. The deformation of the 50mm SOD was always found to be lower than the deformation of the 40mm SOD tests. Representative tests for the VBP 40mm and 50mm SOD tests final deformed shape are shown in Figure 4.14a and 4.14b. A clear increase in deformation can be seen with an increase in charge mass and a decrease in SOD.

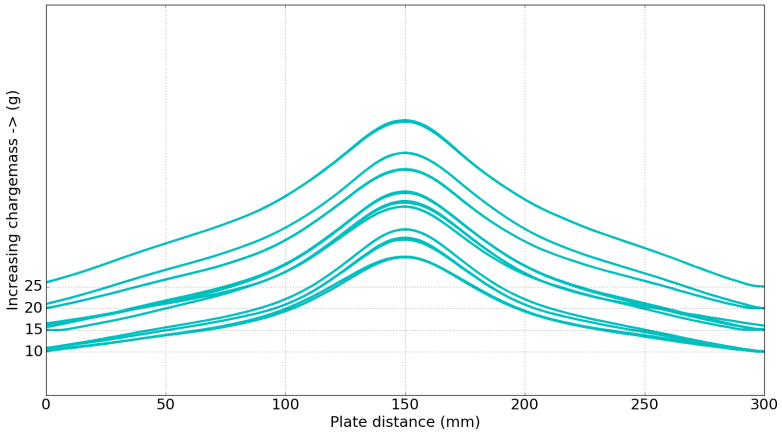

(a) VBP 40mm SOD

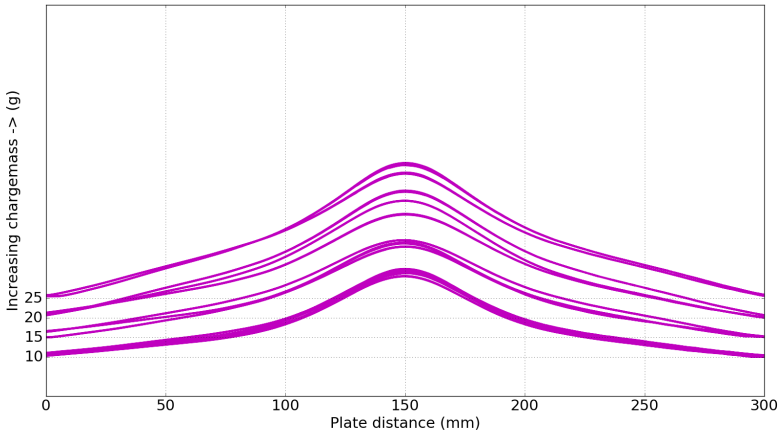

(b) VBP 50mm SOD

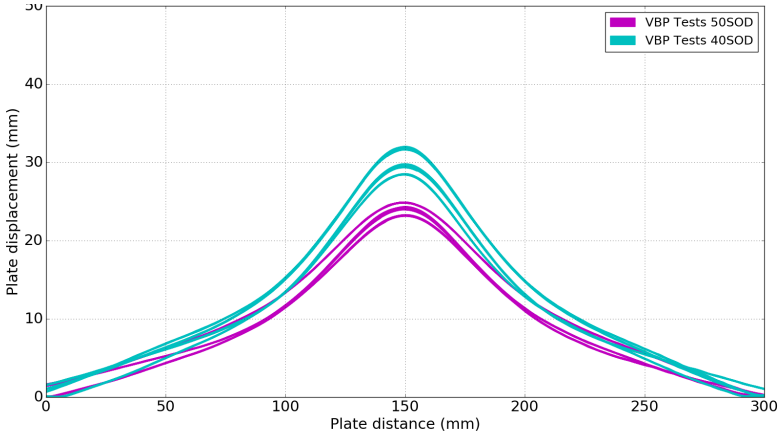

(c) Comparison of VBP 40mm (blue) and 50mm (red) SOD for 15g charge mass.

Figure 4.13: Permanent deformation profiles of VBP series along the centre line of the blasted plates obtained by 3D scanning.

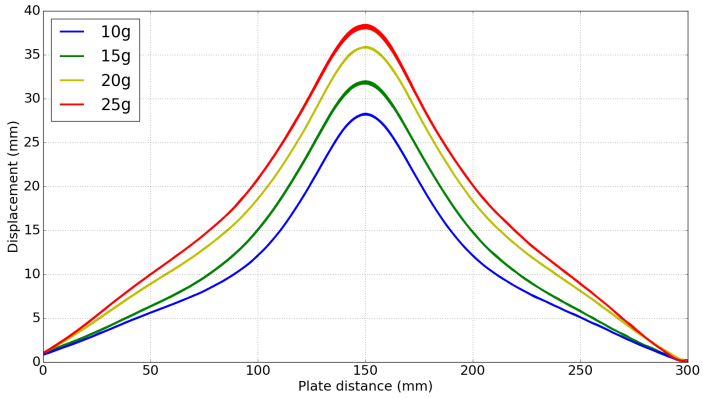

(a) VBP 40mm SOD

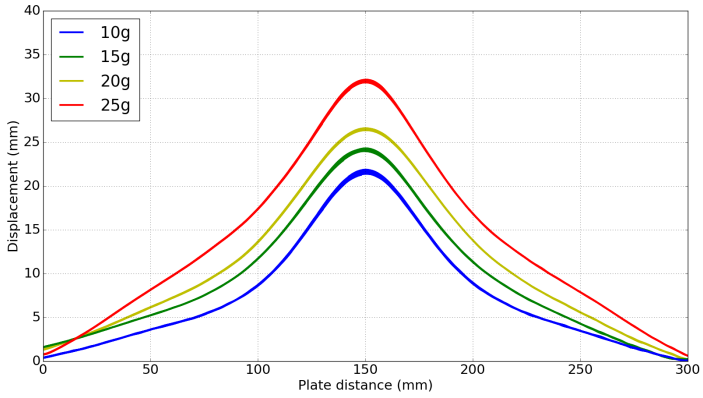

(b) VBP 50mm SOD

Figure 4.14: Representative final deformed profiles of the VBP (a) 40mm and (b) 50mm SOD experiments

4.2.3 VBP Transient Response

The transient deformation profiles at discrete times are shown in Figures 4.15 - 4.18. At 66 μs (blue curve) there is consistently more localised deformation in the 40 SOD series. The 66 μs profiles are either the most irregular due to motion blur, or missing as the DIC technique was unable to correlate the images in some cases. The deformation appears to be localised to a 100mm diameter plastic hinge in the centre of the plate for both SOD's with a higher mid-point deflection in the 40 SOD series, similar to findings by Tiwari et al [123], looking at air blasted plates. At 165 μs the plastic hinge has moved out towards the clamp frame and appears at around 150mm diameter, the shape of the

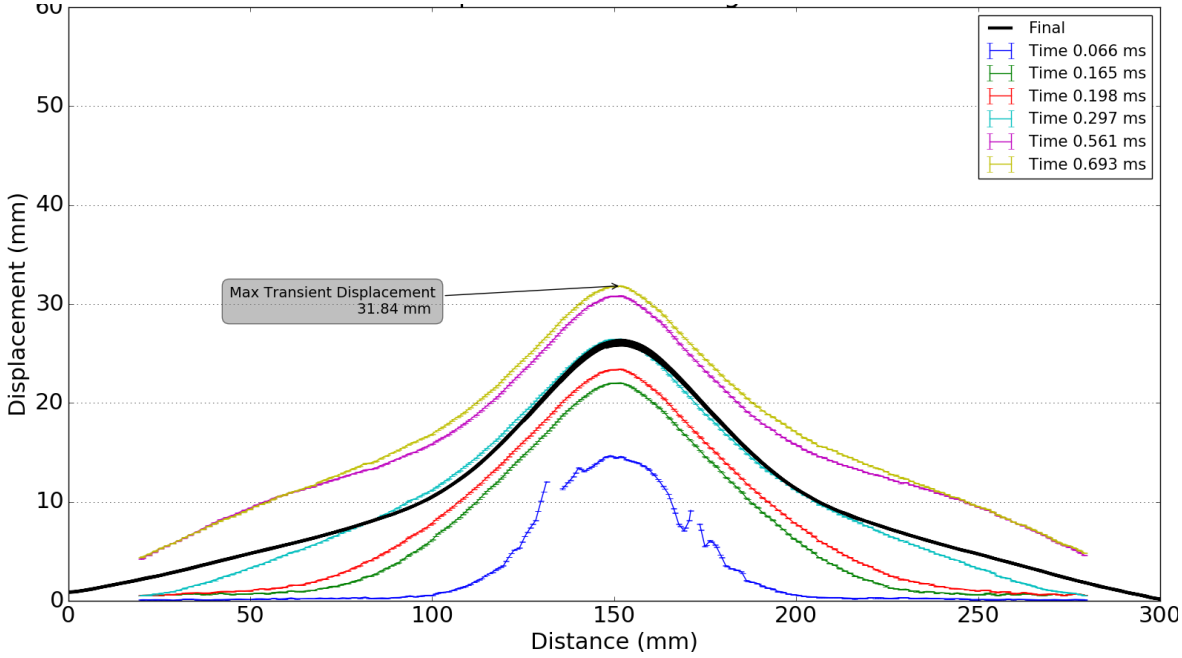

(a) VBP 10g 40mm SOD

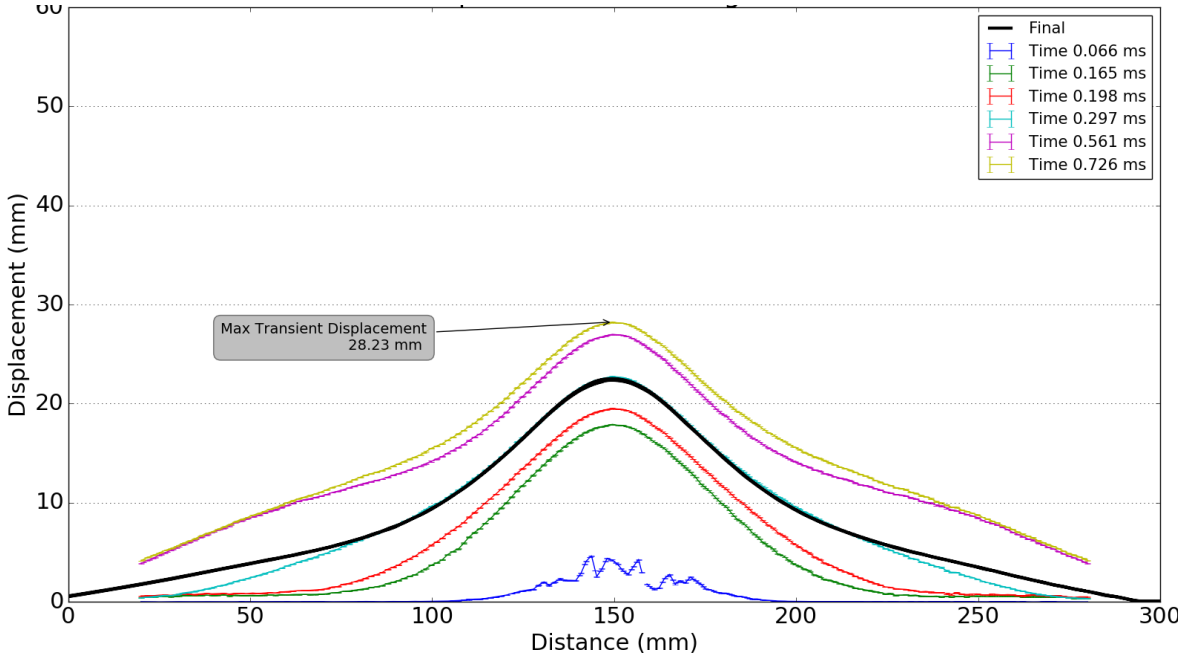

(b) VBP 10g 50mm SOD

Figure 4.15: Transient plate deformation data from DIC for 10g VBP charge detonations

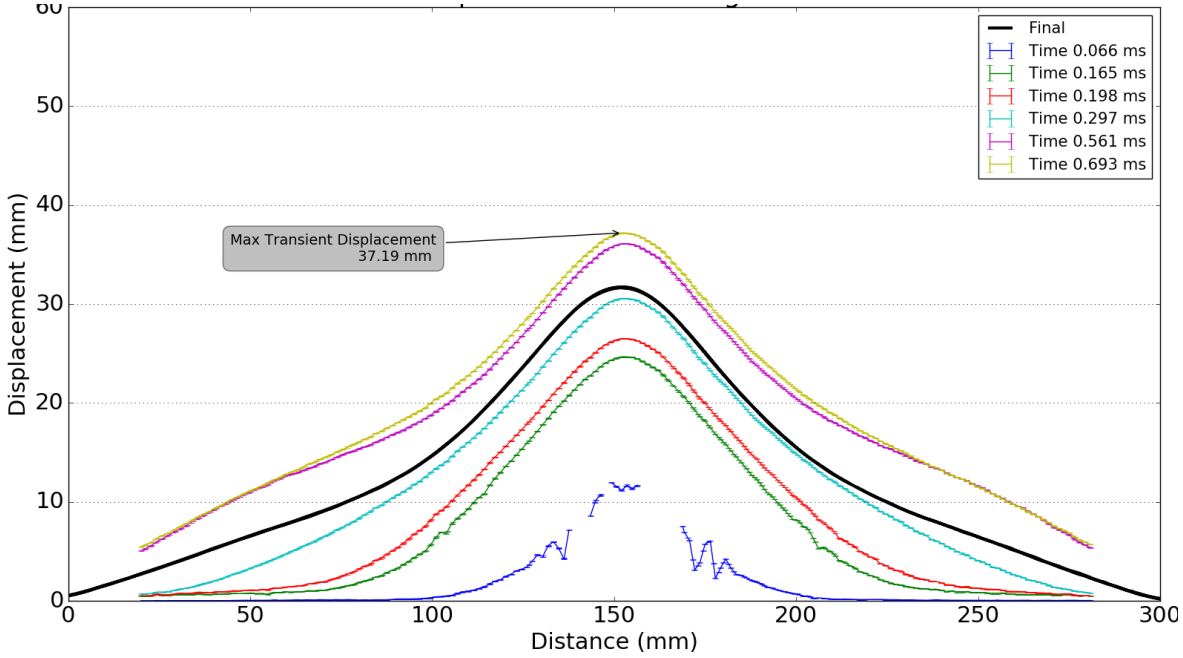

(a) VBP 15g 40mm SOD

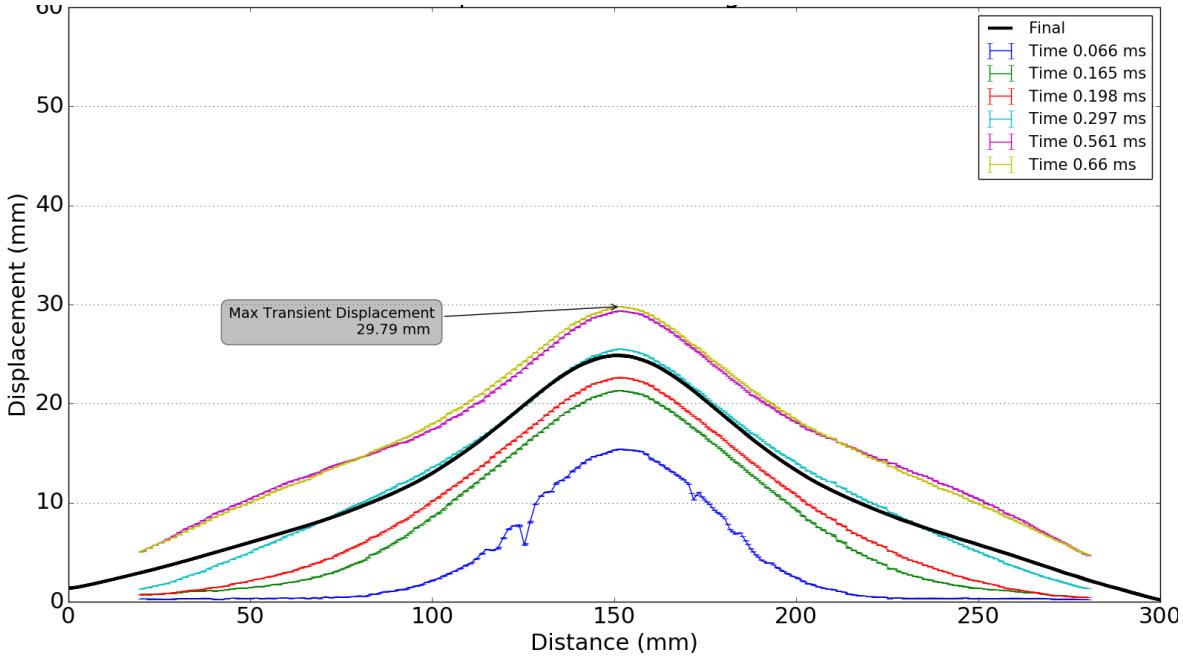

(b) VBP 15g 50mm SOD

Figure 4.16: Transient plate deformation data from DIC for 15g VBP charge detonations

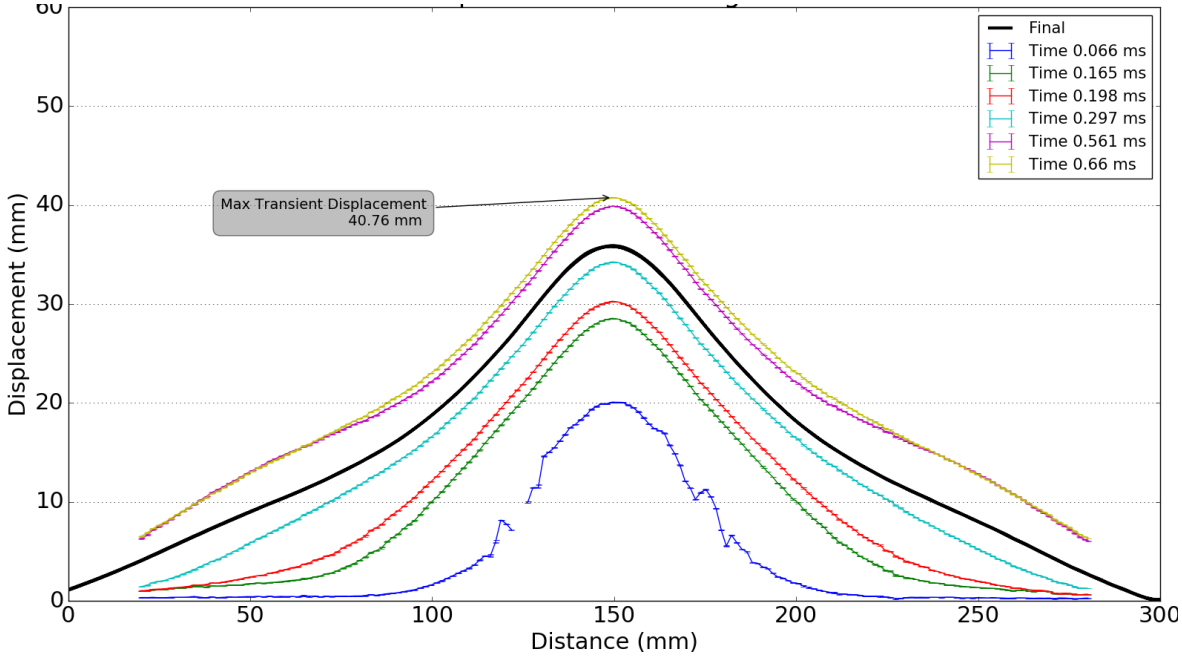

(a) VBP 20g 40mm SOD

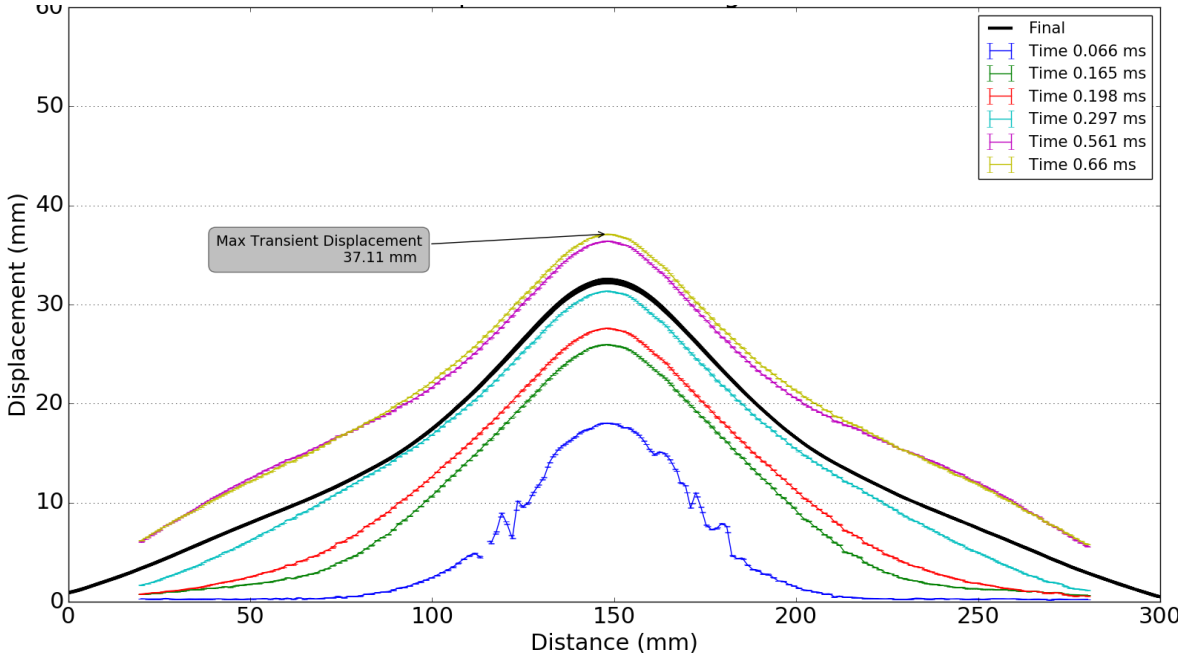

(b) VBP 20g 50mm SOD

Figure 4.17: Transient plate deformation data from DIC for 20g VBP charge detonations

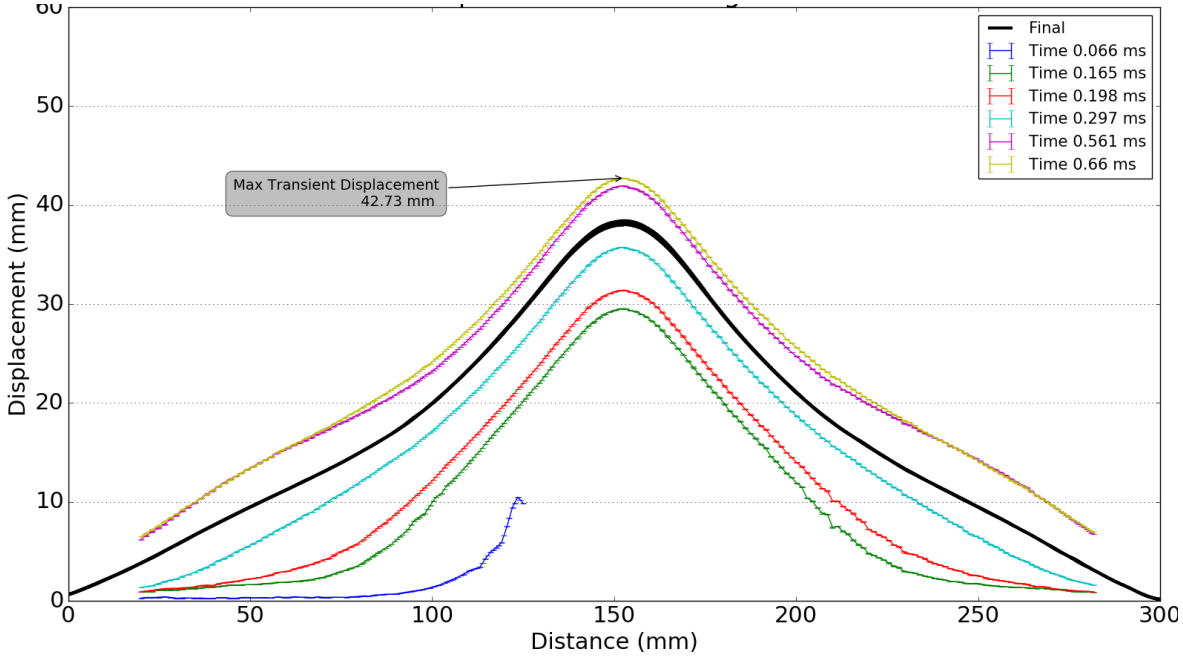

(a) VBP 25g 40mm SOD

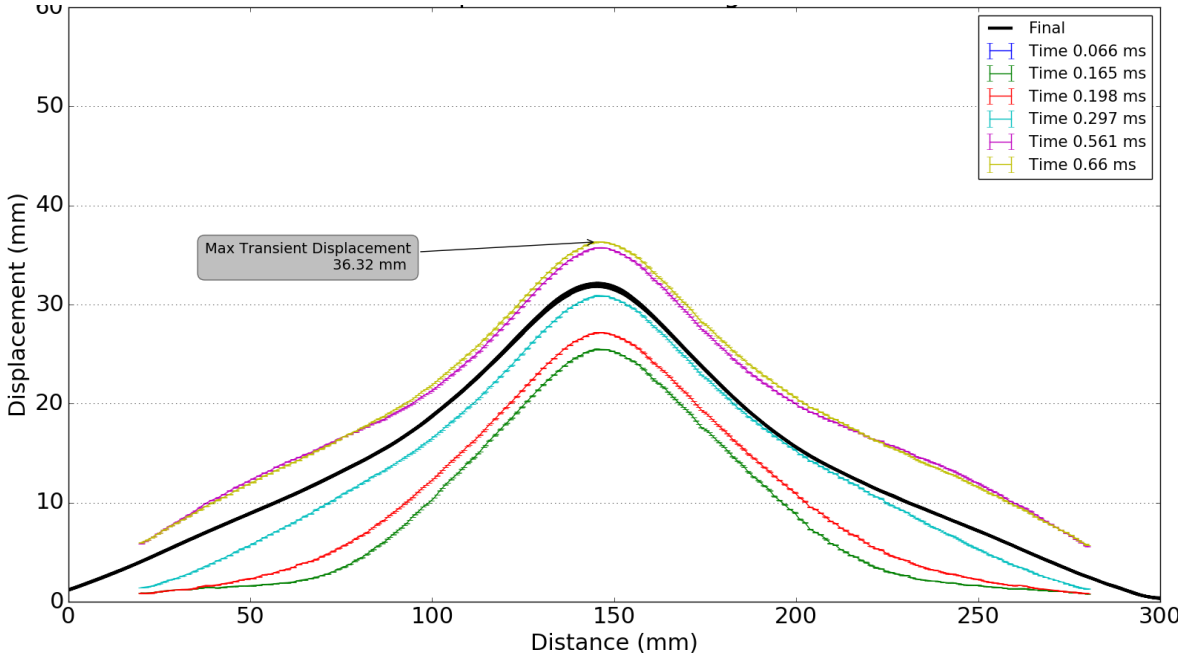

(b) VBP 25g 50mm SOD

Figure 4.18: Transient plate deformation data from DIC for 25g VBP charge detonations

deformed section is conical between the midpoint and the plastic hinge. By 297 $\boldsymbol{\mu s}$, the plastic hinge has reached a diameter of approximately 250mm and the general profile was bell-shaped with a point of inflection forming at approximately 100mm diameter. This point of inflection became more noticeable and was most pronounced at 561$\boldsymbol{\mu s}$ as the plate approaches its maximum transient deformation. The plates reached maximum transient deformation between 660 and 700 $\boldsymbol{\mu s}$, and the point of inflection became less significant. The inflection point was almost undetectable once the plate reached its final shape. During the evolution of the plate profile there is a very localised initial deformation with a radially outward moving plastic hinge that transitions into a more global and final profile after 165 $\boldsymbol{\mu s}$.

The transient midpoint deflection time histories shown in Figure 4.19, show that there is a consistent time to reach peak transient deflection of approximately 0.7 ms regardless of SOD or charge mass. The plates also exhibited similar post-peak oscillations of the mid point displacement between 0.7 - 3 ms. After 3 ms, the midpoint oscillates at a higher but still irregular frequency around the final deformation point illustrated by the dashed lines. Figure 4.19 also shows very good repeatability of the transient midpoint displacement on the 10g charge mass. The overall shape of the midpoint time histories for the charges at different SODs are similar and appear repeatable. It is further noted that the DIC measurements show that the transient deformation profiles do not have the same shape as the permanent plate profiles measured post-test. This has implications for the validation of numerical models of blast loaded steel structures.

4.2.4 Transient strain

The radial plastic strain along the centre line (at the point of maximum transient deflection) is shown in Figure 4.20. It is evident from Figure 4.20 that the strain along the mid line was localised at the plate centre. The strain peaked at the centre and decayed to nominally zero at approximately a 100mm diameter around the plate centre, which coincides with the point of inflection in the permanent deflection profile seen in Figure 4.13c. The maximum strain increased with a decrease in SOD and an increase in charge mass. Representative values of the maximum central strain value along the centre line of the plates are shown in Table 4.4, grouped by SOD. Full plots of the respective strains, at the same time points seen in displacement plots shown in Figure 4.15 - 4.18, are shown in Appendix A.2.

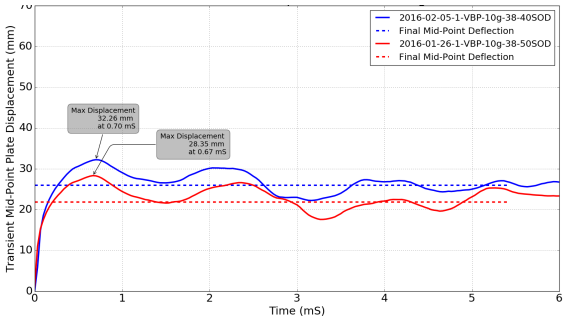

(a) 10g charge detonation

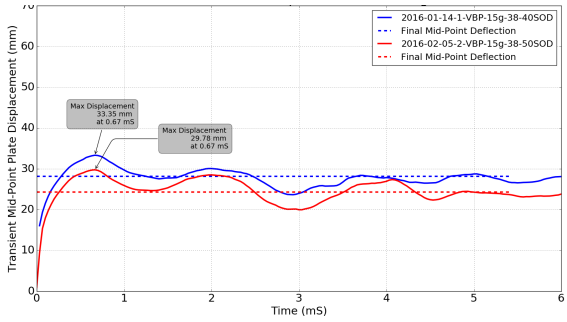

(b) 15g charge detonation

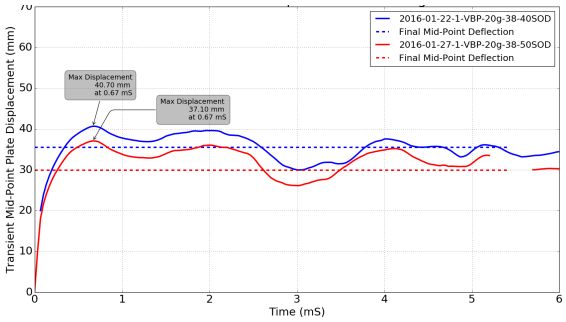

(c) 20g charge detonation

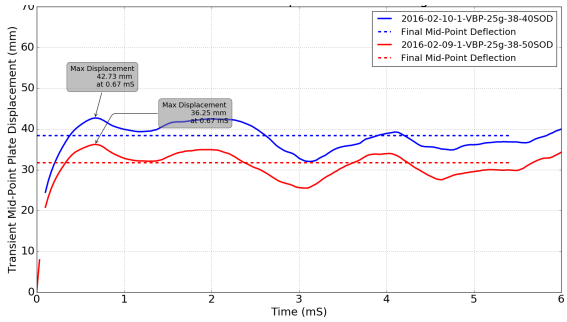

(d) 25g charge detonation

Figure 4.19: Mid-point transient deflection - time histories for the various VBP charge masses

	Maximum central strain value (mstrain)	
Charge Mass (g)	**40 SOD**	**50 SOD**
10	154	140
15	160	102
20	177	148
25	190	150

Table 4.4: The VBP maximum centre point strain along the centre line of the test plates.

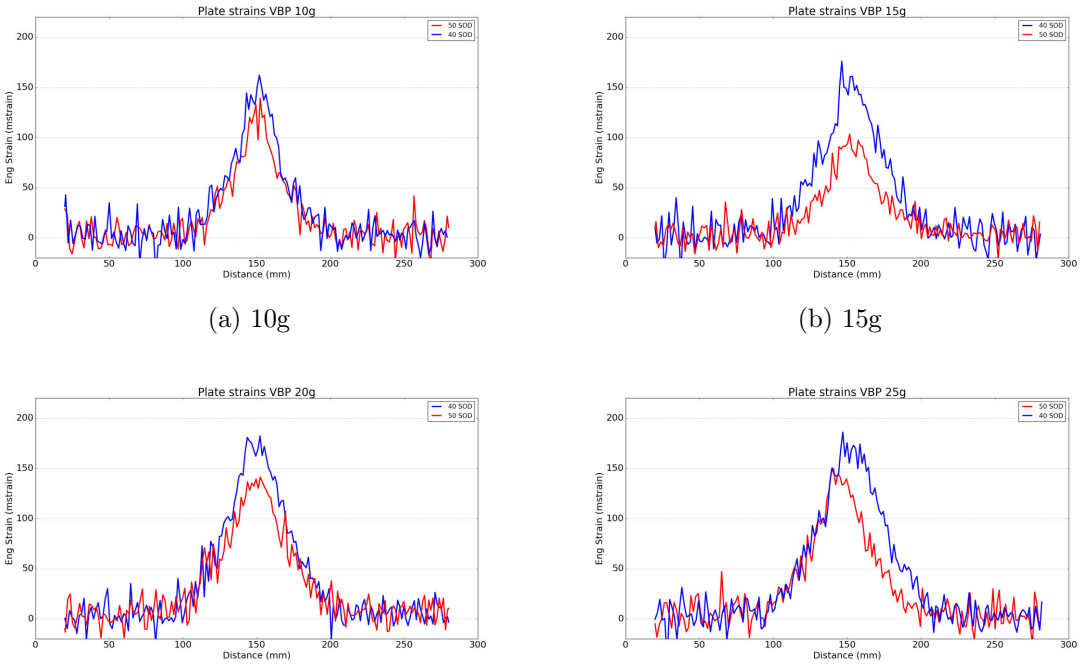

(a) 10g (b) 15g

(c) 20g (d) 25g

Figure 4.20: Typical radial plastic strain through the VBP plate centres at 0.7 ms (point of maximum transient deflection) for various charge mass detonations.

4.3 SBP - Buried sand charge

4.3.1 SBP Test summary

The results of ten buried sand charge experiments with a metal backing plate are presented in Table 4.5. The tests varied in charge mass from 10 - 30g but kept a constant airgap between the test plate and sand of 40mm. In addition a constant depth of burial of 10mm was used through the series, making a total distance from the explosive surface to the test plate (SOD) of 50mm.

All plates exhibited Mode I (that is, large plastic deformation) failure without any indication of tearing or shearing failures, as planned, in order to avoid damaging the camera system or creating discontinuities such as cracks that could be difficult to process during DIC.

A graph of permanent mid-point displacement versus impulse is shown in Figure 4.22. The results show the expected trend of linearly increasing displacement with increasing impulse.

Date	**DIC data available**	**Charge Mass (g)**	**SOD (mm)**	**DOB (mm)**	**Impulse (Ns)**	**δPerm (mm)**	**δPeak (mm)**
2016-01-02		30	50	10	258.81	48.91	
2016-02-10	Yes DIC	25	50	10	242.85	47.53	51.90
2015-12-21		20	50	10	196.15	39.86	
2016-01-20	Yes DIC	20	50	10	230.66	41.74	44.29
2015-12-28		15	50	10	158.24	35.98	
2016-01-18	Yes DIC	15	50	10	147.24	36.11	38.79
2016-01-04		15	50	10	136.78	33.54	
2015-12-21		10	50	10	111.36	26.26	
2016-01-15	Yes DIC	10	50	10	103.23	28.40	31.68
2016-01-04		10	50	10	108.13	29.75	

Table 4.5: Table of SBP experimental results

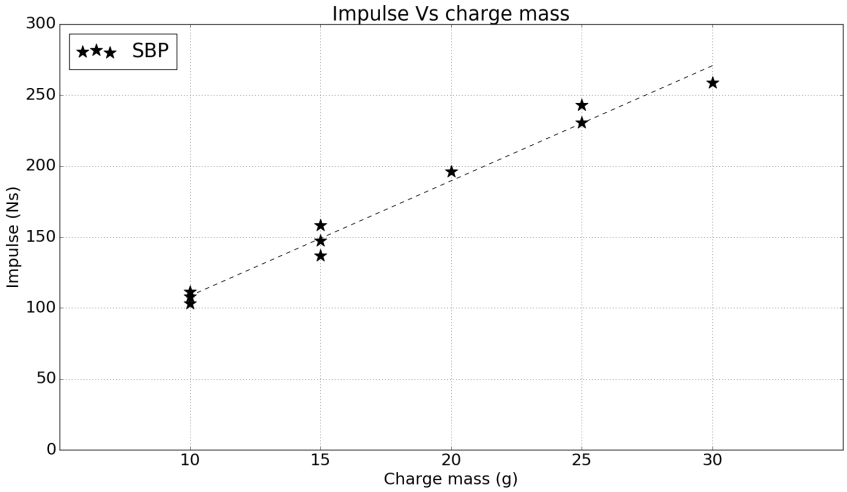

Figure 4.21: Graph of impulse versus charge mass for the SBP tests

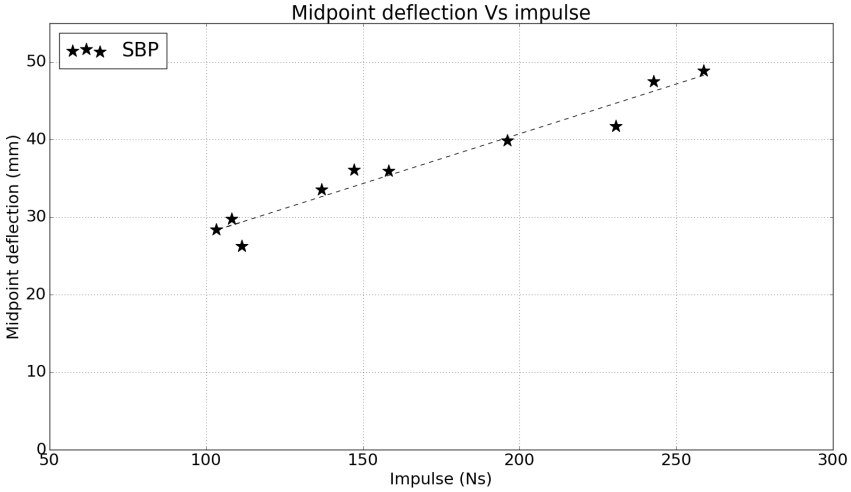

Figure 4.22: Graph of permanent mid-point deflection versus impulse for the SBP tests

4.3.2 Final Deformation profiles of the SBP Specimens

The permanent displacements along the mid-line of the blasted plates are shown in Figure 4.23. The plates are stacked in order of increasing charge mass as indicated by the vertical axis marker. As expected, the larger charges masses produced larger permanent deformation in the plates. It is also evident from Figure 4.23 that the 10g,

15g and 20g tests gave very repeatable profiles shown by the overlapping curves of the repeated tests.

An inspection of the permanent displacement profiles in Figure 4.23 shows that the plates at 10g charge mass exhibit a deformed profile that was almost conical in shape with a small dome at the midpoint. This is consistent with observations by Pickering et al [125], who noted a similar cross sectional profile for rectangular plates exposed to buried charge detonations. At higher charge masses however, the plate profile becomes almost bi-linear. The central 200mm diameter of the plate was still conical in shape while the outer 50mm exhibited an additional plastic hinge with the change in slope moving from the outer clamp toward the centre with an increase in charge mass.

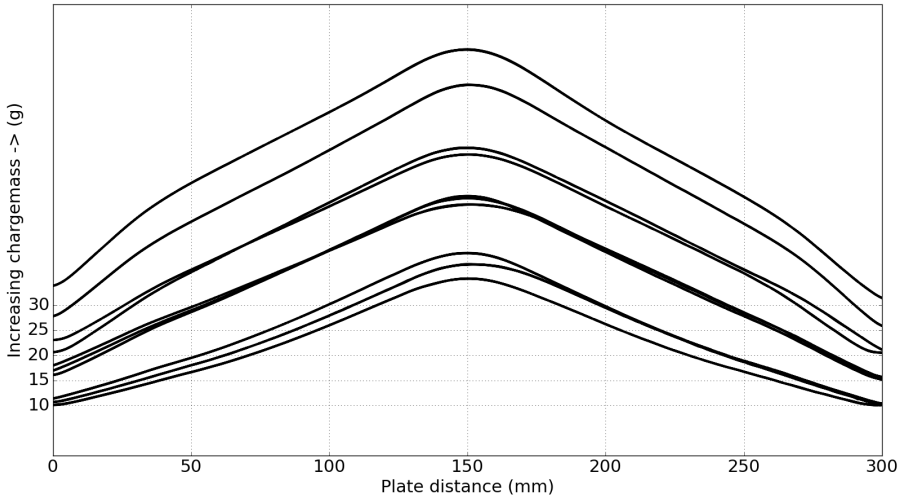

Figure 4.23: Permanent deformation profiles of the SBP series along the centre line of the blasted plates obtained by 3D scanning.

4.3.3 SBP Transient Response

Selected transient deformation profiles at discrete times are shown in Figures 4.24 - 4.27. At 66 $\boldsymbol{\mu s}$ (blue curve) there is motion blur in the 10g and 25g tests, while the 15g test shows a localised central deformation which is almost conical in shape. The deformation was localised to a 100-150mm diameter plastic hinge in the centre of the plate. At 165 $\boldsymbol{\mu s}$, the plastic hinge had moved out towards the clamp frame to a diameter approximately 200mm; the shape of the deformed section was conical

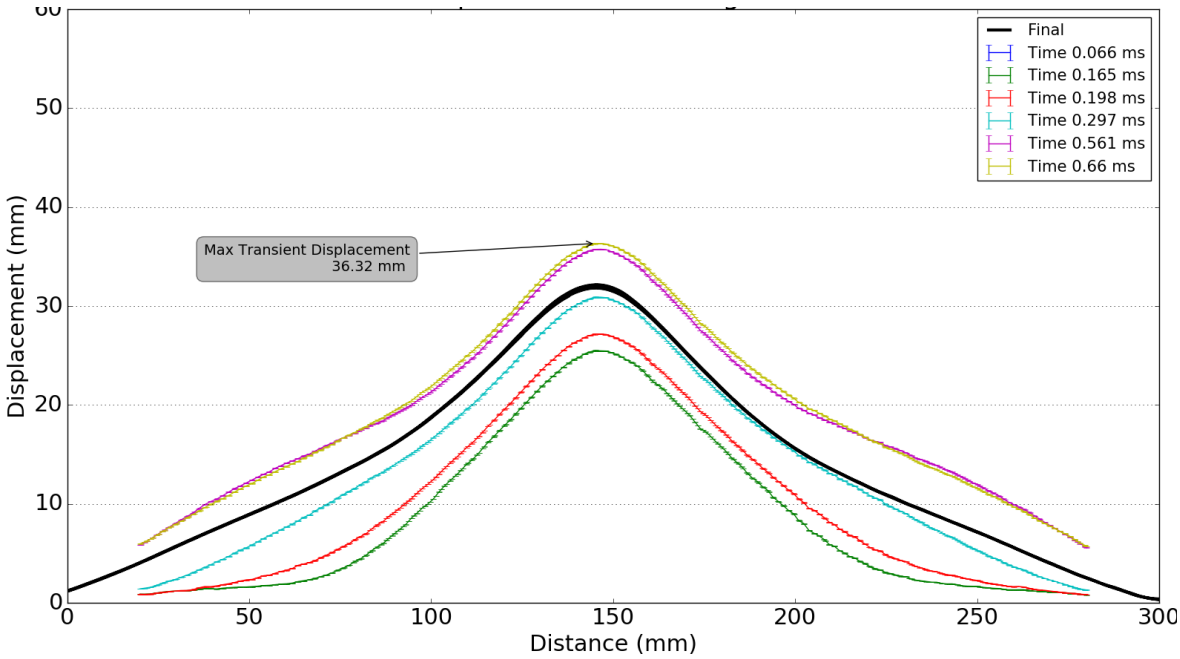

Figure 4.24: Transient plate deformation data from DIC for 10g SBP charge detonations

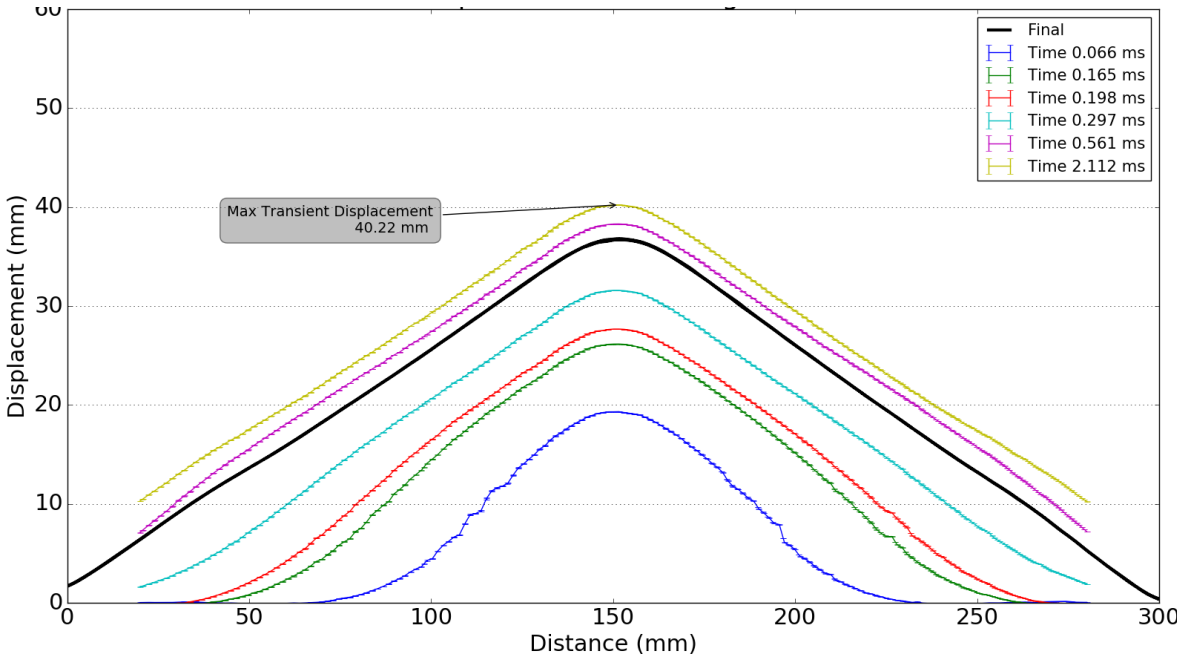

Figure 4.25: Transient plate deformation data from DIC for 15g SBP charge detonations

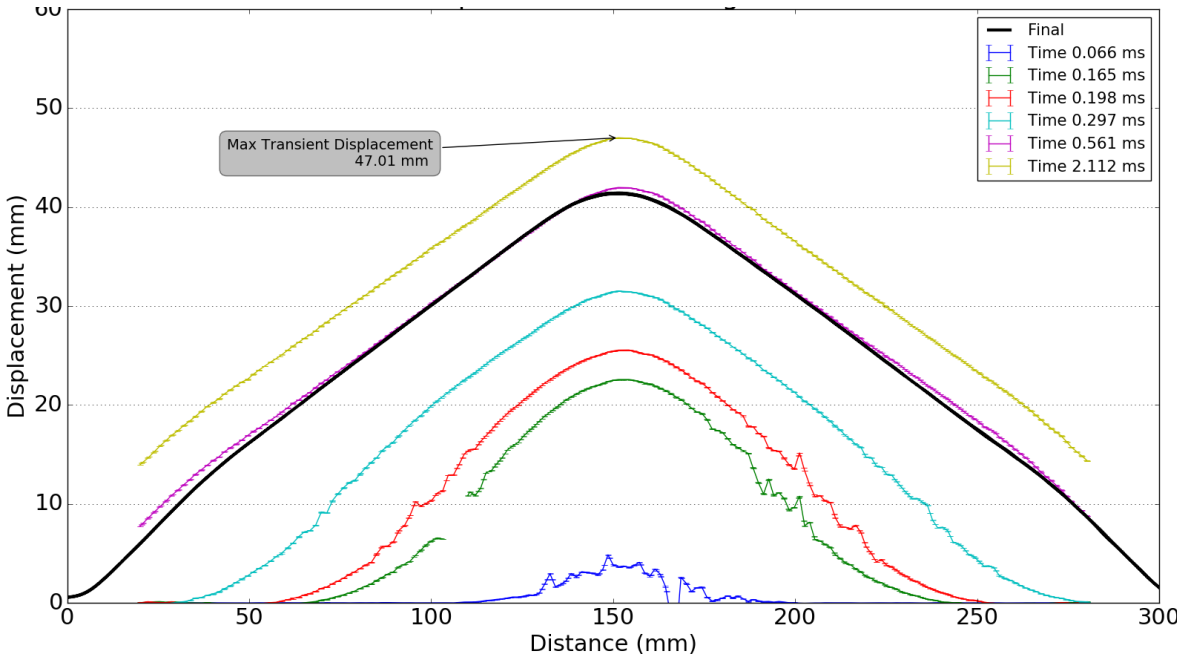

Figure 4.26: Transient plate deformation data from DIC for 20g SBP charge detonations

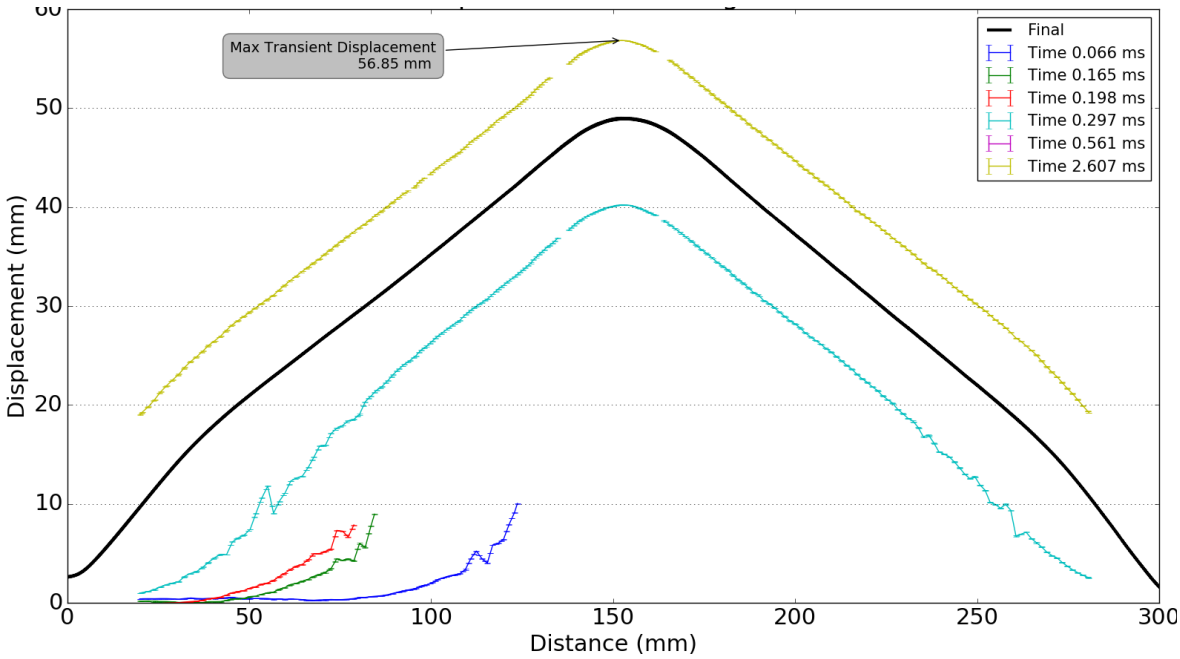

Figure 4.27: Transient plate deformation data from DIC for 25g SBP charge detonations

between the midpoint and the plastic hinge. By 297 μs , the plastic hinge has reached a diameter of approximately 250mm and the general profile was bell-shaped with a point of inflection forming at a diameter of approximately 100mm. This point of inflection is most pronounced by 561 μs. Once the plates reached their maximum transient deformation at about 660 - 700 μs, the point of inflection was less significant, and became virtually undetectable once the plate attained its final shape . During the evolution of the plate profile there was very localised initial deformation, with a radially outward moving plastic hinge that transitioned into a more global and final profile after 198 μs.

The transient midpoint deflection time histories, shown in Figure 4.28, show that there is a consistent time to reach peak transient deflection of approximately 0.7 ms. After 3 ms the midpoint oscillates at a higher but irregular frequency around the final deformation point illustrated by the dashed lines in each sub-Figure.

The transient midpoint displacement profile does not match the final deformed shape at any point prior to elastic recovery.

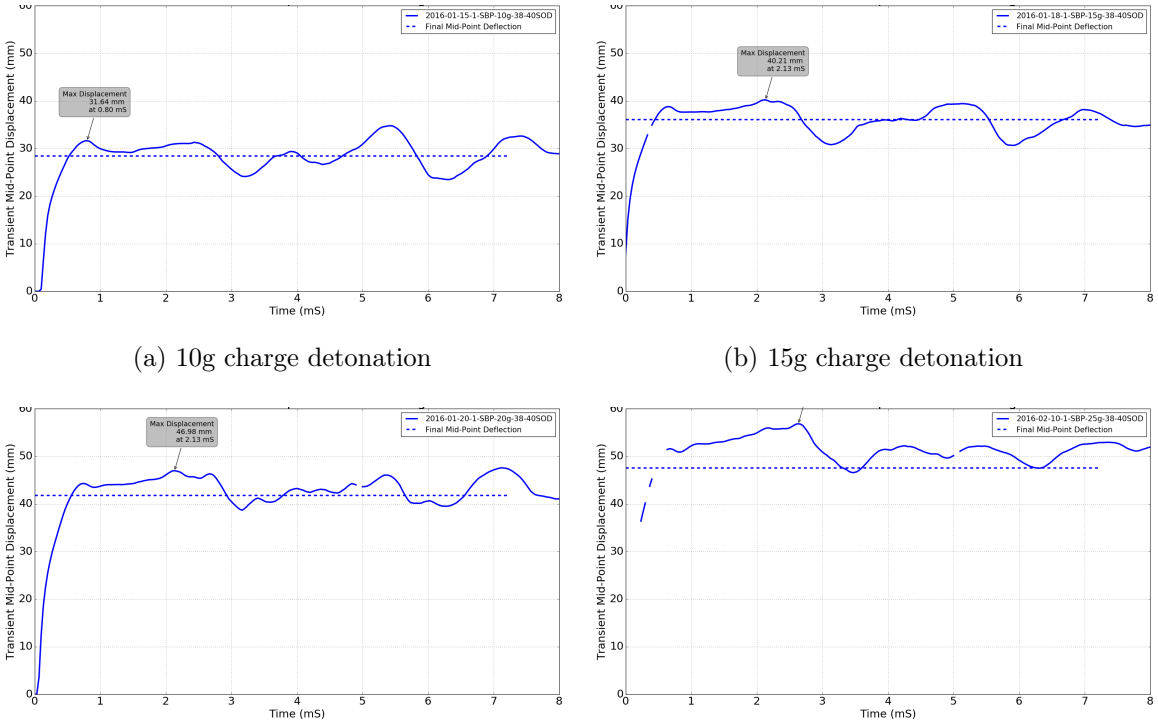

(a) 10g charge detonation

(b) 15g charge detonation

(c) 20g charge detonation

(d) 25g charge detonation

Figure 4.28: Mid-point transient deflection - time histories for the various SBP charge masses

4.3.4 Transient strain

The radial plastic strain along the centre line of the plates (at the point of maximum transient deflection) is shown in Figure 4.29. The radial strain is largest at the plate centre, but not as localised as it was for the AIR and VBP tests. The location where the strain tends to zero coincides with the point of inflection in the permanent deflection profile seen in Figure 4.23. Representative values of the maximum central strain value along the centre line of the plates are shown in Table 4.6. Full plots of the respective strains, at the same time points seen in displacement plots shown in Figures in Appendix A.3. The peak central strains observed in the SBP plates are lower than the AIR and VBP series, but the region of the plate is much larger.

Charge Mass (g)	**Maximum central strain value (mstrain)**
10	52
15	65
20	88
25	128

Table 4.6: The SBP maximum centre point strain along the centre line of the test plates.

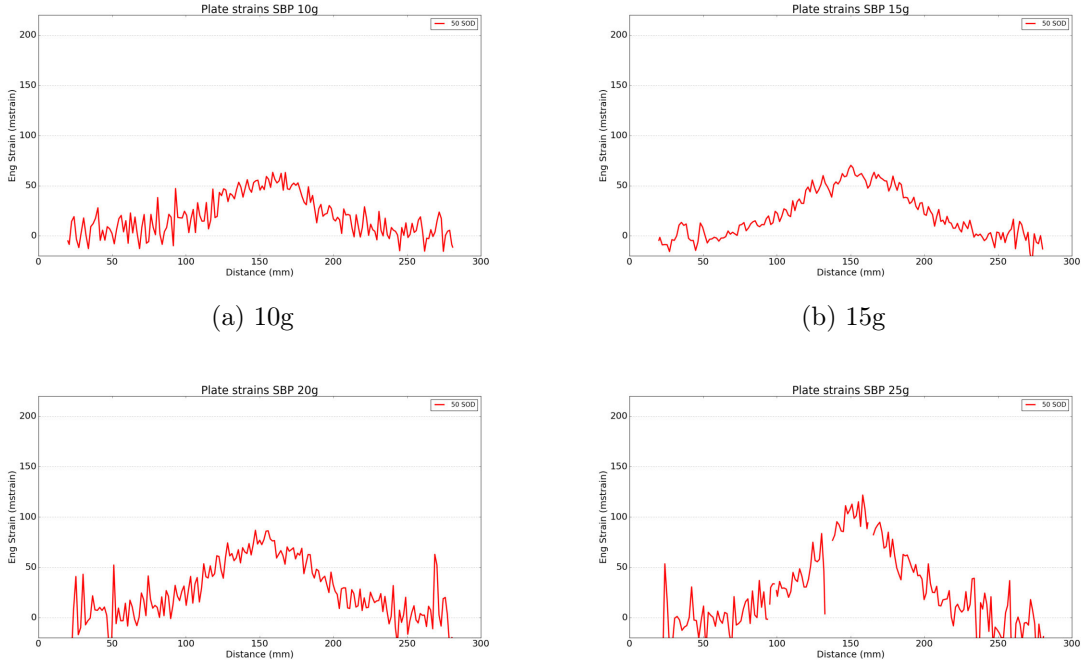

(a) 10g (b) 15g

(c) 20g (d) 25g

Figure 4.29: Typical radial plastic strain through the SBP plate centres at 0.7 ms (point of maximum transient deflection) for various charge mass detonations.

Chapter 5

Material Characterisation

The blast test plates were machined from 3mm thick Domex 355MC hot rolled low alloy steel, sourced from SSAB. The characterisation of Domex 355MC steel for use in the numerical modelling is presented in this chapter.

5.1 Material description

All the characterisation and blast test specimens were sourced from one batch of Domex 355MC sheet steel. The batch comprised seven plates which were 6m x 1.5m and nominally 3mm thick. The mean average specimen thickness was 3.00 $\pm$ 0.01 mm. The Domex 355MC grade is produced under rigorous quality control [120]. It has a fine grain structure produced through thermomechanical rolling and therefore exhibits good cold-forming properties [120]. The chemical composition of the steel is shown in Table 5.1.

Due to the size constraint of the sheet and desired plate size of 400x400mm, it was only possible to cut three plates in each row from the sheets, as shown in the cutting layout in Figure 5.1. The remaining material was used to cut material testing coupons with different orientations. The position of the test coupons was altered to ensure material would be tested from different areas of each sheet. Figure 5.1 shows two rows of the cutting pattern used by the laser cutter to cut the test plates and the material testing coupons from the full material sheet. The longitudinal axes of the dog bone specimens were oriented relative to the rolling direction at 0°, 45°and 90°, to test for any changes in material properties off the rolling direction. The results of these tests indicate the level of isotropy in the material and the degree to which rolling has affected the material

properties. Because the specimens were cut from different regions of the original plate they also indicate the consistency of the material properties through the width and length of the plate.

C (max %)	Si (max %)	Mn (max %)	P (max %)	S (max %)	Al (min %)	Nb (max %)	V (max %)	Ti (max %)
0.10	0.03	1.50	0.025	0.010	0.015	0.09	0.20	0.15

Table 5.1: Chemical composition of Domex 355MC steel.(obtained from ladle analysis [120])

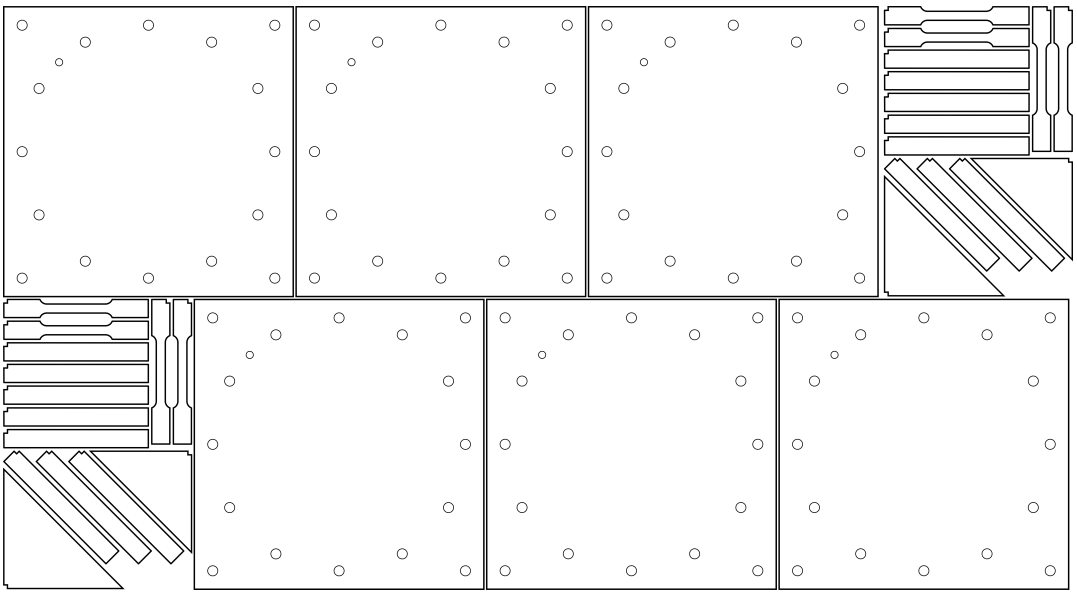

Figure 5.1: Two rows of the cutting pattern used to cut the test plates and material characterization coupons from the full plate.

5.2 Quasistatic tensile testing

Quasistatic tensile tests were performed on the Zwick 1484 quasistatic load frame. Ten specimens were tested at cross head speeds of 2 mm/min and 150 mm/min (corresponding to engineering strain rates of $\mathbf{4.17 \times 10^{-4} s^{-1}}$ and $\mathbf{3.12 \times 10^{-2} s^{-1}}$ respectively). An extensometer was used to determine the specimen elongation in the gauge length eliminating the need for machine compliance correction. The specimens were designed and tested according to ASTM E8 [126] and had overall dimensions of 200 mm by 25 mm wide, with a reduced section that was 80 mm long and 12.5 mm wide as shown in Figure 5.2.

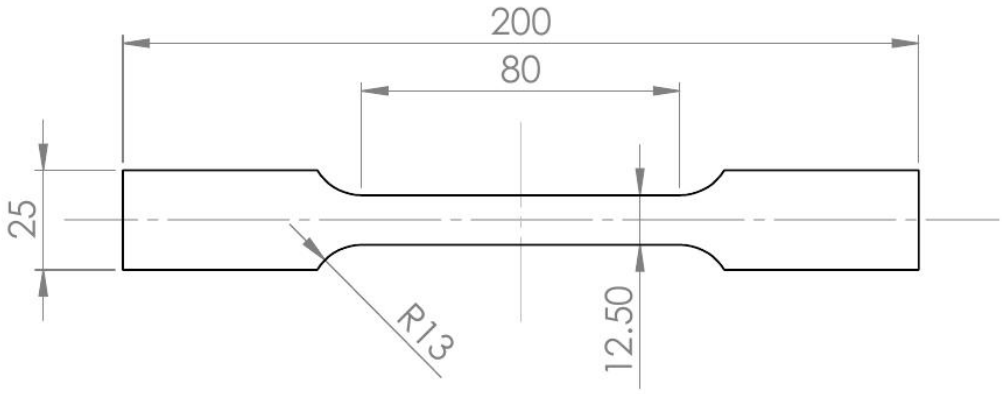

Figure 5.2: Drawing of the tensile specimens which were cut from the material sheet as indicated in Figure 5.1. (all dimensions in mm)

True stress versus true strain curves for specimens tested at a nominal engineering strain rate of $\mathbf{4.17 \times 10^{-4} s^{-1}}$ are shown in Figure 5.3. As expected, the material properties were very consistent within a set and also across the three orientations. The mean average yield strength of the Domex 355 MC was $\mathbf{444 MPa}$, ultimate tensile strength was $\mathbf{627 MPa}$ and the percentage elongation at failure was **20%**. No significant change in material strength could be noted with the change in specimen direction. The failure strain appeared to increase slightly as the angle of rotation was increased towards 90°. This change in failure strain should not have any effect on the validity of the material model developed as the experiments were designed to remain in the plastic failure regime, since fracture and tearing of a test plate could result in

damage to the camera system.

The slight increase noted in the ultimate tensile strength at the higher strain rate of 150mm/min ($\mathbf{3.12 \times 10^{-2} s^{-1}}$) shown in Figure 5.4, indicates some strain rate sensitivity in the material response. There was also a slight decrease in the strain at failure for the faster test suggesting a decrease in ductility with an increase in strain rate.

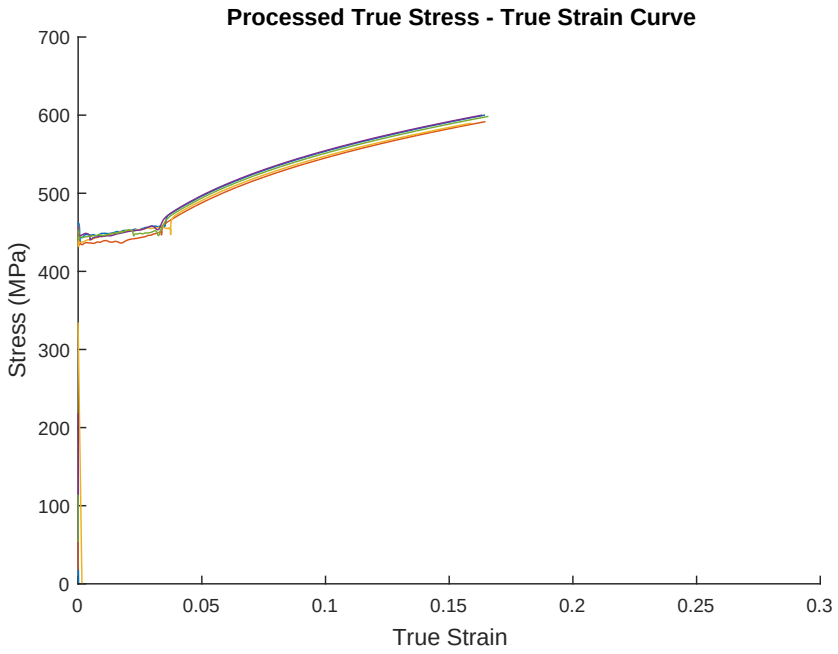

Figure 5.3: Quasistatic test data showing processed True Stress Vs True Strain for the material at 2mm /min cross head speed.

To account for any differences between the standard quasistatic tensile testing and the high strain rate SHPB testing specimens, quasistatic tests were additionally performed on the same 'Fir Tree' specimens that were used in the SHPB testing. The Zwick 1484 load frame was also used and due to space constraints the extensometer was clipped to the bottom edge of the clamps shown in Figure 5.5. This is an important difference to note as the position of the extensometer correlates with the position of tracked displacement points in the model results in Section 5.4.2. The cross head speeds chosen for this were $\mathbf{0.6mm/min}$ and $\mathbf{100mm/min}$.

The difference in the results produced by the smaller specimen geometry are most noticeable after the initial yield point where the effect of the Luders bands become visible. Due to the smaller specimen size, this section is significantly smaller as can be

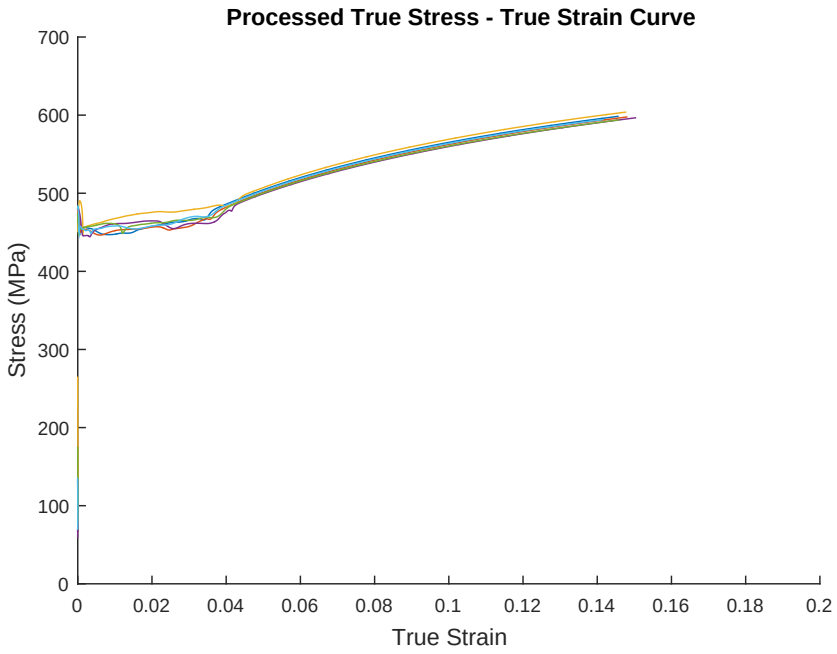

Figure 5.4: Quasistatic test data showing processed True Stress Vs True Strain for the material at 150mm /min cross head speed.

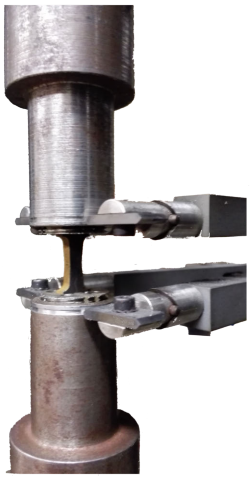

Figure 5.5: Photograph of the extensometer attached to a small 'Fir Tree' specimen on the Zwick quasistatic load frame.

seen in Figure 5.6. Force is plotted against displacement in Figure 5.6 as opposed to a traditional stress against strain, as these curves are used later in the inverse modelling

to determine the material properties of the material.

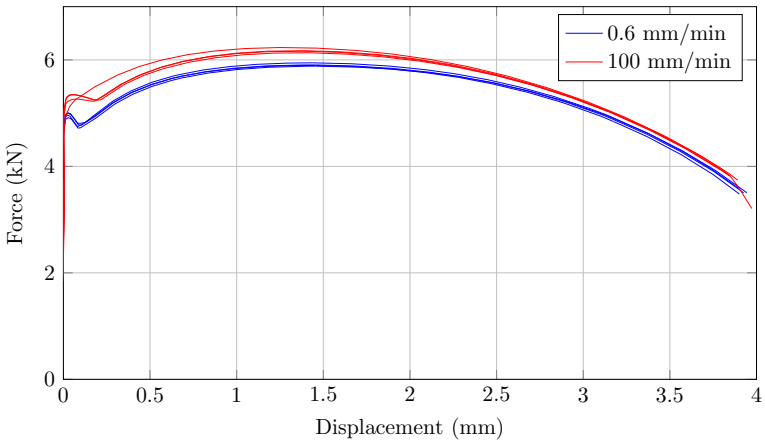

Figure 5.6: Force Displacement curve for the 'Fir Tree' specimens pulled on the quasistatic load frame at at cross head speeds of 0.6mm/min (blue) and 100 mm/min (red).

5.3 High Strain-rate Material Testing

In order to better characterise the strain rate effects in the material, Split Hopkinson Pressure Bar (SHPB) tests were performed on the material. An exhaustive explanation of SHPB testing will not be provided here as an in depth discussion of this technique is available in [127].

5.3.1 Split Hopkinson Pressure Bar Test Setup

The Split Hopkinson Pressure Bar (SHPB) as we know it today is an improvement by Davies [128] and Kolsky [129] on the original design developed by Hopkinson [130]. These improvements [128, 129], allow the measurement of momentum at the two ends of a specimen placed between two bars. The forces and displacements at the specimen interface can be inferred from this data.

The testing technique has become well used for tensile testing of a variety of materials using many different specimen mounting techniques [131–133]. The most successful methods have been reported to be direct bonding and use of threaded connections [134–137].

In this work the initial tensile wave was generated using a backwards firing striker shown in Figures 5.7 and 5.8 designed by Downey [138] and Bowden [139]. The pressure of the gas gun controlled the velocity of the striker, which determined the magnitude of the tensile pulse generated.

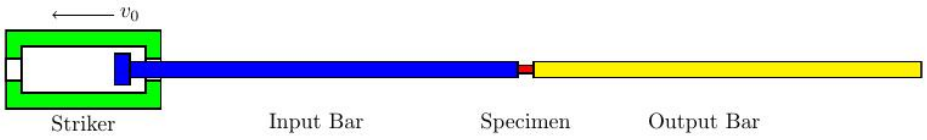

Figure 5.7: A schematic of the tensile setup used with the SHPB apparatus [127].

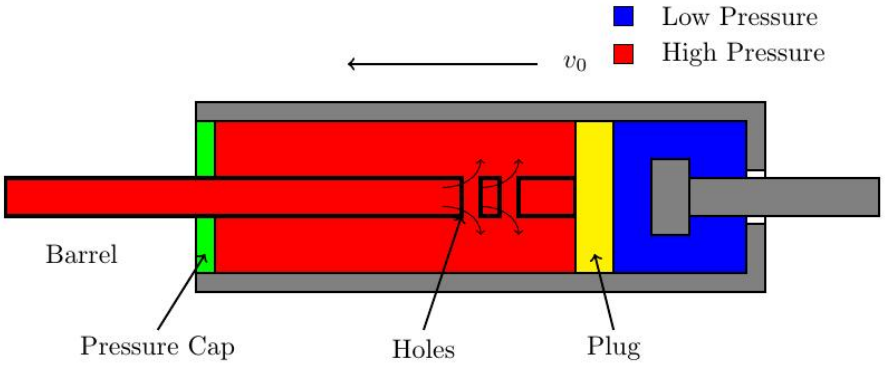

Figure 5.8: A schematic of the tensile adapter mechanism used with the SHPB apparatus [127].

The system was carefully calibrated, and checked by comparing the force equilibrium at the two bar ends, shown in Figure 5.9. This confirmed that the system produced reliable results when the two bar ends were placed in contact with one another (as the bar ends should experience the same force and deflection).

SHPB specimen design

Specimens tested at dynamic strain rates in a tensile SHPB system must be smaller than traditional tensile specimens and no standard exists for the design of the specimens. In addition the SHPB technique is not yet part of any testing standard. The design developed by Cloete and co-workers [140, 141] and Weyer [127] was implemented to secure the tensile specimens for testing. The key advantages of this system are:

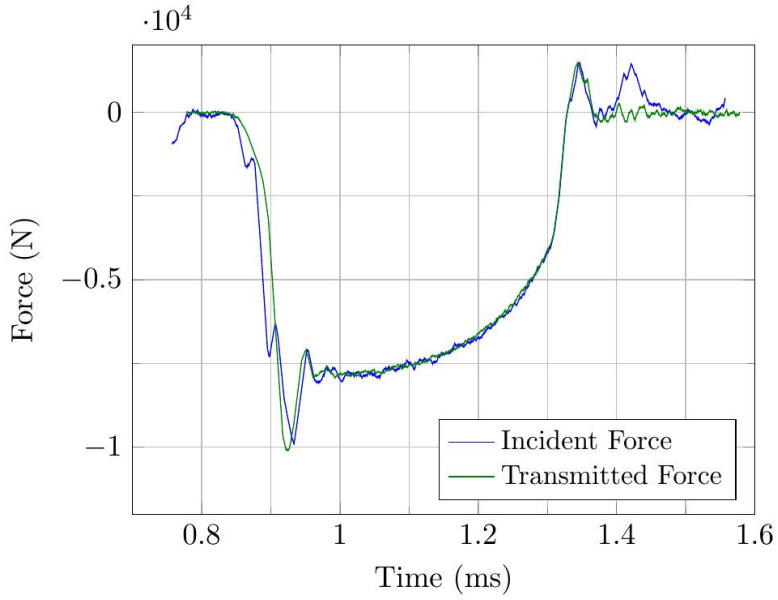

Figure 5.9: The force equilibrium at the specimen interfaces confirming the system was correctly calibrated [127].

- No gluing required.
- Minimum additional mass.
- No play between specimen and clamp.
- Smooth load transfer from bar to specimen.
- Maximum clamping force on specimen.
- Self-centring.

The specimen design and clamps used to hold the specimens are shown in Figure 5.10. The specimens were wire cut from the same sections of material used for the quasistatic specimens shown in Figure 5.1.

The high strain rate material tests were performed at nominal strain rate of $\mathbf{600}\boldsymbol{s^{-1}}$ and the results are shown in Figure 5.11 together with the quasistatic results..

When the stress in the specimens tested at higher strain rates are compared to those tested at the lower strain rate, the strain rate effect can clearly be seen in Figure 5.11. The increase in initial yield from the quasistatic tests (blue) at around 440MPa increases to approximately 700-800 MPa at the higher strain rate of $\mathbf{500 - 1000}\boldsymbol{s^{-1}}$.

(a) SHPB clamp

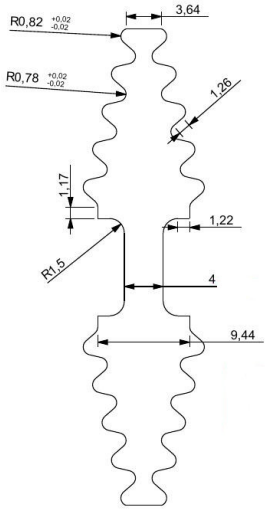

(b) SHPB specimen drawing

(c) SHPB Specimen

Figure 5.10: The 'Fir Tree' SHPB specimens and clamp fixtures.

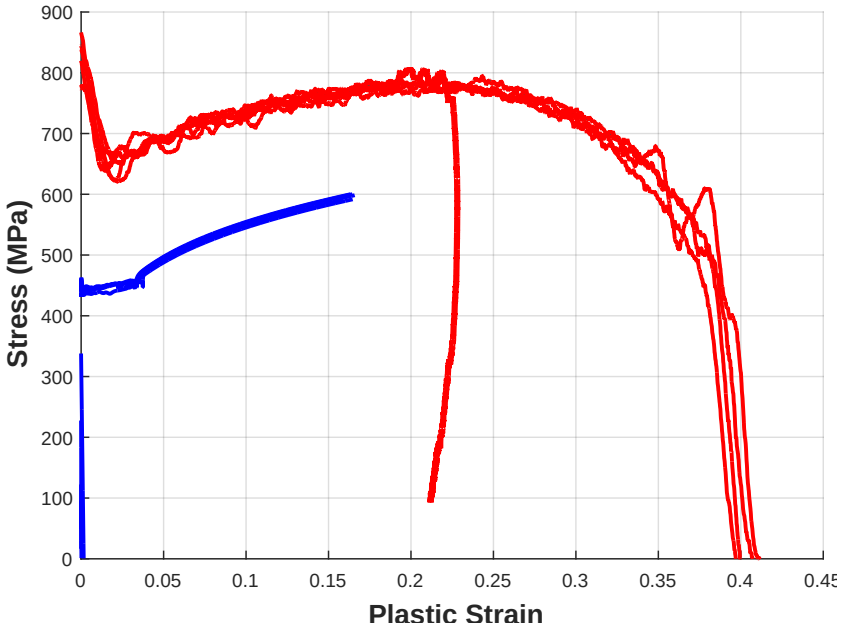

Figure 5.11: Comparison of the True Stress Vs True Strain Quasistatic (blue) and high strain rate SHPB(red) tensile tests.

5.4 Numerical Model Calibration

This section describes the incorporation of the tensile test results into the Johnson-Cook plasticity material model in LS-Dyna. This implementation includes adiabatic heating effects in the formulation. What follows here is a brief description of the setup and optimisation scheme implemented to calibrate the material model for use in the simulations of the different experimental setups.

5.4.1 Johnson and Cook

The Johnson - Cook model is a relatively simple phenomenological model developed for use in numerical computations [142]. The model was based on torsional and tensile test data performed over a range of strain rates and temperatures for three different materials. The description of the flow stress is given in Equation 5.1.

$$\boldsymbol{\sigma} = [\boldsymbol{A} + \boldsymbol{B}\epsilon^{n}][1 + \boldsymbol{C}ln\dot{\epsilon}^{*}][1 - (\boldsymbol{T}^{*})^{m}] \tag{5.1}$$

Where $\boldsymbol{A}$, $\boldsymbol{B}$, $\boldsymbol{n}$ and $\boldsymbol{C}$ are material parameters, $\boldsymbol{\epsilon}$ represents the equivalent plastic strain, $\boldsymbol{\dot{\epsilon}^*}$ represents the dimensionless plastic strain rate, and $\boldsymbol{T^*}$ represents the homologous temperature. The dimensionless strain rate and homologous temperature are described in Equations 5.2 and 5.3 respectively.

$$\boldsymbol{\dot{\epsilon}^* = \frac{\dot{\epsilon}}{\dot{\epsilon}_0}} \tag{5.2}$$

$$\boldsymbol{T^* = \frac{T - T_{ref}}{T_m - T_{ref}}} \tag{5.3}$$

Where $\boldsymbol{\epsilon_0}$ is a reference strain rate, which was taken as $\boldsymbol{1.0 s^{-1}}$ for the data used by Johnson and Cook [142], and $\boldsymbol{T_{ref}}$ and $\boldsymbol{T_m}$ are the reference and melting temperatures respectively.

The homologous temperature is set to zero for temperatures less than the reference temperature such that the temperature function has no effect on the flow stress, and one for temperatures above the melting temperature such that the flow stress is zero and the material exhibits no resistance to flow.

Figure 5.12 illustrates the effect of strain rate on the flow stress for the different materials studied by Johnson and Cook [142].

The strain rate effect in Figure 5.12 appears linear on the logarithmic scale, hence the choice of a logarithmic function for the strain rate dependence function. A popular alteration of the Johnson - Cook model, uses the Cowper - Symonds strain rate equation [143] in place of the standard strain rate dependence function. The Cowper - Symonds equation is shown in Equation 5.4.

$$\boldsymbol{\frac{\sigma}{\sigma_0} = 1 + \left(\frac{\dot{\epsilon}^*}{C}\right)^{\frac{1}{q}}} \tag{5.4}$$

Equation 5.4 is valid over a greater range of strain rates than the equation used in the original Johnson - Cook model, which is not valid for very low strain rates.

Johnson and Cook [142] also developed a damage model of a similar form to the widely used plasticity model. The damage model incorporated the effect of triaxiality on the effective strain at failure using a form similar to that of the Rice and Tracey model [144], however it also includes the effects of strain rate and temperature. The damage function is given as separable functions of triaxiality, strain rate, and temperature as shown in Equation 5.5 [142].

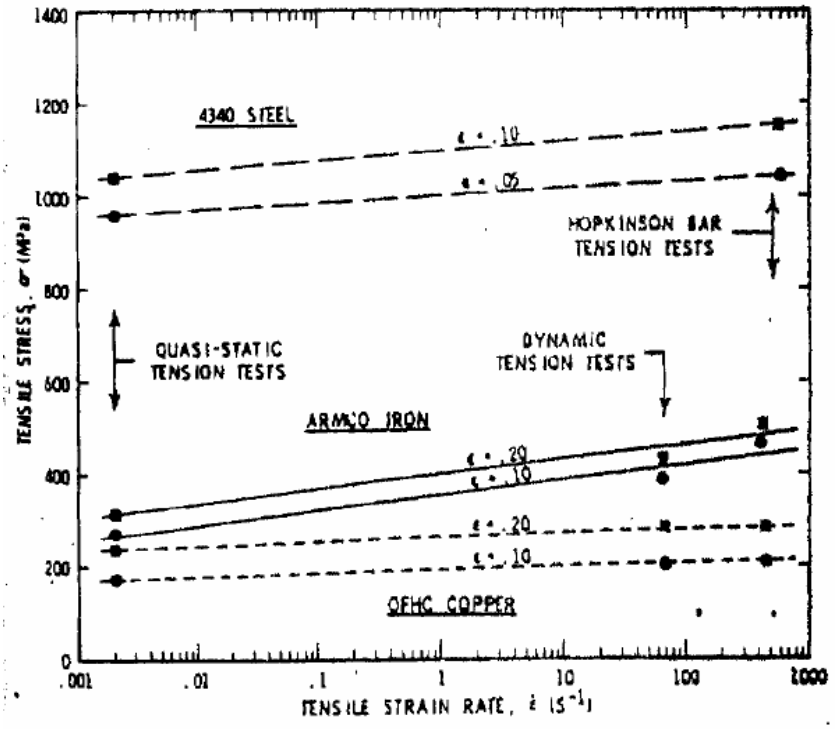

Figure 5.12: The effect of strain rate on the flow stress at different levels of plastic strain [142].

$$\bar{\epsilon}_f = \left[D_1 + D_2 e^{D_4 \eta}\right] \left[1 + D_4 ln(\dot{\epsilon}^*)\right] \left[1 + D_5 T^*\right] \tag{5.5}$$

The damage constants for the triaxiality function were originally calibrated using various tensile and torsional tests at quasistatic strain rates, where the triaxialities were approximated using numerical simulations. Using Hopkinson Bar experiments, the constants for the strain-rate and temperature functions could be determined by preheating specimens to a desired temperature before the tests. Since the duration of the test is short enough for the test to be considered adiabatic, the temperature in the specimen could be calculated as a function of the plastic work accumulated during the test. It is worth noting that the model was not calibrated using experiments in the negative triaxiality range, and the data from the torsional tests performed for 4340 steel did not correspond with the model. This was initially disregarded as an anomaly in the testing procedure, but later work by Bao and Wierzbicki [145] suggested that a the fracture locus could not be calibrated by simply extrapolating the tensile data.

`*MAT_MODIFIED_JOHNSON_COOK`

The Johnson-Cook model was implemented in LS Dyna using the `*MAT_MODIFIED_JOHNSON_COOK` keycard. This allowed for the inclusion of a full damage model and adiabatic temperature effects. The constitutive relation describing the yield criterion is shown in Equation 5.6.

$$\boldsymbol{\sigma_Y} = \left\{ \boldsymbol{A} + \boldsymbol{B}\boldsymbol{r}^{\boldsymbol{n}} + \sum_{\boldsymbol{i}=\boldsymbol{1}}^{\boldsymbol{2}} \boldsymbol{Q_i}[\boldsymbol{1} - \boldsymbol{\exp}^{-\boldsymbol{C_i r}}] \right\} (\boldsymbol{1} + \dot{\boldsymbol{r}}^{*})^{\boldsymbol{C}} (\boldsymbol{1} - \boldsymbol{T}^{*\boldsymbol{m}}) \tag{5.6}$$

Where $\boldsymbol{A}$, $\boldsymbol{B}$, $\boldsymbol{C}$, $\boldsymbol{m}$, $\boldsymbol{n}$, $\boldsymbol{Q_1}$, $\boldsymbol{C_1}$, $\boldsymbol{Q_2}$, $\boldsymbol{C_2}$ are material parameters and the normalised damage equivalent plastic strain rate $\dot{\boldsymbol{r}}^{*}$ is defined by

$$\dot{\boldsymbol{r}}^{*} = \frac{\dot{\boldsymbol{r}}}{\dot{\boldsymbol{\varepsilon}}_{\boldsymbol{0}}} \tag{5.7}$$

In which $\dot{\boldsymbol{\varepsilon}}_{\boldsymbol{0}}$ is a user-defined reference strain rate and the homologous temperature reads

$$\boldsymbol{T}^{*} = \frac{\boldsymbol{T} - \boldsymbol{T_r}}{\boldsymbol{T_m} - \boldsymbol{T_r}} \tag{5.8}$$

In which $\boldsymbol{T_r}$ is the room temperature and $\boldsymbol{T_m}$ is the melting temperature.
The Damage evolution is defined by

$$\dot{\boldsymbol{D}} = \begin{cases} \boldsymbol{0} & \boldsymbol{p} \leq \boldsymbol{p_d} \\ \frac{\boldsymbol{D_c}}{\boldsymbol{p_f} - \boldsymbol{p_d}} & \boldsymbol{p} > \boldsymbol{p_d} \end{cases} \tag{5.9}$$

Where the current equivalent fracture strain $\boldsymbol{p_f} = \boldsymbol{p_f}(\boldsymbol{\sigma}^{*}, \boldsymbol{p}^{*}, \dot{\boldsymbol{T}}^{*})$ is defined as

$$\boldsymbol{p_f} = [\boldsymbol{D_1} + \boldsymbol{D_2 exp}(\boldsymbol{D_3}\boldsymbol{\sigma}^{*})] \, (\boldsymbol{1} + \dot{\boldsymbol{p}}^{*})^{\boldsymbol{D_4}} (\boldsymbol{1} + \boldsymbol{D_5}\boldsymbol{T}^{*}) \tag{5.10}$$

and $\boldsymbol{D_1}$, $\boldsymbol{D_2}$, $\boldsymbol{D_3}$, $\boldsymbol{D_4}$, $\boldsymbol{D_5}$, $\boldsymbol{D_c}$ and $\boldsymbol{p_d}$ are material parameters; the normalised equivalent plastic strain rate $\dot{\boldsymbol{p}}^{*}$ is defined by

$$\dot{\boldsymbol{p}}^{*} = \frac{\dot{\boldsymbol{p}}}{\dot{\boldsymbol{\varepsilon}}_{\boldsymbol{0}}} \tag{5.11}$$

and the stress triaxiality $\boldsymbol{\sigma}^{*}$ reads

$$\boldsymbol{\sigma}^{*} = \frac{\boldsymbol{\sigma_H}}{\boldsymbol{\sigma_e q}}, \boldsymbol{\sigma_H} = \frac{\boldsymbol{1}}{\boldsymbol{3}} \boldsymbol{tr}(\boldsymbol{\sigma}) \tag{5.12}$$

Material Parameters	Density	Youngs modulus	Poissons Ratio	Taylor Quinney	Specific heat	Reference strain rate	
	$\boldsymbol{\rho}$	E	v	$\boldsymbol{\chi}$	$\boldsymbol{C_p}$	$\boldsymbol{\dot{\varepsilon}_0}$	
Numerical Model Parameters							
Johnson Cook Variable	A	B	n	C	m		
Voce Hardening parameters	$\boldsymbol{Q_1}$	$\boldsymbol{C_1}$	$\boldsymbol{Q_2}$	$\boldsymbol{C_2}$			
Damage Parameters	$\boldsymbol{D_c}$	$\boldsymbol{P_d}$	$\boldsymbol{D_1}$	$\boldsymbol{D_2}$	$\boldsymbol{D_3}$	$\boldsymbol{D_4}$	$\boldsymbol{D_5}$

Table 5.2: The material model options in *MAT_MODIFIED_JOHNSON_COOK in LS-Dyna.

The adiabatic heating is calculated as

$$\dot{\boldsymbol{T}} = \boldsymbol{\chi}\frac{\boldsymbol{\sigma}:\ \boldsymbol{d^p}}{\boldsymbol{\rho C_p}} = \boldsymbol{\chi}\frac{\tilde{\boldsymbol{\sigma}}_{\boldsymbol{eq}}\dot{\boldsymbol{r}}}{\boldsymbol{\rho C_p}} \tag{5.13}$$

Where $\boldsymbol{\chi}$ is the Taylor-Quinney parameter, $\boldsymbol{\rho}$ is the density and $\boldsymbol{C_p}$ is the specific heat.

The parameters used in this material model are summarised in Table 5.2.

For this work the Voce hardening parameters $\boldsymbol{Q_1}$, $\boldsymbol{C_1}$, $\boldsymbol{Q_2}$ and $\boldsymbol{C_2}$ were set = 0 and the influence of the damage parameters was eliminated by setting $\boldsymbol{p_d}$ to a big number which according to Equation 5.9 negates the damage parameter. This was done to allow this model to take its simplest form which could easily be applied to other applications where this material would be used.

5.4.2 Numerical model of tensile tests

A simple numerical model of the tensile test was developed to calibrate the material model. This model was used in the Ls-Opt optimisation scheme to refine the material parameters to the actual experimental material response. The full rigour of this model

is not the main focus of this work and so a simple outline is provided here for clarity. The full input deck for the simulation is provided for completeness in Appendix D.

A quarter symmetry 3D model was developed, including the two Hopkinson bars, clamp and specimen shown in Figure 5.13. The nodes at the interface of the clamp and the SHPB were tied together to represent the threaded connection, since it was highly unlikely that the titanium clamp would move in the threaded connection. The contact between the clamp and specimen was modelled as penalty contact between two solids to account for any movement of the specimen in the clamp.

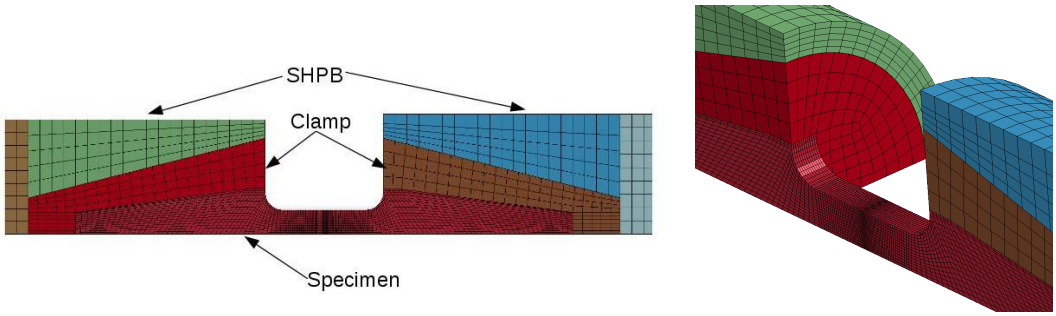

Figure 5.13: Schematic showing the numerical model developed to calibrate the response of the material model using the tensile test results.

To determine the material properties of Domex 355MC, the optimisation scheme in Ls-Opt was first applied to the quasistatic tests, where quasistatic displacement boundary conditions were imposed on the bars holding the specimens. During this portion of the optimisation scheme, the goal was to characterise the material properties that are not affected by strain rate (the $\boldsymbol{A}$, $\boldsymbol{B}$ and $\boldsymbol{n}$ value). This same model was later used to simulate the SHPB tests, performed at strain rates of $\mathbf{600}\boldsymbol{s}^{-\mathbf{1}}$, to determine and validate the strain rate effects on the material model (the $\boldsymbol{C}$ value).

During both models, the displacement of nodes at the end of the bars was monitored. This was done to allow comparison with the extensometer readings which were captured at the bar end shown in Figure 5.5. This was also the case for the SHPB tests described in Section 5.3.1, where the displacement of the bar ends during SHPB tests were also determined.

This model was specifically parametrised so that the input variables used in the material model `*MAT_MODIFIED_JOHNSON_COOK` became parameters that could be changed through a script.

5.4.3 Material model optimisation

In the case of numerical material models, it is not always easy to assign physical meaning to the different material properties required as inputs to the model. The Johnson Cook model implemented here, has only four key parameters which needed to be determined. Ls-Opt is a design optimisation and probabilistic analysis tool which interfaces to LS Dyna. The software implements the Response Surface Method (RSM) which was initially introduced by Box and Wilson in 1951 [146]. The idea behind the method is to minimise the difference between a described model and experimental data. To achieve this, a matrix of experimental test points is proposed using the design of experiments approach, which would bound the optimal response. By iterating this approach the bounds on the test matrix can be reduced and the solution proposed with statistical certainty. A very good overview of the method applied to determination of material properties in helmet crash simulations is provided by Müllerschön [147].

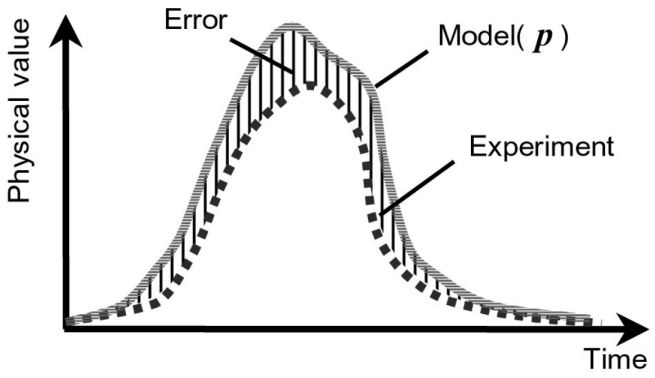

Figure 5.14: The target value optimised by determining the difference between the two curves using RSM.

The approach implemented in this optimisation is simplified in the flow chart shown in Figure 5.15. The process starts by setting the parameters which are constants and variables for the optimisation scheme. The first optimisation that was carried out was on $\boldsymbol{A}$, $\boldsymbol{B}$ and $\boldsymbol{n}$. The experimental input data for the optimisation was taken from the quasistatic experiments performed on the 'Fir Tree' specimens at $\boldsymbol{0.6mm/min}$ cross head speed. The experimental data was used in the form of force and displacement as these were simple to correlate to the measured output in the simulation. An example of one of the initial optimisation steps showing the calculated effect of varying the

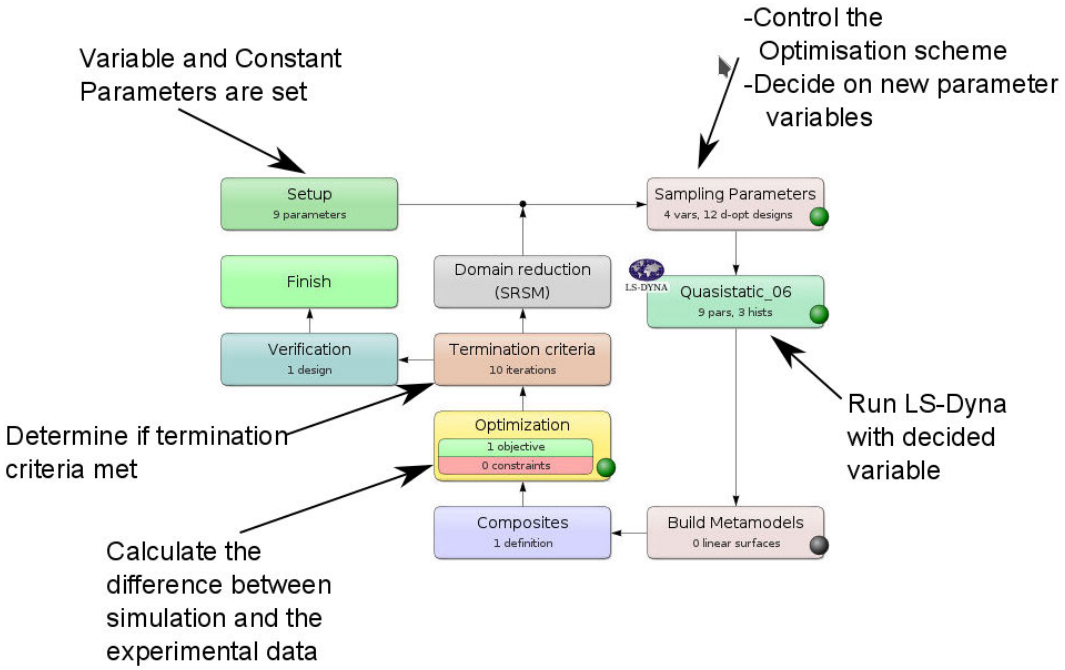

Figure 5.15: Flow diagram showing the methodology applied to optimise the parameters of the models.

$\boldsymbol{A}$ parameter in *MAT_107 can be seen in Figure 5.16. As the optimisation scheme progressed, the band of variation is narrowed to more correctly bound the experimental data seen in Figure 5.17.

The material model parameters that resulted from the optimisation are reported in Table 5.3 together with the bounds placed on them.

Figure 5.18 shows the result of the optimisation and the very good correlation that was achieved at quasistatic and dynamic speeds for this material. It should be noted

Parameter	Lower bound	upper bound	Optimised Value
$\boldsymbol{A}$	250 MPa	450 MPa	352 MPa
$\boldsymbol{B}$	300 MPa	1200 Mpa	642 MPa
$\boldsymbol{n}$	0.3	0.9	0.55977

Table 5.3: The optimised results from the first optimisation scheme and the bounds used to find them.

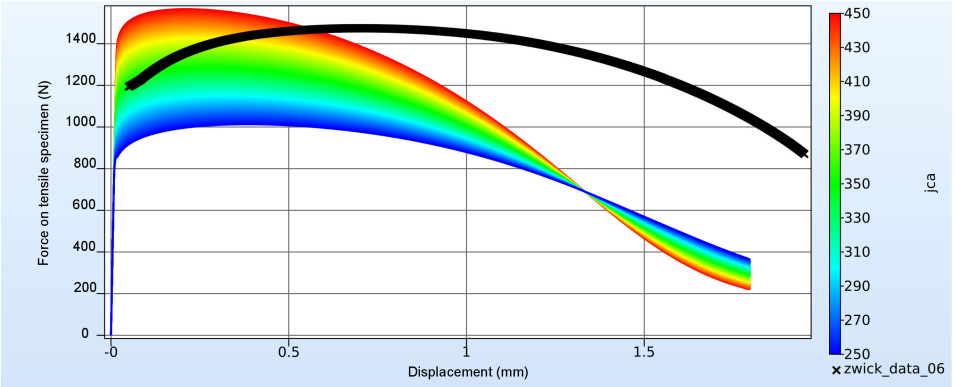

Figure 5.16: Force vs displacement graph showing the effect of varying the $\boldsymbol{A}$ parameter during optimisation between $\mathbf{250}\boldsymbol{MPa}$ and $\mathbf{450}\boldsymbol{MPa}$ while keeping all other variables constant. Experimental data is shown in black

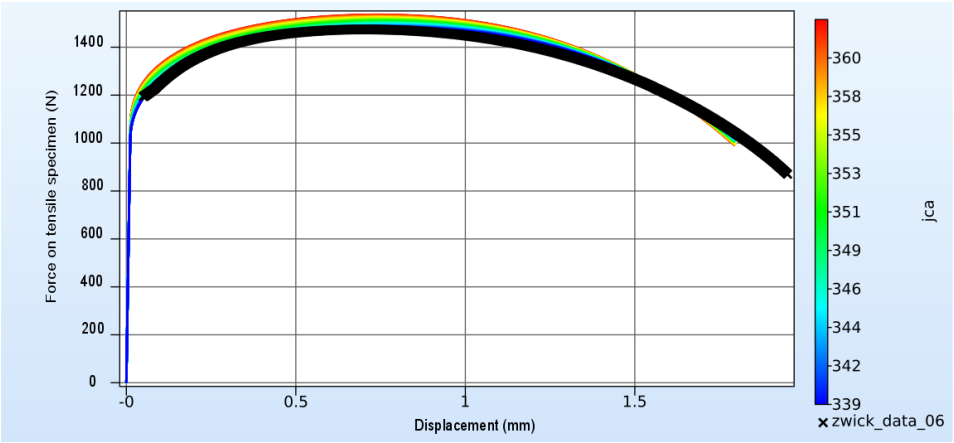

Figure 5.17: The effect of varying the $\boldsymbol{A}$ parameter in the Johnson Cook model during the final stages of optimisation between $\mathbf{339}\boldsymbol{MPa}$ and $\mathbf{360}\boldsymbol{MPa}$ while keeping all other variables constant. Experimental data in black

that this data varies from values published in the literature [148], but in that work the material was not experimentally characterised at high strain rates and data was assumed from the literature.

The second optimisation was performed by fixing the values of $\boldsymbol{A}$, $\boldsymbol{B}$ and $\boldsymbol{n}$, only

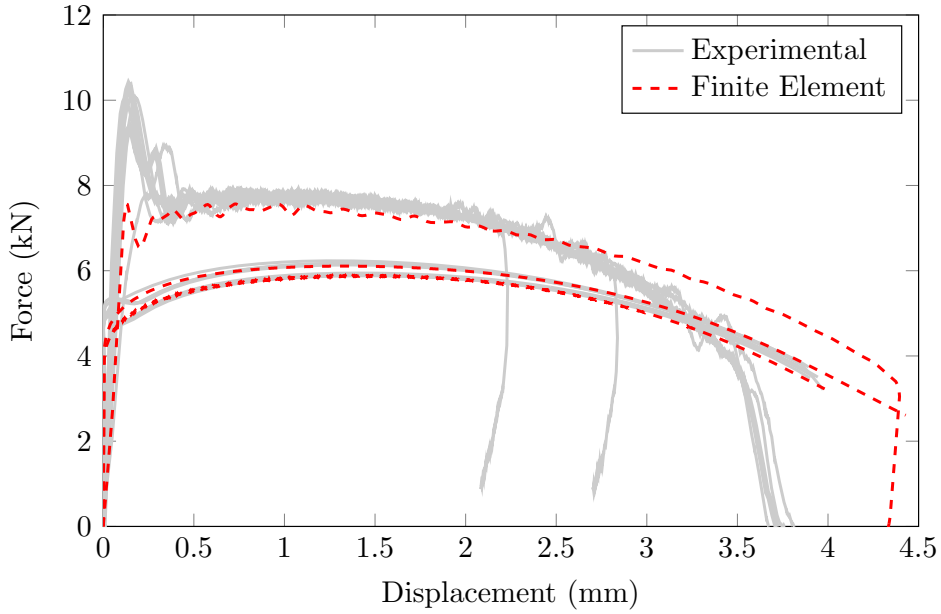

Figure 5.18: The optimised quasistatic and dynamic results for the material parameters showing the experimental data in grey and the FEM results in red.

allowing $\boldsymbol{C}$ to be varied. This optimisation scheme resulted in a value of $\boldsymbol{C} = 0.03278$ for the model. The correlation of the simulated tensile SHPB test together with the

The finalised values for the material model are shown in Table 5.4.

Material Parameters	Density	Youngs modulus	Poissons Ratio	Taylor Quinnery	Specific heat	Reference strain rate	
	$\boldsymbol{\rho}$	E	v	$\boldsymbol{\chi}$	$\boldsymbol{C_p}$	$\boldsymbol{E_0}$	
	7830 $\boldsymbol{kg/m^3}$	206 GPa	0.29	0.9	452 KJ	0.0014	
Numerical Model Parameters							
Johnson Cook Variable	A	B	n	C	m		
	352 MPa	642 MPa	0.5597	0.032	0.81		
Voce Hardening parameters	$\boldsymbol{Q_1}$	$\boldsymbol{C_1}$	$\boldsymbol{Q_2}$	$\boldsymbol{C_2}$			
	0	0	0	0			
Damage Parameters	$\boldsymbol{D_c}$	$\boldsymbol{P_d}$	$\boldsymbol{D_1}$	$\boldsymbol{D_2}$	$\boldsymbol{D_3}$	$\boldsymbol{D_4}$	$\boldsymbol{D_5}$
	0	0	0	0	0	0	0

Table 5.4: The final material model options used in LS Dyna.

Chapter 6

Numerical Modelling

This chapter describes the development of the numerical models to approximate the experimental configurations discussed in Chapter 3. To gain a better understanding of the effect of loading conditions on the test plates, numerical simulation were performed and correlated with the experimental results. As the simulation is not the main focus of this analysis, it was used to augment the understanding of the experimental work.

A simple explanation of the numerical method is followed by the description of the different model components and summary results of the simulations.

6.1 Introduction

The simulations were performed using the LS Dyna explicit solver (LSDYNA V971 R8.10) developed by Livermore Software Technology Corp (LSTC). LS Dyna is a multipurpose explicit and implicit finite element program used to analyze the nonlinear response of structures. It is capable of solving the highly non-linear transient events such as blast loading, making use of Multi Material Arbitrary Lagrange Eulerian (MMALE) Fluid Structure Interaction (FSI).

The three finite element models presented in this chapter represent the three different experimental configurations. These simulations were not intended to exactly replicate the experimental results, but rather to aid in the understanding of the physical experiments.

In the ALE simulations both Lagrangian and Eulerian descriptions are used to describe the deformation of different materials in the same problem. In the Lagrangian description, each node of a finite mesh is deformed together with the continuum material.

The advantage of this is that the Lagrangian description tracks the surface of the continuum material, that is the shape of the deforming material can be determined. A drawback of this description is that it is inaccurate when there are large distortions of the mesh which easily appear with large deformations resulting from explosive detonation. The Lagrangian description was used for the structural analysis of the test plate in these simulations. In contrast, the Eulerian description uses a mesh that is fixed in space. The advantage of the Eulerian description is that it handles large distortions. However it uses a description that is fixed in space, which complicates the surface tracking, and requires that consideration of advection over element boundaries. The Eulerian description was used to describe the fluid dynamics where large deformations occurred. In the ALE method the nodes of the mesh can be moved as in the Lagrangian description or be held as in the Eulerian description. Also, the nodes can move without following the continuum material and this is done to minimize the advection over the boundaries to get a more accurate solution.

The MMALE description is based on three domains: the initial material configuration, the current (deformed) material configuration and the ALE configuration, also called the reference configuration. The initial and current configurations together determine the motion of the material. The current configuration together with the ALE configuration, determine the mesh motion. If the mesh motion is zero, the mesh is considered to be an Eulerian mesh. The advantage of MMALE over ALE is that the MMALE can handle multiple materials in the same element. In the elements of the mesh, the governing equations for mass, momentum and energy are integrated at the centroid, while other variables are stored in the nodes.

In these simulations a quarter symmetry model was developed to reduce simulation run time. An initial set of models looked at the effect of eliminating the clamp frames and bolts as these added to the complexity of the calculation, but the results showed that these had a significant effect on the simulation result and needed to be included for completeness.

6.2 Geometric representation

The problem was modelled making use of quarter symmetry in 3D to increase computational efficiency. A simple representation of the problem can be seen in Figure 6.1. The bolted connections in the experiments were represented by springs which

simplified the representation.

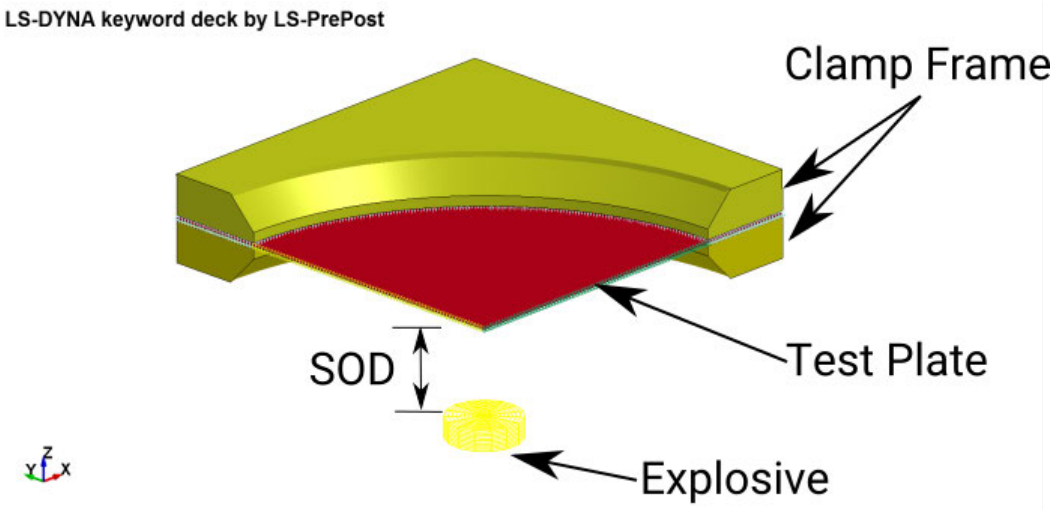

Figure 6.1: Quarter symmetry representation of the AIR numerical model.

6.2.1 Test Plate

The plate was modelled using fully integrated shell elements as advocated by [58, 88]. The element size was set at 2mm and the 200x200mm quarter of the full plate was modelled. Two boundary conditions were imposed on the plate to represent the XZ and YZ symmetry boundary conditions seen in Figure 6.2. The automatic surface to surface contact algorithm was implemented between the clamp frames and the test plate. Figure 6.2 shows the segment set where the clamp frame is expected to interact with the test plate. A coefficient of static friction $\boldsymbol{\mu_s = 0.17}$ was used to model the friction between the two surfaces when they come into contact with one another [58]. Element formulation 16 was used for the shell elements as it is able to full capture element bending as this is a fully integrated element implementation in LS Dyna. The mesh consisted of 2x2mm quad elements only.

The final element mesh size was largely influenced by the work conducted by Geretto [58], Aune and Borvik *et al* [149] and Schwer [88] who all used the MMALE approach to model blast loading of thin test plates. Although a full mesh sensitivity study was not undertaken in this work as the numerical analysis was not the main thrust of this work, the mesh was altered to see that it did not have an effect on the results of the study.

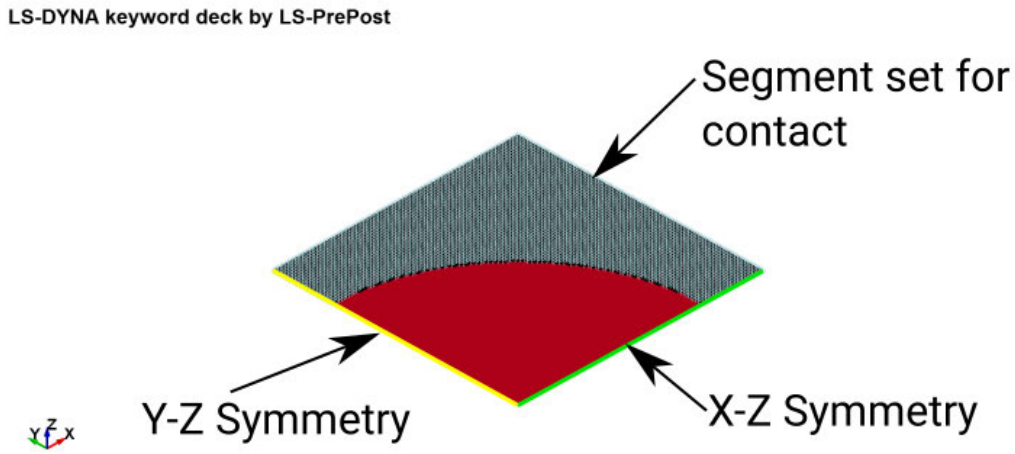

Figure 6.2: Quarter symmetry representation of the test plate.

It was found that when the mesh size of the plate was doubled to 4mm, significant leakage occurred of the blast products passing through the test plate and the impulse transferred to the plate was significantly lower than experimentally recorded. When the mesh size was halved to 1mm, the simulation time increased by a factor of 1.4 and the midpoint displacement of the test plate was found not to differ significantly from the results obtained when using an element size of 2mm. For these reasons the element size was fixed at 2mm for the test plate.

6.2.2 Clamp Frame

The clamp frames are modelled as solid parts with an element size of approximately 4mm. The elements were a mixture of hex and tet elements. Two boundary conditions were imposed on both clamp frames seen in Figure 6.3 to represent the XZ and YZ symmetry boundary conditions. An additional rigid boundary condition was imposed on the rear clamp frame (on the pendulum side of the plate) to represent the point where the clamp frame is mounted to the pendulum seen in Figure 6.4.

The material was modelled as an elastic material with Youngs modulus $\boldsymbol{E = 210GPa}$ as the permanent deformation of the clamp frame was determined to be minimal. The bolt clamping force was achieved by enforcing an initial elongation in the spring element with the initial offset command in the $*\boldsymbol{ELEMENT\_DISCRETE}$ card. This initial offset results in an equivalent bolted pressure of 240MPa being

developed in the region under the bolt head which is consistent with the results reported by Geretto [58]. The bolted connections between the two clamp frames were modelled as simple spring elements which had the stiffness and bolt preload defined to represent the loading seen by a real bolt. Figures 6.5 and 6.6 show the spring elements and the resulting pre-stress which clamps the two plates together. Although this method is not as thorough as modeling the entire bolt and connection, it is effective in producing the clamping force between the two clamp frames which restrain the test plate. Because no significant pull in or tearing failure was noted at the clamp boundary during the initial experiments this method is considered suitable.

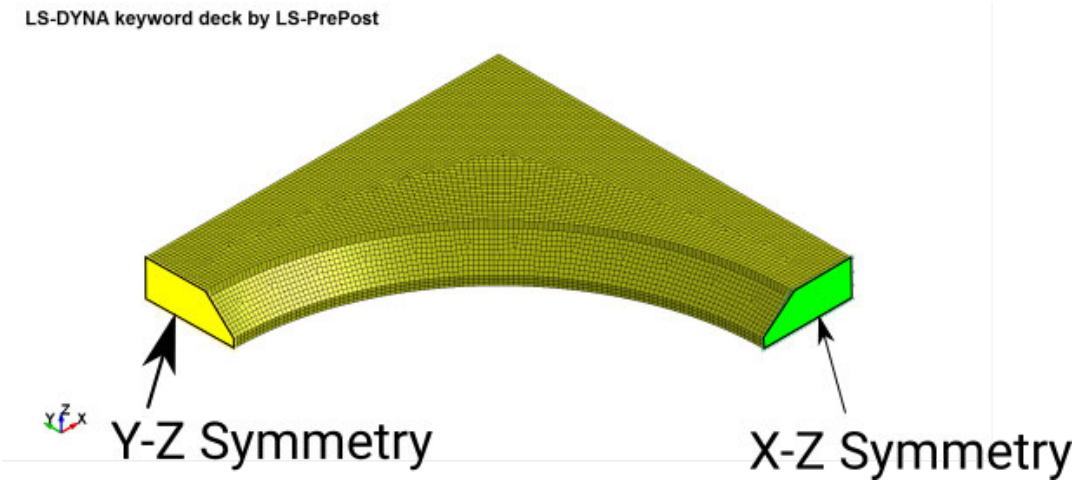

Figure 6.3: Quarter symmetry representation of the plate clamp.

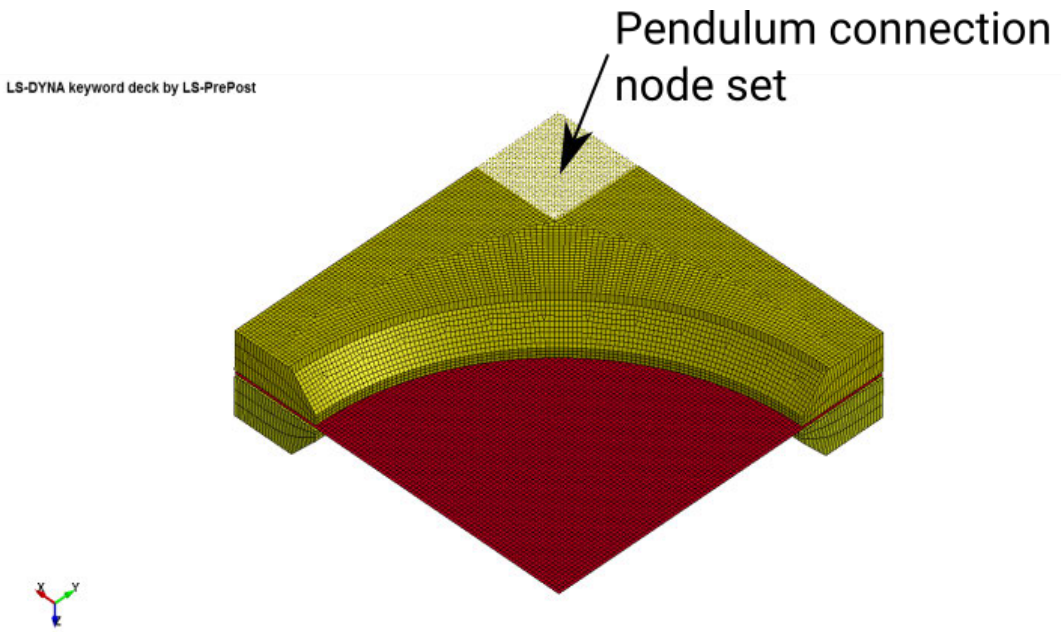

Figure 6.4: Quarter symmetry representation of the plate clamp assembly showing the pendulum connection point.

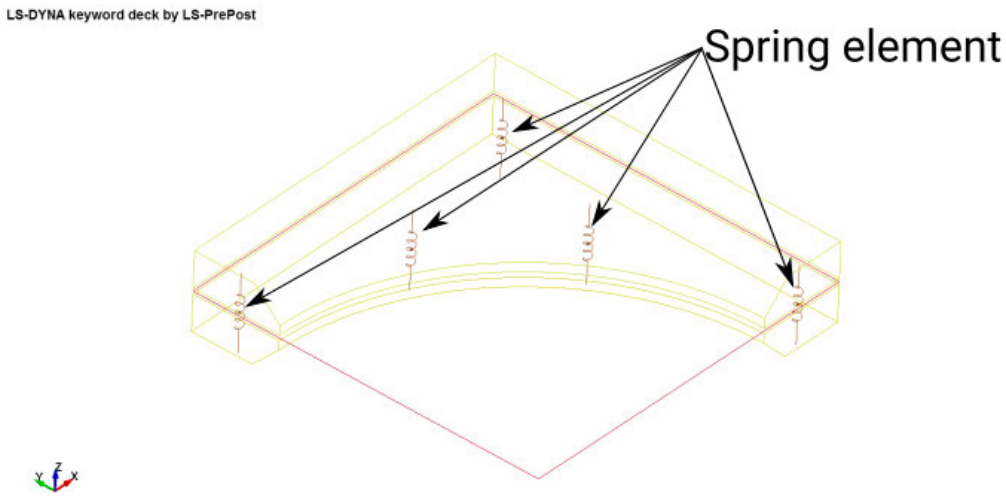

Figure 6.5: Wire-frame Quarter symmetry representation of the plate clamp assembly showing the spring elements used to represent the bolted connections.

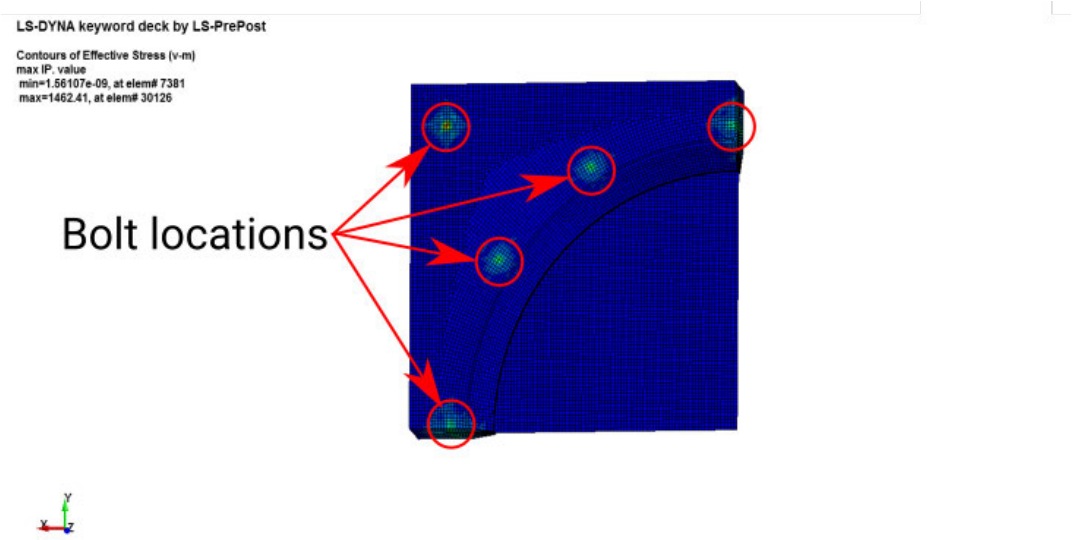

Figure 6.6: Quarter symmetry representation of the plate clamp assembly showing the clamp bolt points which were represented by spring elements.

6.2.3 Air Block

The air surrounding the explosive charge and plate was represented as a 200x200x200mm block which was divided into 2mm cubed elements following the results of the mesh convergence study conducted by Geretto [58] for a similar configuration. Geretto [58] found that the size of the air mesh had a much smaller effect than the size of the plate mesh. Two boundary conditions were imposed on this block to represent the XZ and YZ symmetry conditions seen in Figure 6.7. All other surfaces were defined as free boundaries which allow out flow of the Eulerian air formulation.

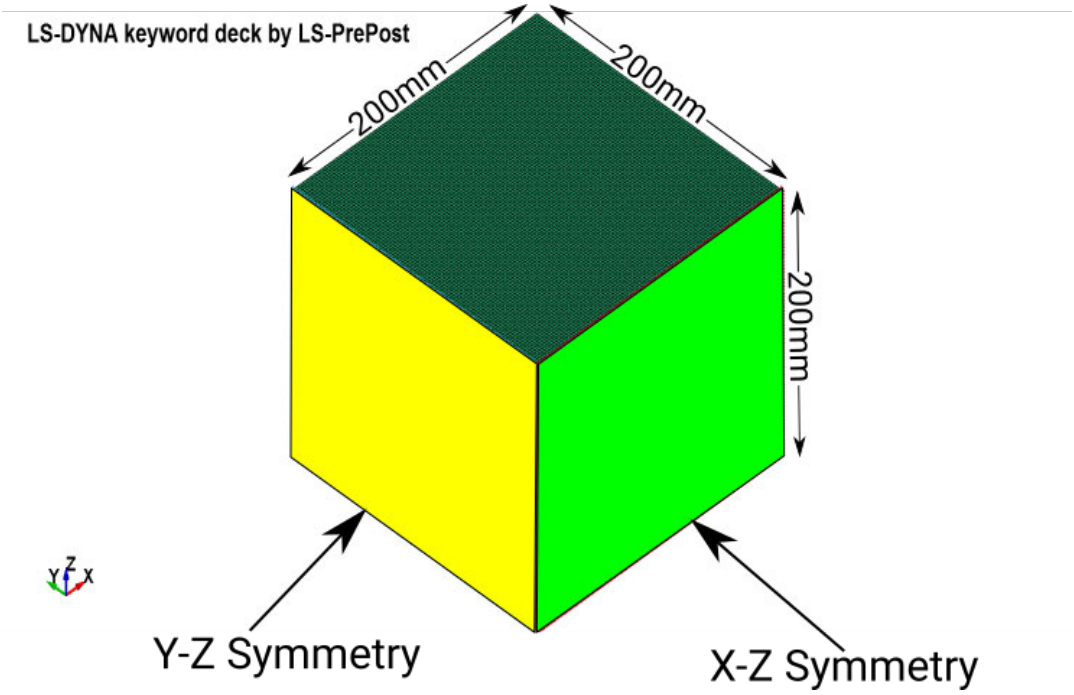

Figure 6.7: Quarter symmetry representation of the air block showing the symmetry boundary conditions.

6.2.4 Vertical Back plate

The metal back plate seen in the experimental configuration was numerically represented as a rigid reflecting boundary condition. This is to mimic the effect that the back plate had on the charge and it was assumed that any deformation of the plate would be minimal. This was imposed on the lower node set of the air block in the VBP and SBP numerical simulations where the displacement conditions $\boldsymbol{\delta_x}$, $\boldsymbol{\delta_y}$ and $\boldsymbol{\delta_z = 0}$ were

imposed on the node sets. The ALE fluid flow through the boundary was controlled by implementing the ∗***ALE_ESSENTIAL_BOUNDARY*** card which allows for no flow in all directions to be defined on an element set.

6.2.5 Explosive

The PE4 was modelled as a cylinder using an ∗***INITIAL_VOLUME_FRACTION*** description, which fills a container of background Eulerian material (air in this instance) with the explosive material. This method of explosive modelling has become common practice in the literature and has proven computationally efficient at reproducing the loading conditions experienced as a result of detonating explosives in close proximity to a structure. The volume of the defined cylindrical geometry is discretised into elements which fill the air mesh. This description is not perfect as shown in Figure 6.8 as the defined volume of the explosive is based on the charge mass and the density of the explosive material. This meant that if the volume could not be exactly created by filling the underlying air mesh then portions of these elements were filled resulting in the tesselations seen in Figure 6.8.

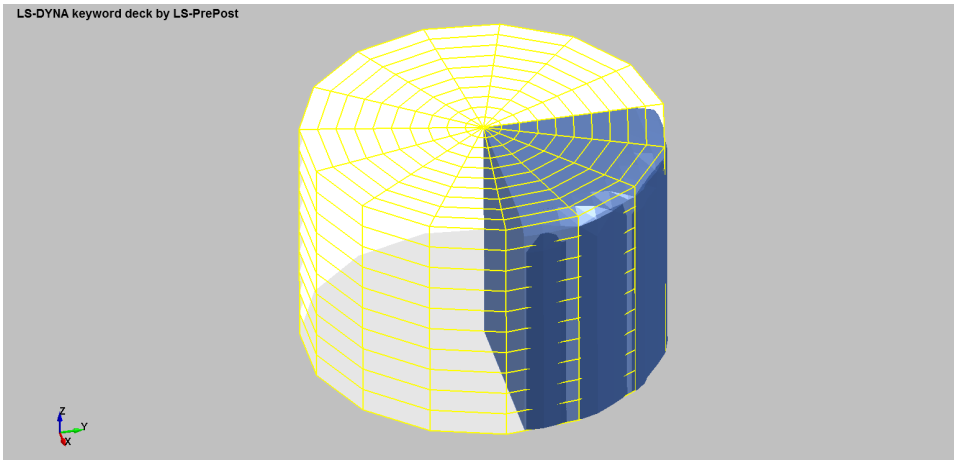

Figure 6.8: Numerical representation of the explosive showing the initial volume fraction definition in yellow and the resulting elements in blue.

6.2.6 Sand

The sand was modelled using a similar approach to that described in Section 6.2.5 using an initial volume fraction. This can be done as the Eulerian model for the sand could be conveniently implemented using this geometric description. The initial volume that the sand occupied was described as a cube with its base in the same plane as the bottom of the explosive and its upper surface defined as 10mm above the upper surface of the explosive. In the simulation series, the upper surface of the explosive was parametrized, meaning that the upper surface of the sand could be parametrized and calculated based on that value.

6.3 EOS and Material Models

The response of the different element types in the MMALE simulation are defined by Equations Of States (EOS) of the different materials. Here, the implemented parameters are outlined that were used in the MMALE.

6.3.1 Test Plate

The test plate was modelled using the simple Johnson Cook material definition described in Chapter 5. The material formulation ***MAT_MODIFIED_JOHNSON_COOK*** was implemented with material parameters outlined in Table 6.1. The decision to use a Johnson-Cook material description is largely based on its ease of implementation in the model. Other material descriptions such as that of Gurson [150] and Bai-Wierzbicki [151] were considered but were found to be too computationally expensive for the purposes of this limited investigation. Future work should include an exploration of other appropriate material descriptions.

Material Parameters	Density	Youngs modulus	Poissons Ratio	Taylor Quinnery	Specific heat	Reference strain rate	
	$\boldsymbol{\rho}$	E	v	$\boldsymbol{\chi}$	$\boldsymbol{C_p}$	$\boldsymbol{E_0}$	
	7830 $\boldsymbol{kg/m^3}$	210 $\boldsymbol{GPa}$	0.29	0.9	452 J	0.0014 $\boldsymbol{s^{-1}}$	
Numerical Model Parameters							
Johnson Cook Variable	A	B	n	C	m		
	352 $\boldsymbol{MPa}$	642 $\boldsymbol{MPa}$	0.5597	0.032	0.81		
Voce Hardening parameters	$\boldsymbol{Q_1}$	$\boldsymbol{C_1}$	$\boldsymbol{Q_2}$	$\boldsymbol{C_2}$			
	0	0	0	0			
Damage Parameters	$\boldsymbol{D_c}$	$\boldsymbol{P_d}$	$\boldsymbol{D_1}$	$\boldsymbol{D_2}$	$\boldsymbol{D_3}$	$\boldsymbol{D_4}$	$\boldsymbol{D_5}$
	100	100	0.1	0.2	0.3	0.4	0.5

Table 6.1: The material model options in ∗MAT_MODIFIED_JOHNSON_COOK used in LS-Dyna.

6.3.2 Clamp Frame

The clamp frames were modelled using a simple elastic material definition. This approach has the advantage of being able to reproduce any elastic bending of the clamp frames while reducing the computational cost of having to calculate plasticity because no permanent deformation of the clamp frames were reported in the experimental results.

6.3.3 Air

The Air was modelled with the LS Dyna built in Null material (*MAT_NULL) and an ideal gas EOS, Equation 6.1.

$$\boldsymbol{P} = (\boldsymbol{\gamma} - \mathbf{1}) \left[\frac{\boldsymbol{\rho}}{\boldsymbol{\rho_0}} \boldsymbol{E} \right] \tag{6.1}$$

where $\boldsymbol{P}$ is the pressure, $\boldsymbol{\rho}$ is the current density, $\boldsymbol{\rho_0}$ is the initial density, $\boldsymbol{E}$ is the internal energy per unit reference volume and $\boldsymbol{\gamma}$ is the ratio of specific heats ($\frac{\boldsymbol{C_p}}{\boldsymbol{C_v}} = 1.4$ for air).

The Air was modelled with a linear polynomial Equation of State, Equation 6.2, by setting $\boldsymbol{C_0} = \boldsymbol{C_1} = \boldsymbol{C_2} = \boldsymbol{C_3} = \boldsymbol{C_6} = \mathbf{0}$ and $\boldsymbol{C_4} = \boldsymbol{C_5} = \boldsymbol{\gamma} - \mathbf{1}$ in the ideal gas equation.

$$\boldsymbol{P} = \boldsymbol{C_0} + \boldsymbol{C_1}\boldsymbol{\mu} + \boldsymbol{C_2}\boldsymbol{\mu^2} + \boldsymbol{C_3}\boldsymbol{\mu^3} + (\boldsymbol{C_4} + \boldsymbol{C_5}\boldsymbol{\mu} + \boldsymbol{C_6}\boldsymbol{\eta^2})\boldsymbol{E} \tag{6.2}$$

where $\boldsymbol{C_1} - \boldsymbol{C_6}$ are user defined constants, $\boldsymbol{E}$ is the internal energy per unit reference volume and $\boldsymbol{\mu}$ is a volumetric parameter defined as,

$$\boldsymbol{\mu} = \frac{\boldsymbol{\rho}}{\boldsymbol{\rho_0}} - \mathbf{1} \tag{6.3}$$

where $\boldsymbol{\rho}$ is the current density and $\boldsymbol{\rho_0}$ is the initial density.

The Equation of State properties of air implemented in the simulations are shown in Table 6.2.

$\boldsymbol{\rho_0}$ $(\boldsymbol{kg/m^3})$	$\boldsymbol{\gamma}$	$\boldsymbol{E_0}$ $(\boldsymbol{kJ/m^3})$
1.184	1.4	2.533

Table 6.2: EOS properties for air [8].

6.3.4 Explosive

The Jones-Wilkins-Lee (JWL) EOS was implemented in conjunction with the high explosive burn material model to describe the explosive materials. The JWL EOS has been widely implemented due to its simplicity and accuracy over a wide range of

explosive materials. The JWL EOS defines the pressure as a function of the internal energy per unit reference volume $\boldsymbol{E}$ and the relative volume $\boldsymbol{\nu}$ and is expressed as:

$$\boldsymbol{P = A\left(1 - \frac{\omega}{R_1\nu}\right)e^{R_1\nu} + B\left(1 - \frac{\omega}{R_2\nu}\right)e^{-R_2\nu} + \frac{\omega E}{\nu}} \tag{6.4}$$

Where $\boldsymbol{A}$, $\boldsymbol{B}$, $\boldsymbol{R_1}$, $\boldsymbol{R_2}$ and $\boldsymbol{\omega}$ are material constants.

$\boldsymbol{\rho_0}$ $(\boldsymbol{kg/m^3})$	$\boldsymbol{D}$ $(\boldsymbol{m/s})$	$\boldsymbol{P_{CJ}}$ $(\boldsymbol{GPa})$	$\boldsymbol{A}$ $(\boldsymbol{GPa})$	$\boldsymbol{B}$ $(\boldsymbol{GPa})$	$\boldsymbol{R_1}$	$\boldsymbol{R_2}$	$\boldsymbol{\omega}$	$\boldsymbol{E_0}$ $(\boldsymbol{GPa})$
1616	8193	28	609.77	12.95	4.5	1.4	0.25	9

Table 6.3: Explosive material properties [152]

The detonation process was modelled with the high explosive burn material model. The material model controls the release of energy during the detonation process with the implementation of a burn fraction (See [58] for further information). The pressure during the detonation process was a function of the JWL EOS pressure $\boldsymbol{P_{JWL}}$ and the burn fraction $\boldsymbol{F}$ and is expressed as:

$$\boldsymbol{P = P_{JWL} \times \underbrace{min(1, max(F_1, F_2))}_{\text{Burn Fraction(F)}}} \tag{6.5}$$

Where $\boldsymbol{F_1}$ and $\boldsymbol{F_2}$ are the burn fractions defined by:

$$\boldsymbol{F_1 = \begin{cases} \frac{2(t-t_1)DA_{e_{max}}}{3v_e} & \text{for} t > t_1 \\ 0 & \text{for} t \leq t_1 \end{cases}} \tag{6.6}$$

$$\boldsymbol{F_2 = \beta = \frac{1 - V}{1 - V_{CJ}}} \tag{6.7}$$

Where $\boldsymbol{t}$ is the current time, $\boldsymbol{t_1}$ is the lighting time, $\boldsymbol{D}$ is the detonation velocity, $\boldsymbol{A_{e_{max}}}$ is the maximum surface area of the element, $\boldsymbol{v_e}$ is the volume of the element, $\boldsymbol{V}$ is the actual specific volume and $\boldsymbol{V_{CJ}}$ is the specific volume at the Chapman-Jouguet pressure ($\boldsymbol{P_{CJ}}$). The relation between $\boldsymbol{V_{CJ}}$ and $\boldsymbol{P_{CJ}}$ is given by:

$$\boldsymbol{V_{CJ} = 1 - \frac{P_{CJ}}{\rho_0 D^2}} \tag{6.8}$$

The lighting time $\boldsymbol{t_1}$ of an element was determined by dividing the distance between the centre of the element and the defined detonation point by the detonation velocity $\boldsymbol{D}$.

Equation 6.6 represents the programmed burn model in LS-DYNA [153], which controls the detonation process with the lighting times of the explosive elements. The programmed burn model smears the detonation process over several time steps. Equation 6.7 represents the beta burn model in which volumetric compression of an explosive element resulted in the detonation of the explosive element.

The formulation of this investigation employed both the programmed and beta burn models to describe the detonation of the explosives.

6.3.5 Sand

The majority of the sand properties in the literature are based upon Sjobo sand, as characterized by Laine & Sandvik [75], which included compaction, strength, and modulus. Yield strength properties for varying levels of saturation were derived from Kerley [83–85]. For dry sand, Laine and Kerley [83–85] show nominal agreement which suggests that both approaches are relevant.

Modification of the Sjobo properties to represent alternate dry densities was considered by Barsotti and Sammarco [82]. Barsotti and Sammarco [82] assumed that the terminal density and modulus of fully compacted sand was nominally the same for different species, that of pure quartz ($\boldsymbol{\rho = 2,650 kg/m^3}$). Variations in dry density can be influenced by particulate gradation, particulate sphericity, and material consolidation arising from tamping or vibration. The ratio of the loose and terminal density for Sjobo sand indicates a void fraction of approximately 37%. For higher or lower dry sand densities, the pressure-density curve was either compressed or dilated from the left end while leaving the terminal density unaltered. Barsotti ans Sammarco [82] noted that density had a strong effect on impulse, while soil strength and plate friction proved to be far less influential. Plate friction was almost negligible for flat plate impacts, but not for the V-plate tests, where sliding friction has a vertical component. The most important observation made was with regard to the criticality of compression properties of the sand material, as defined in $\boldsymbol{*EOS\_TABULATED\_COMPACTION}$. The effects of the compression curve were, if anything, more important than those of material density. Phenomenologically, the rapidly expanding explosive products are contained, at least in

a transient sense, by the "spongy" soil surrounding them. The degree of compliance in this pseudo container determines how much energy is immediately absorbed from the expanding explosive products.

For these reasons the Laine and Sandvik Sjobo sand model [75] was selected and used directly without adjustment. The density of the sand used in this experimental setup was measured and calibrated according to the recommendation of Barsotti and Sammarco [82] and inserted into the model as recommended.

The soil material was described with the elastic-plastic hydro spall model in LS-Dyna, with properties shown in Table 6.4.

Density	1370 $\boldsymbol{kg/m^3}$
Shear Modulus	76.9 $\boldsymbol{MPa}$
Yield Stress	0
Plastic hardening modulus	0
Pressure cutoff	-0.0069
Effective plastic strain at failure	0
Element length for deletion	0
Linear pressure hardening coefficient	1.39642
Quadratic pressure hardening coefficient	0
Spallation type	Spalls in tension

Table 6.4: Sand material properties used for
*$\boldsymbol{MAT\_ELASTIC\_PLASTIC\_HYDRO\_SPALL}$
[75]

The EOS used to define the sand compaction of the sand followed Laine and Sandvik [75], shown in Table 6.5 and was implemented with the *$\boldsymbol{EOS\_TABULATED\_COMPACTION}$ keyword. Due to the importance of the EOS noted in the work by Barsotti and Sammarco [82] and Schwer [88], this parameter was not altered as it had already been validated by the two authors. The density of the sand was reduced until the impulse and plate deflection in the simulation matched the experimental values, as recommended by Barsotti and Sammarco [82].

Strain	Pressure ($\boldsymbol{MPa}$)
0.000	0
0.113	14.98
0.176	29.15
0.247	58.18
0.296	98.1
0.352	179.44
0.395	289.44
0.433	450.20
0.467	650.66
0.470	800.00

Table 6.5: The EOS used to describe the sand compaction outlined by Laine and Sandvik [75]

6.3.6 Coupling

Two different types of coupling between elements were important in this investigation. The first was the coupling of the explosive products and sand to the test plate enabling the energy transfer to the plate. The second was the contact between the test plate and the clamp frame.

ALE coupling between the test plate and blast products

The coupling between the explosive products, sand and test plate were modelled using the *$\boldsymbol{CONSTRAINED\_LAGRANGE\_IN\_SOLID}$ formulation.

The penalty based approach was used where coupling forces are added to both ALE and Lagrangian elements if the Lagrangian part is penetrating the ALE material. The magnitude of this force is proportional to the penetrating distance. The formulation has many different options for controlling the interaction between the fluid and test plate. Advice in the user manual [154] was applied with specific reference to the relevant parts used in the simulation. The full usage of the card can be seen in Appendix C. The implementation of this specific card has many different variables which control aspects such as leakage (which describes a fluid passing through a solid Lagrangian surface it

should interact with). Finding a solution to leakage problems was not trivial, with advice in the user manual [154] or published literature indicating parameters should be varied until leakage stops, with no clear guidelines being defined. In this investigation the default parameters with respect to leakage were implemented to evaluate whether the leakage was significant enough to effect the simulation results.

Lagrangian contact between surfaces

The contact between the test plate and clamp frames was controlled using a surface to surface penalty based contact algorithm. The friction between the surfaces was defined by Coulomb friction with a constant coefficient of friction. A parametric study of the frictional coefficient ($\boldsymbol{\mu}$) between the surfaces was carried out by Geretto [58] who found that the frictional coefficient of 0.17 resulted in a solution that correlated with his experimental results. The same friction coefficient was used herein as the setup and fastening method used was similar to Geretto [58].

6.4 Models and Summary Results

The final numerical configuration of each series is presented here, with a selection of results for completeness. A full set of numerical simulation results are presented in Appendix B. An example configuration of the input deck for the numerical simulation is shown in Appendix C (with the exception of the nodal and element geometry definitions).

Data was extracted from the numerical models in two very similar ways to the methods used to represent the experimental transient plate deformations in Chapter 4. The first was by extracting the nodal results of the central node of the test plate seen in Figure 6.9. The second form of data presented, is along the line of nodes through the centre of the plate as seen in Figure 6.9

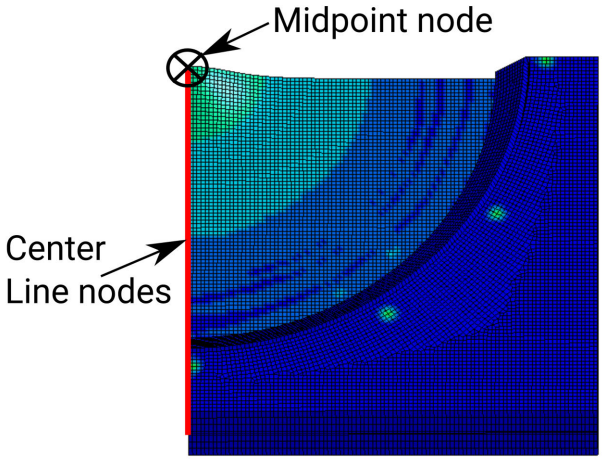

Figure 6.9: The nodes along the centre of the simulated test plated where information was extracted for the midpoint (black) and along the centre line (Red).

6.4.1 Simulation phases

The simulation is executed in three phases illustrated in Figure 6.10. Each phase following the first one is initiated with a small restart in LS-Dyna which reads in the final state of the previous simulation step and then modifies the input deck according to the contents of the small restart file. Further information on the small restart can be found in reference [154]. The three phases are:

1. Loading Phase
2. Deformation phase
3. Damping phase

The first phase is the loading phase where the explosives detonate and the explosive products expand with the resulting pressure wave which interacts with the plate. This phase contains the complete interaction of the MMALE and the test plate. This phase was terminated after 450 microseconds which was determined to be enough time for the impulse transfer to occur between the Eulerian blast wave, the explosive products and the test plate.

During the second phase, the Eulerian elements are deleted from the simulation and the Lagrangian elements are allowed to deform after the loading phase. This phase was purposely extended to allow the simulated test plate to plastically deform into its final shape and then elastically oscillate in a similar fashion to that seen in the experimental data. This phase was allowed to run between 450 microseconds and 5 milliseconds.

The final phase was used to apply damping to the plate. This damping allowed the elastic oscillation of the test plate to settle to its final deformation profile.

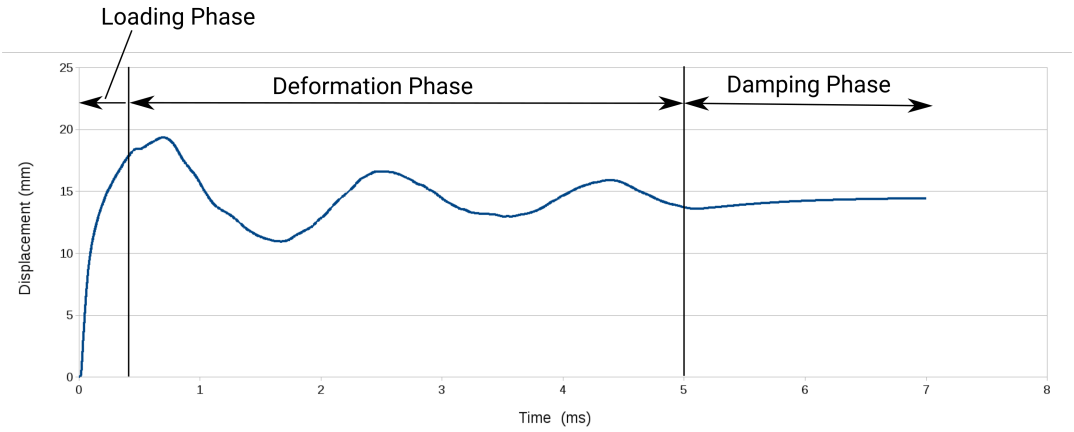

Figure 6.10: The three simulation phases shown tracking the central node on a test plate.

6.4.2 AIR - Air Charge

A summary of the results from the AIR configuration simulations are presented here. Figure 6.11 shows a representation of the simulation layout.

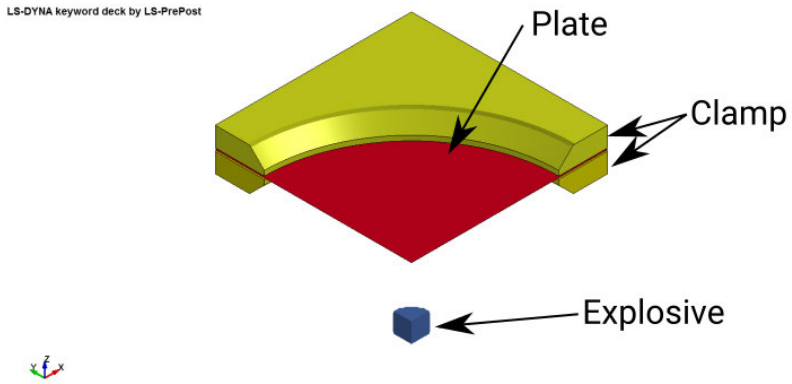

Figure 6.11: Quarter symmetry representation of the AIR numerical model.

The results for the simulated AIR series are summarised in Table 6.6. The results show that the final plate deformation typically varied by less than one plate thickness from the experimental final midpoint deflection. The 15g simulation had a significantly higher final variation of between 4 - 5 mm for the two stand off distances. The maximum transient measurements are closer to the experimental values, typically varying by 1-2mm between the simulation and the experimental values. This was considered

acceptable as the transient deformation was the primary focus of this investigation.

Charge Mass	**SOD (mm)**	**Sim δ_{Trans} (mm)**	**Exp δ_{Trans} (mm)**	**Sim δ_{Final} (mm)**	**Exp δ_{Final} (mm)**
25g	40	33.9	36.3	30.0	31.3
20g	40	32.0	31.1	28.4	26.0
15g	40	28.1	25.3	24.6	19.2
10g	40	22.8	22.0	17.0	16.2
25g	50	29.4	30.5	25.5	25.5
20g	50	27.6	26.2	24.1	21.0
15g	50	24.2	21.7	20.4	16.1
10g	50	19.3	16.8	13.7	11.3

Table 6.6: The Simulation results for the AIR series of models

A typical transient midpoint deflection trace can be seen in Figure 6.12 for the 20g AIR simulations with experiments overlaid. Figure 6.12 shows the original experimental values in red and blue with the experimental final midpoint deflection represented by the dashed lines and the simulations in black. These simulations closely replicate the transient experimental data from the DIC up to 1.2 ms, but do not replicate the final midpoint deflection of the experiment. In most cases the simulated final deformation is higher than the recorded experimental value indicating that more plastic deformation has occurred in the simulation while the experimental plates retained more elastic deformation, allowing the plate to rebound slightly more.

Figure 6.13 depicts the plastic strain in the numerical model for the AIR 20g 50mm SOD simulation. This closely resembles the final deformation of the plates.

The final deformations of the plates for two representative AIR 20g charge experiments are shown in Figure 6.14 with the experimental plates shown in black and the simulations in green. It can clearly be seen in Figure 6.14 that while the plate midpoint deflections do not match at the plate centre, the plate profile is similar in shape to the experimental plate profile along the mid-line. Looking at the normalised plate profiles in Figure 6.15, which are normalised to the peak midpoint deflection, the profiles are much closer for the 50mm SOD than for the 40mm SOD. The 40mm

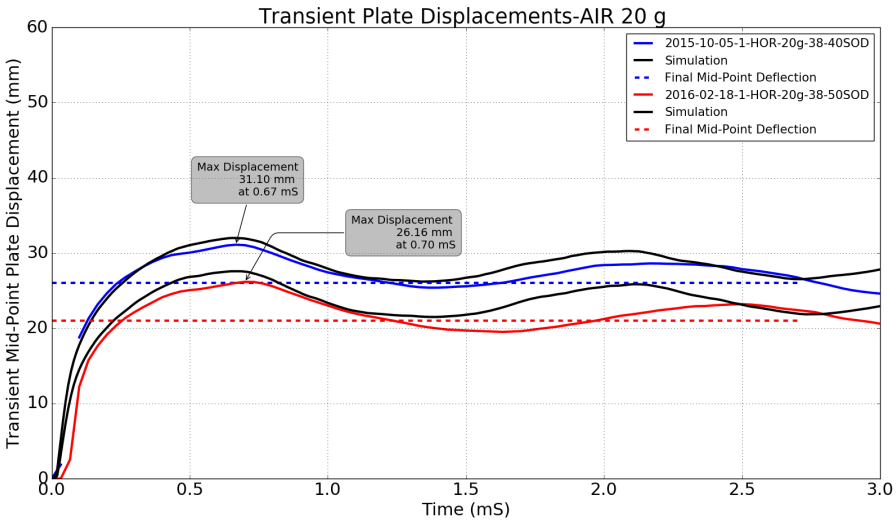

Figure 6.12: Typical transient midpoint deflection values for the AIR 20g simulations (black) and the experimental values (blue and red)

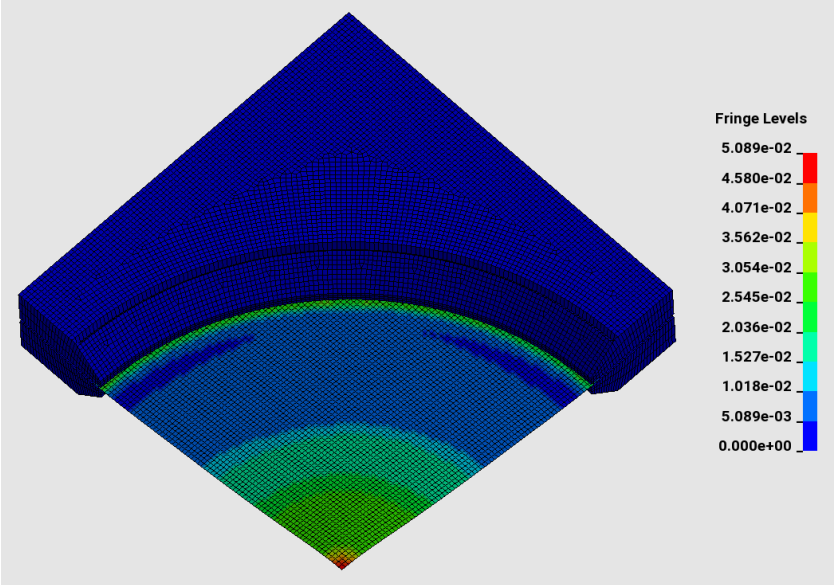

Figure 6.13: Transient plastic strain shown for the point of peak transient deflection for the AIR20g 50mm SOD simulation.

SOD experimental plate represented in black appears to have experienced more localised loading in the plate centre than what the simulated plate experienced.

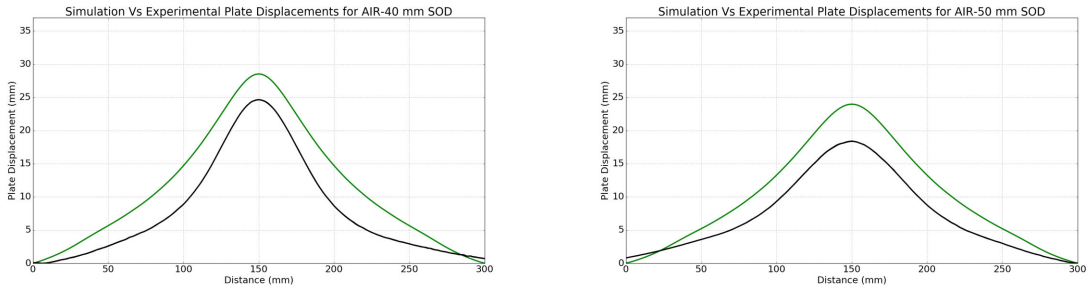

Figure 6.14: Comparison of the AIR 20g Simulations (green) and the experimental (black) final plate deformations for 40 and 50mm SOD.

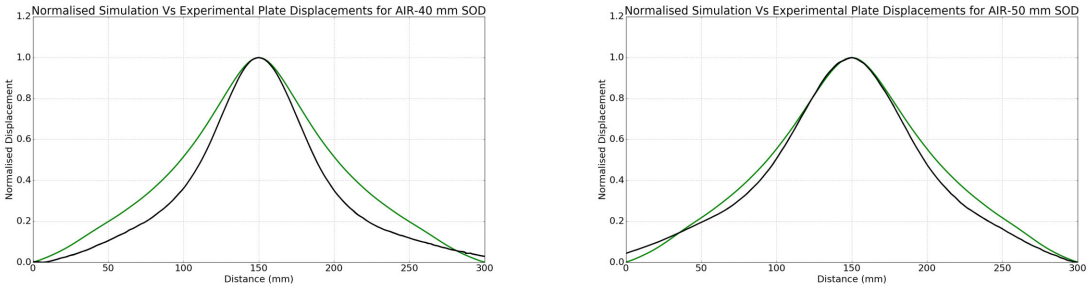

Figure 6.15: Comparison of the normalised 20g AIR Simulations (green) and the experimental (black) final plate deformations for 40 and 50mm SOD.

The loading on the simulated plate can be assessed by looking at the pressure at tracer points located along the centre line of the plate. Tracers were placed at the indicated points in Table 6.7 measured radially from the plate centre and placed 1mm below the plate surface. The pressure traces are shown in Figure 6.16 for the tracer points moving radially outward from the plate centre. By integrating the pressure at these points a specific impulse can be obtained for the point of the tracer, enabling a spatial plot to be produced of the specific impulse for each of the loading conditions. Looking at this normalised specific impulse distribution seen in Figure 6.17, a large portion of the impulsive load is located in the central 100mm of the plate.

The transient plate profiles from the 20g simulations are shown in Figure 6.18. Figure 6.18 shows the 40mm SOD and the 50mm SOD simulations with the temporal evolution of the out of plane deformations. The temporal steps have been adjusted to line up

Tracer	Radial distance (mm)
T1	0
T2	10
T3	20
T4	40
T5	60
T6	80
T7	100
T8	140
T9	180
T10	200

Table 6.7: Tracer point location in the numerical model located 1mm bleow the plate surface. Radial distance measured from the plate centre.

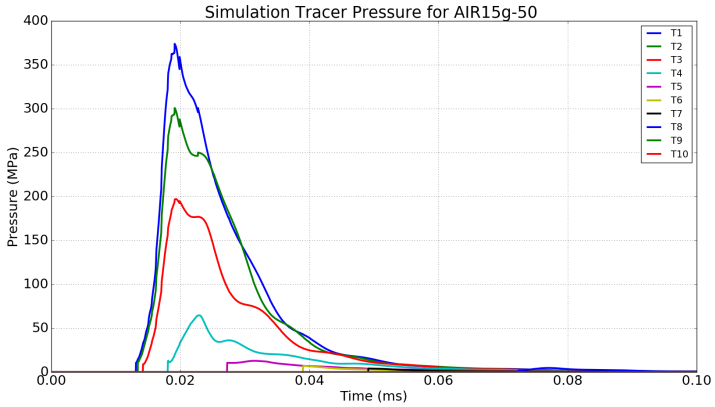

Figure 6.16: Pressure at the tracer points moving radially outward from the plate centre.

with those from the DIC data for easy comparison. The simulation deformation can be seen to initiate centrally and move radially outward toward the clamp boundary. The progression of the deformation closely follows the deformation described in the experimental results section. The most significant difference was the plate shape at 0.561 ms where an easily observable point of inflection can be seen forming between 50-

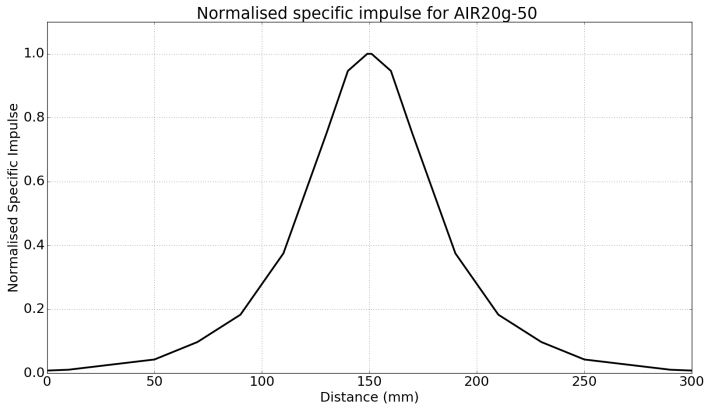

Figure 6.17: Normalised specific impulse distribution for the simulated AIR 20g 50SOD test plate.

100mm from the plate centre in the experimental observations. This point of inflection is less pronounced in the numerical simulation.

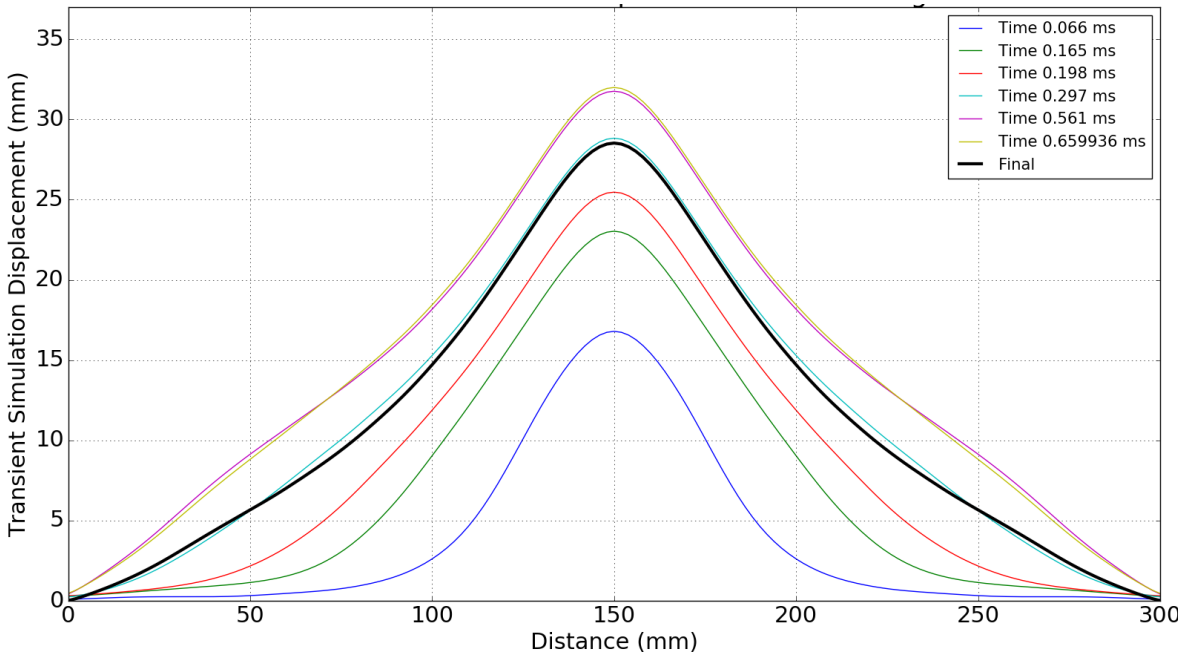

(a) 40mm SOD

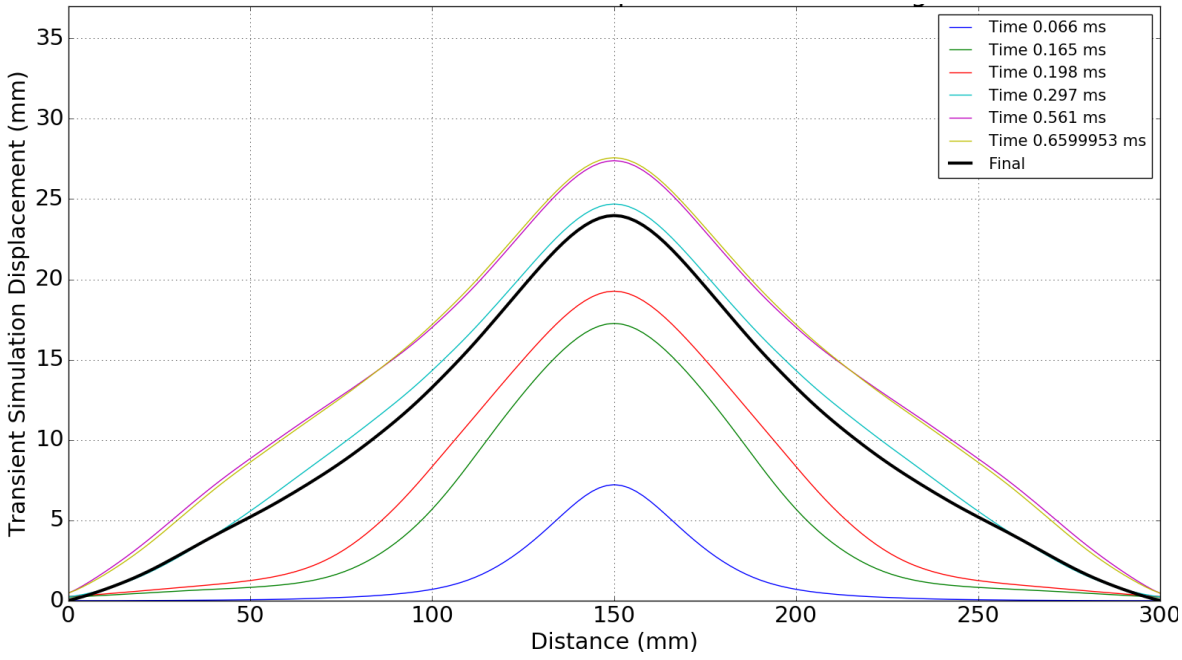

(b) 50mm SOD

Figure 6.18: Transient plate deformation data from simulation for 20g AIR charge detonations

6.4.3 VBP - Vertical Back Plate Charge

A summary of the results from the VBP configuration simulations are presented here in. Figure 6.19 shows a representation of the simulation layout.

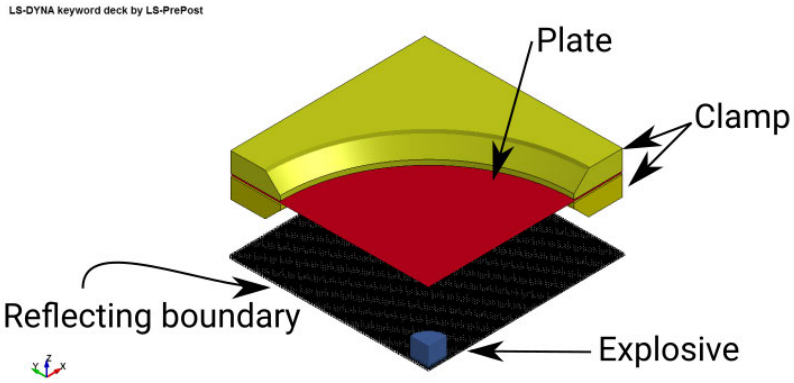

Figure 6.19: Quarter symmetry representation of the VBP numerical model.

The simulation results for the VBP series are summarised in Table 6.8. The results show that the final plate deformation varies by up to 5mm from the experimental final midpoint deflection. The maximum transient deformation matched very closely with the exception of the 25g charge for both the 40mm and 50mm SOD.

The typical transient midpoint deflection values can be seen in Figure 6.20 for the 20 VBP simulations and experiments overlaid. It shows the original experimental values in red and blue with the experimental final midpoint deflection in the dashed lines and the simulations in black. These simulations closely replicate the transient experimental data from the DIC but do not replicate the final deformation of the midpoint. It can be seen that the simulated transient behavior starts deviate from the experimental data at about 2.5 ms. The final deformation is under-predicted for the 25g charge masses and slightly over-predicted for the lower charge masses despite following the experimental transient data more closely.

Figure 6.21 depicts the plastic strain in the numerical model for the VBP 20g 50mm SOD simulation. This closely resembles the final deformation of the plates.

The final deformations of the 20g charge series are shown in Figure 6.22 with the experimental plates shown in black and the simulations in green. It can be seen in Figure 6.22 that the 40mm SOD simulations slightly over predict the experimental value while the 50mm SOD more closely predicts the final deformation. The general shapes of the

Charge Mass	SOD (mm)	Sim δ_{Trans} (mm)	Exp δ_{Trans} (mm)	Sim δ_{Final} (mm)	Exp δ_{Final} (mm)
25	40	36.2	42.7	32.3	38.4
20	40	40.7	40.8	38.0	35.6
15	40	35.1	37.2	31.1	31.5
10	40	33.2	32.3	29.1	26.0
25	50	31.1	36.3	26.9	34.4
20	50	36.3	37.1	32.7	30.0
15	50	30.1	29.8	26.0	24.3
10	50	28.4	28.2	24.4	22.3

Table 6.8: The Simulation results for the VBP series of models

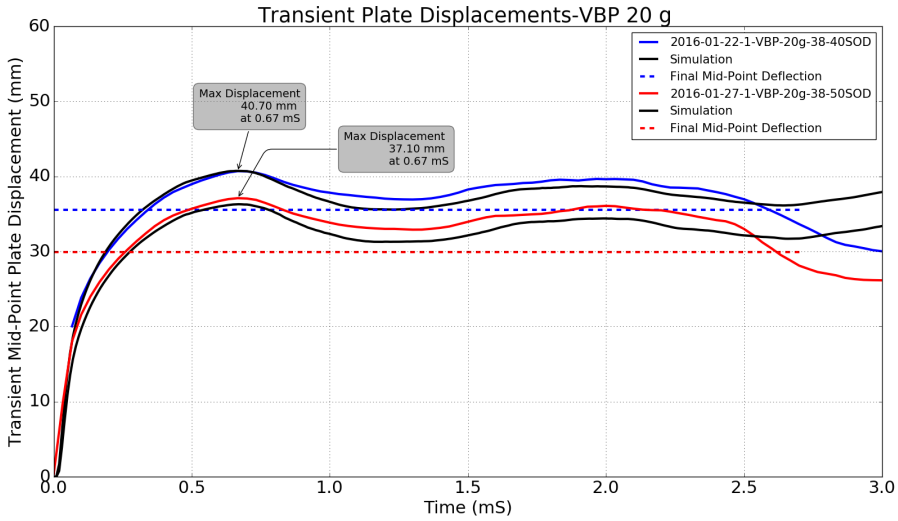

Figure 6.20: Typical transient midpoint deflection values for the VBP 20g simulations(black) and the experimental values (blue and red)

plate profiles for both SODs' appear to match well. Looking at the normalised plate profiles in Figure 6.23, which are normalised to the peak final midpoint deflection, the profiles are very similar to the experiments.

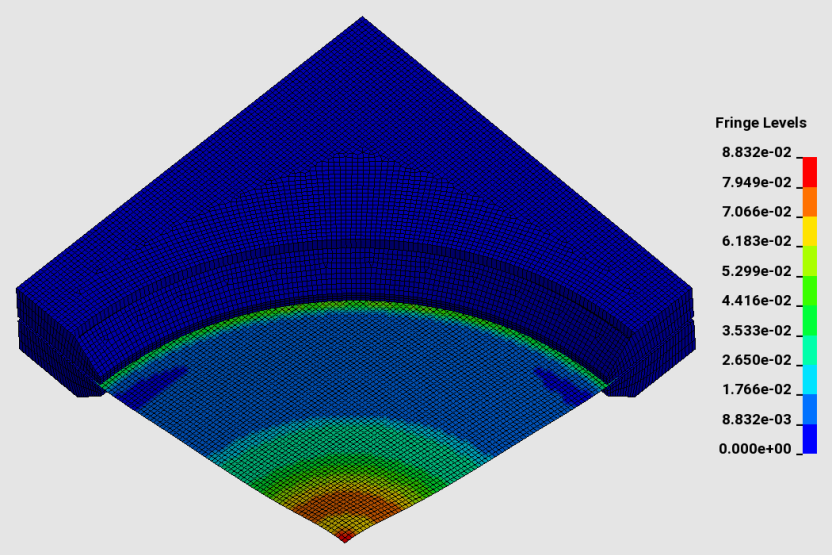

Figure 6.21: Transient plastic strain shown for the point of peak transient deflection for the VBP20g 50mm SOD simulation.

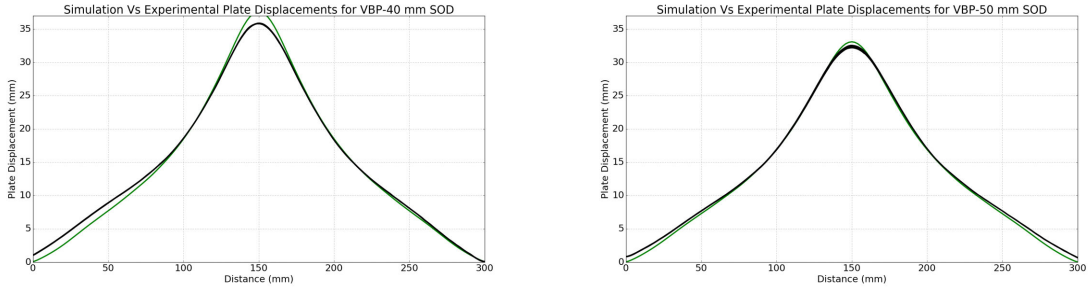

Figure 6.22: Comparison of the 20g VBP Simulations (green) and the experimental (black) final plate deformations for 40 and 50mm SOD.

The loading on the simulated plate can be assessed by looking at the pressure at tracer points located along the centre line of the plate extending radially from the plate centre, similar to the AIR simulations. The normalised specific impulse distribution is shown in Figure 6.24; once again a large portion of the impulsive load was located in the central 100mm of the plate.

The transient plate profiles from the 20g VBP simulations are shown in Figure

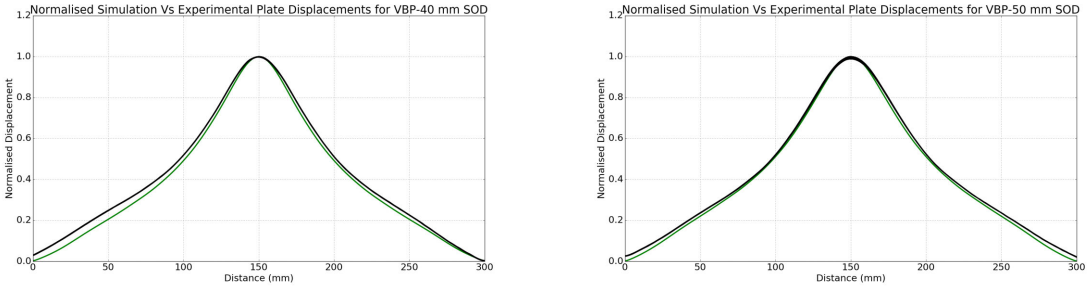

Figure 6.23: Comparison of the normalised 20g VBP Simulations (green) and the experimental (black) final plate deformations for 40 and 50mm SOD.

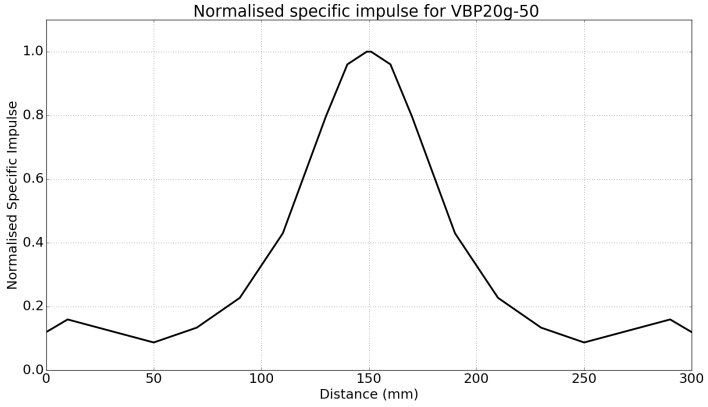

Figure 6.24: Normalised specific impulse distribution for the simulated VBP 20g 50SOD test plate.

6.25. Figure 6.25 shows the 40mm SOD and the 50mm SOD simulations with the temporal evolution of the out of plane deformations. The simulation deformation can be seen to initiate centrally and move radially outward toward the clamp boundary. The progression of the deformation closely follows the deformation evolution observed experimentally. The most significant difference was the plate shape at 0.561 ms, where the point of inflection is less pronounced in the numerical simulations.

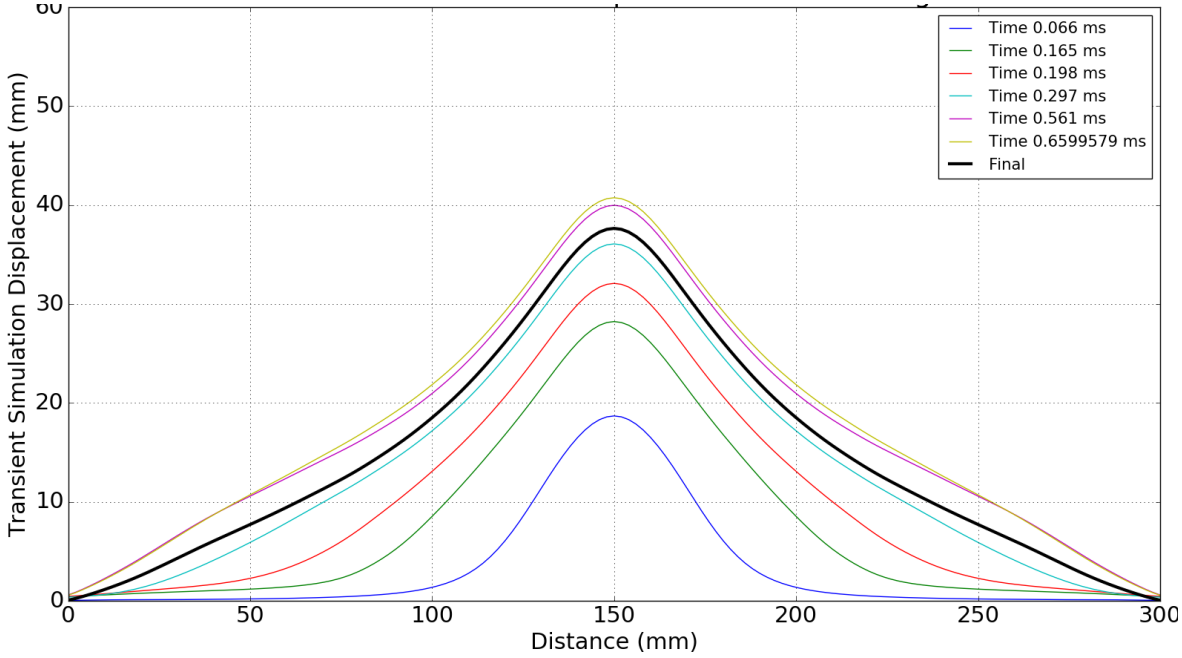

(a) 40mm SOD

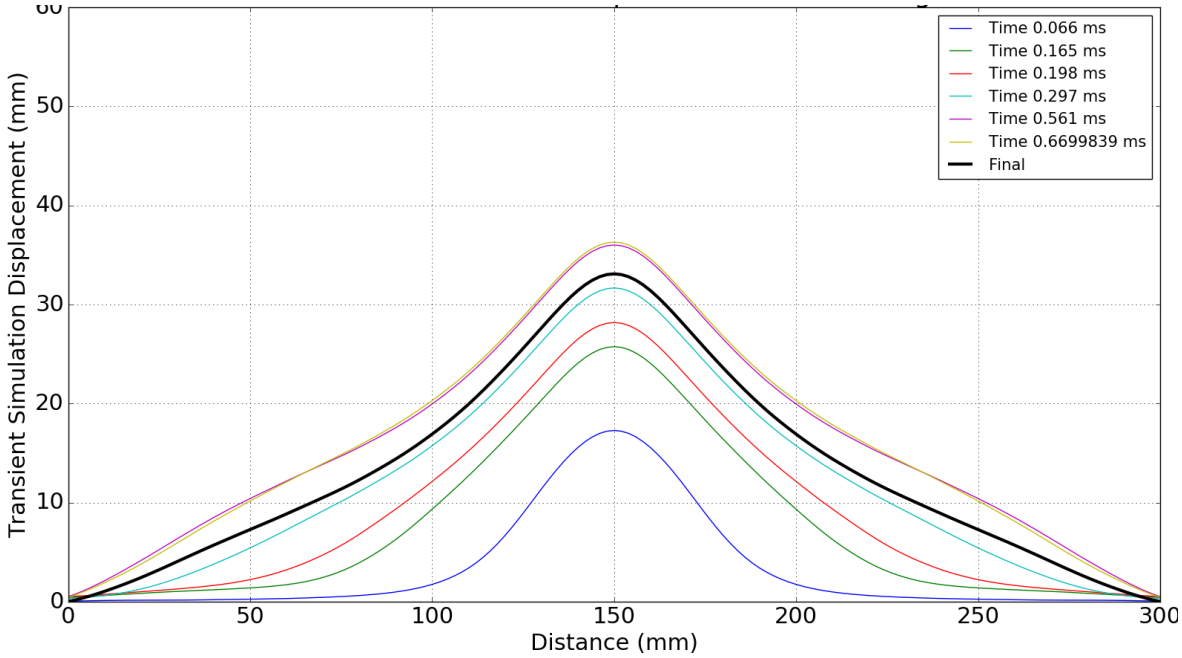

(b) 50mm SOD

Figure 6.25: Transient plate deformation data from simulation for 20g VBP charge detonations

6.4.4 SBP - Buried sand charge

A summary of the results from the SBP configuration simulations are presented here. Figure 6.26 shows a representation of the simulation layout. The results for the simulated SBP series are summarised in Table 6.9. The results show that the final plate deformation varies by up to 6mm from the experimental final midpoint deflection. The maximum transient had a slightly smaller difference but was still not very close with the exception of the 25g charge which more closely replicated the experimental result.

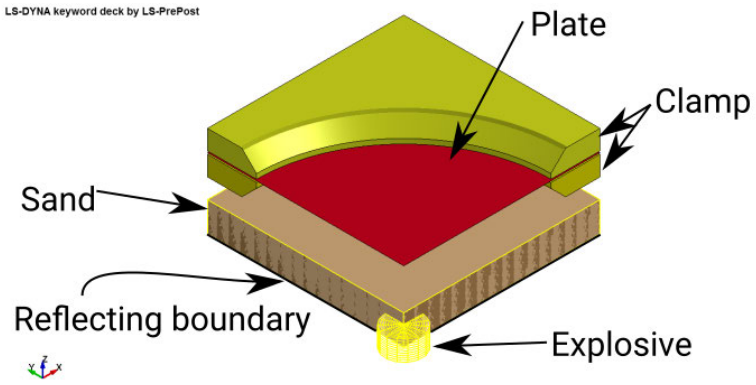

Figure 6.26: Quarter symmetry representation of the SBP numerical model.

Charge Mass	SOD (mm)	DOB (mm)	Sim δ_{Trans} (mm)	Exp δ_{Trans} (mm)	Sim δ_{Final} (mm)	Exp δ_{Final} (mm)
25	40	10	52.0	51.9	48.9	47.5
20	40	10	49.6	44.3	46.8	41.7
15	40	10	45.0	38.8	42.0	36.1
10	40	10	39.1	31.7	36.2	28.4

Table 6.9: The simulation results for the SBP series of models

The typical transient midpoint deflection values are shown in Figure 6.27 for the 20g SBP simulations and experiments overlaid. It shows the original experimental

values in blue with the experimental final midpoint deflection in the dashed lines and the simulations in black. These simulations replicate portions of the transient experimental data from the DIC, with the numerical simulation typically over estimating the plate deformation, leading to the final deformation being significantly higher than the experiments.

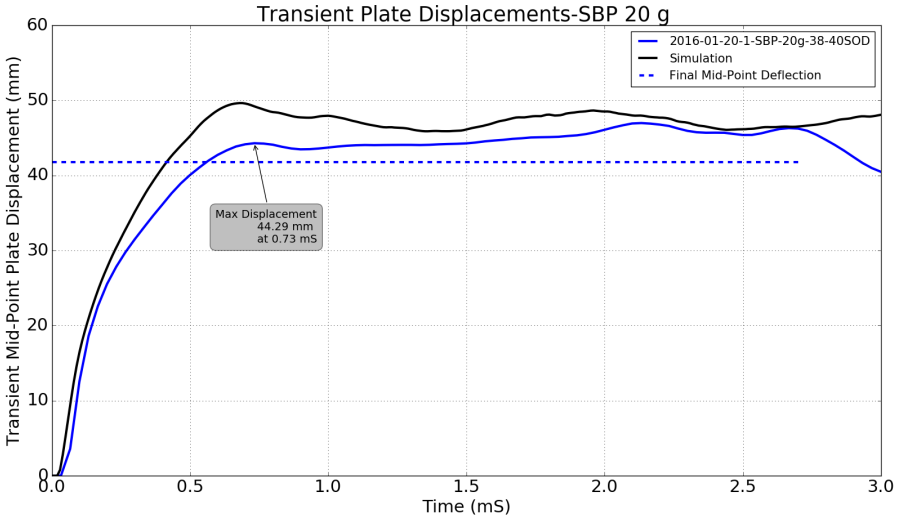

Figure 6.27: Typical transient midpoint deflection values for the SBP 20g simulations(black) and the experimental values (blue)

Figure 6.28 depicts the plastic strain in the numerical model for the SBP 20g 50mm SOD 10mm DOB simulation. This closely resembles the final deformation of the plates.

The final deformations of the plates for typical SBP 20g charge tests are shown in Figure 6.29, with the experimental plates shown in black and the simulations in green. The simulation overpredicts deflection deflection across the plate, as seen in Figure 6.29. The profile shapes were compared using the normalised plate profiles shown in Figure 6.30, (normalised to the peak midpoint deflection) which shows that there is a slight difference in shape. The experimental profiles were conical, whereas the simulation predicted that the plate would bulge beyond the conical profile. The simulation also predicts a point of inflection near to the clamp frame boundary that is not present in the experimental result.

The normalised specific impulse for the SBP 20g charge, seen in Figure 6.31, is clearly very different from the previous configurations which showed a very localised

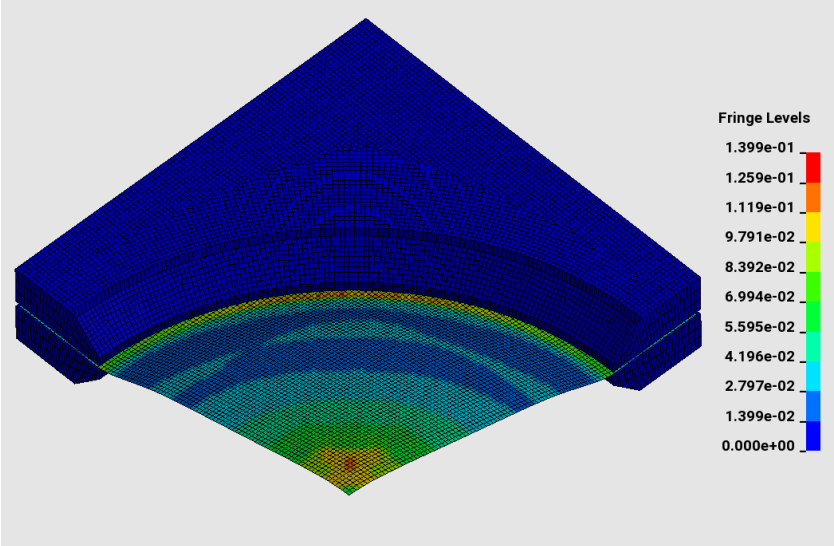

Figure 6.28: Transient plastic strain shown for the point of peak transient deflection for the SBP20g 50mm SOD 10mm DOB simulation.

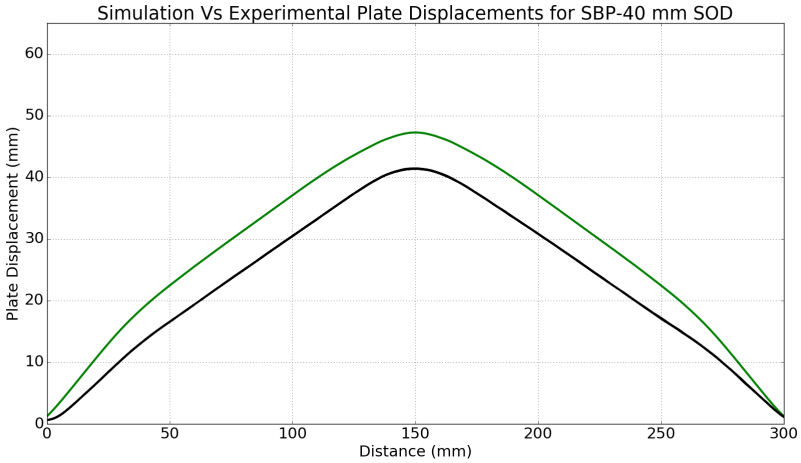

Figure 6.29: Comparison of the 20g SBP Simulations (green) and the experimental (black) final plate deformation.

impulsive loading in the central 100mm of the plate. The loading profile seen in Figure 6.31 appears discontinuous with a sharp spike in the centre and the pressure remaining constant for a central portion of the plate. Further discussion about this point can be found in Section 7.5.1.

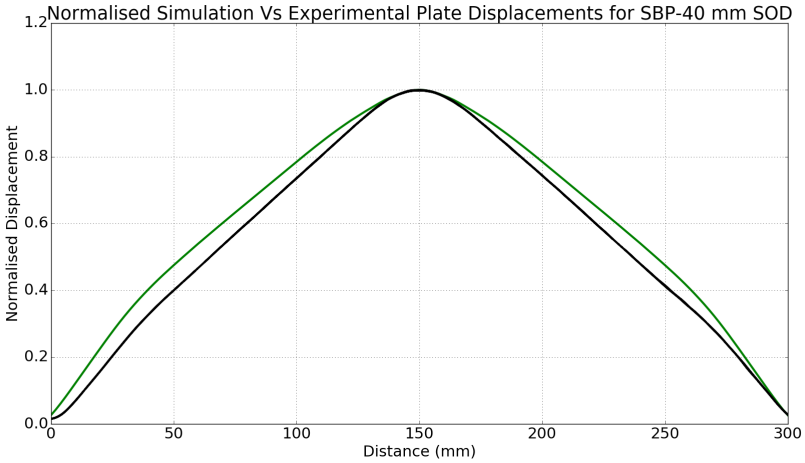

Figure 6.30: Comparison of the normalised 20g SBP Simulations (green) and the experimental (black) final plate deformation.

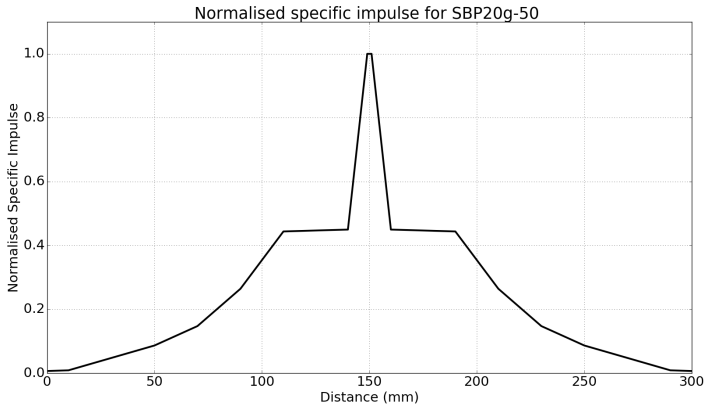

Figure 6.31: Normalised specific impulse distribution for the simulated SBP 20g test plate.

The transient plate profiles from the 20g SBP simulation is shown in Figure 6.32. The deformation profile follows the same progression outlined in the experimental section. The deformation starts at the centre of the plate and moves radially outward towards the clamp boundary. At its peak transient deformation the plate profile is almost conical in shape.

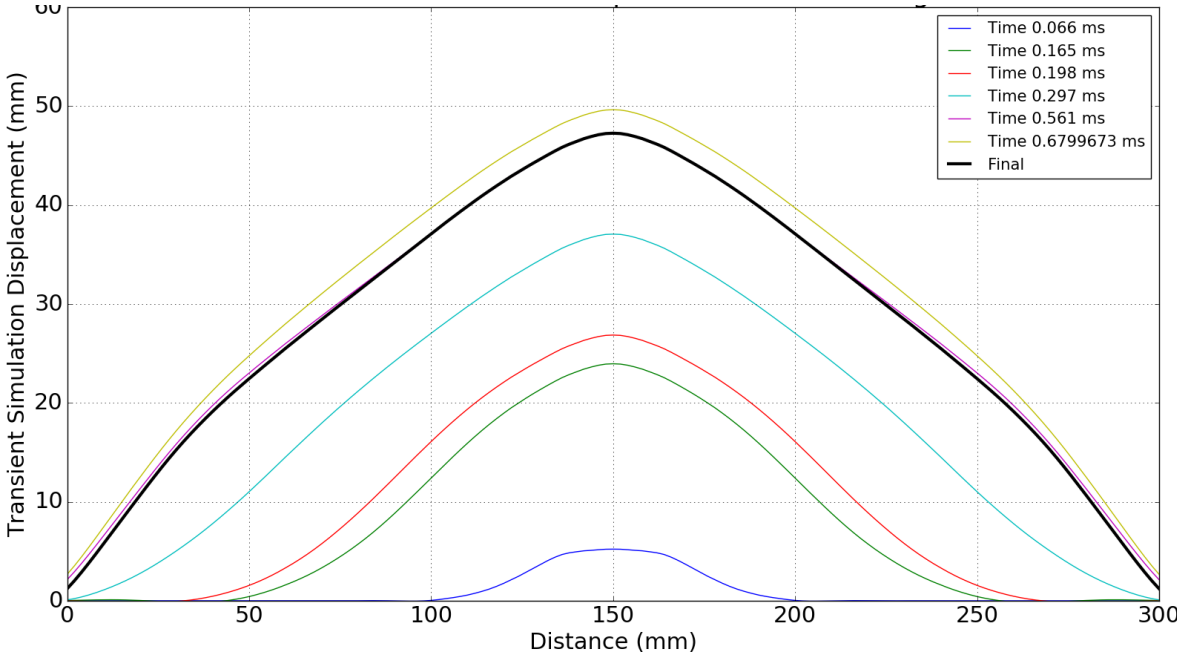

Figure 6.32: Transient plate deformation data from simulation for 20g SBP charge detonation

6.4.5 Initial plate velocity

The initial velocity of the plates in the simulations were assessed by plotting the nodal velocities along the centre line of the plate. The nodal velocities at the initial stage of the plate deformation were a direct result of the loading magnitude and distribution across the plates. The velocities for the 20g charge series are displayed in Figures 6.33 and 6.34. Each of the different charge series are represented and in Figure 6.33b the spatial velocity distribution is shown 0.08ms after detonation, when the plates individual velocities reached their maximum. In Figure 6.33a it can very clearly be seen that the velocity distribution for the AIR and VBP series are similar in shape and area which they act on. The general profile could be described as almost Gaussian in shape with the majority of the movement taking place in the central 100mm of the plate and the velocity clearly tapers off to a nominal value of zero by a diameter of 200mm. The SBP series clearly has a very different velocity profile and distribution with the general shape being almost V-like in the central 120mm of the plate and the velocity sharply dropping to a value of zero at a diameter of 120mm and then oscillating around zero towards the plate boundary.

In Figure 6.34a, at 0.13ms the velocity profiles of different charge configurations look more similar in shape than what was seen at 0.08ms. The AIR and VBP series are tightly grouped together while the SBP series has higher velocity. An almost horizontal plateau in the velocity profile exists in the central portion of the plates with the AIR and VBP series assuming an almost bi-linear decrease in the velocity profile towards the clamp boundary while the SBP decreases linearly to a zero value at a diameter of of about 240mm and then drops below zero till the clamp boundary. This indicates that in the SBP series the outer portion of the plate closest to the clamp frame has an initial velocity in the opposite direction of the central deformation of the plate which is just visible in the experimental DIC data on the 10g charge.

By 0.28ms, the velocity profiles of the AIR and VBP series are hard to distinguish in Figure 6.34a, while the velocity of the SBP series was still higher. The velocity profiles display an almost horizontal constant central section which reduces towards the clamp boundary.

It should be noted that the initial velocity profile closely resembles the shape that the plate assumes in its final deformed profile.

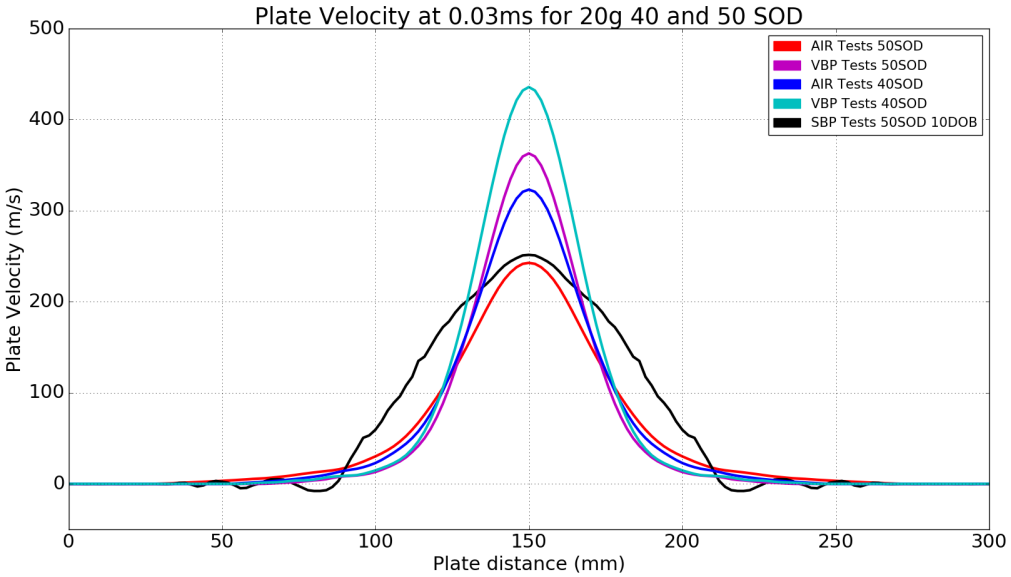

(a) Numerical Plate velocities at 0.03ms

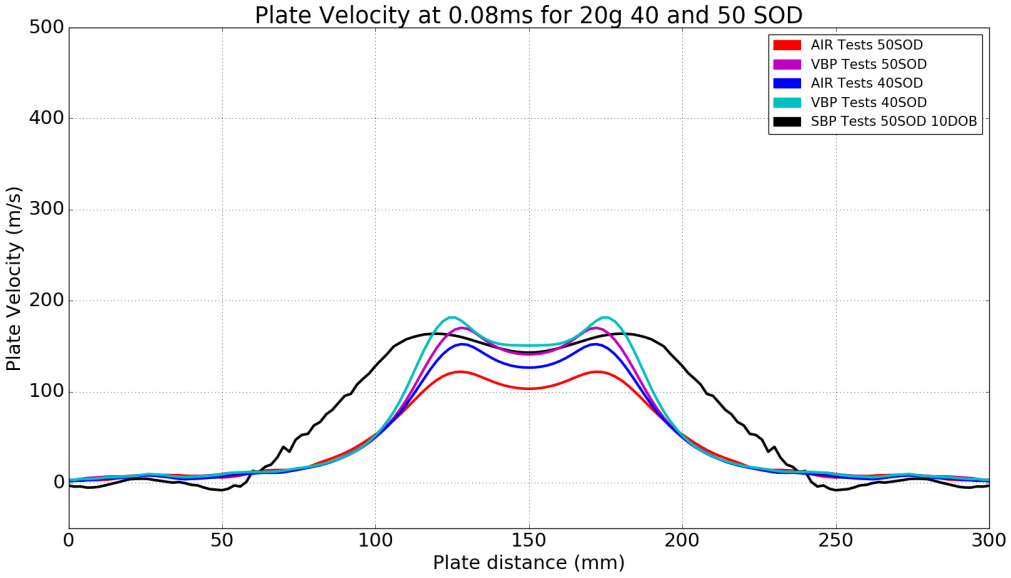

(b) Numerical Plate velocities at 0.08ms

Figure 6.33: Transient plate velocity data from simulation for 20g charge series

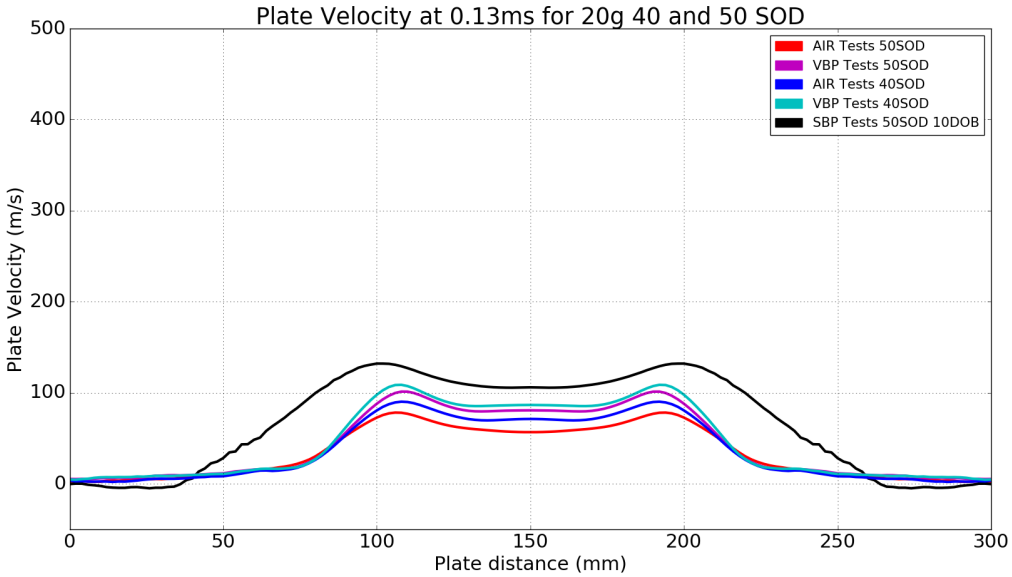

(a) Numerical Plate velocities at 0.13ms

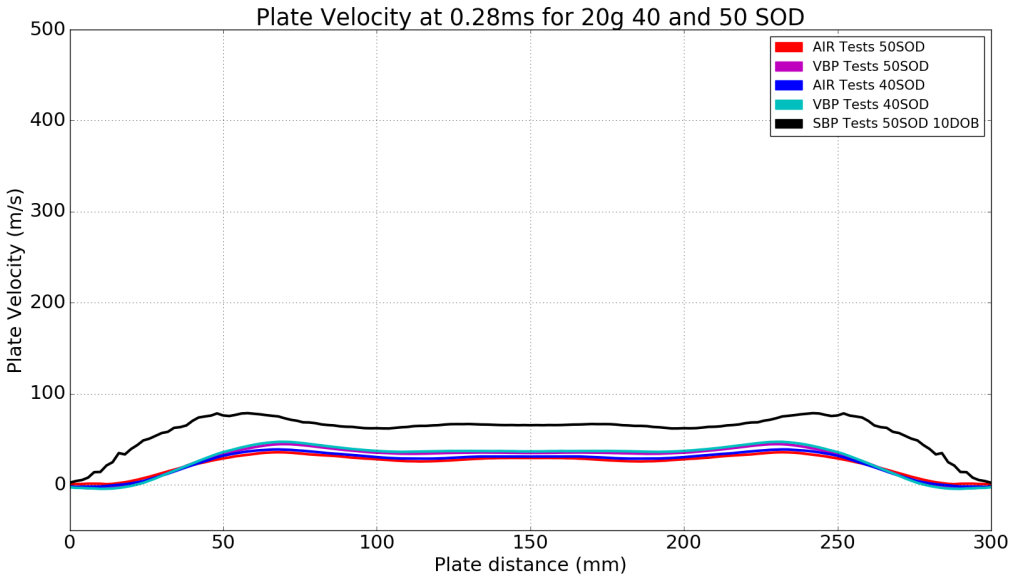

(b) Numerical Plate velocities at 0.28ms

Figure 6.34: Transient plate velocity data from simulation for 20g charge series

Chapter 7

Discussion

This chapter discusses different observations found during the course of this investigation. It starts by evaluating the validity of the experiments performed and the variations in the numerical model. Each of the three loading conditions is evaluated in order of complexity, AIR, VBP and SBP; where possible comparing the results between the different loading conditions.

7.1 Evaluation of Experiments

With every type of measurement taken, some level of uncertainty exists. The aim of this section is to compare the measurements achieved through DIC, 3D scanning and conventional mechanical measurements; this allows the repeatability of the loading conditions to be compared and the comparison of the experiments to other trends in the literature.

7.1.1 Measurement correlation

Two different types of measurements (permanent deflection and transient deflection) were made that need to be evaluated. Although transient deflection measurements are challenging to evaluate, static measurements made with DIC can be compared to 3D scans and midpoint deflections with a vernier height gauge.

Figures 7.1, 7.2 and 7.3 show the measurements from 3D scanning in color and the DIC measurement in grey for a test from each of the different experimental configurations. The final midpoint deflection measured by DIC, 3D scanning and vernier height gauge are within 0.02mm of each other, indicating a high level of repeatability

between measurement types for static deformation across all three experimental configurations.

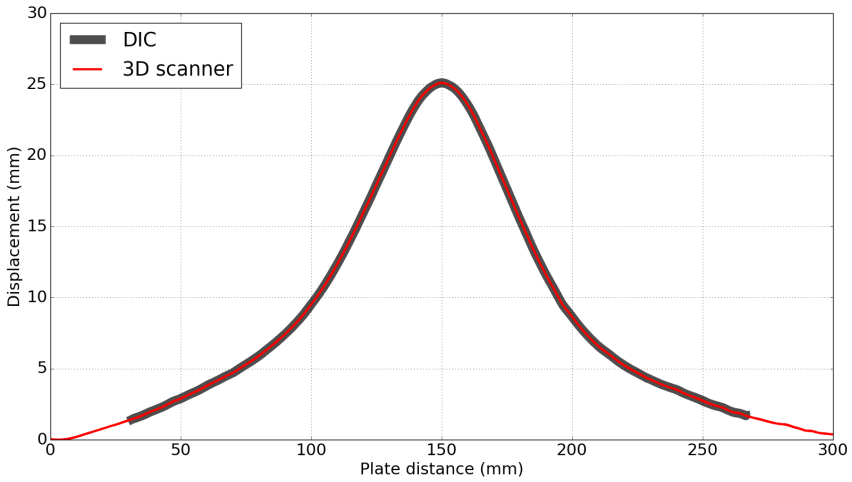

Figure 7.1: Final plate profile comparison for the 3D scanned profile (red) and the DIC measurement (gray) for a 20g AIR charge

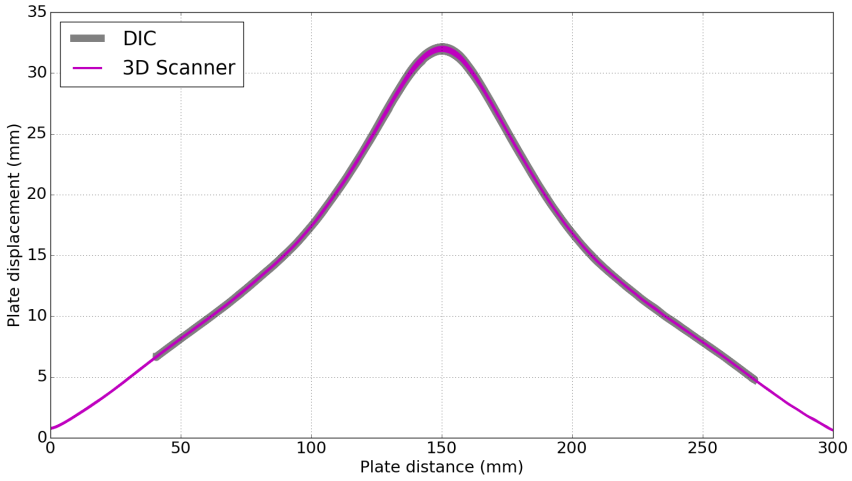

Figure 7.2: Final plate profile comparison for the 3D scanned profile (magenta) and the DIC measurement (gray) for a 25g VBP charge

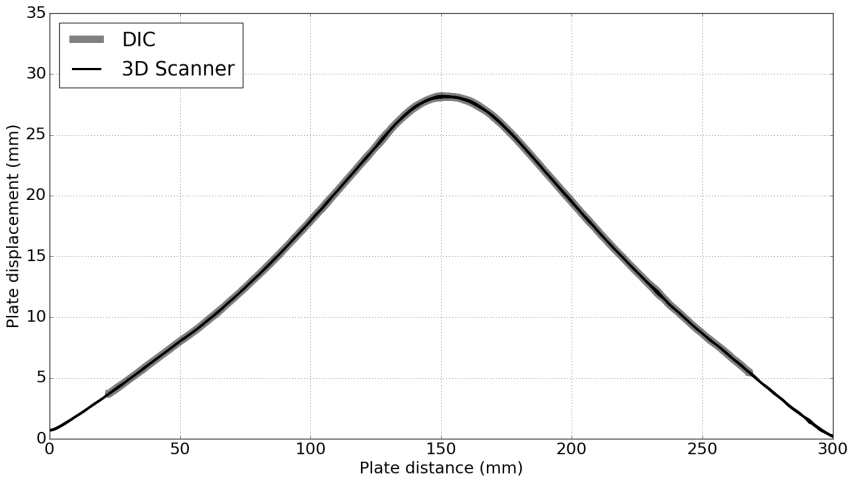

Figure 7.3: Final plate profile comparison for the 3D scanned profile (black) and the DIC measurement (gray) for a 10g SBP charge

7.1.2 Experimental repeatability

The repeatability of the experimental method appears to be very good, as seen in Figure 7.4 which shows the 15g VBP blasts at 40mm and 50mm SOD. The maximum displacement variation was exhibited in this series with an average displacement of 29.8mm for the 40mm SOD and a standard deviation of 1.8mm. The mean impulse for the 40mm SOD tests was 112Ns, with a standard deviation of 4.4 Ns. The SBP series exhibited consistently high variations in impulse reading and displacement for all charge masses indicating the loading condition had the highest variation in consistency.

The experimental loading conditions were considered repeatable with a standard deviation of $\pm$ 2 Ns for AIR, $\pm$ 9 Ns for VBP and $\pm$ 22 Ns for SBP. The midpoint deflections of the test plates varied from the experimental average by less than one plate thickness for all tests.

To check that the horizontal and vertical pendulum results were equivalent, additional tests were performed on the vertical pendulum using the same loading conditions as the AIR configuration used on the horizontal pendulum. The results are presented in Table 7.1. A very good correlation between the measured impulses on the two pendula was observed and a variance of about 2Ns was observed which is well within the experimental scatter that was observed.

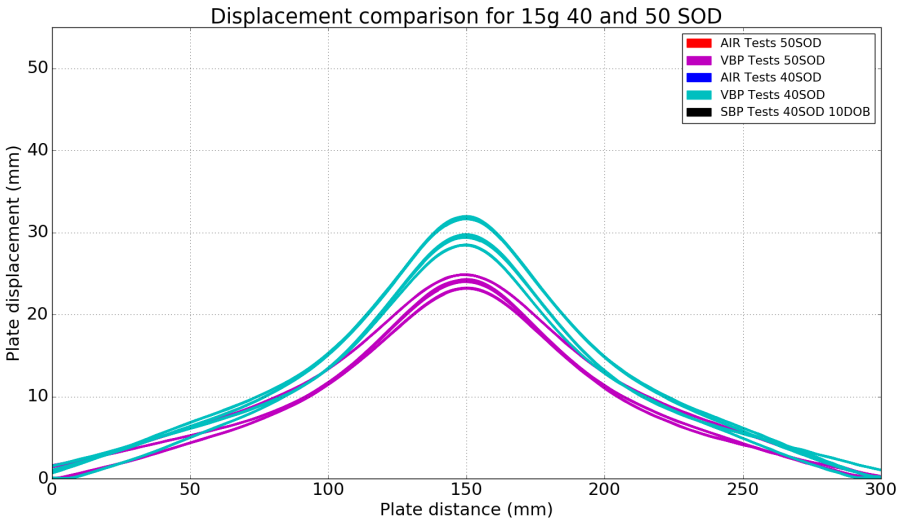

Figure 7.4: Final experimental plate profile comparison for the VBP 15g series, showing 3 tests at each SOD indicating the repeatability of the experimental method.

	Pendulum Type and impulse reading (Ns)	
Test type	Vertical	Horizontal
AIR 20g 40 SOD	33	36
	35	34
	36	34
		34
AIR 10g 40SOD	20.57	19
		18
		18
		19
		18
		17

Table 7.1: The recorded impulses for two test configuration performed on the horizontal and vertical pendulums.

7.1.3 Correlation with other work

The loading condition which has been most widely covered in the literature is the free air blast. Nurick and Martin [36,37], proposed a dimensionless impulse $\boldsymbol{\phi_c}$, which could be used to compare both uniform and localised impulsive blast loading on plates, shown in Equation 7.1:

$$\phi_c = \frac{I\left(1 + \ln \frac{R}{R_0}\right)}{\pi R H^2 \sqrt{\rho \sigma_0}} \tag{7.1}$$

Where $\boldsymbol{I}$ is Impulse, $\boldsymbol{\sigma_0}$ is static yield stress, $\boldsymbol{R}$ is the plate radius, $\boldsymbol{R_0}$ is the charge radius, $\boldsymbol{\rho}$ is the material density, $\boldsymbol{H}$ is the plate thickness. To account for the effect of stand-off distance on the plate response, a stand-off distance parameter $\boldsymbol{\zeta_s}$ was introduced:

$$\zeta_s = 1 + \ln \frac{S}{R_0} \tag{7.2}$$

Where $\boldsymbol{S}$ is the stand-off distance and $\boldsymbol{R_0}$ is the charge radius. This allows Equation 7.1 to be rewritten as:

$$\phi_{cs} = \frac{I\gamma}{\pi R H^2 \sqrt{\rho \sigma_0}} \tag{7.3}$$

Where $\boldsymbol{\gamma}$ is the new loading parameter:

$$\gamma = \frac{1 + \ln \frac{R}{R_0}}{1 + \ln \frac{S}{R_0}} \tag{7.4}$$

The resulting plot of midpoint deflection-thickness ratio versus modified dimensionless impulse is shown in Figure 7.5 for the AIR and VBP tests. The AIR (red) experiments data is similar to the data and trendline fits of Nurick and Martin [36] that is, $\frac{\delta}{H} = \mathbf{0.425}\phi_c$ [36] with the SOD modifier applied [52]. The VBP (magenta) experiments do not follow the same trend as the free air blasts but rather form their own grouping $\frac{\delta}{H} = \mathbf{0.190}\phi_c$. The dimensionless impulses are much greater for the VBP tests, as might be expected due to the reflected pressure from the metal back plate directing all the loading towards the tests plate.

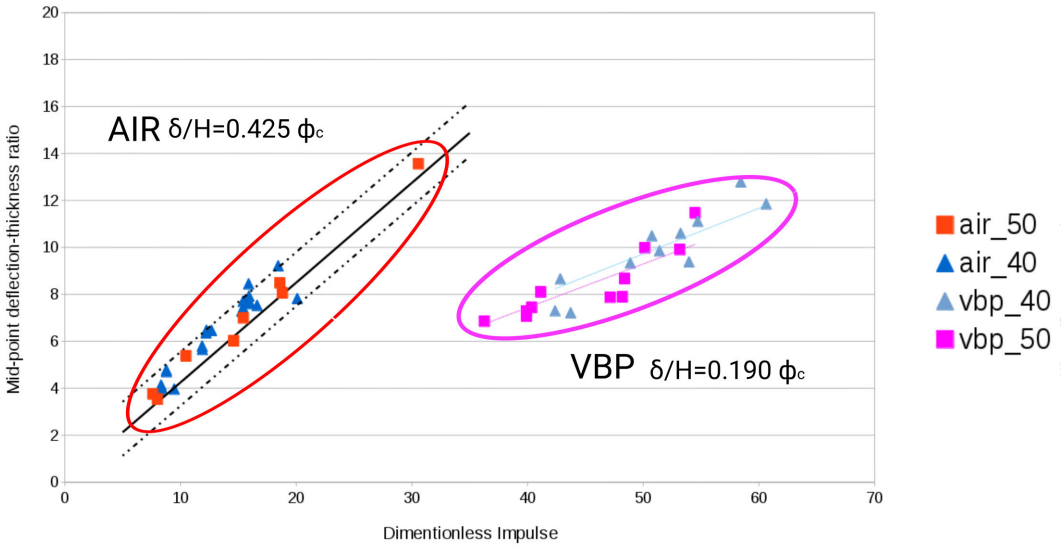

Figure 7.5: Graph of experimental measured midpoint deflection-thickness ratio versus modified dimensionless impulse ϕ_{cs}.

7.2 Numerical model validation

The numerical models were not created to exactly replicate the experimental results, which often takes many iterations and refinements to the model parameters and loading controls. Instead, these models were specifically created to provide further insights into the plate response which were not available in the experimental data. The numerical models were validated against the transient midpoint deflections available from the DIC data, in contrast to most other models which are validated using permanent deflections [21,54,56,57,64,70,71,77–80,88]. The test plate material properties had been carefully calibrated in the quasistatic and dynamic material tests and models presented in Chapter 5; no changes were made to the test plate material throughout the modelling of the different loading conditions. Additionally, numerical model control parameters such as leakage control and contact models were kept constant across these different configurations in a effort to remain consistent in the analysis.

7.2.1 Mid-point deflection

The transient midpoint deflections from the simulations are shown plotted against the transient midpoint deflections from the DIC results in Figure 7.7b. The 45°dashed line shows where an exact match would have been achieved between the simulation and experimental data, with the upper and lower bound of one plate thickness error plotted parallel. In general, the results show a good correlation between the simulation and experimental values for the transient data, however the SBP series does overpredict the deflection in the simulations. The correlation between the simulation and experimental permanent deflections in Figure 7.7a shows a slightly worse correlation than the transient data, this is believed to be due to the selection of the Johnson Cook numerical material model for the plate material.

The Johnson Cook material model artificially initiates plastic deformation earlier than observed in the quasistatic and dynamic material tests due to the power law strain hardening as shown in Figure 7.6. When the material parameters are selected for the model, the plastic hardening portion of the data in normally the focus. When the model is fitted through this portion of the data, the "A" value has to reduce to fit the data. As a result there is a small portion of the initial plastic strain in the numerical approximation that would not exist in the experimental data. Therefore a portion of the recoverable elastic energy of the experimental plate does not exist in the numerical models, meaning the simulations over predicted the permanent midpoint deformation as seen in Figure 7.7a.

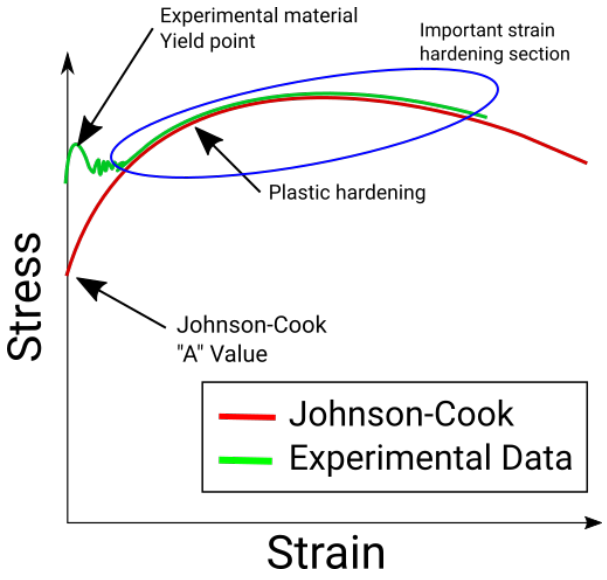

Figure 7.6: Representation of the fitting of Johnson-Cook material model (red) to the experimental data (green), showing the plastic hardening portion (blue) which is often matched.

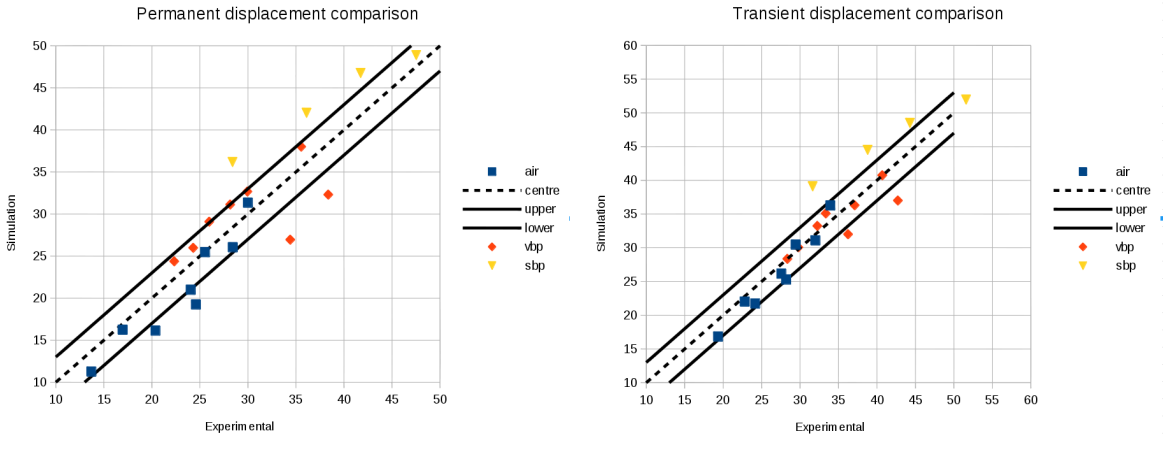

(a) Permanent displacement comparison (b) Transient displacement comparison

Figure 7.7: Graph of simulated versus experimental midpoint deflection for (a) permanent and (b) transient deflections.

7.2.2 Profile and shape

The level of agreement between the numerical and experimental work varies slightly with changes in loading. The simulations of the SBP series show the least agreement as the simulation over predicted the plate deformation by 7.8mm, shown in Figure 7.8. The normalised plate deformations show similar plate profiles even though there is a variation in the midpoint deflection, shown in Figure 7.9. Other simulations, such as the VBP 20g 50mm SOD, shown in Figure 7.10, much more accurately replicate the midpoint plate deformation and general plate profile.

The variations in the general plate shape are thought to be due to the numerical model not fully capturing the plate response, together with slight variation in the loading conditions on the numerical test plates due to the explosive detonation not being precisely captured. With this in mind, the plate profiles generally align with the experimental values, with displacement variations often deemed acceptable in experimental work.

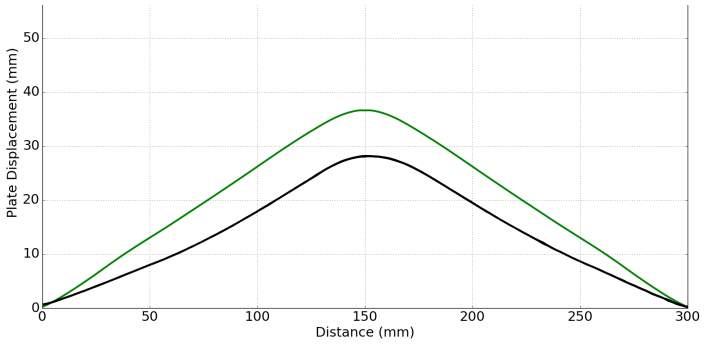

Figure 7.8: Numerical simulation (green) and experimental (black) final plate deformation profile for SBP 10g charge mass with 10mm sand overburden.

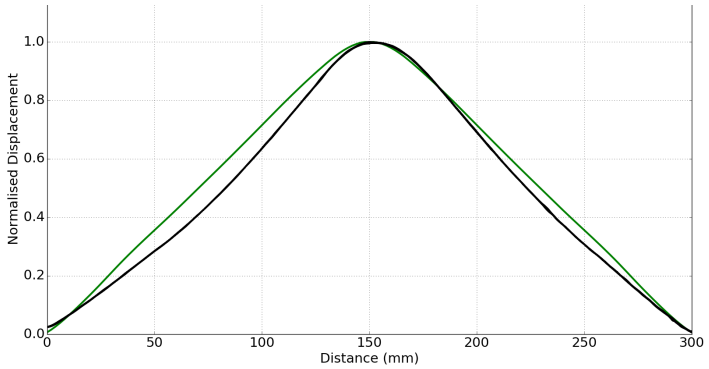

Figure 7.9: Normalised Numerical simulation (green) and experimental (black) final plate deformation profile for SBP 10g charge mass with 10mm sand overburden.

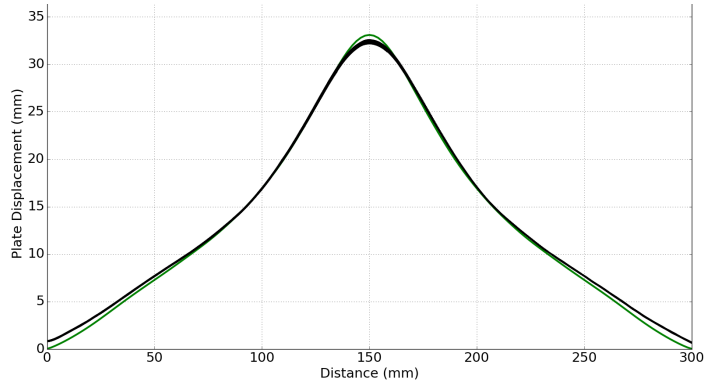

Figure 7.10: Numerical simulation (green) and experimental (black) final plate deformation profile for VBP 20g charge mass 50mm SOD.

7.2.3 Sand modelling

There is ongoing research in the blast and materials characterization community attempting to better characterise sand and its properties under blast loading. There is no "one case fits all" model available for sand and as a result models are selected according to their agreement with experimental data. In this investigation the decision was made to utilise an existing sand model from the literature and fit it to the experimental data as recommended in the literature [83]. In this process the compaction model proposed by Laine and Sandvik [75] was implemented and the density of the sand was altered until it came close to matching the experimental results. It was outside the

scope of this investigation to specifically characterise a new sand model in a similar way to the work conducted by Barr [76, 87] who completed his PhD research on the development of a sand model to more accurately characterise the dynamic loading of a specific sand. As a result, the results of the numerical models used in this investigation are not ideally calibrated to the specific sand which was used. The results seen from the numerical results here are clearly not ideal as the simulations over predict the experimental displacement predictions for the lower charge masses and under-predict the transient and final displacements for the higher charge masses. Additionally the simulations produce large instabilities in the advection methods for the MMALE which cause the simulations to stop.

7.3 Influence of SOD in AIR

In the AIR series of experiments, the cylindrical charge was detonated at two SODs with only air surrounding the charge and a small section of polystyrene supporting the back of the charge. This configuration allows for the response of the test plate to be evaluated at varying charge masses for these two SODs and determine if any significant changes were detected by interrogating the impulse and pressure distribution, initial plate velocity, transient displacements, springback, strain distribution and final plate profile.

7.3.1 Impulse and pressure distribution

Specific impulse has been used in previous investigations to infer the loading experienced by a plate [27, 29–31, 34]. These investigations typically make use of a rigid test plate with a means of measuring the pressure at different radial points from the centre to determine the pressure loading profile. In this investigation, the pressure was measured in the numerical simulation, which displays similar transient displacement behaviour to that of the experimental plate. It is important to note that these pressure measurements are not from the experimental tests but rather from the numerical work. Figure 7.11 shows an example of the specific impulse from the AIR 20g 40mm and 50mm SOD simulations, clearly showing the localisation of the loading in the 40mm SOD. A similar trend can be seen in the other charge masses with the 40mm SOD always displaying a higher central peak at the plate centre and closely matching the 50mm SOD profile closer towards the clamp frame boundary.

7.3.2 Initial plate velocity

While the specific impulse measurements are all pressure related and are susceptible to large variations and discontinuities with changes in pressure, the initial plate velocity is not because it is a measure of a continuous plate.

The initial plate velocity for the AIR 20g 40mm and 50mm SOD plates are shown in Figure 7.12, illustrating the effect that the change in SOD has on the loading conditions. The initial plate velocity is displayed at 0.03 ms which was the point at which the plate velocity reached its maximum value. In Figure 7.12, the 40mm SOD (blue) velocity has a higher central peak value than the 50mm SOD (red), but the 50mm SOD displays a

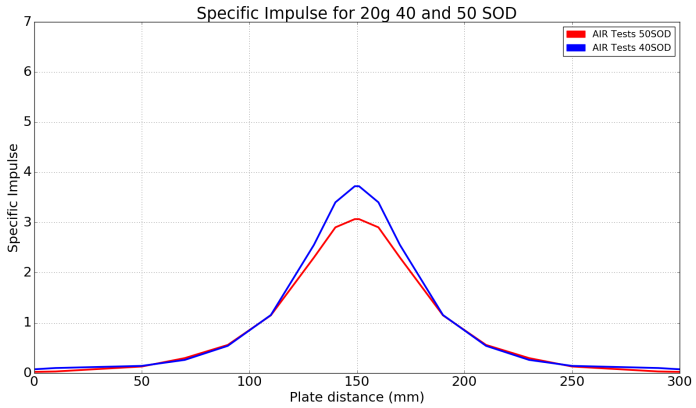

Figure 7.11: Numerical specific impulse (in MPa.ms) shown for the AIR 20g 40mm (blue) and 50mm (red) SOD blasts.

higher initial velocity for a large portion of the distance between the midpoint and the clamp boundary. This trend was observed through the entire test series, indicating that the localisation effect of decreasing the SOD had a direct influence on the central plate velocity.

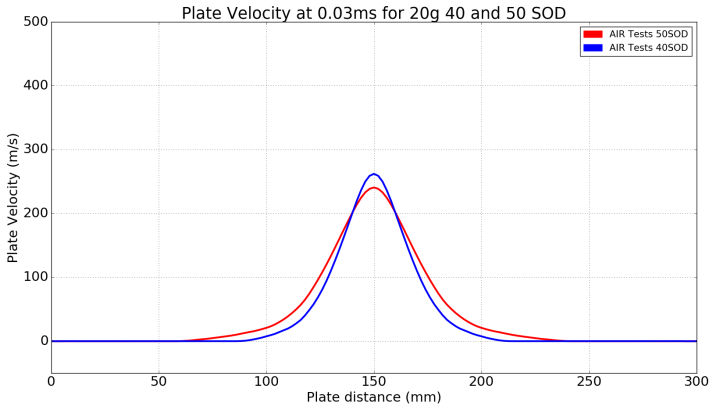

Figure 7.12: Numerical initial plate velocity for the AIR 20g 40mm (blue) and 50mm (red) SOD blasts at 0.03ms after detonation.

7.3.3 Transient displacements

Typical transient plate displacements captured by DIC are shown in Figures 4.5 - 4.8 for the AIR 20g experiments. Figures 4.5 - 4.8 show the difference in transient displacement of the plate profiles at discrete points in time. In the AIR series, the local deformation of the plates starts in the plate centre and moves radially outward towards the clamp boundary. The key difference between the 40mm and 50mm SOD is the shape produced as a result of the changes in the localised loading conditions evident in the initial velocity of the different plates. The maximum transient deformation of the plates is also visible. By tracking the midpoint of the plate, the midpoint deflection versus time curves were produced as shown in Figure 7.13. The AIR series experiments were all found to produce similar midpoint deflection versus time curves, indicating that the loading conditions resulted in similar modes of elastic oscillation.

7.3.4 Springback

As the plates displaced they deformed beyond the elastic limit of the material and plastically deform, resulting in permanent deformation. The elastic energy remaining in the plates caused them to elastically springback once the loading was over, producing oscillations shown in Figure 7.13. The initial phase of the deformation, seen in Figure 7.13, from 0 - 0.7 ms, was the plastic deformation up to maximum transient deformation. From 0.7 ms onwards, the AIR series plates were found to oscillate elastically and eventually settle to the final plate profile as the elastic energy was dissipated. The elastic springback from the peak transient deflection of the plates in the AIR series was noted to decrease slightly with an increase in charge mass and permanent deflection.

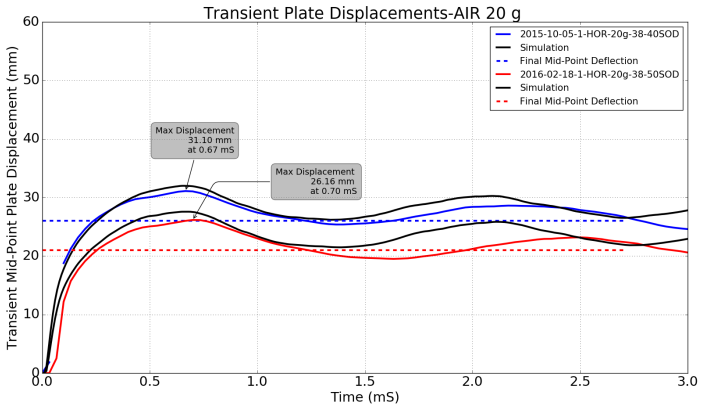

Figure 7.13: Transient midpoint deflection for the AIR 20g 40mm and 50mm SOD experiments

7.3.5 Strain distribution

The strain distribution in the experimental plates was found to be fairly consistent after 0.03 ms, as can be seen in Appendix A. The typical strain in the AIR series plates, shown in Figure 7.14, was similar in shape but varied in magnitude, particularly at the plate centre.

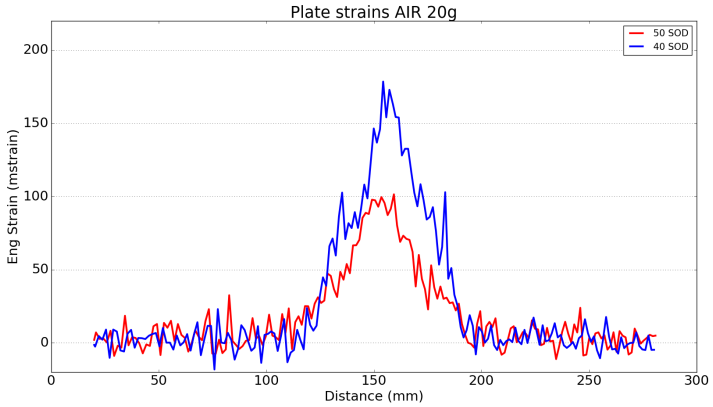

Figure 7.14: Transient strain distribution for the AIR 20g 40mm and 50mm SOD experiments at 0.7 ms.

7.4 Influence of metal back plate

In the VBP series of experiments, the cylindrical charge was detonated at two SOD's with a rigid metal plate directly behind the charge. The metal backplate was introduced to control the effect of the medium below the charge in the buried charge configuration (SBP). This improved repeatability of the testing as conditions below the charge remained constant throughout the testing. A form of this testing is recommended in the NATO AEP-55 [17] standards for testing of vehicles exposed to mine blasts, where the charge is placed on a thick metal plate with a recess for the charge, but without the overburden of sand. The flat metal backing plate was first used in this form by Pickering *et al* [26] for the same reasons, however no direct comparison to free air blast testing was available.

In light of this, the metal back plate (VBP) charge configuration was investigated to provide similar uniform boundary conditions below the charge that would be found in the buried charge (SBP), but without the overburden of sand. This configuration allows for the response of the test plate to be evaluated at varying charge masses for these two SOD's and determine if any significant changes were detected as a result of the metal back plate by interrogating the impulse and pressure distribution, initial plate velocity, transient displacements, springback, strain distribution and final plate profile. This configuration was specifically selected because it is similar to the buried charge configuration without the overburden of sand on the charge.

7.4.1 Impulse and pressure distribution

As mentioned previously, specific impulse has been used in previous investigations to infer the loading experienced by a plate [27,29–31,34]. Many previous investigations use the specific impulse to measure effects of changes in loading conditions on structures, but no previous literature was found to investigate the effect of a metal backplate on the loading and response of a test plate.

The numerical model pressure readings, shown in Figure 7.15 at discrete tracer points, were used to calculate the specific impulse by integrating the pressure-time at the tracer points. Figure 7.16 shows an example of the specific impulse distribution across the test plate for the VBP 20g simulations at 40mm and 50mm SOD. The 40mm SOD displays a higher central specific impulse, which decreases to a similar value to that of the 50mm SOD tests towards the clamp boundary. There is a visible rise in

the 40mm SOD specific impulse at the clamp boundary, which is not present in the 50mm SOD results, indicating that a small pressure build up at the clamp boundary as described by Bonorchis [38], could be occurring. The specific impulse is similar in shape to that of the AIR series but higher in magnitude, particularly toward the clamp boundary, indicating that an overall higher impulse was imparted on the VBP series for the same charge mass.

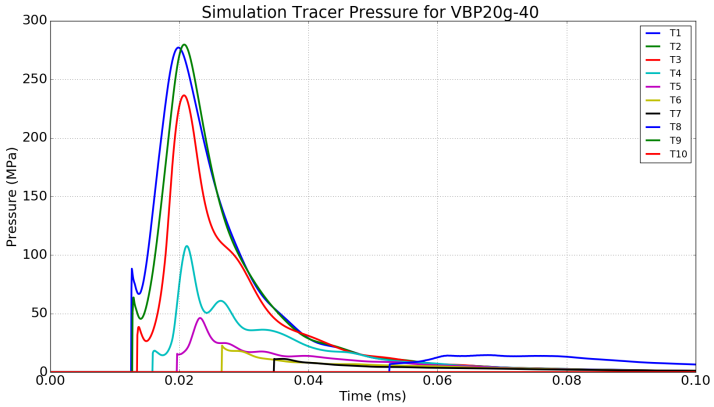

Figure 7.15: Specific pressure-time graph for VBP 20g 40mm SOD blast simulation

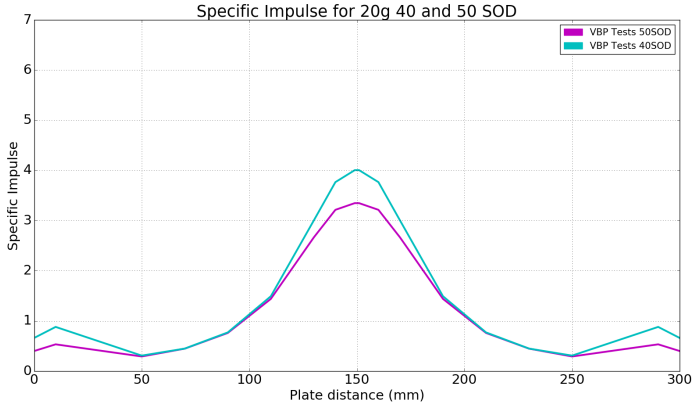

Figure 7.16: Specific impulse distribution for VBP 20g 40mm and 50mm SOD blast simulations.

The comparison of the different experimental charge impulses seen in Figure 7.17 shows that there is a clear correlation visible between the AIR and VBP charge configurations which appears to be proportional to the charge mass and SOD.

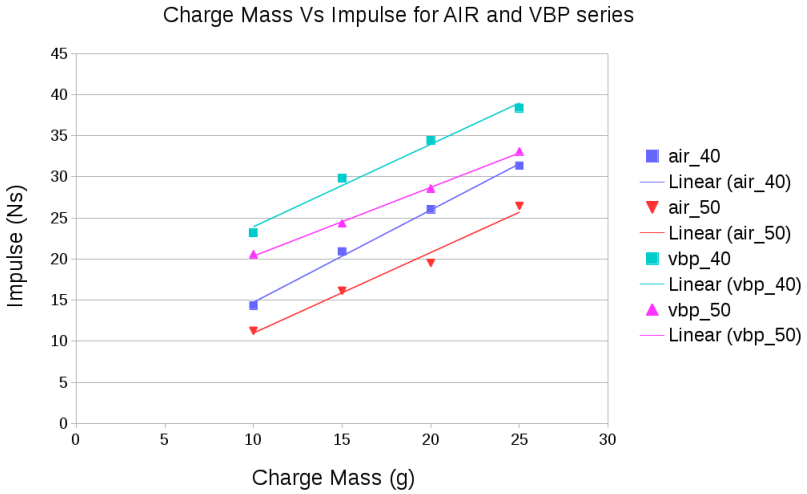

Figure 7.17: Comparison of AIR and VBP series experimental impulses for the different charge masses.

7.4.2 Initial plate velocity

The initial plate velocity for the VBP 20g 40mm and 50mm SOD plates are shown in Figure 7.18, illustrating the effect the change in SOD has on the loading conditions for the VBP 20g charges. The initial plate velocity is displayed at 0.03 ms, shown in Figure 7.18. The 40mm SOD (blue) velocity had a higher central peak value than the 50mm SOD (red), with both velocities decreasing to nominally zero at a diameter of about 100mm. This trend was observed through the entire test series, indicating that the localisation effect of decreasing the SOD had a direct influence on the central plate velocity. When comparing the initial plate velocity to that of the AIR series shown in Figure 7.19, the similarities in the velocity profiles between the two loading conditions indicate the while the focusing effect of the backplate causes a much higher initial central velocity, the initial profiles are similar.

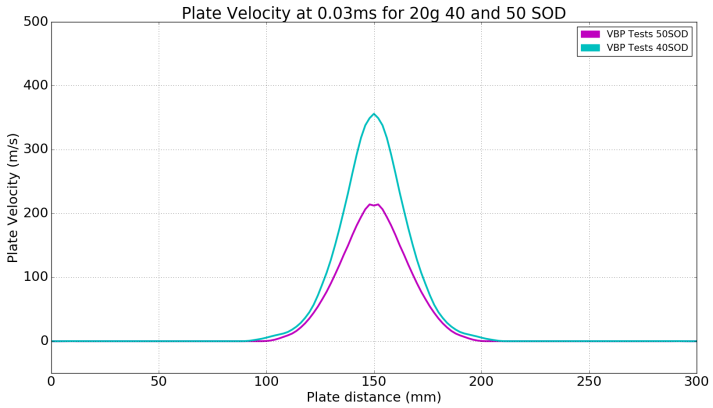

Figure 7.18: Experimental initial plate velocity for the VBP 20g 40mm (cyan) and 50mm (magenta) SOD blasts at 0.03ms after detonation.

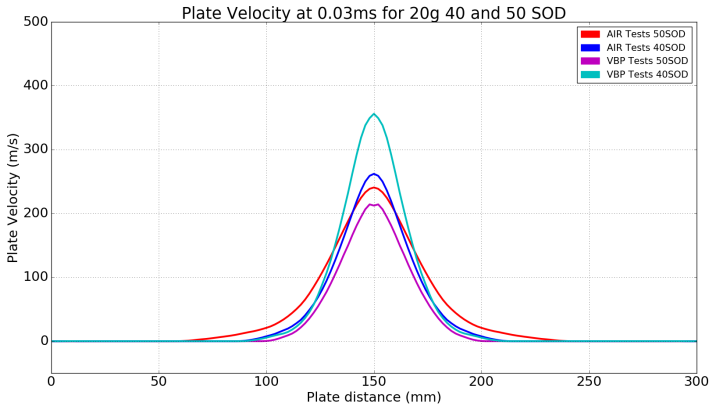

Figure 7.19: Experimental initial plate velocity comparison for the AIR and VBP 20g blasts at 0.03ms after detonation.

7.4.3 Transient displacements

The transient plate displacements for the VBP 20g 40mm and 50mm SOD tests, which are representative of the results seen for the remaining charge masses in the series, are shown in Figures 4.15 - 4.18. The evolution of the deformation profiles is similar to that of the AIR series of experiments. In the 40mm and 50mm SOD tests, the deformation starts centrally and moves radially outward toward the clamp boundary. The plate

profile has a larger transient maximum displacement than the final deformation of the plates, with the springback of the plates being similar to the AIR series.

A comparison of the transient midpoint deflection versus time graphs for the 20g 50mm SOD AIR and VBP tests is shown in Figure 7.20. The similarity in the response of these plate under two different loading conditions can clearly be seen for the same SOD. The midpoint on the VBP test does not rebound below the permanent deformation (red dashed line) in the first 2 ms as it does in the AIR test. This was consistently observed through VBP series.

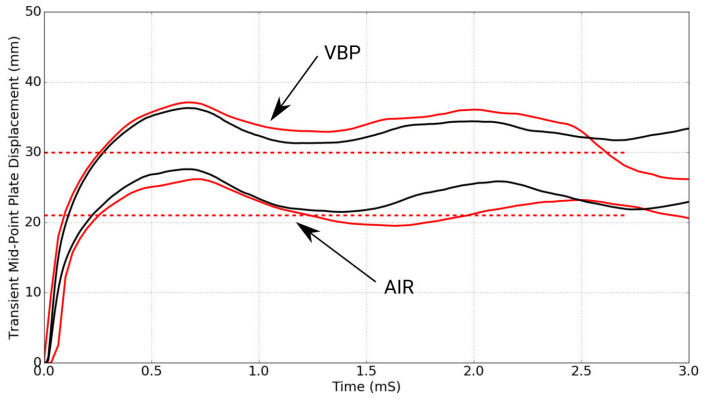

Figure 7.20: Transient midpoint deflection for the AIR and VBP 20g 50mm SOD experimental (red) and simulated (black) values.

7.4.4 Strain distribution

The strain distribution in the experimental plates was found to be fairly consistent after 0.03 ms as can be seen in Appendix A. The typical strain in the VBP series plates, shown in Figure 7.21 for the 20g VBP tests, was similar in shape but varied in magnitude specifically in the plate centre. The influence of SOD was less significant in the VBP tests than in the AIR results.

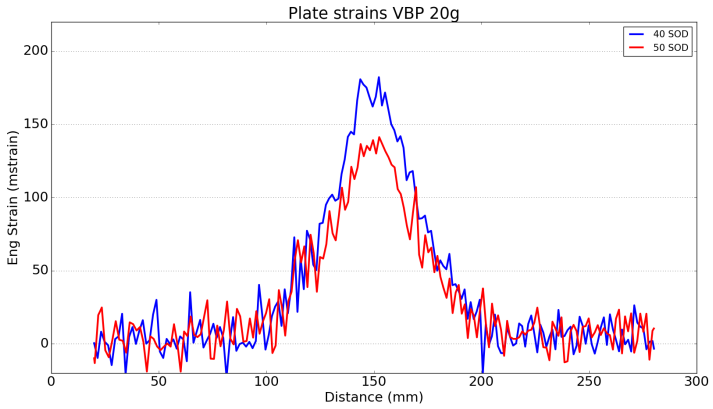

Figure 7.21: Transient strain distribution for the VBP 20g 40mm and 50mm SOD experiments.

7.4.5 Final deformed shape

The effect of the back plate can most clearly be evaluated by looking at the deformation profile of the AIR and VBP series charge masses on the same plot seen in Figure 7.22. There is a significant change in midpoint deflection with the addition of the back plate, seen in Table 7.2. The increase in midpoint deflection increases by between 7 - 9mm. The effect of the metal backing plate on the loading of the test plates focused the loading of the charge and increased the impulse transfer to the plate. The normalised deflections in Figure7.22 shows how similar the profiles are. The two VBP tests (cyan and magenta) lie almost on top of one another, while the two AIR tests (blue and red) exhibit slightly different profiles with the AIR 50mm SOD tests more closely resembling the profile of the VBP tests.

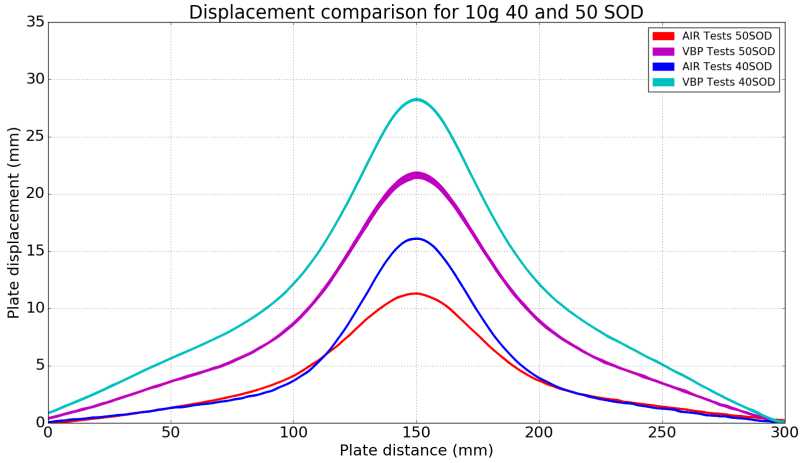

(a) Experimental displacement comparison

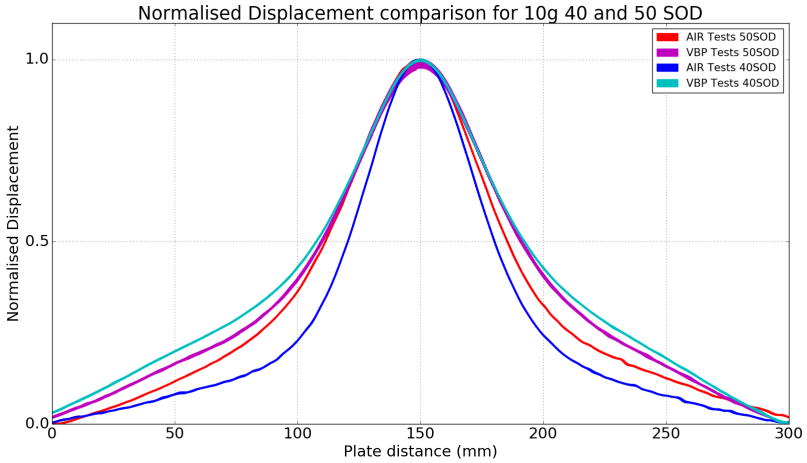

(b) Normalised displacement comparison

Figure 7.22: Comparison of 10g charges for AIR and VBP series experiments (a) displacement and (b) normalised displacements.

Charge mass	**SOD**	**Midpoint displacement (mm)**		**Difference**
(g)	(mm)	**AIR**	**VBP**	(mm)
25	40	31.34	38.37	7.0
20	40	26.04	34.44	8.4
15	40	20.91	29.80	8.9
10	40	14.33	23.20	8.9
25	50	26.46	33.08	6.7
20	50	19.52	28.56	9.0
15	50	16.13	24.31	8.2
10	50	11.26	20.56	9.3

Table 7.2: Table of average midpoint deflections for AIR and VBP series.

7.5 Influence of sand

In the SBP series of experiments, the buried cylindrical charge was detonated at only one SOD from the test plate. This configuration allows for the response of the test plate to be evaluated at varying charge masses and contrasted with the VBP configuration to determine if any significant changes were detected by interrogating the impulse and pressure distribution, initial plate velocity, transient displacements, springback, strain distribution and final plate profile.

7.5.1 Impulse and pressure distribution

The specific pressure measurements at tracer points in the numerical model for the SBP 20g results are shown in Figure 7.23 which were used to calculate the specific impulse distribution in Figure 7.24. Large variations in pressure were observed across the plate profile causing the large discontinuities in specific impulse shown in Figure 7.24. These discontinuities were noted in previous work [88] which looked specifically at the pressure distribution in buried charge experiments.

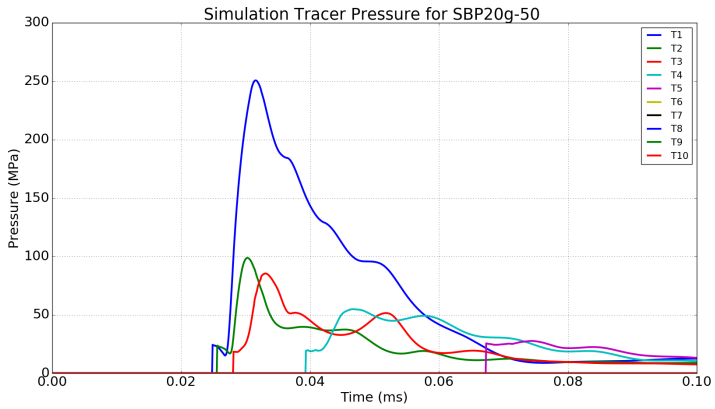

Figure 7.23: Specific pressure-time graph for SBP 20g 50mm SOD blast simulation

By comparing the experimental impulses of the VBP 50mm SOD and the SBP loading conditions directly, we can deduce the impact the sand has on the impulsive loading of the the test plate. Increases in the impulse can be seen in Table 7.3, increasing with charge mass, from 19% for 10g, up to 100 % for the 25g detonations.

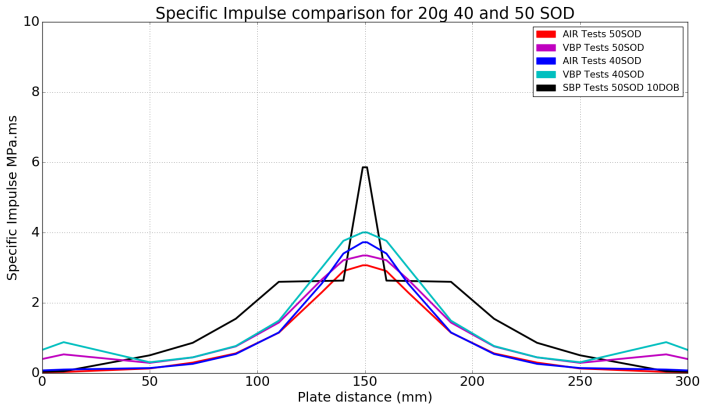

Figure 7.24: Comparison of numerical specific impulse distribution for all loading conditions.

Charge Mass	SOD	Impulse (Ns)		Difference
(g)	(mm)	VBP	SBP	(Ns)
25	50	120	243	123
20	50	110	200	90
15	50	91	150	59
10	50	88	105	17

Table 7.3: Comparison of the impulses between VBP 50SOD and SBP loading configurations

7.5.2 Initial plate velocity

When comparing the transient plate deformation in the three different charge configurations, the different loading conditions displayed slightly different responses. In the AIR configuration and the VBP series, the responses are similar in profile but vary in magnitude. The focusing effect of the VBP configuration increased the loading in the centre of the plate which was evident in the specific impulse and velocity distribution. This resulted in causing an increase in the deformation for the same charge mass when comparing the AIR and VBP configurations, however the evolution of the profiles were similar. The VBP series has a loading profile with a higher central loading than the AIR series, which, counter-intuitively, leads to a less localised normalised deflection. As

the deformation increases, the point of inflection observed in the AIR and VBP profiles at a diameter of approximately 100mm, became less pronounced.

The profile evolution of the SBP series originated in the centre of the plate and moved radially outward, toward the clamp boundary. The difference could most clearly be seen by looking at the velocity distribution of the plates which is shown in Figure 7.25 containing the 20g charge simulation for each configuration. In Figure 7.25 the SBP initial velocity, shown in black, displays a fundamentally different profile to the other loading conditions, even including a small negative velocity around the central 150mm diameter. These small negative displacements were detected and reported in the DIC results for these experiments, confirming the observation from the simulations.

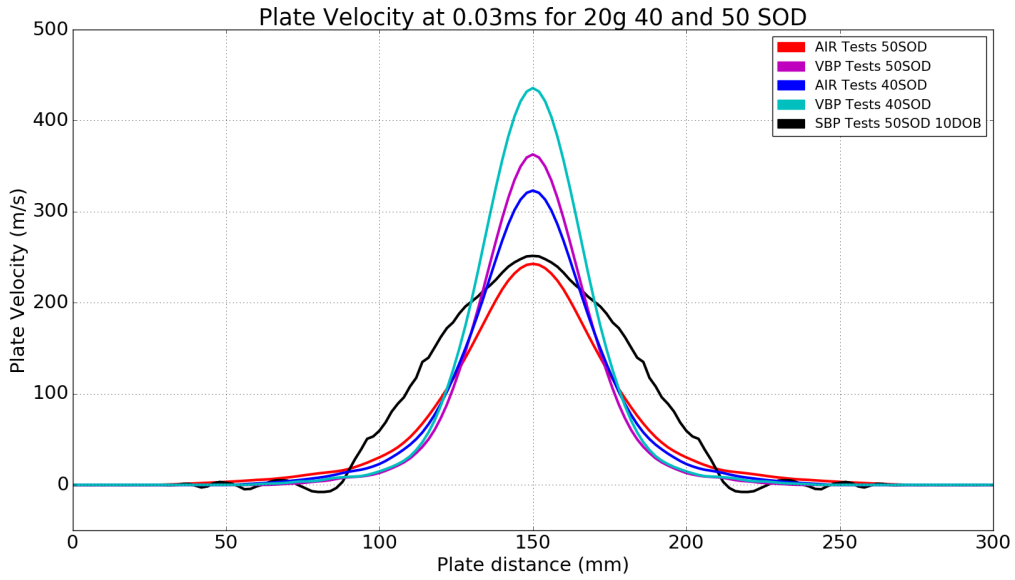

Figure 7.25: Transient plate velocity data from simulation for 20g charge series

7.5.3 Transient displacements

The transient plate displacements for the SBP 20g 50mm SOD test, which was representative of the results observed for the remaining charge masses in the series, are shown in Figure 7.26. The evolution of the deformation profiles are similar to that of the other series, the deformation started centrally and moved radially outward, toward the clamp boundary. The shape of the deformation for the SBP series is significantly

different from the AIR and VBP series. The transient plate profile displays a maximum displacement that is larger than the final deformation of the plates. Up to this maximum deflection the profile does not match the shape of the final deformed plate.

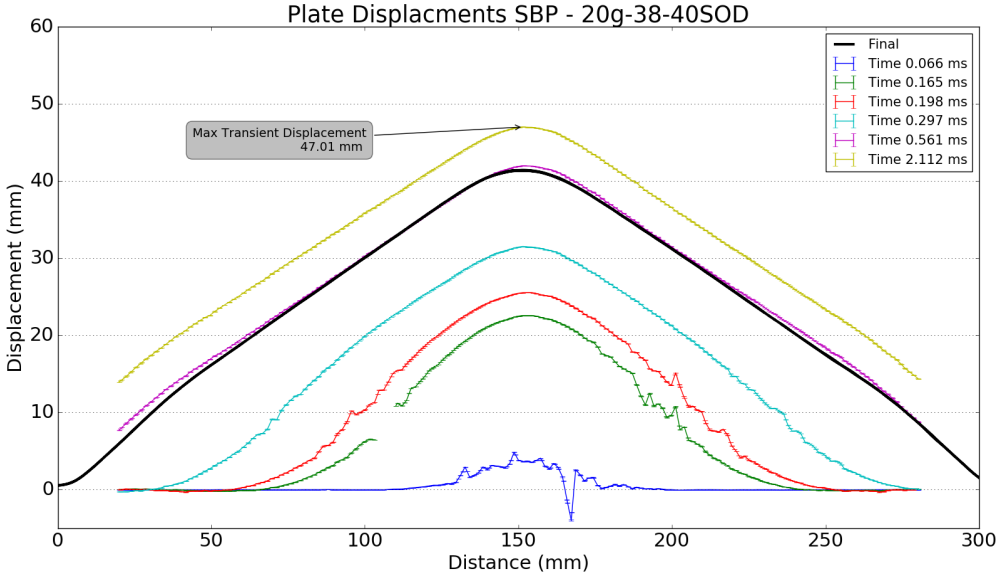

Figure 7.26: Experimental transient plate displacement data for SBP 20g test.

7.5.4 Springback

The exact measure of the springback in the SBP plates proved challenging to define as the point in time at which to measure the displacements is uncertain. In the typical tests of the AIR and VBP series, the point of maximum transient deformation was clearly defined and usually located around 0.7ms after detonation. The displacement profiles of the midpoint for the SBP series, shown in Figure 7.27, had an initial peak at around the same point of 0.7 ms after detonation, but exhibited a plateau for almost 2ms where the midpoint deflected slightly more (typically 2mm). This point changed for different tests, indicating that there is an extended loading on the back-face of the plate that varied with charge mass. This prevented the plate from oscillating around the permanent deformation as seen in the AIR and VBP series. This plateau differed between tests and was not found to be uniform or extremely repeatable, confirming author's reports in the literature describing variability in buried charge testing [26, 88].

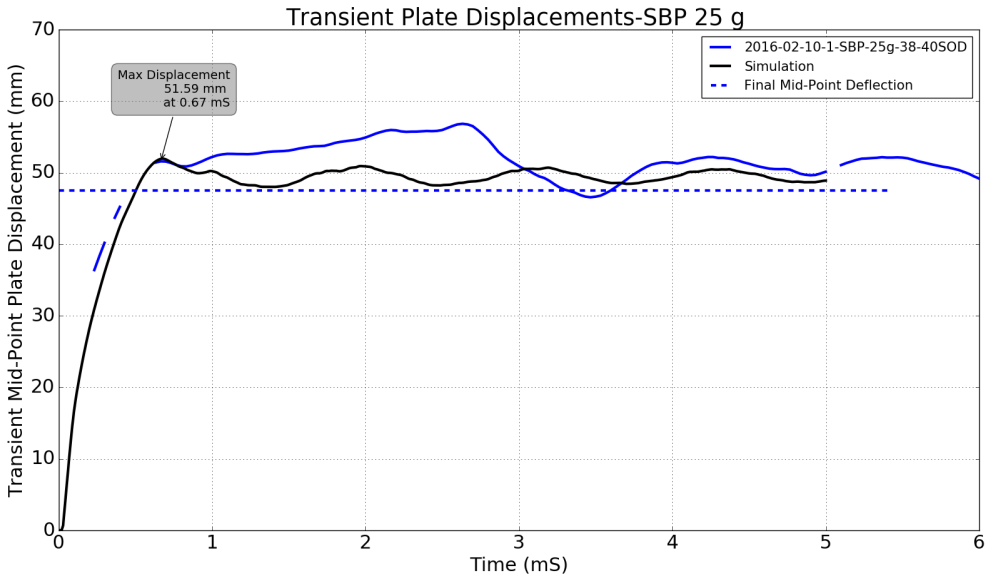

Figure 7.27: Transient midpoint deflection for the SBP 20g 50mm SOD experiment.

7.5.5 Strain distribution

The transient strain reported in the experimental results section, remained nominally constant after 33 $\boldsymbol{\mu s}$ in each of the charge configurations. This was consistently observed in all DIC results shown in Appendix A.1 - A.3 and a representative plot of the strain distribution for the SBP 20g test is shown in Figure 7.28. Interestingly, the transient strain captured in the SBP series displayed a plastic wave which moved radially toward the clamp frame, which agreed with the numerical simulation that suggested there was a radial deformation wave at the edge of the moving plastic hinge.

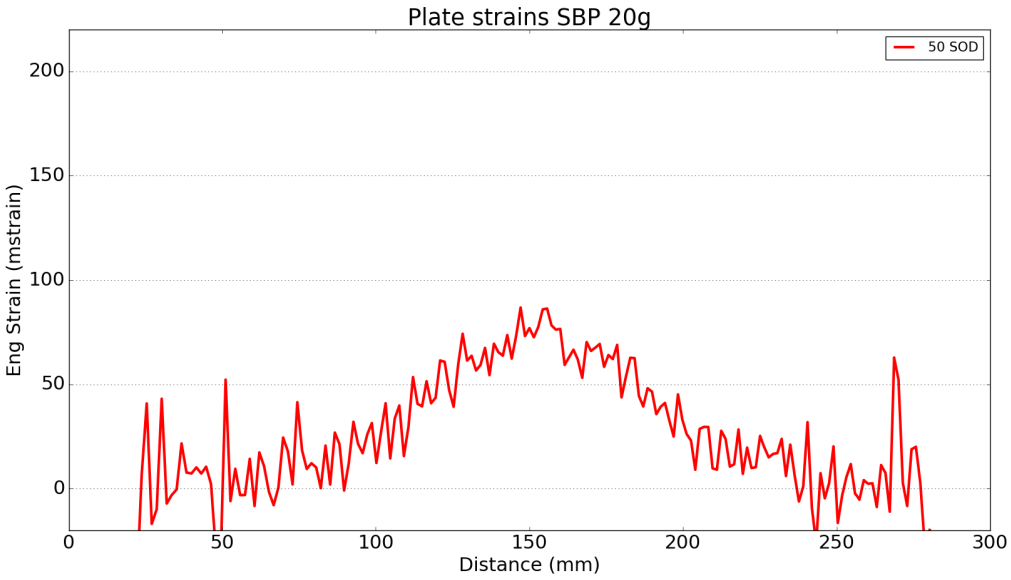

Figure 7.28: Transient strain distribution for the SBP 20g 50mm SOD experiment.

7.5.6 Final deformed shape

The normalised displacement profiles of 58 individual plates across the three loading conditions are shown in Figures 7.29 and 7.30 for the 40mm and 50mm SOD respectively. Very clear groupings of the different loading conditions are shown in Figure 7.30, where the grouping of the AIR (red) and VBP (magenta) series overlap while the SBP (black) series which displays a different displacement profile.

If the scatter in the individual series loading conditions due to the changes in charge height are taken into consideration, the bands which the normalised profiles form are considered acceptable. These bands correlate with the experimental and simulation results showing that the specific impulse and initial velocity profiles of the plates indicate that the loading conditions created by the addition of a 10mm overburden of sand created a fundamentally different loading condition with a unique deformation profile. In each loading condition the transient and final deformation profiles appear to be strongly driven by the initial velocity profile of the test plates.

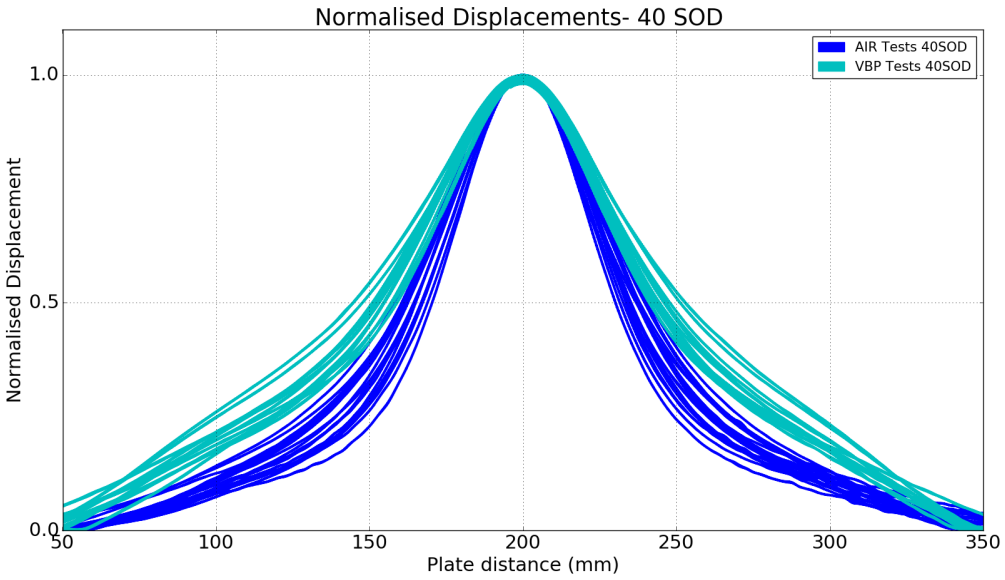

Figure 7.29: Normalised plate displacements for all 40 SOD plate tests.

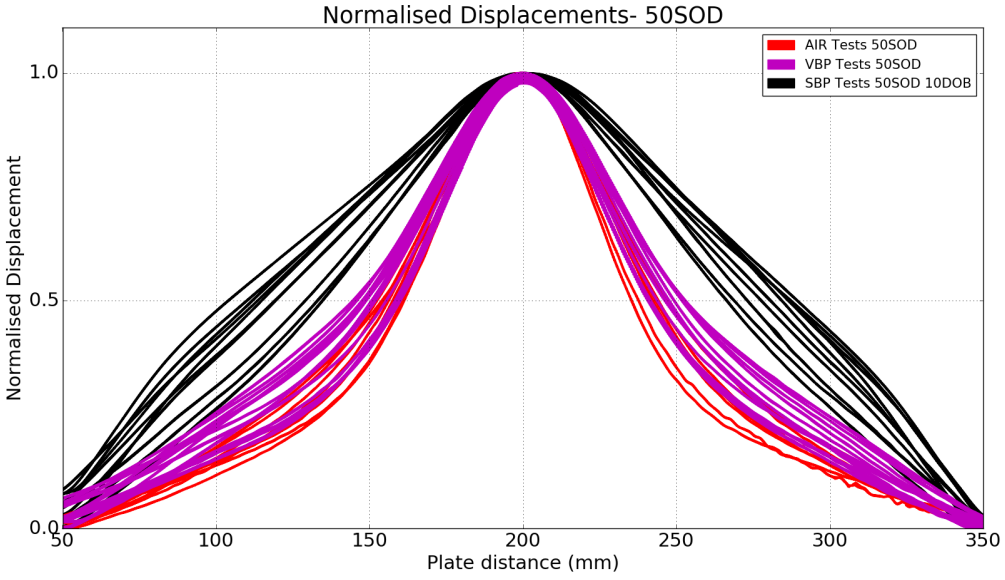

Figure 7.30: Normalised plate displacements for all 50 SOD plate tests.

7.6 Charge mass effects

Across all three series of experiments (AIR, VBP and SBP) an increase in charge mass resulted in an increased impulse being recorded by the blast pendulum and an increased midpoint deflection. This trend was mirrored in the simulations, but the results display an element of scatter in the experimental results.

As the charge diameter was constant, as the charge mass was increased by changing the aspect ratio (charge height to diameter). According to Kennedy [13], the axial impulse transfer from a cylindrical charge originates from a cone with a 60°included angle and the remaining charge contributes to the "side losses" as shown in Figure 2.3 in Chapter 2. This is most obviously seen in the AIR test series where the increase in charge mass results in a less localised deformation profile as more of the charge contributes to side losses discussed in [13], shown in Figures 7.31 and 7.32. This indicated that as the charge mass increased, there was an increase in the specific impulse radially.

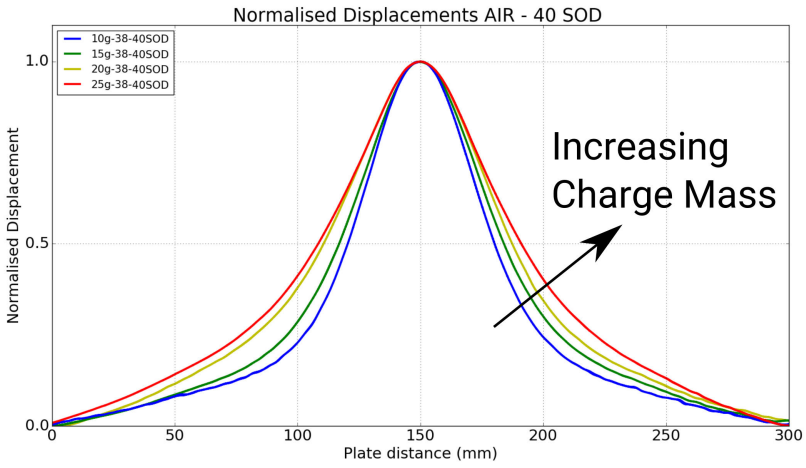

Figure 7.31: Normalised final plate displacement profile showing representative profiles for each of the AIR 40 SOD charge masses.

This phenomenon was also observed in the VBP and SBP series seen in Figure 7.33-7.35 with the metal back plate and buried charge configurations.

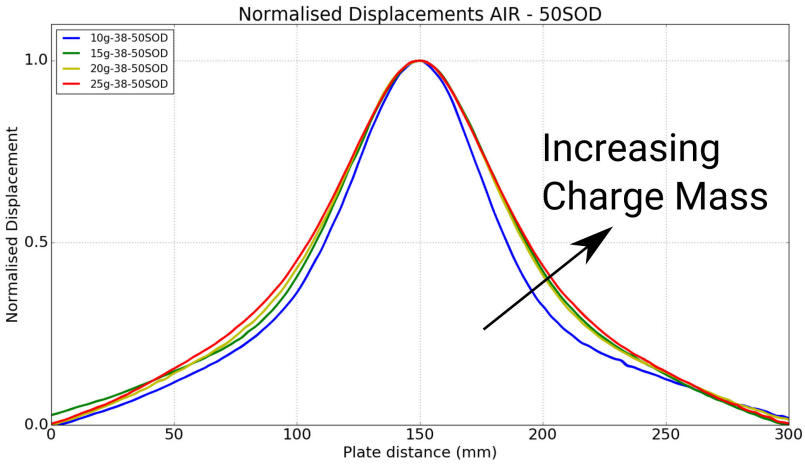

Figure 7.32: Normalised final plate displacement profile showing representative profiles for each of the AIR 50 SOD charge masses.

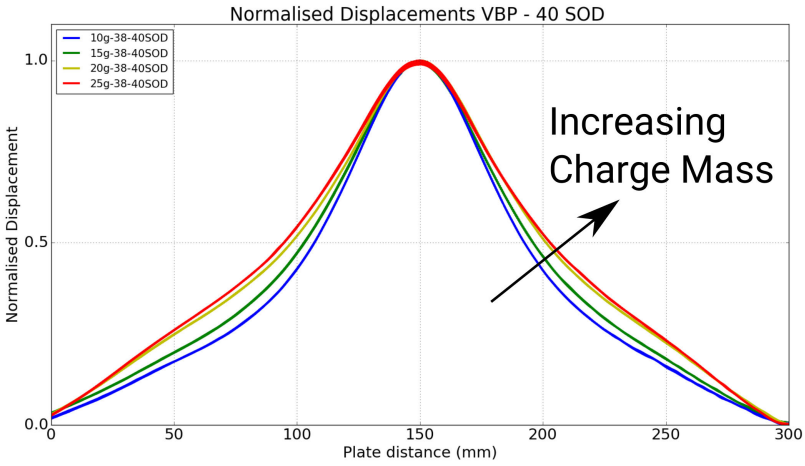

Figure 7.33: Normalised final plate displacement profile showing representative profiles for each of the VBP 40 SOD charge masses.

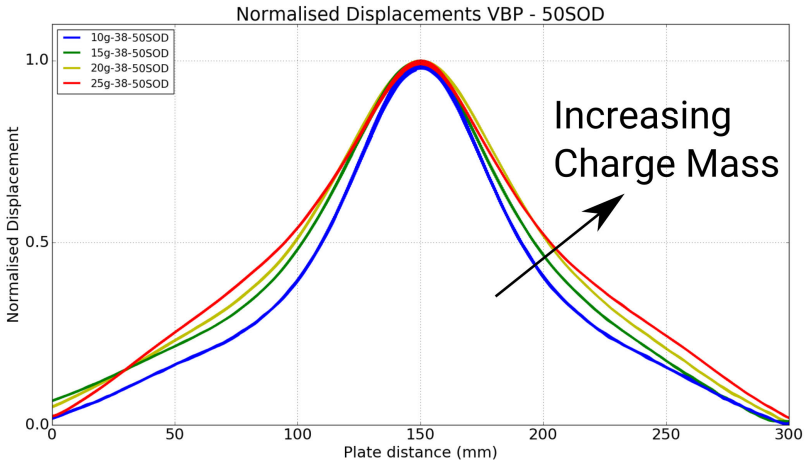

Figure 7.34: Normalised final plate displacement profile showing representative profiles for each of the VBP 50 SOD charge masses.

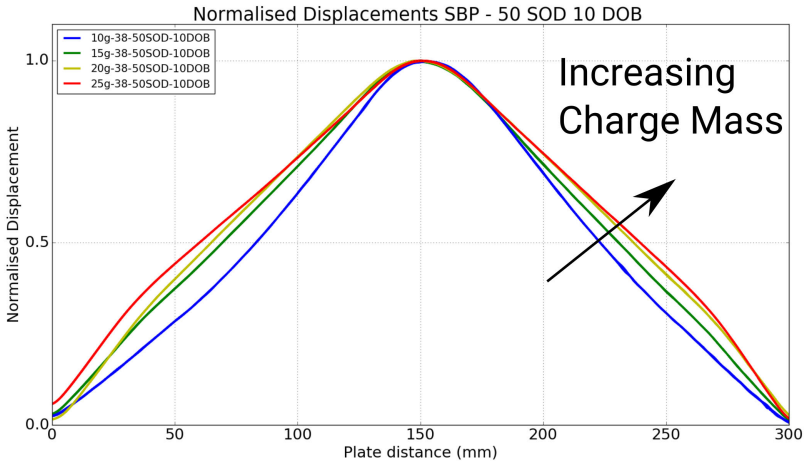

Figure 7.35: Normalised final plate displacement profile showing representative profiles for each of the SBP 50 SOD charge masses.

7.7 Comparison of loading conditions

The best way to contrast the loading conditions investigated is to compare the impulse versus deflection graph shown in Figure 7.36. The distinct grouping of the three loading conditions can clearly be seen, with the AIR 40mm (blue) and 50mm (red) SOD experiments forming two distinct trends at the low impulse values.

The VBP 40mm (cyan) and 50mm (magenta) SOD experiments, form a grouping in the centre of the impulse range which is hard to easily differentiate at this scale. The normalised specific impulse distribution, initial plate velocity and normalised plate profiles were observed to be very similar at 40mm and 50mm SODs.

The SBP (black) experiments form a distinct trend which appears to form its own trend. This is clearly seen in all the measurable readings of the experiments (specific impulse, initial plate velocity, transient response and final deformation profile), which all showed that the addition of sand had an influence in changing the response of the test plate.

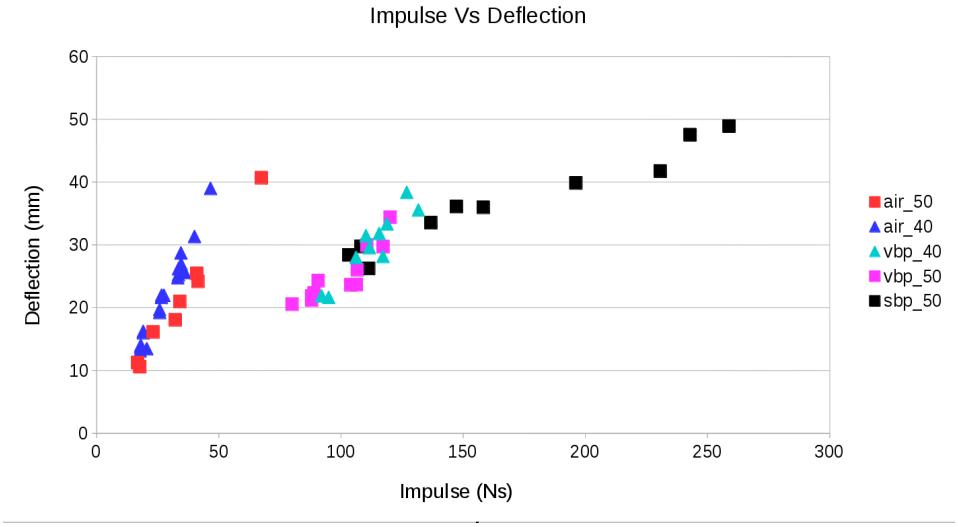

Figure 7.36: Experimental impulse versus permanent midpoint displacement for all the loading conditions.

Chapter 8

Conclusions

This chapter presents the conclusions of this work in relation to experimental, material characterisation and numerical modelling.

The objective of the thesis was to capture and evaluate the effect of sand and a metal back plate on the loading of laboratory scale test plates compared to free air blasts.

The transient response and permanent deformation of fully clamped, circular, Domex 355MC steel plates to air-blast and buried charge explosions is reported. The loading was generated by detonating varying quantities of cylindrical PE4 charges under 3 loading conditions (AIR, VBP and SBP). The test plate material was fully characterised, allowing for numerical simulations to be completed which replicate the loading conditions. The results of the numerical simulations were validated against the experimental plate response, providing additional understanding about the response such at pressure distribution, specific impulse and initial plate velocity. The method presented allowed for the effect of sand and a metal back plate to be compared to free air blast with similar initial conditions.

8.1 Experimental results

58 experiments were conducted and the results of 25 of these captured the transient response of the plate using high speed imaging.

The experimental technique which comprised the use of high speed DIC together with the explosive loading of plates was determined to be reliable and repeatable. The Digital Image Correlation technique was successfully used to capture the experimental plate response for each of the loading conditions. The DIC technique was able to provided

reliable displacement measurements with an average repeatability of ± 0.02mm. The experimental loading conditions proved repeatable to within ± 2 Ns for AIR, ± 4 Ns for VBP and ± 20 Ns for SBP. The midpoint deflections of the test plates varied from the experimental average by less than one plate thickness for all tests.

Small changes of 10mm in the SOD had a measurable effect on the impulse and midpoint deflection recorded in AIR series. SOD had less influence on the impulse distribution and initial plate velocity which acted over a similar area but with a change in magnitude. In general, a decrease in the SOD resulted in a more localised plate response.

The metal back plate in the VBP series had a focusing effect the explosive charge, resulting in an average increase of 77 Ns for the 50mm SOD and 85 Ns for the 40mm SOD when compared to the AIR series. The focusing effect of the back plate generally appeared to result in a similar normalised plate deformation profile, when compared to the AIR series. The normalised specific impulse distribution and initial plate velocities for the VBP 40mm and 50mm SOD were very similar, indicating that the changes in the SOD had less of an effect on the loading profile across the test plate for the VBP series when compared to the AIR series.

The inclusion of sand had the most significant impact on the plate response. The initial plate velocity profile of the test plate is significantly different from the AIR and VBP tests, initially forming a cone in the centre of the plate which plateaued as it radially expanded toward the clamp boundary. The specific impulse distribution, which drives the deformation of the test plate, was also observed to be visibly different from the AIR and VBP tests, often exhibiting discontinuities across the plate which were only seen with the inclusion of sand. The transient midpoint deflection versus time curve for the SBP tests showed changes to the late time response of the plates, with the sand causing the introduction of a clear plateau in the displacement after the initial 0.7ms deformation. The transient strain distribution across the SBP plate centre was located over a larger area of the plate than the AIR and VBP series.

Overall, an increase in midpoint deflection of between 90-160% and 30-40% when compared to AIR and VBP 50mm SOD tests respectively was observed. The impulse recorded was observed to increase by 490-540% and 19-100% when compared to AIR and VBP 50mm SOD tests respectively.

8.2 Material characterisation

The material was successfully characterised through quasistatic and dynamic material tests. The material was fitted to a Johnson Cook numerical material model with basic parameters of $\boldsymbol{A = 352}$, $\boldsymbol{B = 642}$, $\boldsymbol{n = 0.5597}$ and $\boldsymbol{C = 0.03278}$.

The material was successfully modelled and the numerical material tests reproduced the experimental results appropriately.

The Johnson Cook material model used did not appear to fully capture the elastic rebound of the experimental plates, but managed to reproduce the general plate profile well.

8.3 Numerical model results

The numerical model total impulse predictions were found to be unreliable and did not fully capture the impulse imparted on the plate in the experiments, especially in the buried charge modelling.

The transient midpoint deflections of the models matched the experimental results to within one plate thickness with the exception of the SBP series where the models exhibited much higher deflections than the experimental values recorded.

The numerical model was found to give valuable insight into the plate deformation that was not able to be recorded in these tests, validating observations in the experimental transient plate deformation.

Chapter 9

Recommendations

While the work performed has involved many developments to the testing technique, furthering the understanding of the transient plate deformation under different loading conditions, the following could be addressed in future research:

Consider the work done by Zhao and Sutton [7, 53] and examine scaling effects with the new experimental arrangement.

Increase the camera capture speed to more accurately capture the images during the initial plate deformation. This would enable the determination of the initial velocity profile of plate from the experimental data. This is could then be used to infer the specific impulse distribution across the plate profile. Better lighting would have to be arranged to account for the reduced exposure time of the images.

Extend the tests on the VBP series to fully quantify the effect of the metal back plate over a large range of test conditions and determine if the correlation with the damage number extends to form its own trend.

Perform additional buried charge tests to change the depth of burial and determine the effect the depth of burial has on the specific impulse distribution across the test plate.

The decision to use a Johnson-Cook material description was largely based on its ease of implementation in the model. Other material descriptions such as that of Gurson [150] and Bai-Wierzbicki [151] were considered but were found to be too computationally expensive for the purposes of this limited investigation. Future work should be conducted exploring the use of other appropriate material descriptions.

Perform a more thorough numerical investigation into the response of the plates to different loading conditions and eliminate some of simplifications or assumptions which have been made here such as finding a better material model, investigating the effect of different loading mechanisms such as DEM and development of a better sand model able to more accurately capture the response of the sand.

Further investigation into the moving plastic hinge observed during the transient deformation of the plates could shed light on the theory used in single degree of freedom models which state that the plastic hinge moves radially outward towards the clamp frame doing work as it moves. The transient data from the deformed plates could be used to determine the radius of curvature of the plate at a specific point and determine if plastic work could have occurred. This would shed light on the theory that no energy is dissipated as this wave propagates.

References

[1] Landmine montior report. Online, 2016. http://www.the-monitor.org.

[2] Army Times Website, March 2012. http://www.armytimes.com/news/2011/02/usat-ied-toll-in-afghanistan-reduced-by-37-percent-021711/.

[3] Operation enduring freedom report.

[4] United Nations website, January 2016. http://www.un.org/apps/news/story.asp?NewsID=3903

[5] A. Neuberger, S. Peles, and D. Rittel. Scaling the response of circular plates subjected to large and close-range spherical explosions. part 1: Air-blast loading. *International Journal of Impact Engineering*, 34:859–873, 2007.

[6] A. Neuberger, S. Peles, and D. Rittel. Scaling the response of circular plates subjected to large and close-range spherical explosions. part 2: Buried charges. *International Journal of Impact Engineering*, 34:874–882, 2007.

[7] M.A. Sutton, X.M. Deng, V. Tiwari, X. Zhao, W.L. Fourney, and H.U. Leiste. Scaling of bast loading experiments for buried explosives. In *Proceedings of the IMPLAST 2010 Conference*, 2010.

[8] G.F. Kinney and K.J. Graham. Explosive shocks in air. *The Macmillan Company, New York, 2nd edition*, 1985.

[9] US Army Corps of Engineers. Structure to resist the effects of accidental explosions. techreport UFC 3-340-02 formally TM 5-1300, Naval Facilities Engineering Command, Air Force Civil Engineer Support Agency, 2008.

[10] G. Ben-Dor, O. Igra, and T. Elperin. *Handbook of Shock Waves, volume 1 âĂŞ Theoretical, Experimental, and Numerical Technique*. Academic Press, 2001.

[11] John Hetherington and Peter Smith. *Blast and Ballistic Loading of Structures*. CRC Press, 1994.

[12] W.E. Baker, P.A. Cox, P.S. Westine, and J.J. Kulez. *Explosion Hazards and Evaluation, Volume 5*. Elsevier Science, 1983.

[13] J. E. Kennedy. Explosive output for driving metal. In *12th Annual Symposium of the New Mexico Section of the ASME*, 1972.

[14] B. SIMOENS and M.H LEFEBVRE. Influence of the shape of an explosive charge: Quantification of the modification of the pressure field. *Central European Journal of Energetic Materials*, 12(2):195–213, 2015.

[15] Pushkaraj Sherkar, Jinwon Shin, Andrew Whittaker, and Amjad Aref. Influence of charge shape and point of detonation on blast-resistant design. *Journal of Structural Engineering*, 142(2):04015109, 2016.

[16] S. Davids. The influence of charge geometry on the response of cylinders a to internal air blasting. Master's thesis, University of Cape Town, 2016.

[17] NATO Standardization Agency. Procedures for evaluating the protection level of logistic and light armoured vehicles volume 2 for mine threat. Technical Report aep-55 vol 2, North Atlantic Treaty Organization, 2014.

[18] D. Bergeron, R. Walker, and C. Coffey. Detonation of 100-gram anti-personnel mine surrogate charges in sand a test case for computer code validation. Technical report, Defence Research Establishment Suffield, 1998.

[19] J.E. Tremblay. Impulse on blast deflectors from a landmine explosion. Technical report, Defence Research Establisment Centre Valcartier, 1998.

[20] D. Bergeron and J. Tremblay. Canadian research to characterise mine blast output. In *16th International Symposium n the Military Aspects of Balst and Shock*, pages 501–511, 2000.

[21] S.L. Hlady. Effect of soil parameters on land mine blast. In *Proceedings of the 18th MABS Conference*, 2004.

[22] W.L. Fourney, U. Leiste, R. Bonenberger, and D.J. Goodings. Mechanism of loading on plates due to explosive detonation. *Fragblast*, 9:205–217, 2005.

[23] C.E. Anderson, T. Behner, and C.E. Weiss. Mine blast loading experiments. *International Journal of Impact Engineering*, 38(8-9):697–706, aug 2011.

[24] D.M. Fox, X. Huang, D. Jung, W.L. Fourney, U. Leiste, and J.S. Lee. The response of small scale rigid targets to shallow buried explosive detonations. *International Journal of Impact Engineering*, 38(11):882–891, nov 2011.

[25] J.Q. Ehrgott, R.G. Rhett, S.A. Akers, and D.D. Rickman. Design and fabrication of an impulse measurement device to quantify the blast environment from a near-surface detonation in soil. *Experimental Techniques*, 35(3):51–62, dec 2009.

[26] E.G. Pickering, S. Chung Kim Yuen, G.N. Nurick, and P. Haw. The response of quadrangular plates to buried charges. *International Journal of Impact Engineering*, 49:103–114, nov 2012.

[27] S. D. Clarke, J. Warren, and A. Tyas. The influence of soil density and moisture content on the impulse from shallow buried explosive charges. In *14th International Symposium on Interaction of the Effects of Munitions with Structures (ISIEMS), At Seattle, USA*, 2011.

[28] H.N.G. Wadley, T. BÃÿrvik, L. Olovsson, J.J. Wetzel, K.P. Dharmasena, O.S. Hopperstad, V.S. Deshpande, and J.W. Hutchinson. Deformation and fracture of impulsively loaded sandwich panels. *Journal of the Mechanics and Physics of Solids*, 61(2):674 – 699, 2013.

[29] S.D Clarke, S.D Fay, A Tyas, J Warren, S.E Rigby, I Elgy, and R. Livesey. Repeatability of buried charge testing. In *Military Aspects of Blast and Shock 23. Oxford, UK*, 2014.

[30] S.D Clarke, S.E Rigby, A Tyas, S.D Fay, J.J Reay, J.A Warren, M. Gant, and I Elgy. Reflected pressures from explosives buried in idealised cohesive soils. In *Proceedings of the 24th Military Aspects of Blast and Shock. Halifax, Nova Scotia, Canada,*, 2016.

[31] S.E. Rigby, S.D. Fay, S.D. Clarke, A. Tyas, J.J. Reay, J.A. Warren, M. Gant, and I. Elgy. Measuring spatial pressure distribution from explosives buried in dry leighton buzzard sand. *International Journal of Impact Engineering*, 96:89–104, oct 2016.

[32] L.C. Taylor, W.L. Fourney, U. Leiste, and B. Cheeseman. Loading mechanisms from shallow buried explosives. In *The 24th international symposium on ballistics, New Orleans, USA*, 2008.

[33] W.L. Fourney, U. Leiste, and L.C. Taylor. Pressure irregularities in the loading of vehicles by buried mines. In *The 34th annual conference on explosives and blasting technique, Cleveland, Ohio, USA*, 2008.

[34] H.U. Leiste. *Experimental studies to investigate pressure loading on target plates.* PhD thesis, Department of Mechanical Engineering, University of Maryland, 2012.

[35] N. Jones. *Structural Impact.* Cambridge University Press, 1989.

[36] G.N. Nurick and J.B. Martin. Deformation of thin plates subjected to impulsive loading - a review. part 1: Theoretical consideration. *International Journal of Impact Engineering*, 8:159–169, 1989.

[37] G.N. Nurick and J.B. Martin. Deformation of thin plates subjected to impulsive loading - a review. part 2: Experimental studies. *International Journal of Impact Engineering*, 8:171–186, 1989.

[38] D. Bonorchis. *Analysis and simulation of welded plates subjected to blast loading.* PhD thesis, University of Cape Town, 2007.

[39] D. Bonorchis and G.N. Nurick. The effect of welded boundaries on the response of rectangular hot-rolled mild steel plates subjected to localised blast loading. *International Journal of Impact Engineering*, 34:1729–1738, 2007.

[40] S.L. Lemanski, G.N. Nurick, G.S. Langdon, M.C. Simmons, W.J. Cantwell, and G.K. Schleyer. Behaviour of fibre metal laminates subjected to localised blast loading—part II: Quantitative analysis. *International Journal of Impact Engineering*, 34(7):1223–1245, jul 2007.

[41] G.S. Langdon, S.L. Lemanski, G.N. Nurick, M.C. Simmons, W.J. Cantwell, and G.K. Schleyer. Behaviour of fibre–metal laminates subjected to localised blast loading: Part i—experimental observations. *International Journal of Impact Engineering*, 34(7):1202–1222, jul 2007.

[42] S. Chung Kim Yuen, G.N. Nurick, G.S. Langdon, and Y. Iyer. Deformation of thin plates subjected to impulsive load: Part III – an update 25 years on. *International Journal of Impact Engineering*, jun 2016.

[43] S.B. Menkes and H.J. Opat. Tearing and shear failures in explosively loaded clamped beams. *Experimental Mechanics*, 13:480–486, 1973.

[44] V. Deshpande, R. McMeeking, H. Wadley, and A. Evans. Constitutive model for predicting dynamic interactions between soil ejecta and structural panels. *Journal of Mechanics and Physics of Solids*, 57:1139–1164, 2009.

[45] R.G. Teeling-Smith and G.N. Nurick. The deformation and tearing of thin circular plates subjected to impulsive loads. *International Journal of Impact Engineering*, 11:77–91, 1991.

[46] M.D. Olson, J.R. Fagnan, and G.N. Nurick. Deformation and rupture of blast loaded square plates - predictions and experiments. *International Journal of Impact Engineering*, 12:279–291, 1993.

[47] G.N. Nurick, M.E. Gelman, and N.S. Marshall. Tearing of blast loaded plates with clamped boundary conditions. *International Journal of Impact Engineering*, 18:803–827, 1996.

[48] G.N. Nurick and G.C. Shave. The deformation and tearing of thin square plates subjected to impulsive loads - an experimental study. *International Journal of Impact Engineering*, 18:99–116, 1996.

[49] D. Bonorchis and G.N. Nurick. The influence of boundary conditions on the loading of rectangular plates subjected to localised blast loading - importance in numerical simulations. *International Journal of Impact Engineering*, 36:40–52, 2009.

[50] *B. Hopkinson. British Ordonance Board Minutes, 13565*, 1915.

[51] C. Cranz. *Lehrbuch der Ballistik (textbook of Ballistics)*. Springer Verlag, Berlin, 1926.

[52] N. Jacob, S. Chung Kim-Yuen, G.N. Nurick, D. Bonorchis, and S.A. Desai. Scaling aspects of quadrangular plates subjected to localised blast loads - experiments and predictions. *International Journal of Impact Engineering*, 30:1179–1208, 2004.

[53] X. Zhao, V. Tiwari, M.A. Sutton, X. Deng, W.L. Fourney, and U. Leiste. Scaling of the deformation histories for clamped circular plates subjected to blast loading by buried charges. *International Journal of Impact Engineering*, 54:31–50, apr 2013.

[54] V.H. Balden and G.N. Nurick. Numerical simulation of the post-failure motion of steel plates subjected to blast loading. *International Journal of Impact Engineering*, 32:14–34, 2005.

[55] T. Borvik, A.G. Hanssen, M. Langseth, and L. Olovsson. Response of structures to planar blast loads âĂŞ a finite element engineering approach. *Computers & Structures*, 87(9):507 – 520, 2009.

[56] S. Chung Kim Yuen and G.N. Nurick. Experimental and numerical studies on the response of quadrangular stiffened plates. part i: subjected to uniform blast load. *International Journal of Impact Engineering*, 31(1):55 – 83, 2005.

[57] G.S. Langdon, S.Chung Kim Yuen, and G.N. Nurick. Experimental and numerical studies on the response of quadrangular stiffened plates. part ii: localised blast loading. *International Journal of Impact Engineering*, 31(1):85 – 111, 2005.

[58] C. Geretto. *The Effects of Different Degrees of Confinement on the Deformation of Square Plates Subjected to Blast Loading*. PhD thesis, University of Cape Town, 2012.

[59] K. Spranghers, I. Vasilakos, D. Lecompte, H. Sol, and J. Vantomme. Numerical simulation and experimental validation of the dynamic response of aluminum plates under free air explosions. *International Journal of Impact Engineering*, 54:83–95, apr 2013.

[60] K. Spranghers, I. Vasilakos, D. Lecompte, H. Sol, and J. Vantomme. Identification of the plastic behavior of aluminum plates under free air explosions using inverse methods and full-field measurements. *International Journal of Solids and Structures*, 51(1):210–226, jan 2014.

[61] Y.M. Aiyesimi, A. A. Mohammed, and S. Sadiku. A finite element analysis of the dynamic response of a thick uniform elastic circular plate subjected to an exponential blast loading. *American Journal of Computational and Applied Mathematics*, 1(2):57–62, aug 2012.

[62] G.R. Johnson and W.H. Cook. Fracture characteristics of three metals subjected to various strains, strain rates, temperatures and pressures. *Engeneering Fracture Mechanics*, 21:31–48, 1985.

[63] C.E. Anderson, I.S. Chocron, and A.E. Nicholls. Damage modeling for taylor impact simulations. In *EuroDymat*, 2006.

[64] K. Spranghers, D. Lecompte, H. Sol, and J. Vantomme. Material identification of blast loaded aluminum plates through inverse modeling. In *Dynamic Behavior of Materials, Volume 1*, pages 319–326. Springer International Publishing, aug 2013.

[65] D.C. Bretall. Inverse hybrid method for determining explosive loading on plates due to buried mines. Master's thesis, University of Maryland, 2007.

[66] Michael Hubertus Helena Meuwissen. *An inverse method for the mechanical characterisation of metals*. See notes, 1973.

[67] I. Oliveira, P. Teixeira, F. Ferreira, and A. Reis. Inverse characterization of material constitutive parameters for dynamic applications. *Procedia Engineering*, 114(Supplement C):784 – 791, 2015. ICSI 2015 The 1st International Conference on Structural Integrity Funchal, Madeira, Portugal 1st to 4th September, 2015.

[68] L. Fratini, A. Lombardo, and F. Micari. Material characterization for the prediction of ductile fracture occurrence: An inverse approach. *Journal of Materials Processing Technology*, 60(1):311 – 316, 1996. Proceedings of the 6th International Conference on Metal Forming.

[69] P.-A. Eggertsen and K. Mattiasson. An efficient inverse approach for material hardening parameter identification from a three-point bending test. *Engineering with Computers*, 26(2):159–170, Apr 2010.

[70] M. Grujicic, B. Pandurangan, and B.A. Cheeseman. A computational analysis of detonation of buried mines. *Multidisipline Modeling in Materials and Structures*, 2:363 – 387, 2005.

[71] M. Grujicic, B. Pandurangan, B.A. Cheeseman, W.N. Roy, and R.R. Skaggs. Impulse loading resulting fromm shallow buried explosives in water saturated sand. *Proceedings of the I Mech E Part L Journal of Materials:Design and Applications*, 221:21–35, 2007.

[72] S. Chung Kim Yuen, G.N. Nurick, G.S. Langdon, and Y. Iyer. Deformation of thin plates subjected to impulsive load: Part {III} âĂŞ an update 25 years on. *International Journal of Impact Engineering*, 107:108 – 117, 2017.

[73] V. Aune, G. Valsamos, F. Casadei, M. Langseth, and T. Borvik. On the dynamic response of blast-loaded steel plates with and without pre-formed holes. *International Journal of Impact Engineering*, 108(Supplement C):27 – 46, 2017. In Honour of the Editor-in-Chief, Professor Magnus Langseth, on his 65th Birthday.

[74] J.J. Rimoli, B. Talamini, J.J. Wetzel, K.P. Gharmasena, R. Radovitzky, and H.N.G. Wadley. Wet-sand impulse loading of metallic plates and corrugated core sandwich panels. *International Journal of Impact Engineering*, 38:837–848, 2011.

[75] L. Laine and A. Sandvik. Derivation of mechanical properties for sand. In *4th Asia-Pacific Conference on Shock and Impact Loads on Structures*, 2001.

[76] A.D. Barr, S.D. Clarke, M. Petkovski, A. Tyas, S.E. Rigby, J. Warren, and S. Kerr. Effects of strain rate and moisture content on the behaviour of sand under one-dimensional compression. *Experimental Mechanics*, 56(9):1625–1639, aug 2016.

[77] M. Grujicic, B. Pandurangan, C.B. Pandurangan, and B.A. Cheeseman. The effect of degree of saturation of sand on detonation phenomena associated with shallow-buried and ground-laid mines. *Shock and Vibration*, 12:1–21, 2005.

[78] M. Grujicic, B. Pandurangan, and B.A. Cheeseman. Application of the modified compaction material model to the analysis of landmine detonation in soil with various degrees of water saturation. *Shock and Vibration*, 14:1–21, 2007.

[79] M. Grujicic, B. Pandurangan, and A. Hariharan. Comparative discrete-particle versus continuum-based computational investigation of soil response to impulse loading. *Journal of Materials Engineering and Performance*, 20:1520–1535, 2011.

[80] M. Grujicic, B. Pandurangan, N. Coutris, B.A Cheeseman, W.N. Roy, and R.R.Skaggs. Derivation, parameterization and validation of a sandy-clay material model for use in landmine detonation computational analyses. *Journal of Materials Engineering and Performance*, 19:434–450, 2010.

[81] J. Froedinger. Methodology for improved characterisation of landmine explosions. Technical report, SBIR Phase-II Plus Program, Technical Exchange Meeting, Material Science Corperation, 2005.

[82] M. Barsotti and E Sammarco. Comparison of strategies for landmine modeling in ls-dyna with sandy soil material model development. In *14th International LS-DYNA Users Conference*, 2016.

[83] G.I Kerley. The effects of soil type on numerical simulations of buried mine explosions: Report kts02-3. Technical report, Kerley Technical Services, 2002.

[84] G.I Kerley. Documentation of data on sandia aneos library file. albuquerque. Technical report, andia National Laboratories, 2001.

[85] G.I Kerley. Arl-cr-461: Numerical modeling of buried mine explosions s.l. Technical report, Aberdeen Proving Ground, 2001.

[86] T. Borvik, L. Olovsson, A.G. Hanssen, K.P. Dharmasena, H. Hansson, and H.N.G. Wadley. A discrete particle approach to simulate the combined effect of blast and sand impact loading of steel plates. *Journal of the Mechanics and Physics of Solids*, 59(5):940 – 958, 2011.

[87] A.D. Barr. *Strain-rate effects in quartz sand.* PhD thesis, University of Sheffield, 2016.

[88] L. Schwer and S.E. Rigby. Buried charges: The challenge of computing target pressure distributions. Technical report, 2016. Private correspondance with.

[89] Hubert Schreier, Jean-José Orteu, and Michael A. Sutton. *Image Correlation for Shape, Motion and Deformation Measurements.* Springer US, 2009.

[90] D Garcia, J.J Orteu, and L Penazzi. A combined temporal tracking and stereo-correlation technique for accurate measurement of 3d displacements: application to sheet metal forming. *Journal of Materials Processing Technology*, 125-126:736–742, sep 2002.

[91] D. Lei, Z. Huang, P. Bai, and F. Zhu. Experimental research on impact damage of xiaowan arch dam model by digital image correlation. *Construction and Building Materials*, 147:168–173, aug 2017.

[92] Róbert Huňady and Martin Hagara. A new procedure of modal parameter estimation for high-speed digital image correlation. *Mechanical Systems and Signal Processing*, 93:66–79, sep 2017.

[93] Y. Sieffert, F. Vieux-Champagne, S. Grange, P. Garnier, J.C. Duccini, and L. Daudeville. Full-field measurement with a digital image correlation analysis of a shake table test on a timber-framed structure filled with stones and earth. *Engineering Structures*, 123:451–472, sep 2016.

[94] Van-Thuong Nguyen, Seong-Jin Kwon, Oh-Heon Kwon, and Young-Suk Kim. Mechanical properties identification of sheet metals by 2d-digital image correlation method. *Procedia Engineering*, 184:381–389, 2017.

[95] F. Grytten, H. Daiyan, M. Polanco-Loria, and S. Dumoulin. Use of digital image correlation to measure large-strain tensile properties of ductile thermoplastics. *Polymer Testing*, 28(6):653–660, sep 2009.

[96] Xiaochuan Zhang, Yong Wang, Jia Yang, Zhixia Qiao, Chunhua Ren, and Cheng Chen. Deformation analysis of ferrite/pearlite banded structure under uniaxial tension using digital image correlation. *Optics and Lasers in Engineering*, 85:24–28, oct 2016.

[97] V. Savic, L.G. Hector Jr, and J.R. Fekete. Digital image correlation study of plastic deformation and fracture in fully martensitic steels. *Experimental Mechanics*, 50(1):99–110, nov 2008.

[98] M. A. Sutton, N. Li, D. C. Joy, A. P. Reynolds, and X. Li. Scanning electron microscopy for quantitative small and large deformation measurements part i: SEM imaging at magnifications from 200 to 10,000. *Experimental Mechanics*, 47(6):775–787, mar 2007.

[99] M. A. Sutton, N. Li, D. Garcia, N. Cornille, J. J. Orteu, S. R. McNeill, H. W. Schreier, X. Li, and A. P. Reynolds. Scanning electron microscopy for quantitative small and large deformation measurements part II: Experimental validation for magnifications from 200 to 10,000. *Experimental Mechanics*, 47(6):789–804, mar 2007.

[100] M.A. Sutton, J.H. Yan, V. Tiwari, H.W. Schreier, and J.J. Orteu. The effect of out-of-plane motion on 2d and 3d digital image correlation measurements. *Optics and Lasers in Engineering*, 46(10):746–757, oct 2008.

[101] Liping Yu and Bing Pan. Single-camera stereo-digital image correlation with a four-mirror adapter: optimized design and validation. *Optics and Lasers in Engineering*, 87:120–128, dec 2016.

[102] F. Chen, Xu Chen, Xin Xie, Xiu Feng, and L. Yang. Full-field 3d measurement using multi-camera digital image correlation system. *Optics and Lasers in Engineering*, 51(9):1044–1052, sep 2013.

[103] D. Gerbig, A. Bower, V. Savic, and L.G. Hector. Coupling digital image correlation and finite element analysis to determine constitutive parameters in necking tensile specimens. *International Journal of Solids and Structures*, 97-98:496–509, oct 2016.

[104] P.F. Luo, Y.J. Chao, M.S. Sutton, and W.H. Peters. Accurate measurement of three-dimensional deformations in deformable and rigid bodies using computer vision. In *SEM Spring Conference on Experimental Mechanics held in Cambridge, MA*, 1989.

[105] V. Tiwari, M. A. Sutton, and S. R. McNeill. Assessment of high speed imaging systems for 2d and 3d deformation measurements: Methodology development and validation. *Experimental Mechanics*, 47(4):561–579, jan 2007.

[106] J. Park, S. Yoon, T.H. Kwon, and K. Park. Assessment of speckle-pattern quality in digital image correlation based on gray intensity and speckle morphology. *Optics and Lasers in Engineering*, 91:62 – 72, 2017.

[107] P.L. Reu and T.J. Miller. The application of high-speed digital image correlation. *Journal of Strain Analysis for Engineering Design*, 43:673–688, 2008.

[108] Jens Kristian Holmen, Odd Sture Hopperstad, and Tore Børvik. Low-velocity impact on multi-layered dual-phase steel plates. *International Journal of Impact Engineering*, 78:161–177, apr 2015.

[109] B. Pan, L. Yu, Y. Yang, W. Song, and L. Guo. Full-field transient 3d deformation measurement of 3d braided composite panels during ballistic impact using single-

camera high-speed stereo-digital image correlation. *Composite Structures*, 157:25–32, dec 2016.

[110] L. Yu and B. Pan. Full-frame, high-speed 3d shape and deformation measurements using stereo-digital image correlation and a single color high-speed camera. *Optics and Lasers in Engineering*, 95:17–25, aug 2017.

[111] O. Rijensky and D. Rittel. Polyurea coated aluminum plates under hydrodynamic loading: Does side matter? *International Journal of Impact Engineering*, 98:1 – 12, 2016.

[112] H. Arora, P.A. Hooper, and J.P. Dear. Dynamic response of full-scale sandwich composite structures subject to air-blast loading. *Composites Part A: Applied Science and Manufacturing*, 42(11):1651–1662, nov 2011.

[113] H. Arora, P. Del Linz, and J.P. Dear. Damage and deformation in composite sandwich panels exposed to multiple and single explosive blasts. *International Journal of Impact Engineering*, 104:95–106, jun 2017.

[114] P.A. Hooper, R.A.M. Sukhram, B.R.K. Blackman, and J.P. Dear. On the blast resistance of laminated glass. *International Journal of Solids and Structures*, 49(6):899–918, mar 2012.

[115] K. Spranghers, I. Vasilakos, D. Lecompte, H. Sol, and J. Vantomme. Full-field deformation measurements of aluminum plates under free air blast loading. *Experimental Mechanics*, 52(9):1371–1384, jan 2012.

[116] M.A. Louar, B. Belkassem, H. Ousji, K. Spranghers, D. Kakogiannis, L. Pyl, and J. Vantomme. Explosive driven shock tube loading of aluminium plates: experimental study. *International Journal of Impact Engineering*, 86:111–123, dec 2015.

[117] V. Aune, E. Fagerholt, K.O. Hauge, M. Langseth, and T. Borvik. Experimental study on the response of thin aluminium and steel plates subjected to airblast loading . *International Journal of Impact Engineering*, 90:106–121, 2016.

[118] G.N. Nurick. *Large deformation of thin plates subjected to impulsive loading.* PhD thesis, University of Cape Town, 1987.

[119] M. S. Ahmad. *Study of dynamic behaviour of multilayered structures subjected to blast loading.* PhD thesis, University of Cape Town, 2012.

[120] SSAB. Domex 355mc material data sheet. Technical report, SSAB, 2015.

[121] R.J. Curry and G.S. Langdon. Transient response of steel plates subjected to close proximity explosive detonations in air. *International Journal of Impact Engineering*, 102(Supplement C):102 – 116, 2017.

[122] Matt J. Crompton Thorsten Siebert. Application of high speed digital image correlation for vibration mode shape analysis (white paper). Technical report, Dantec Dynamics, 2010.

[123] V. Tiwari, M.A. Sutton, S.R. McNeill, S. Xu, X. Deng, W.L. Fourney, and D. Bretall. Application of 3d image correlation for full-field transient plate deformation measurements during blast loading. *International Journal of Impact Engineering*, 36(6):862 – 874, 2009.

[124] A. Neuberger, S. Peles, and D. Rittel. Springback of circular clamped armor steel plates subjected to spherical air-blast loading. *International Journal of Impact Engineering*, 36(1):53ï£¡ï£¡ï£¡60, 2009.

[125] E.G. Pickering. The response of quadrangular plates to buried charges. Master's thesis, University of Cape Town, 2013.

[126] ASTM. E8/e8m-15a standard test methods for tension testing of metallic materials. Technical report, ASTM International, 2015.

[127] M. Weyer. An experimental and theoretical study on the effect of strain rate on ductile damage. Master's thesis, University of Cape Town, 2016.

[128] R.M. Davies. A critical study of the hopkinson pressure bar. *Philosophical Transactions of the Royal Society of London A: Mathematical, Physical and Engineering Sciences*, 240(821):375–457, 1948.

[129] H Kolsky. An investigation of the mechanical properties of materials at very high rates of loading. *Proceedings of the Physical Society. Section B*, 62(11):676, 1949.

[130] B. Hopkinson. A method of measuring the pressure produced in the detonation of high explosives or by the impact of bullets. *Philosophical Transactions of the Royal*

Society of London. Series A, Containing Papers of a Mathematical or Physical Character, 213:437–456, 1914.

[131] S Ellwood, L J Griffiths, and D J Parry. A tensile technique for materials testing at high strain rates. *J. Phys. E: Sci. Instrum.*, 15:1169–1172, 1982.

[132] D. Mohr and G. Gary. M-shaped specimen for the high-strain rate tensile testing using a split hopkinson pressure bar apparatus. *Exp. Mech.*, 47(5):687–692, 2007.

[133] D. Mohr and M. Oswald. A new experimental technique for the multi-axial testing of advanced high strength steel sheets. *Experimental Mechanics*, 48(1):65–77, 2008.

[134] C.Y. Wang and Y.M. Xia. Validity of one-dimensional experimental principle for flat specimen in barÂśbar tensile impact apparatus. *International Journal of Solids and Structures*, 37:3305–3322, 2000.

[135] J. Peirs, P. Verleysen, W. Van Paepegem, and J. Degrieck. Determining the stressestrain behaviour at large strains from high strain rate tensile and shear experiments. *International Journal of Impact Engineering*, 38:406–415, 2011.

[136] M.M. LeBlanc and D.H. Lassila. Dynamic tensile testing of sheet materialsal using the split-hopkinson bar technique. *Experimental Techniques*, 17(1):37–42, 1993.

[137] C.P. Koh, V.P.W. Shim, V.B.C. Tan, and B.L. Tan. Response of a high-strength flexible laminate to dynamic tension. *International Journal of Impact Engineering*, 35:559–568, 2008.

[138] M. Downey. Design, build and test a tensile split hopkinson bar. Honours thesis, University of Cape Town, 2007.

[139] A. Bowden. Experimental and numerical study on the effect of strain rate to ductile damage. Master's thesis, University of Cape Town, 2009.

[140] T.J. Cloete. PhD work and various technical consultations.

[141] R.J Curry and T.J. Cloete. Experimental calibration of ductile damage model using notched specimens. In *DYMAT Hopkinson Centenary Conference, Cambridge, UK*, 2014.

[142] G.R. Johnson and W.H. Cook. Fracture characteristics of three metals subjected to various strains, strain rates, temperatures and pressures. *Engenreering fracture mechanics*, 21:31–48, 1985.

[143] G.R. Cowper and P.S. Symonds. Strain-hardening and strain-rate effects int eh impact loading of cantilever beams. Technical report, Division of Applied Mathemetics, Brown University, 1957.

[144] J.R. Rice. On the ductile enlargement of voids in triaxial stress fields. *Journal of mechanics and Solids*, 17:201–217, 1969.

[145] Y. Bao and T. Wierzbicki. On fracture locus in the equivalent strain and stress triaxiality space. *International Journal of Mechanical Sciences*, 46(1):81 – 98, 2004.

[146] G. Box and K.B Wilson. On the experimental attainment of optimum conditions (with discussion). *Journal of the Royal Statistical Society Series B*, 13:1–45, 1951.

[147] H. Mullerschon, F. Ulrich, T. Munz, and N. Stander. The identification of rate dependent material properties in foams using ls-opt. Technical report, LSTC, 2004.

[148] G. Gruben, S. SÃÿlvernes, T. Berstad, D. Morin, O.S. Hopperstad, and M. Langseth. Low-velocity impact behaviour and failure of stiffened steel plates. *Marine Structures*, 54(Supplement C):73 – 91, 2017.

[149] V. Aune, G. Valsamos, F. Casadei, M. Larcher, M. Langseth, and T. BÃÿrvik. Numerical study on the structural response of blast-loaded thin aluminium and steel plates. *International Journal of Impact Engineering*, 99(Supplement C):131 – 144, 2017.

[150] Abdelkader Slimane, Benattou Bouchouicha, Mohamed Benguediab, and Sid-Ahmed Slimane. Parametric study of the ductile damage by the gursonâĂŞtvergaardâĂŞneedleman model of structures in carbon steel a48-ap. *Journal of Materials Research and Technology*, 4(2):217 – 223, 2015.

[151] Y. Bai and T. Wierzbicki. A new model of metal plasticity and fracture with pressure and lode dependence. *International Journal of Plasticity*, 24(6):1071 – 1096, 2008.

[152] B.M. Dobratz and P.C. Crawford. *LLNL explosives handbook : properties of chemical explosives and explosive simulants*. Livermore, Calif. : Lawrence Livermore National Laboratory, University of California ; Springfield, Va. : Available from National Technical Information Service, 1985.

[153] John O. Halllquist. *LS-DYNA Theory Manual*. LSTC, March 2006.

[154] LS-Dyna. Keyword manual volume i. Technical report, LS-Dyna, 2016.

Appendix A

Experimental DIC Results

A.1 AIR Transient Strain

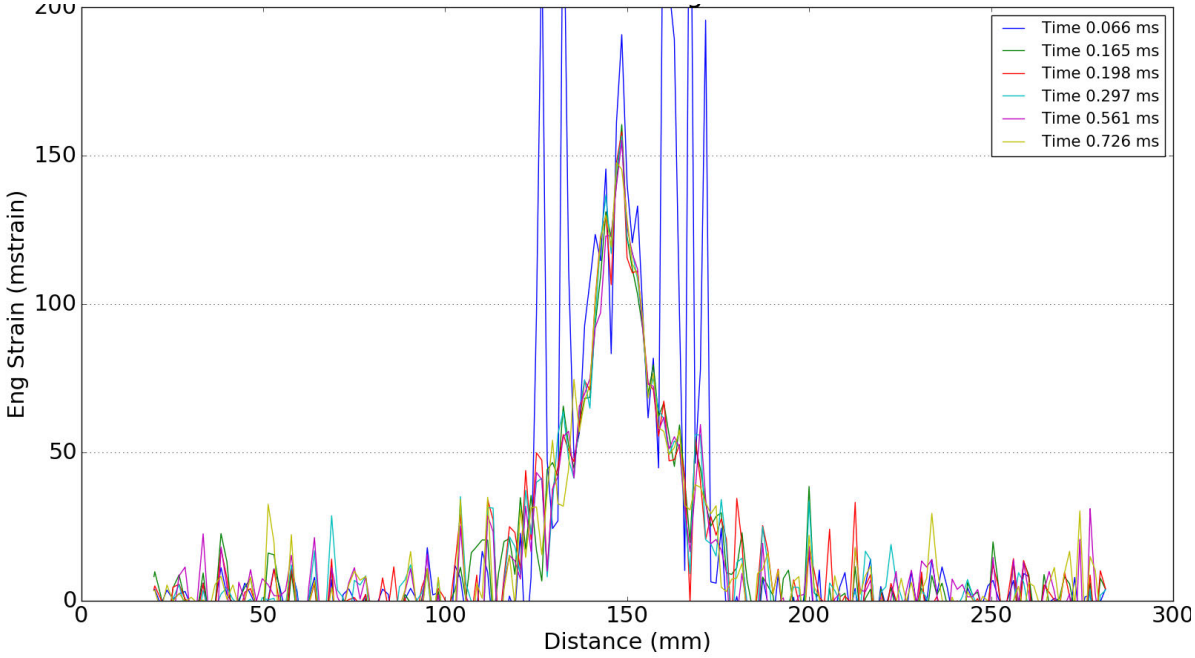

(a) AIR 10g 40 SOD Transient Strain

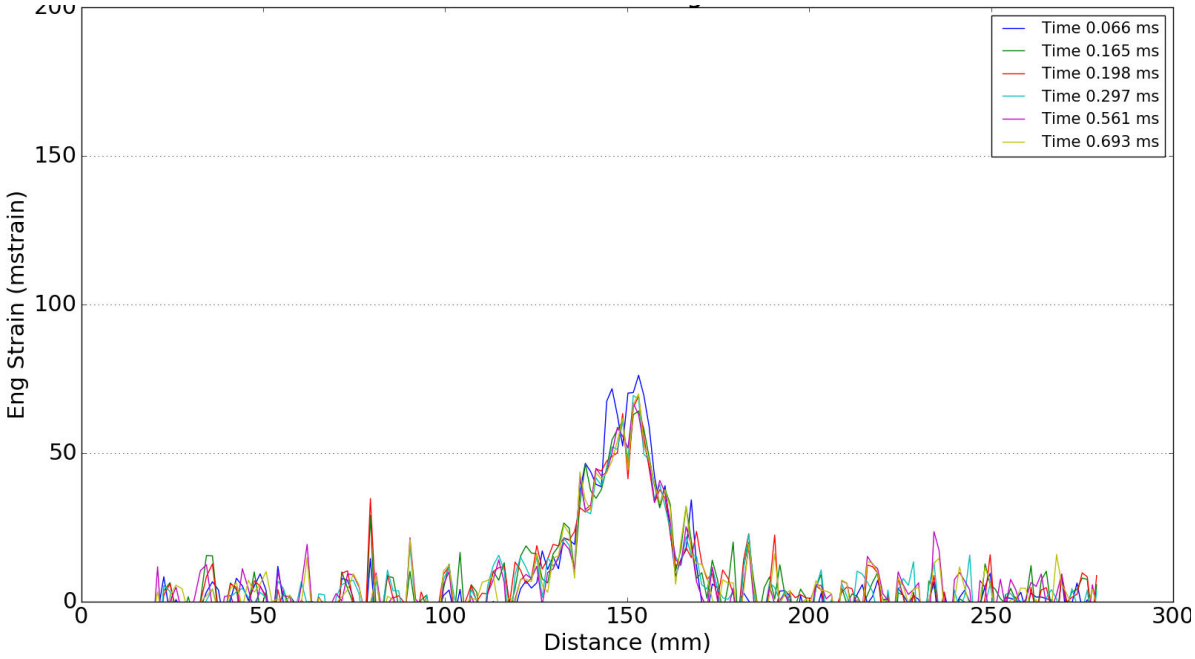

(b) AIR 10g 50 SOD Transient Strain

Figure A.1: Transient strain in the radial direction along the center line extracted by DIC for the AIR 10g experiments

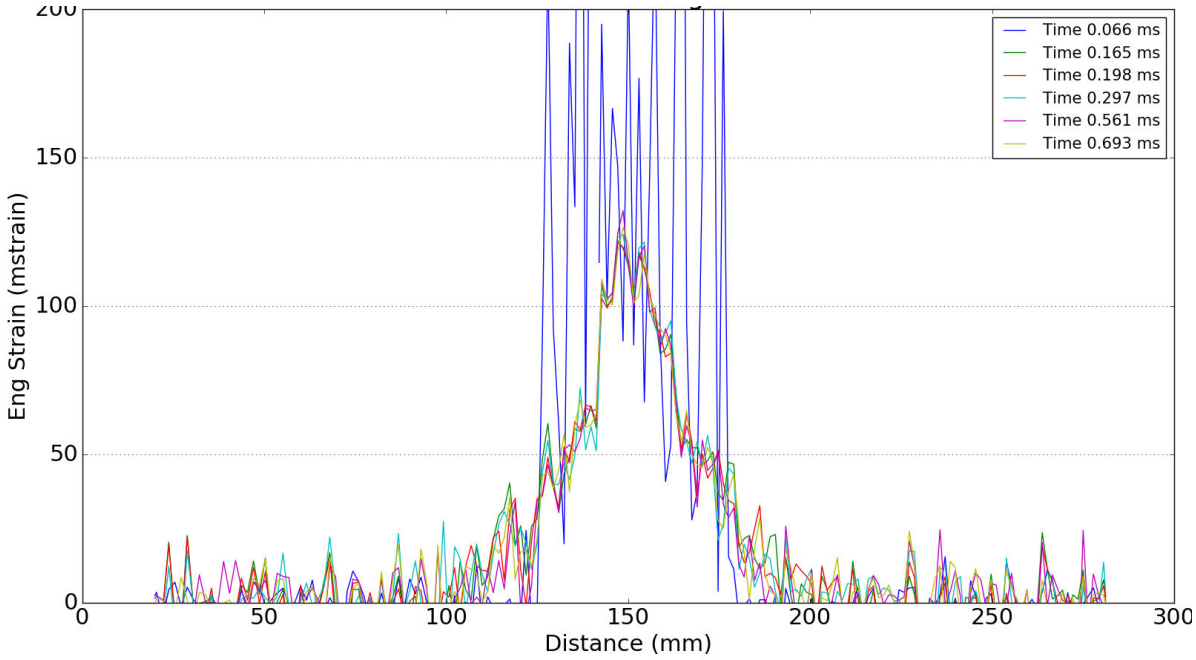

(a) AIR 15g 40 SOD Transient Strain

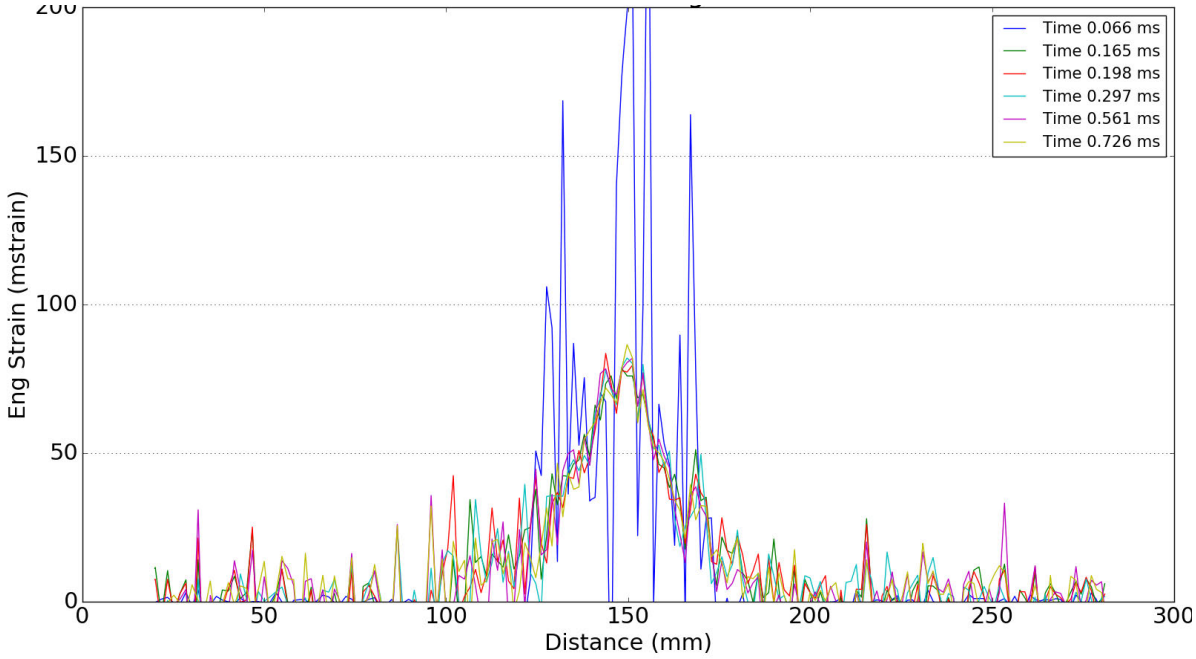

(b) AIR 15g 50 SOD Transient Strain

Figure A.2: Transient strain in the radial direction along the center line extracted by DIC for the AIR 15g experiments

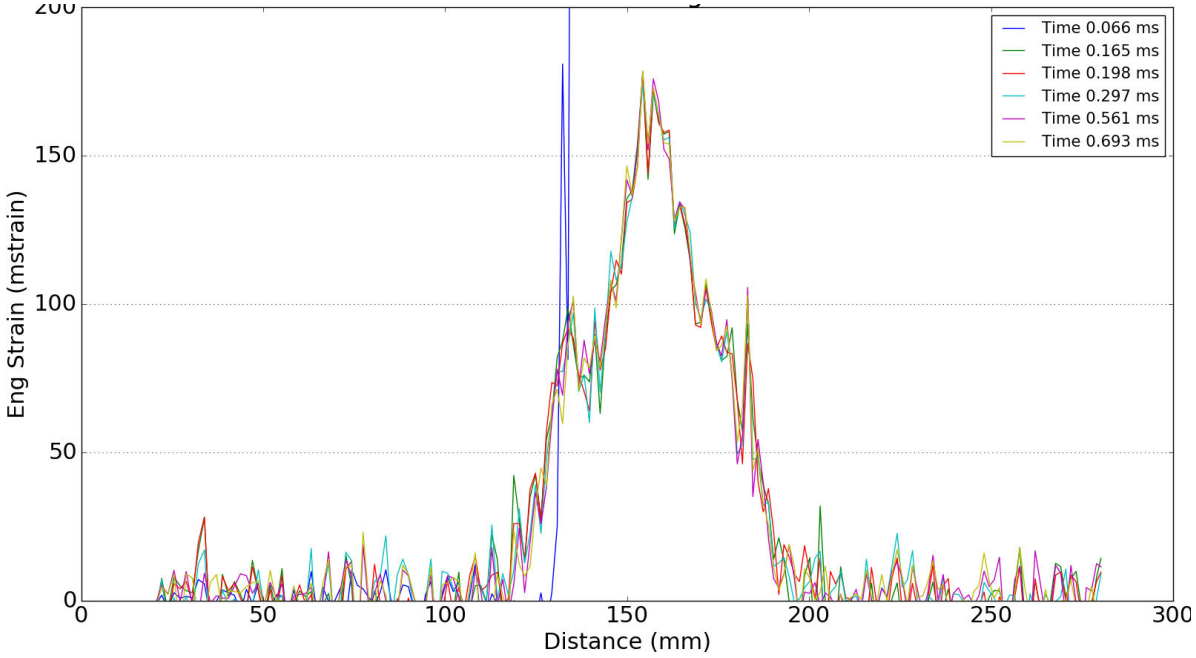

(a) AIR 20g 40 SOD Transient Strain

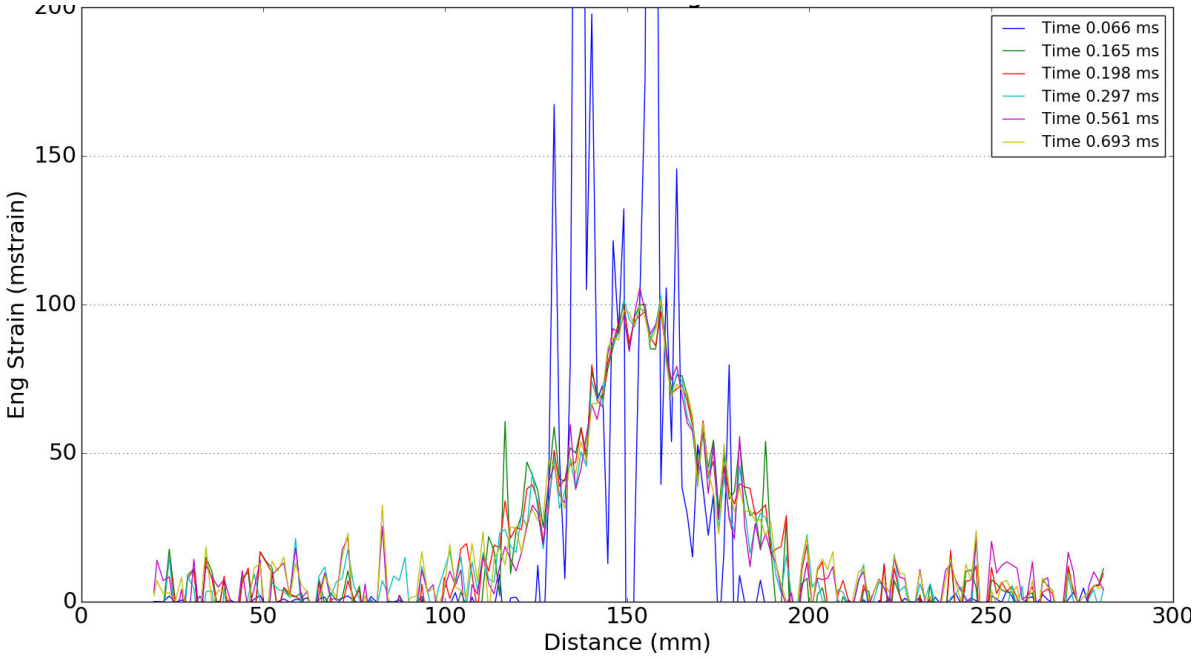

(b) AIR 20g 50 SOD Transient Strain

Figure A.3: Transient strain in the radial direction along the center line extracted by DIC for the AIR 20g experiments

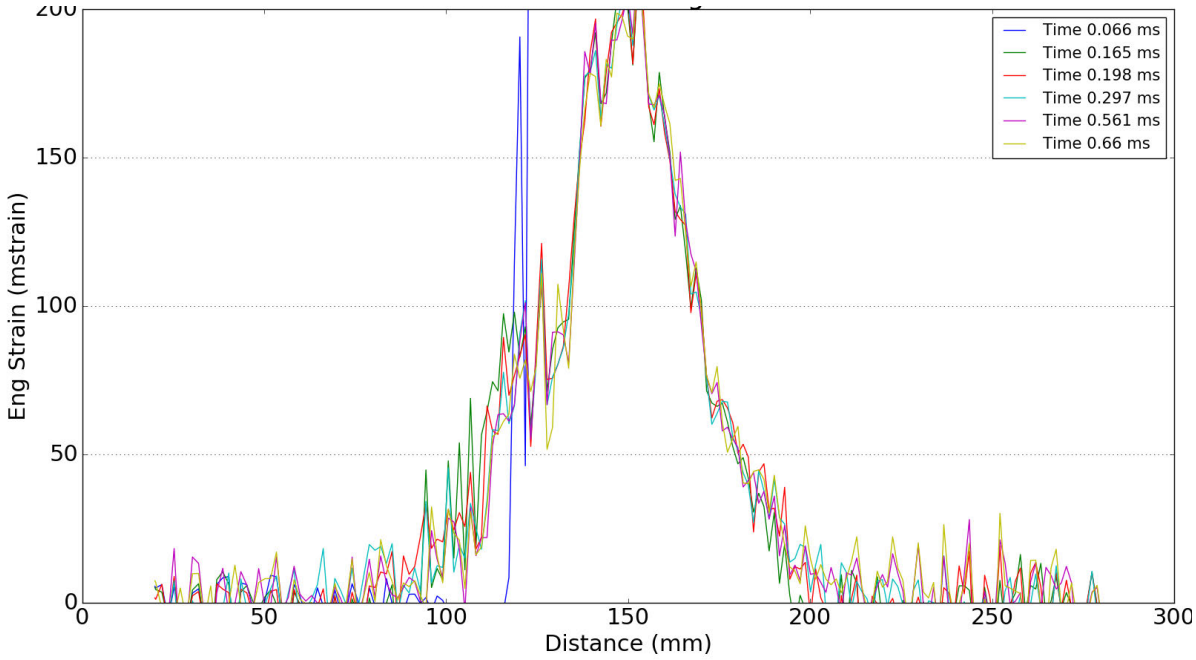

(a) AIR 25g 40 SOD Transient Strain

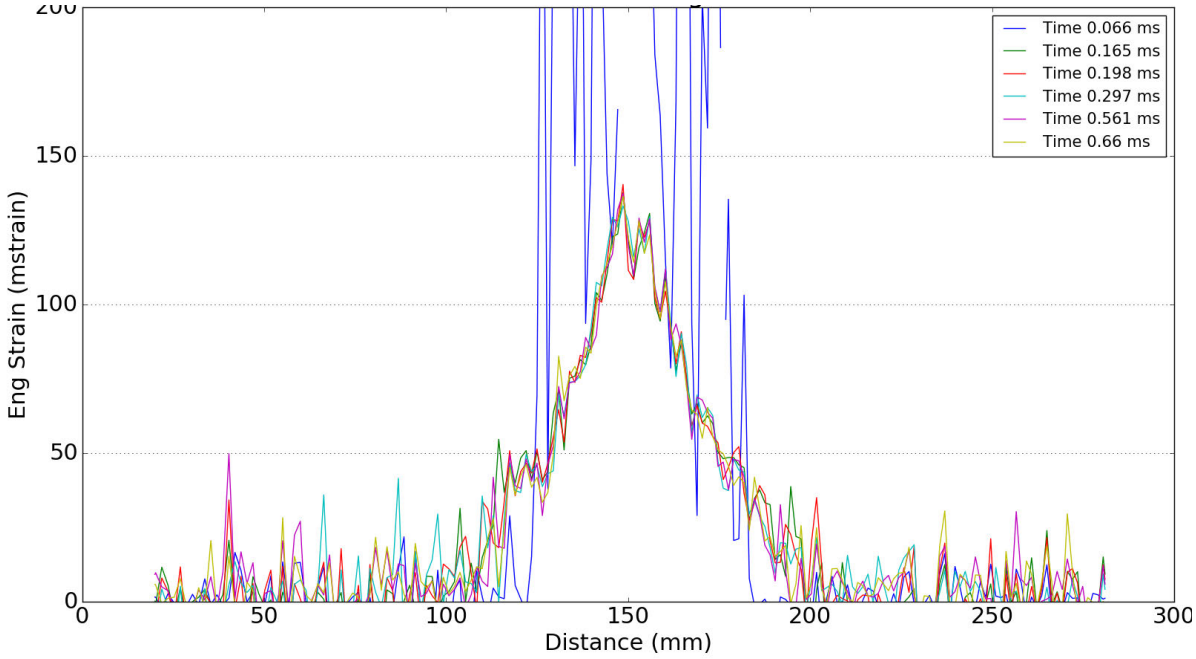

(b) AIR 25g 50 SOD Transient Strain

Figure A.4: Transient strain in the radial direction along the center line extracted by DIC for the AIR 25g experiments

A.2 VBP Transient strain

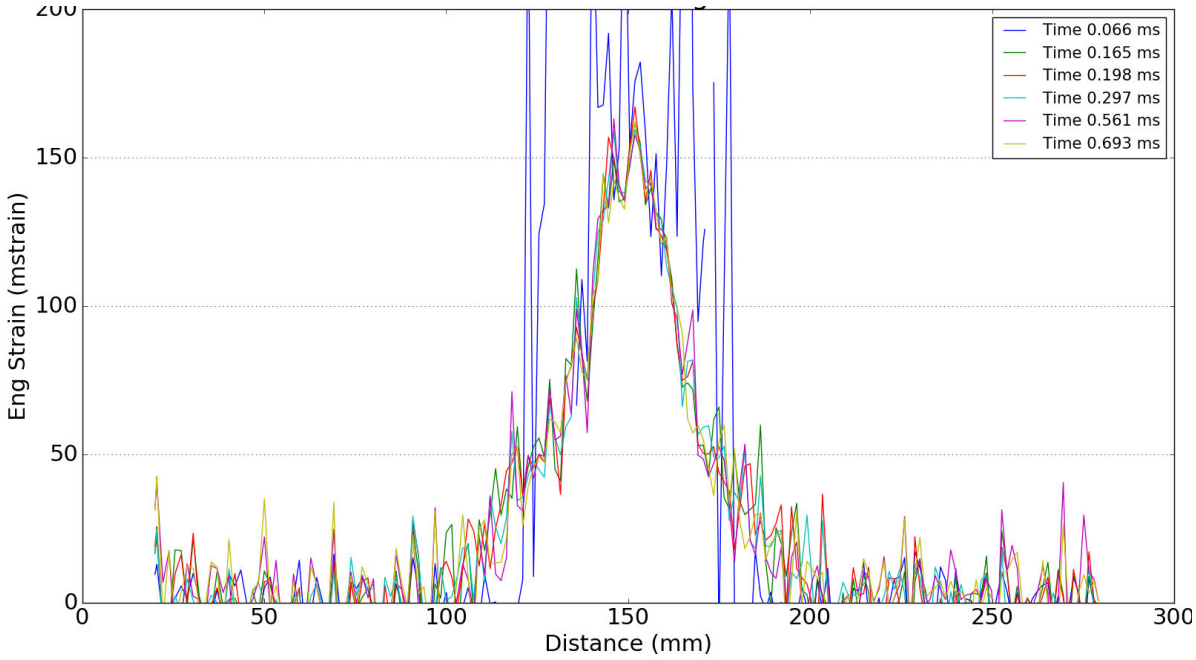

(a) VBP 10g 40 SOD Transient Strain

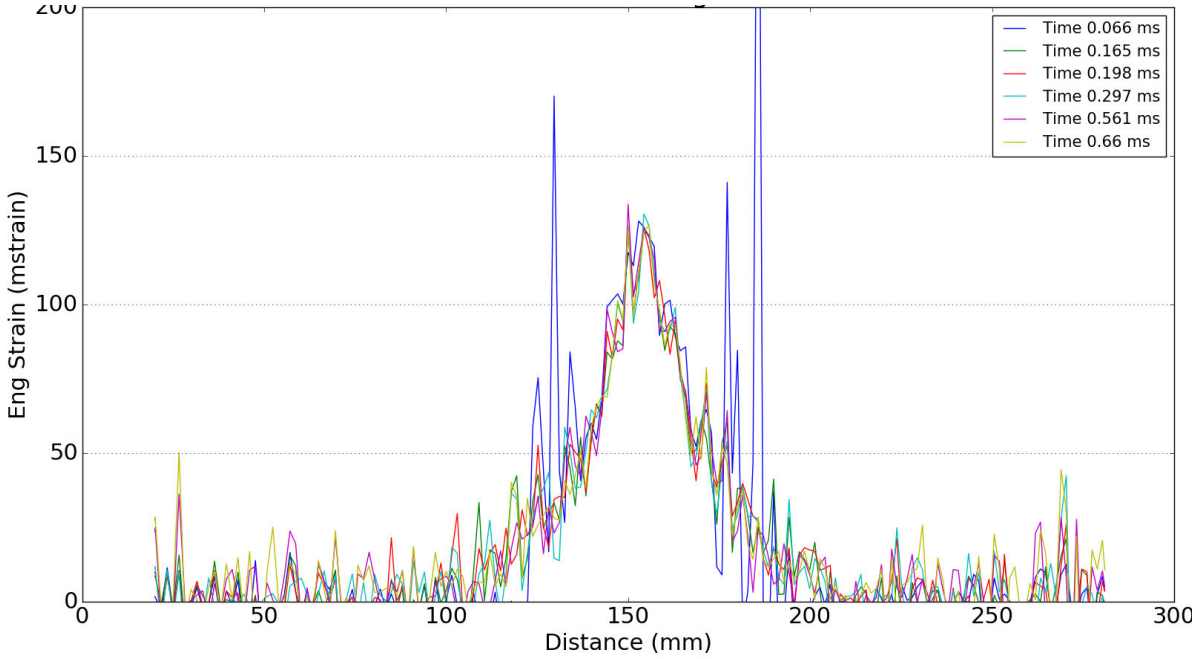

(b) VBP 10g 50 SOD Transient Strain

Figure A.5: Transient strain in the radial direction along the center line extracted by DIC for the VBP 10g experiments

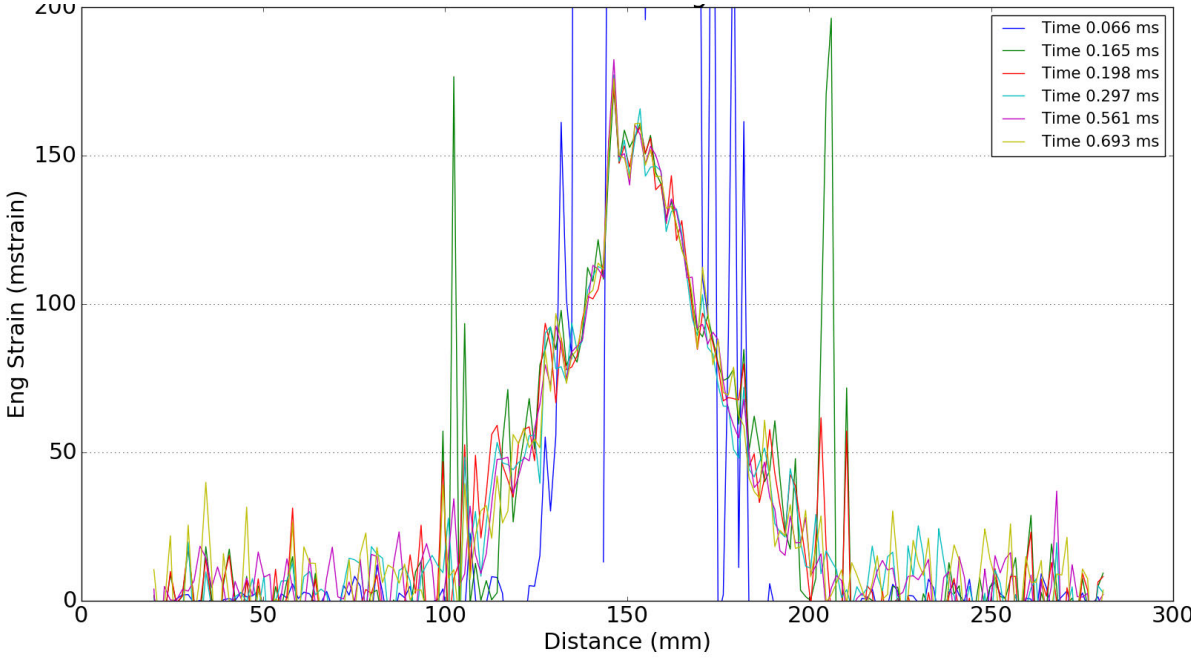

(a) VBP 15g 40 SOD Transient Strain

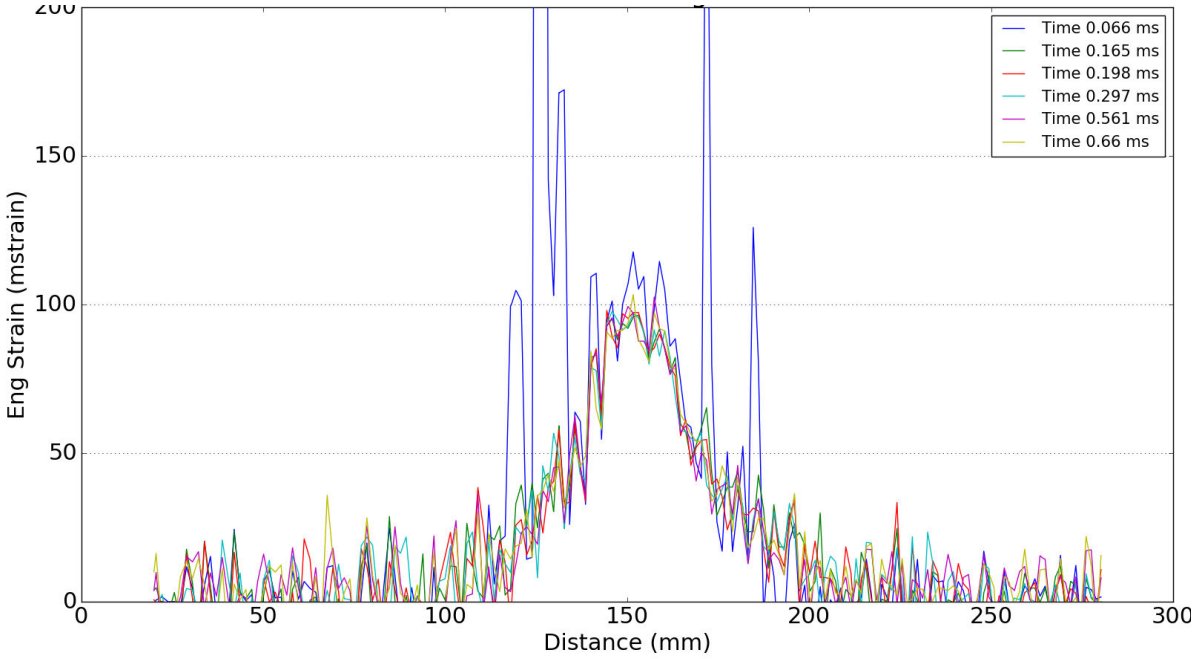

(b) VBP 15g 50 SOD Transient Strain

Figure A.6: Transient strain in the radial direction along the center line extracted by DIC for the VBP 15g experiments

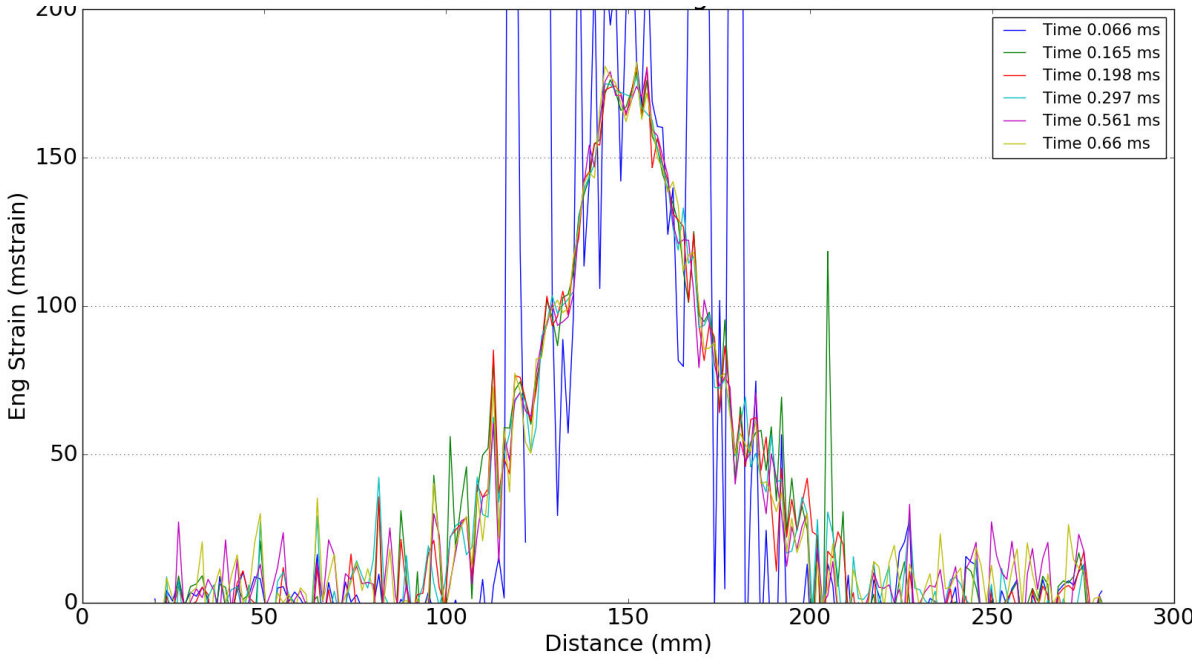

(a) VBP 20g 40 SOD Transient Strain

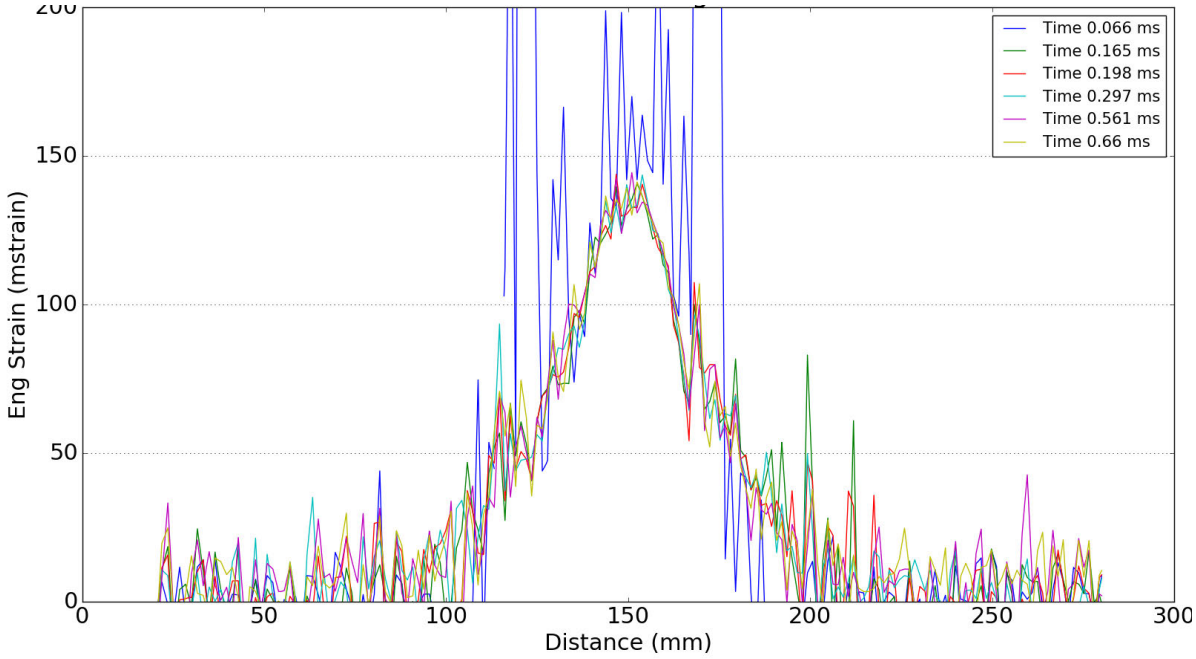

(b) VBP 20g 50 SOD Transient Strain

Figure A.7: Transient strain in the radial direction along the center line extracted by DIC for the VBP 20g experiments

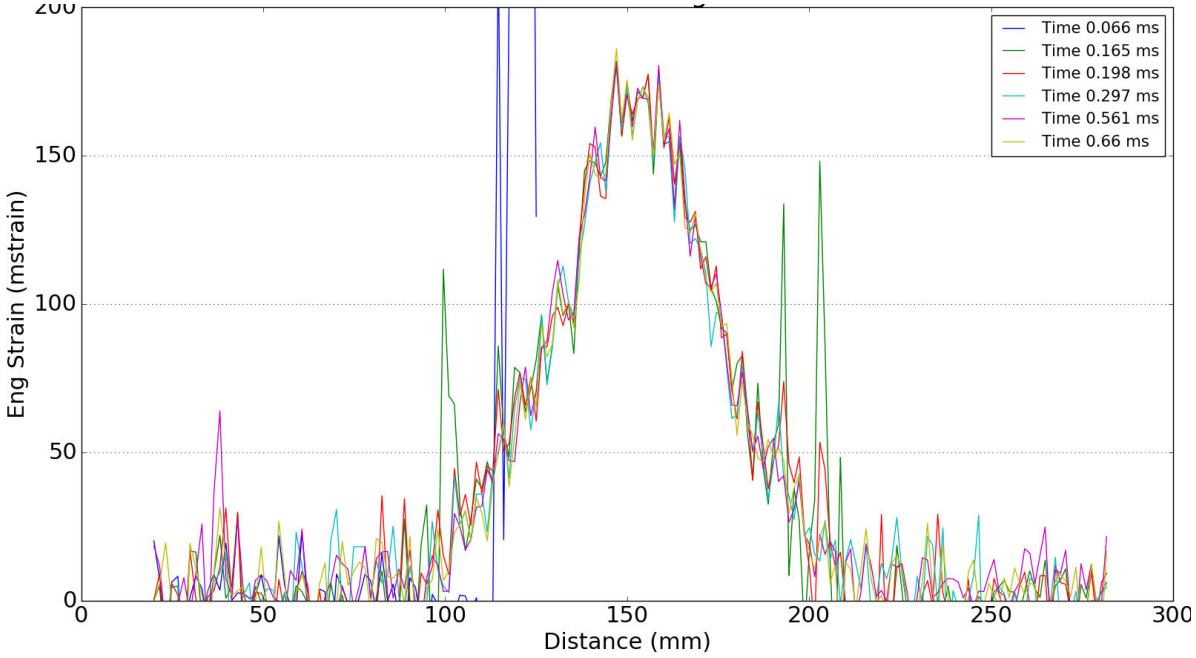

(a) VBP 25g 40 SOD Transient Strain

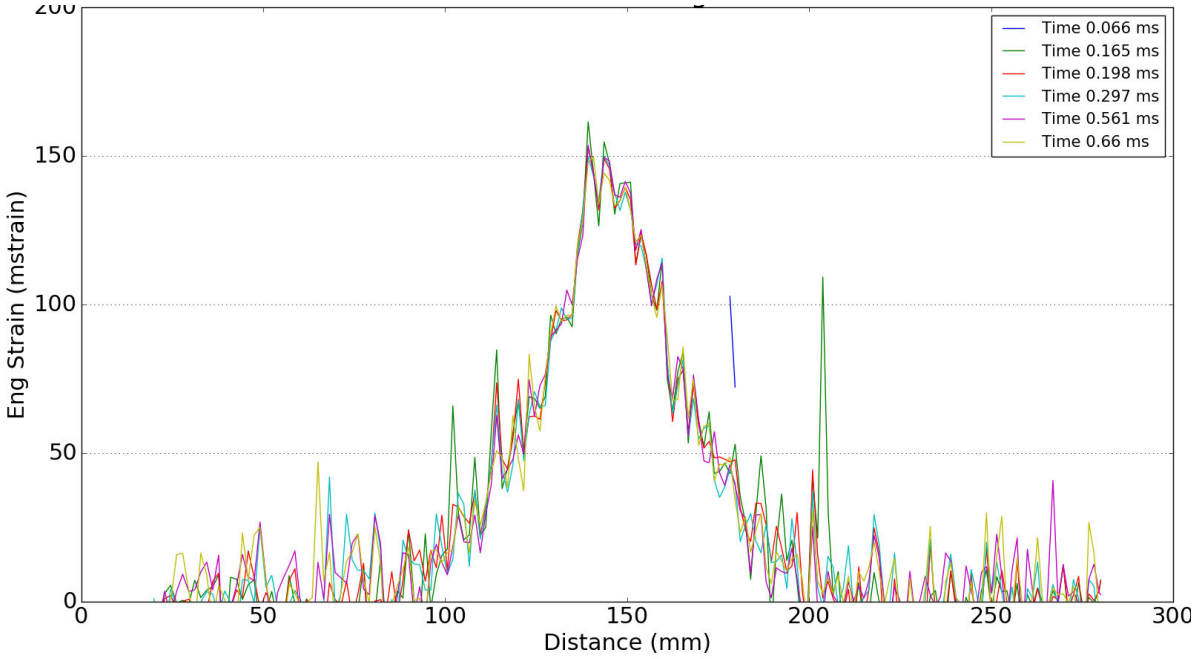

(b) VBP 25g 50 SOD Transient Strain

Figure A.8: Transient strain in the radial direction along the center line extracted by DIC for the VBP 25g experiments

A.3 SBP Transient strain

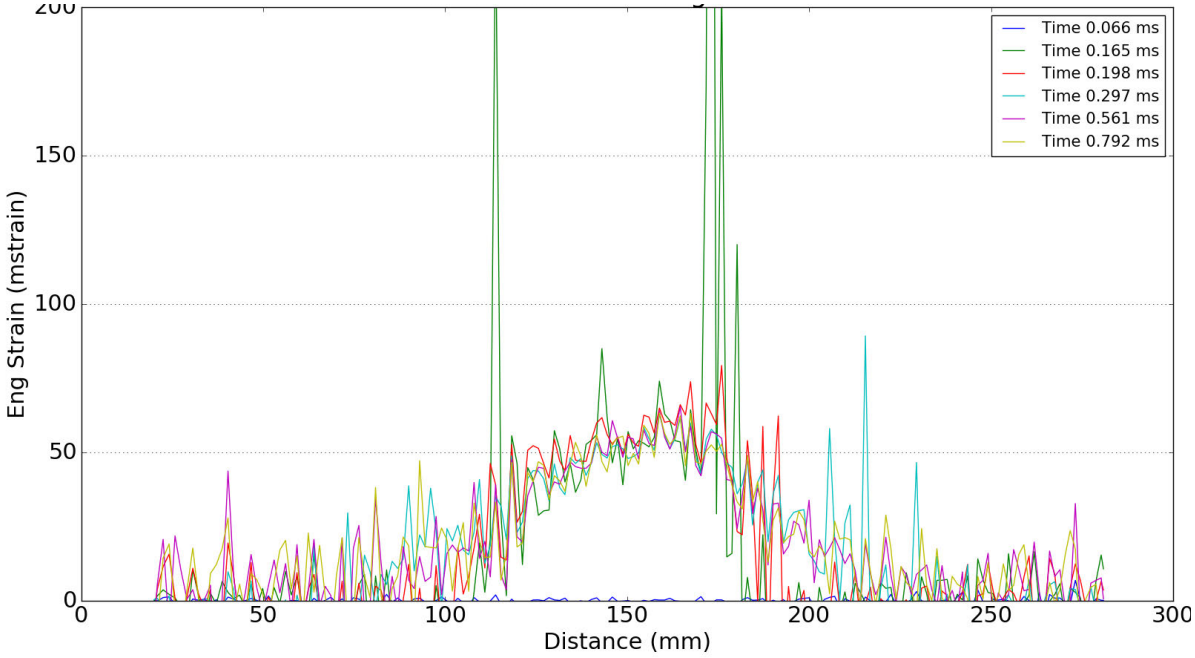

(a) SBP 10g 40 SOD 10 DOB Transient Strain

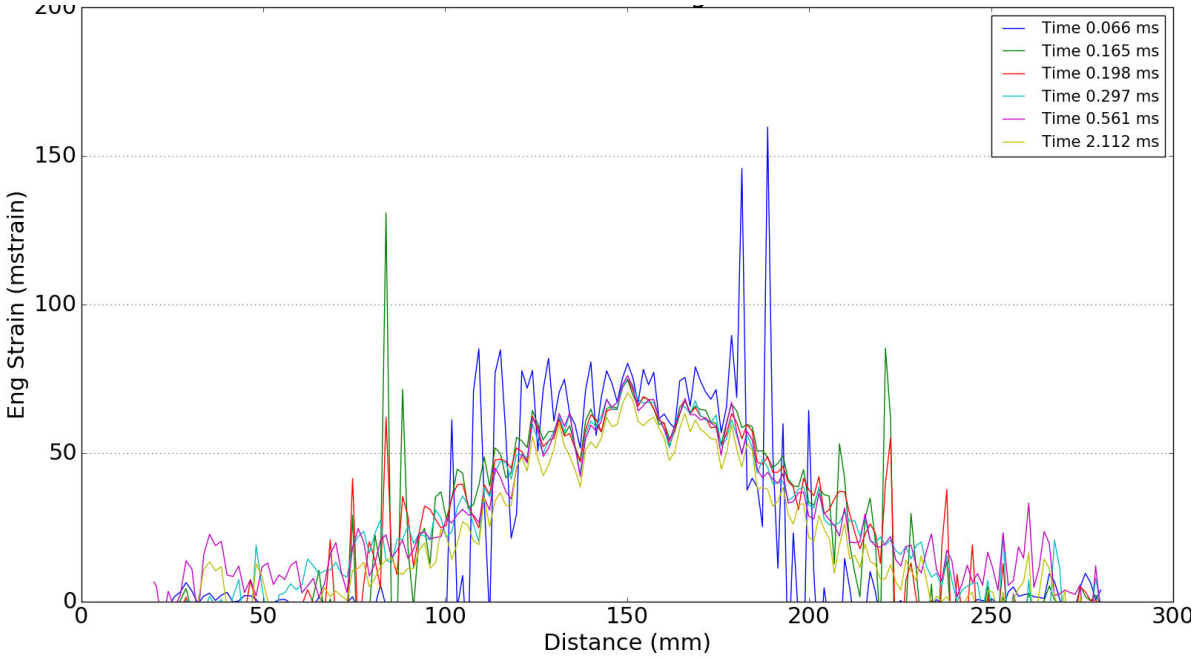

(b) SBP 15g 40 SOD Transient Strain

Figure A.9: Transient strain in the radial direction along the center line extracted by DIC for the SBP 10g and 15g experiments

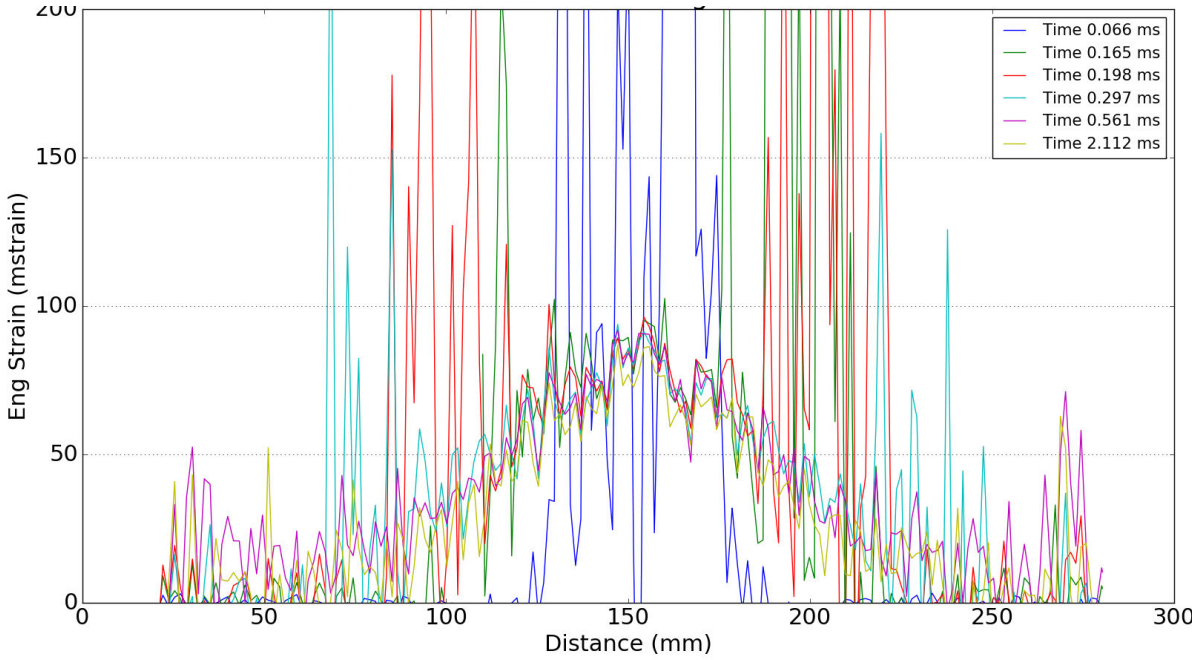

(a) SBP 20g 40 SOD 10 DOB Transient Strain

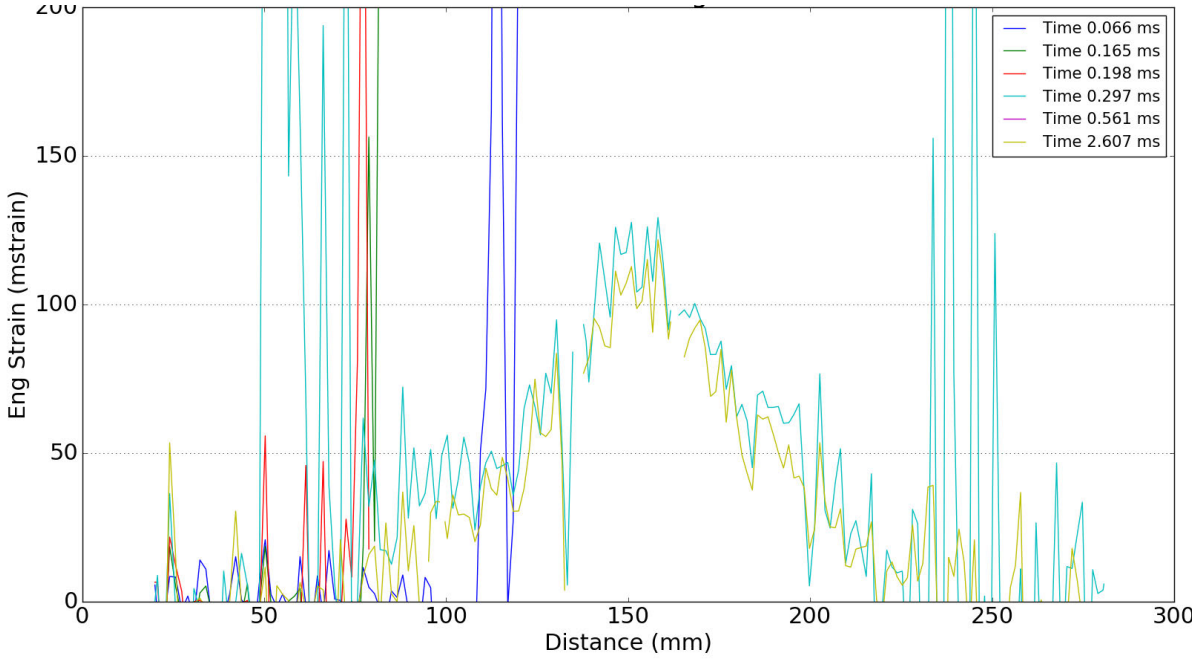

(b) SBP 25g 40 SOD Transient Strain

Figure A.10: Transient strain in the radial direction along the center line extracted by DIC for the SBP 20g and 25g experiments

Appendix B

Simulation Results

B.1 AIR

B.1.1 AIR - Midpoint Deflection

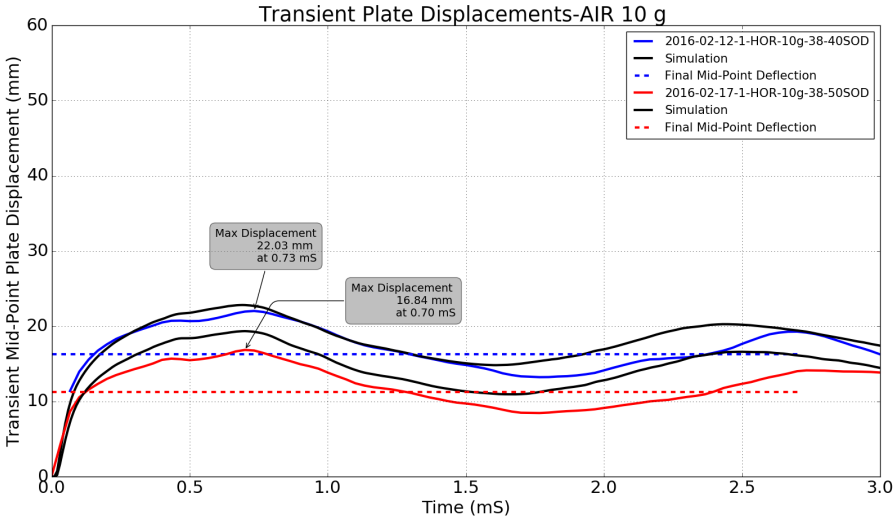

Figure B.1: Transient midpoint deflection values for the AIR 10g simulations(black) and the experimental values (blue and red)

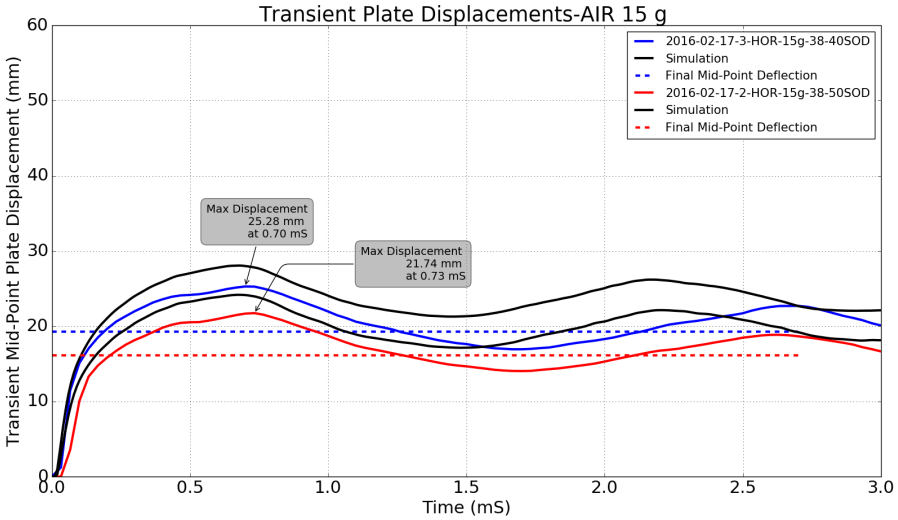

Figure B.2: Transient midpoint deflection values for the AIR 15g simulations(black) and the experimental values (blue and red)

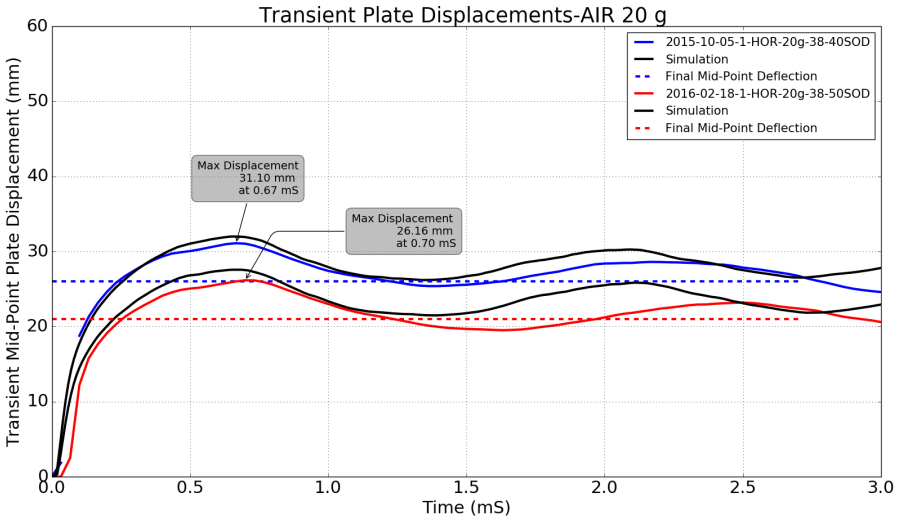

Figure B.3: Transient midpoint deflection values for the AIR 20g simulations(black) and the experimental values (blue and red)

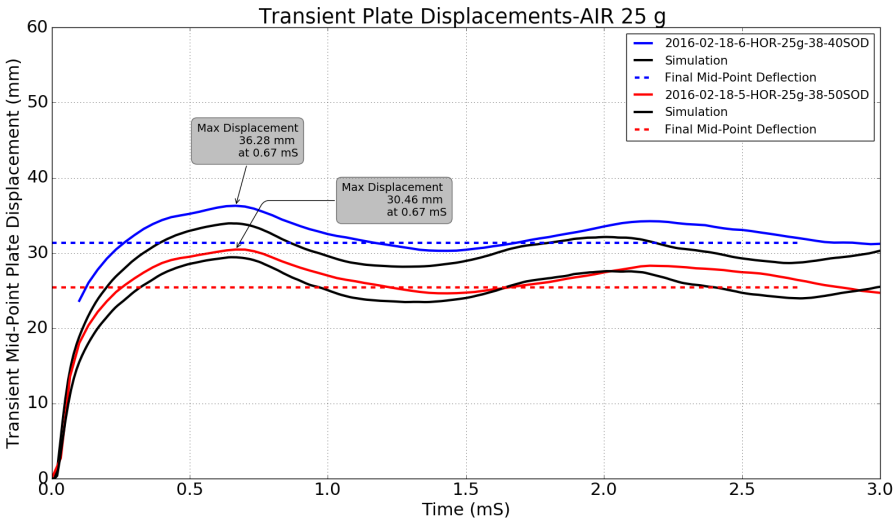

Figure B.4: Transient midpoint deflection values for the AIR 25g simulations(black) and the experimental values (blue and red)

B.1.2 AIR - Tranient Deflection Results

B.1.3 AIR - Final Plate Profiles

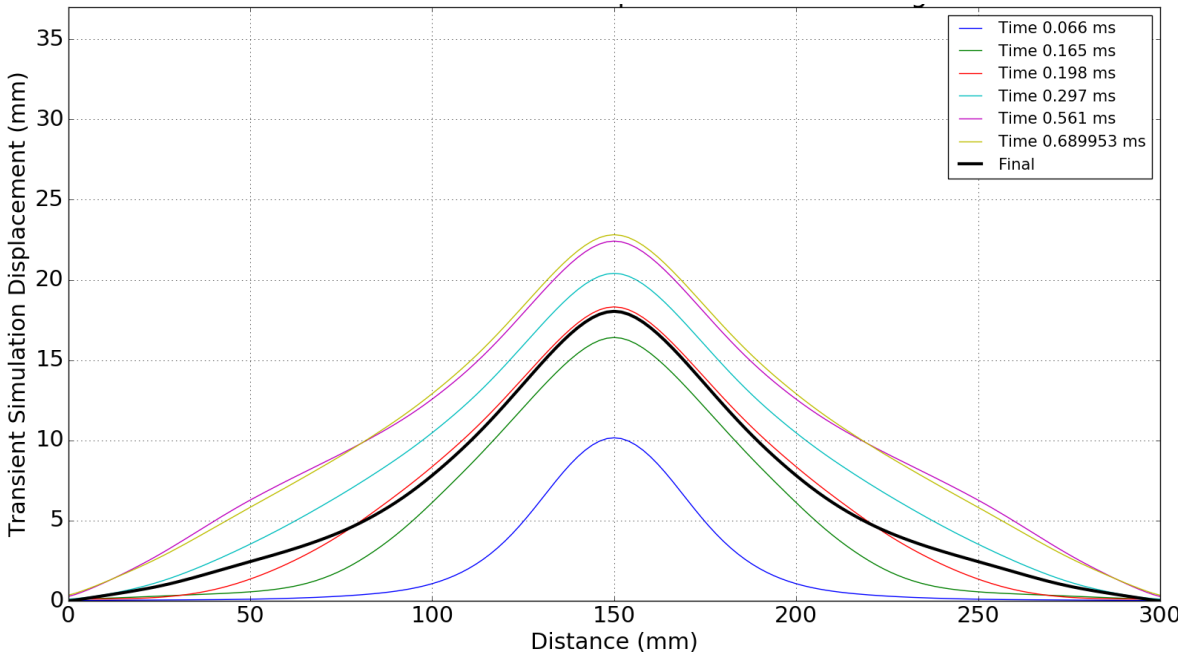

(a) 40mm Stand-off distance

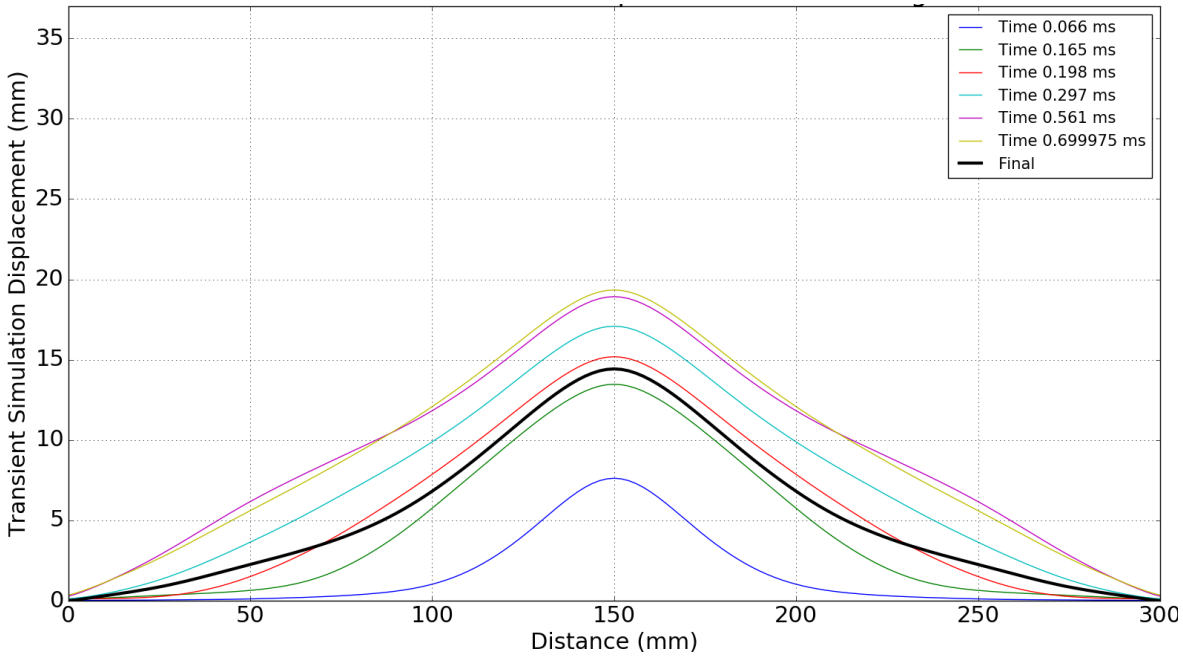

(b) 50mm Stand-off distance

Figure B.5: Transient plate deformation data from simulation for 10g AIR charge detonations

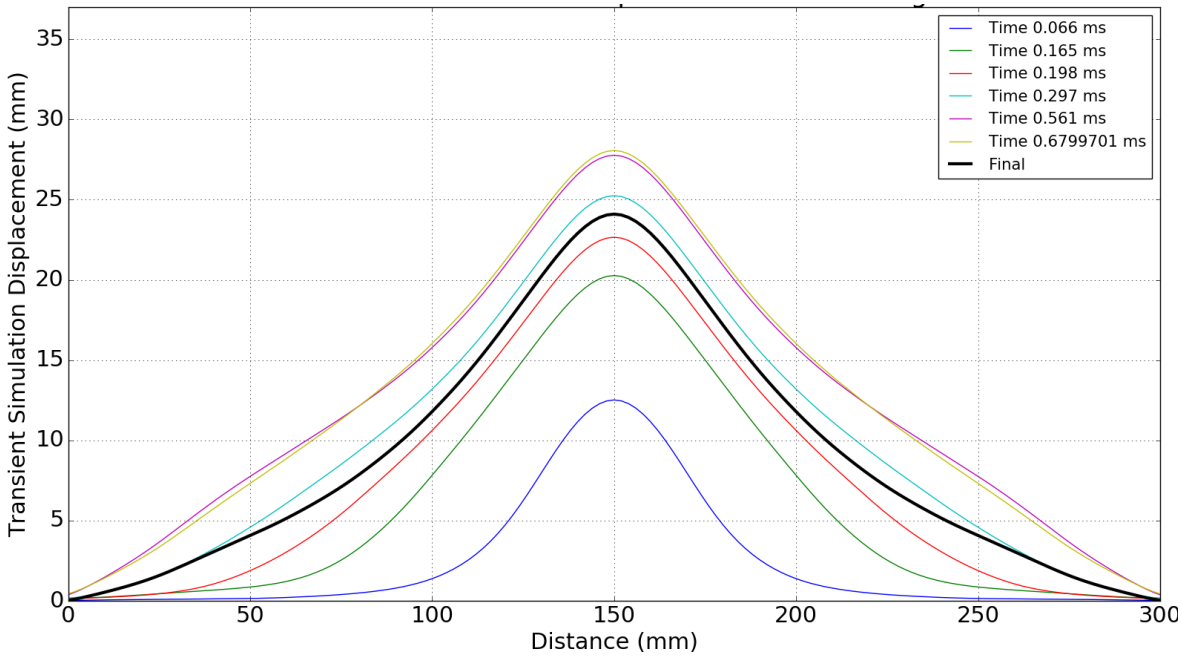

(a) 40mm Stand-off distance

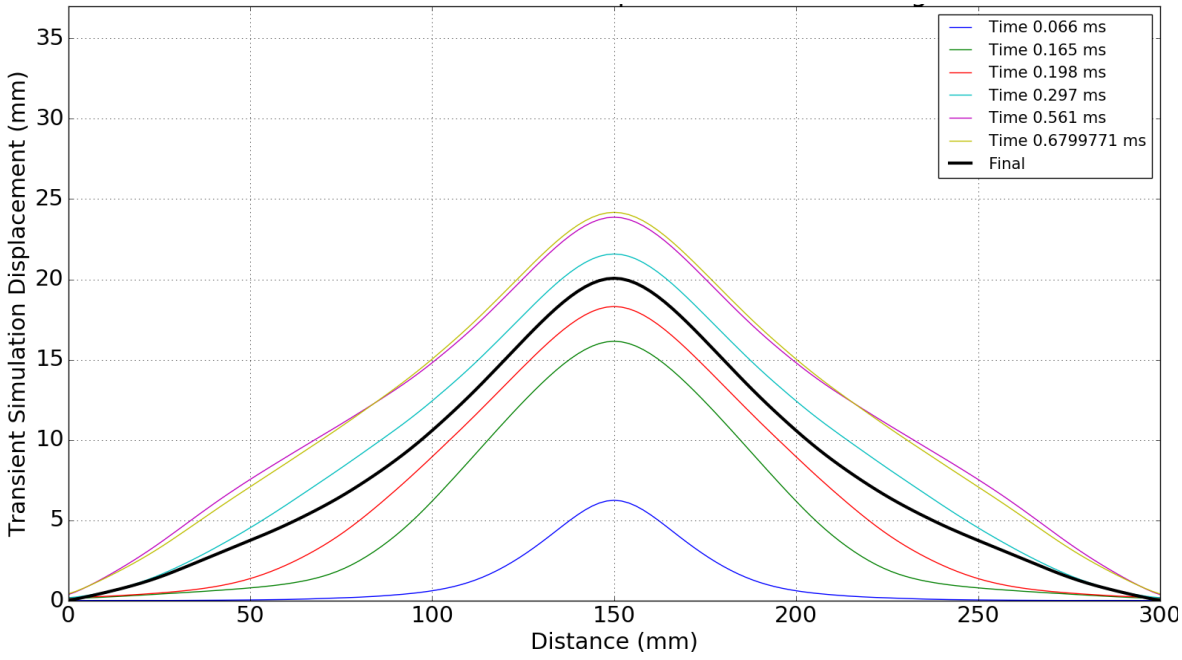

(b) 50mm Stand-off distance

Figure B.6: Transient plate deformation data from simulation for 15g AIR charge detonations

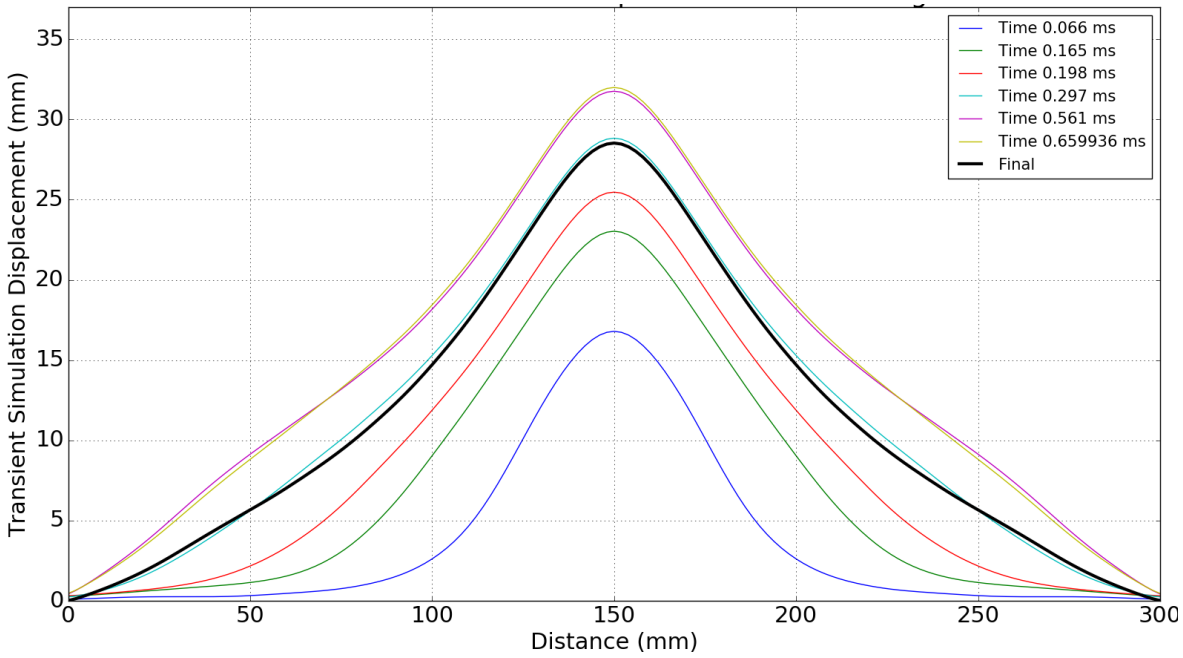

(a) 40mm Stand-off distance

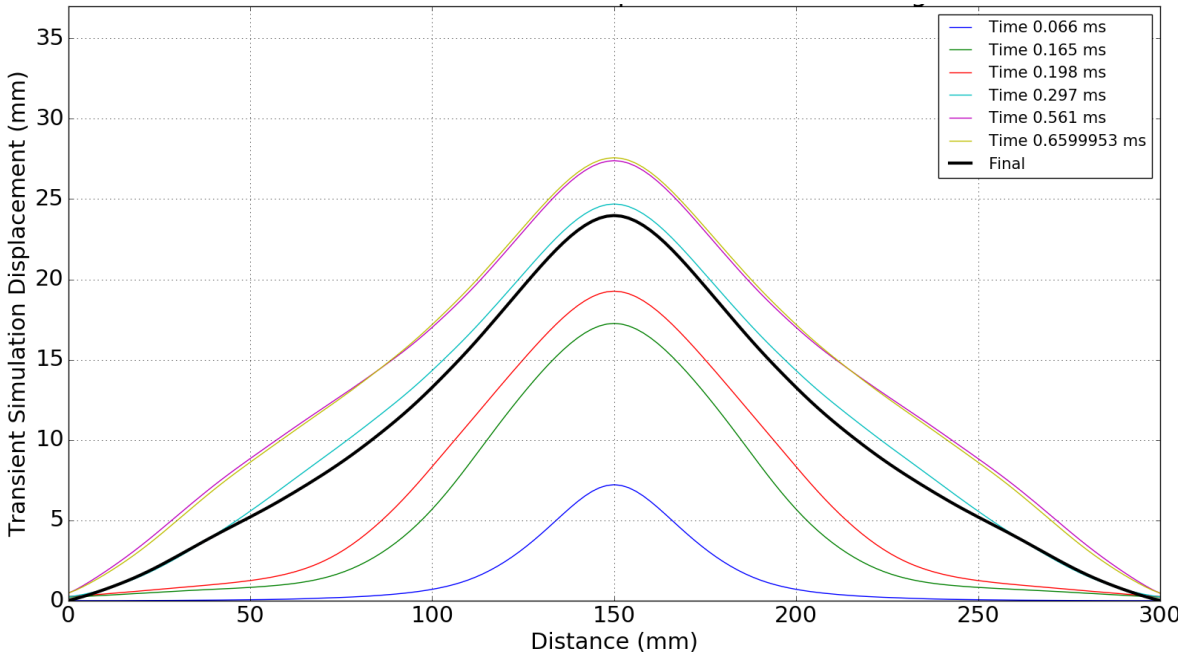

(b) 50mm Stand-off distance

Figure B.7: Transient plate deformation data from simulation for 20g AIR charge detonations

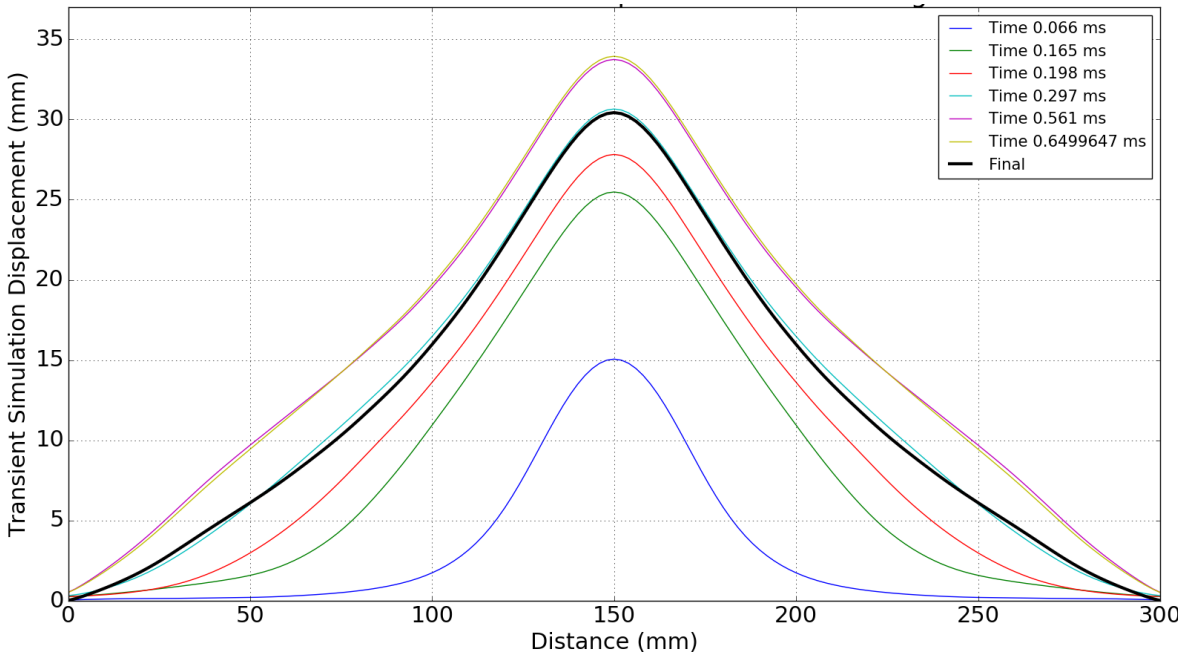

(a) 40mm Stand-off distance

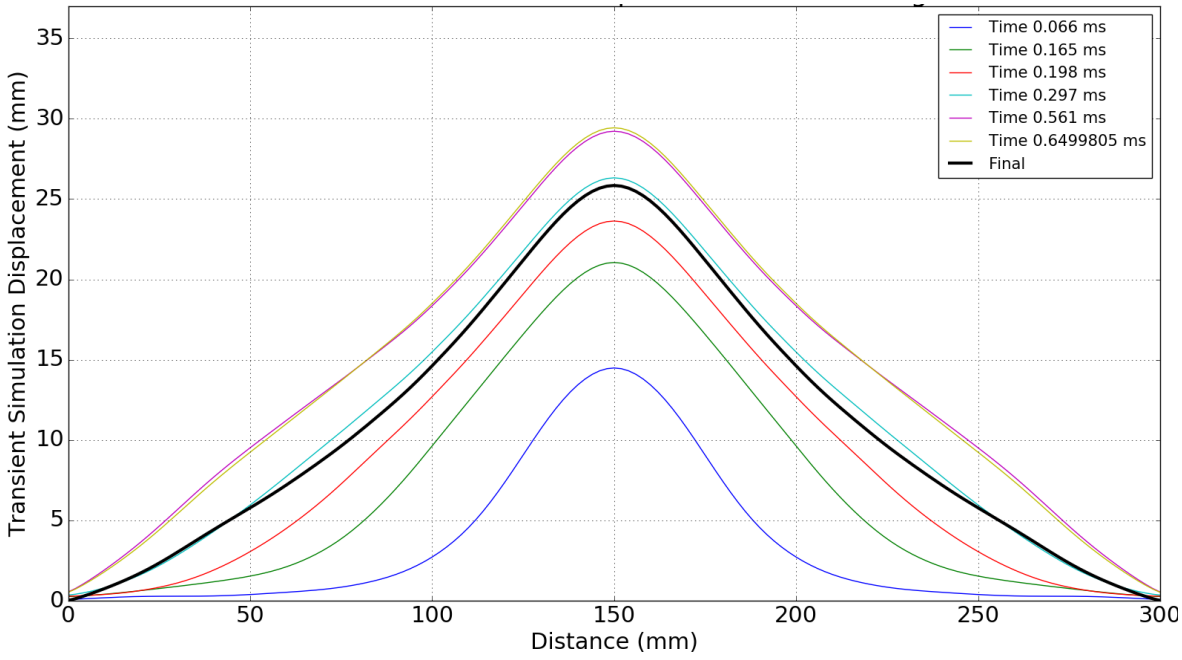

(b) 50mm Stand-off distance

Figure B.8: Transient plate deformation data from simulation for 25g AIR charge detonations

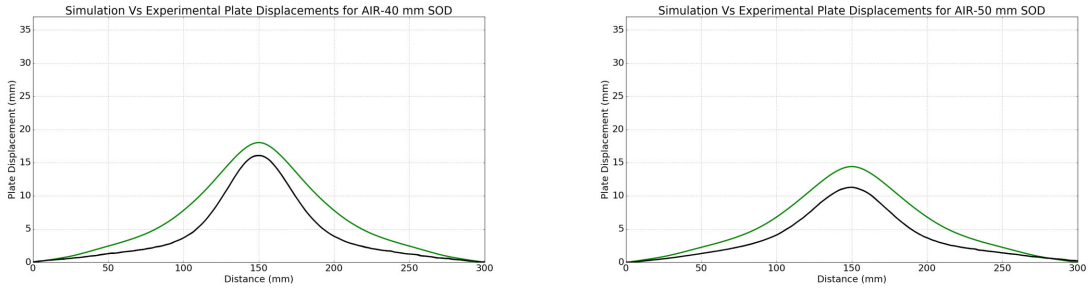

Figure B.9: Comparison of the Simulation (green) and the experimental (black) final plate deformations for AIR 10g 40 and 50mm SOD.

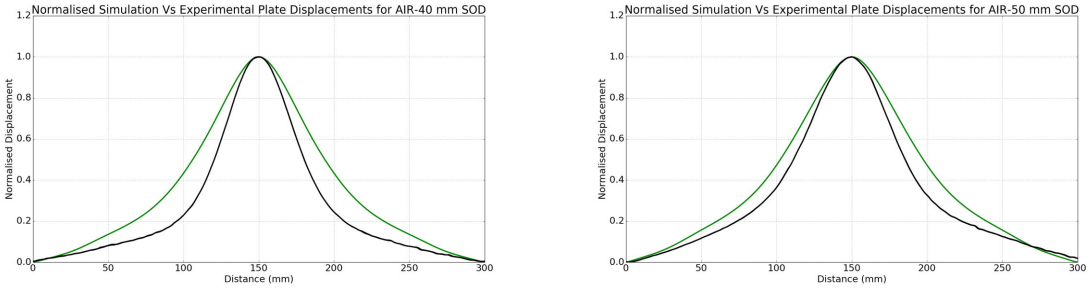

Figure B.10: Comparison of the normalised Simulation (green) and the experimental (black) final plate deformations for AIR 10g 40 and 50mm SOD.

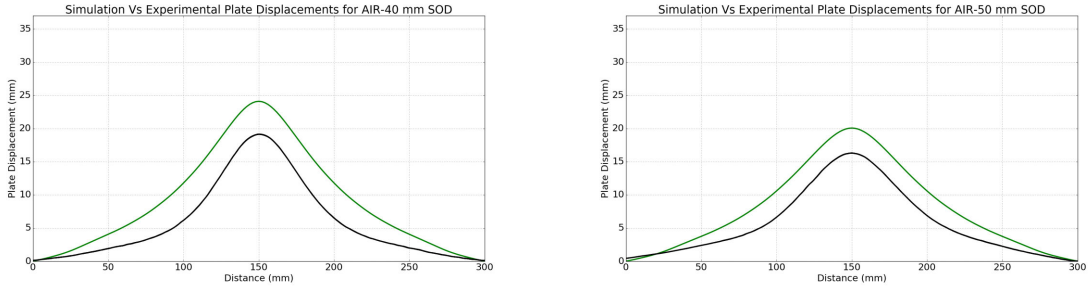

Figure B.11: Comparison of the Simulation (green) and the experimental (black) final plate deformations for AIR 15g40 and 50mm SOD.

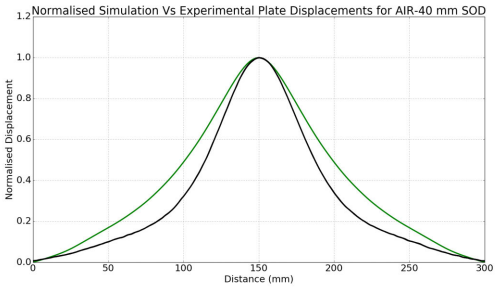

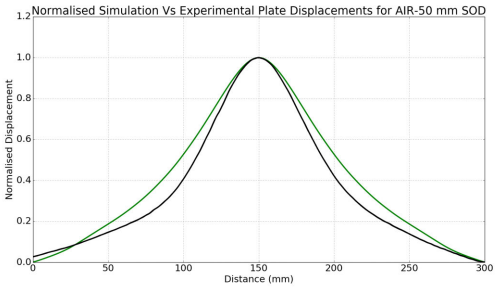

Figure B.12: Comparison of the normalised Simulation (green) and the experimental (black) final plate deformations for AIR 15g 40 and 50mm SOD.

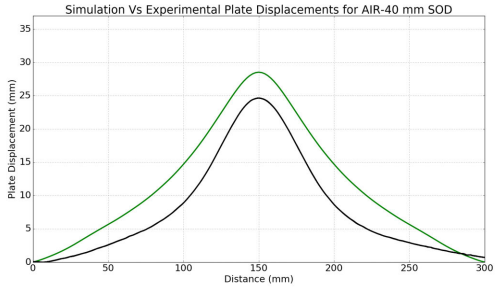

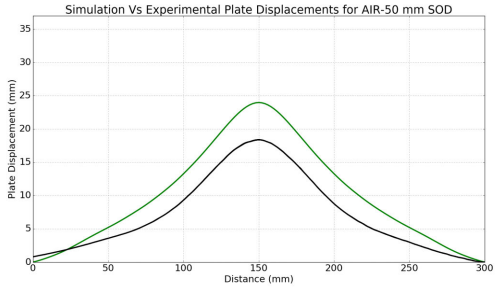

Figure B.13: Comparison of the Simulation (green) and the experimental (black) final plate deformations for AIR 20g 40 and 50mm SOD.

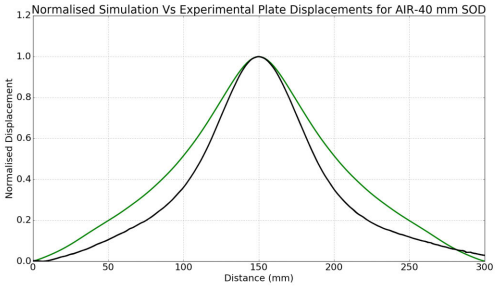

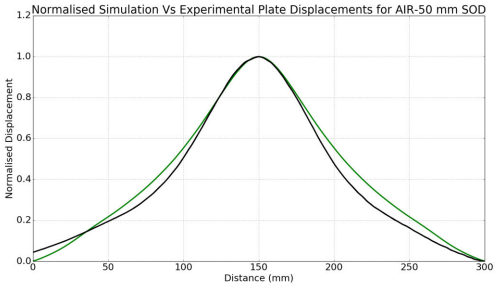

Figure B.14: Comparison of the normalised Simulation (green) and the experimental (black) final plate deformations for AIR 20g 40 and 50mm SOD.

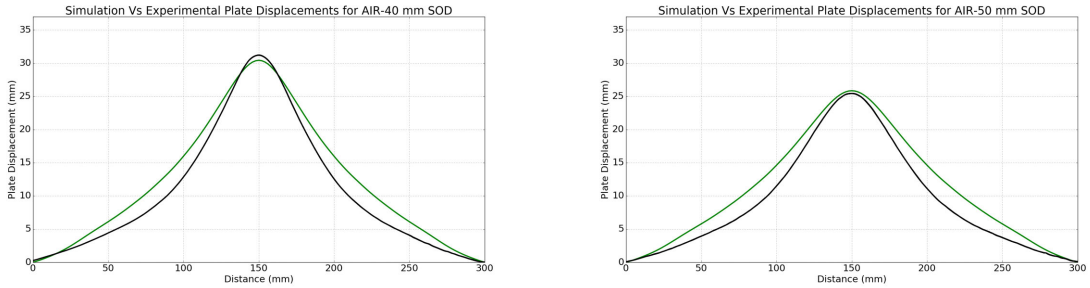

Figure B.15: Comparison of the Simulation (green) and the experimental (black) final plate deformations for AIR 25g 40 and 50mm SOD.

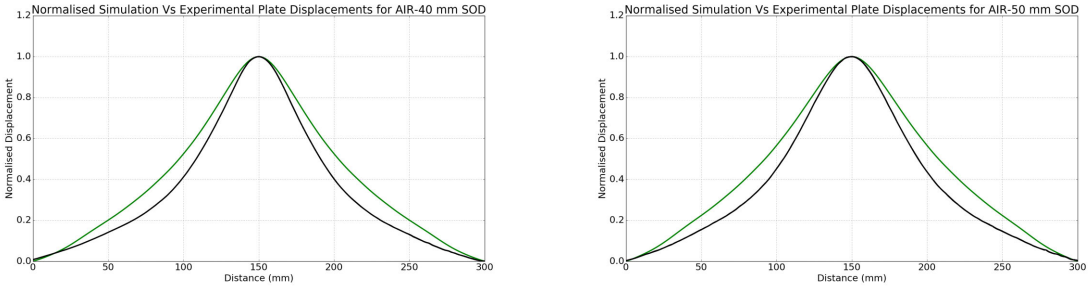

Figure B.16: Comparison of the normalised Simulation (green) and the experimental (black) final plate deformations for AIR 25g 40 and 50mm SOD.

B.2 VBP

B.2.1 VBP - Midpoint Deflection

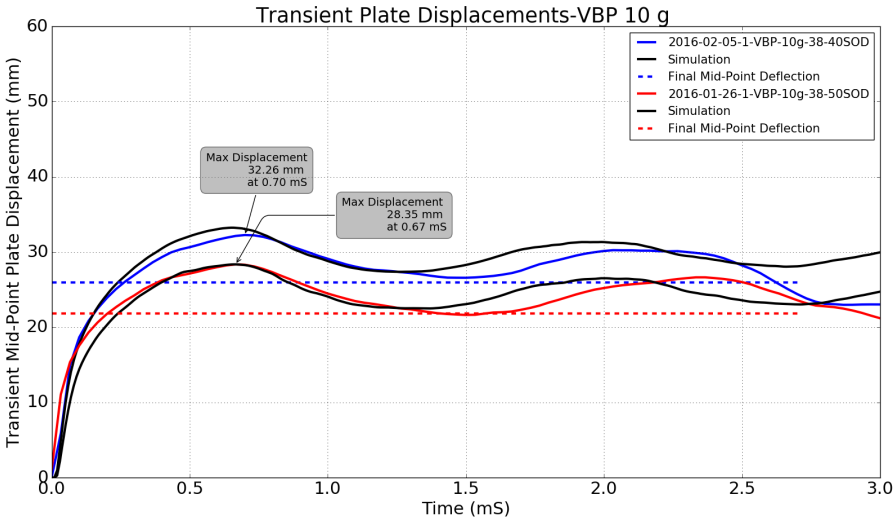

Figure B.17: Transient midpoint deflection values for the VBP 10g simulations(black) and the experimental values (blue and red)

B.2.2 VBP - Tranient Deflection Results

B.2.3 VBP - Final Plate Profiles

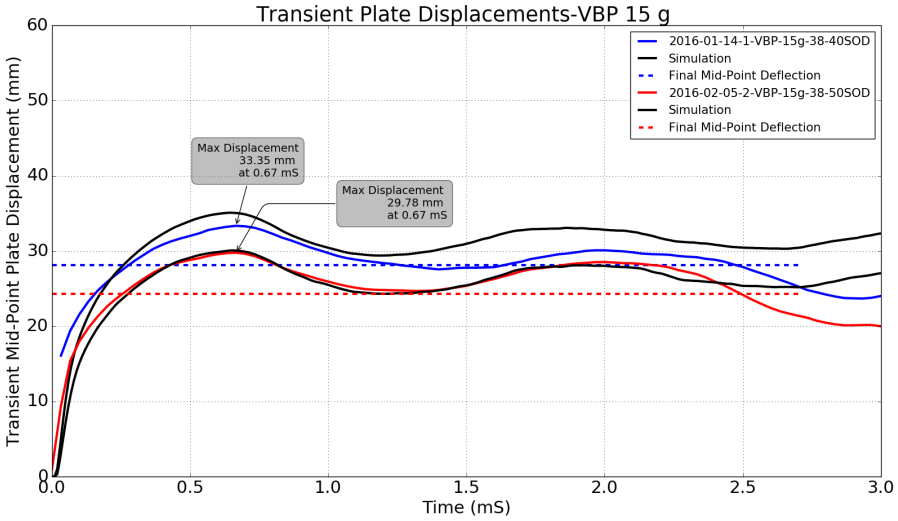

Figure B.18: Transient midpoint deflection values for the VBP 15g simulations(black) and the experimental values (blue and red)

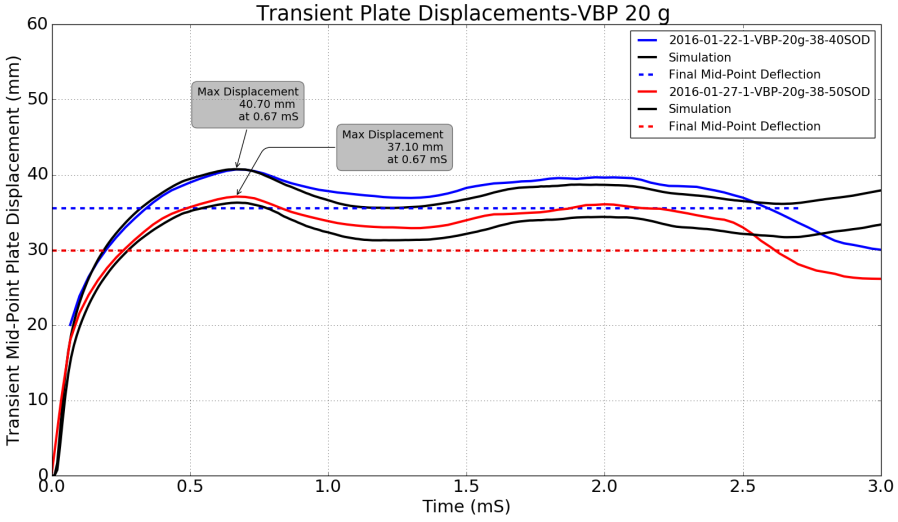

Figure B.19: Transient midpoint deflection values for the VBP 20g simulations(black) and the experimental values (blue and red)

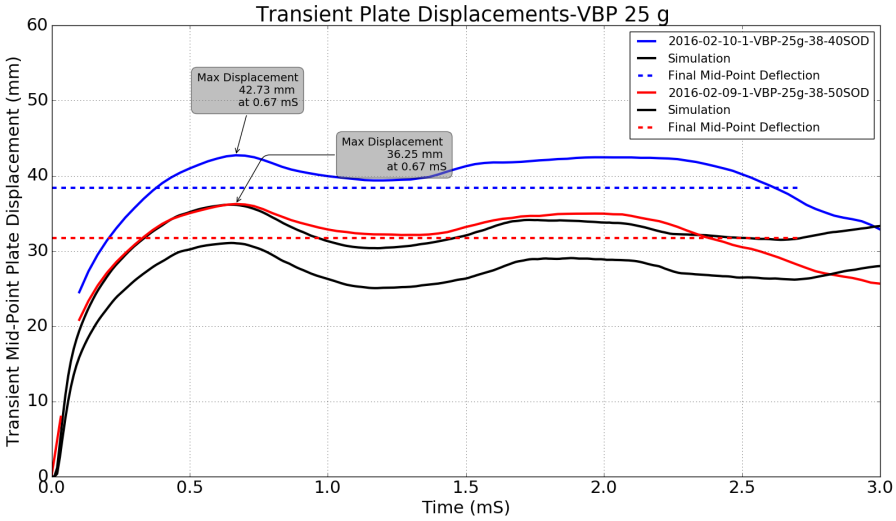

Figure B.20: Transient midpoint deflection values for the VBP 25g simulations(black) and the experimental values (blue and red)

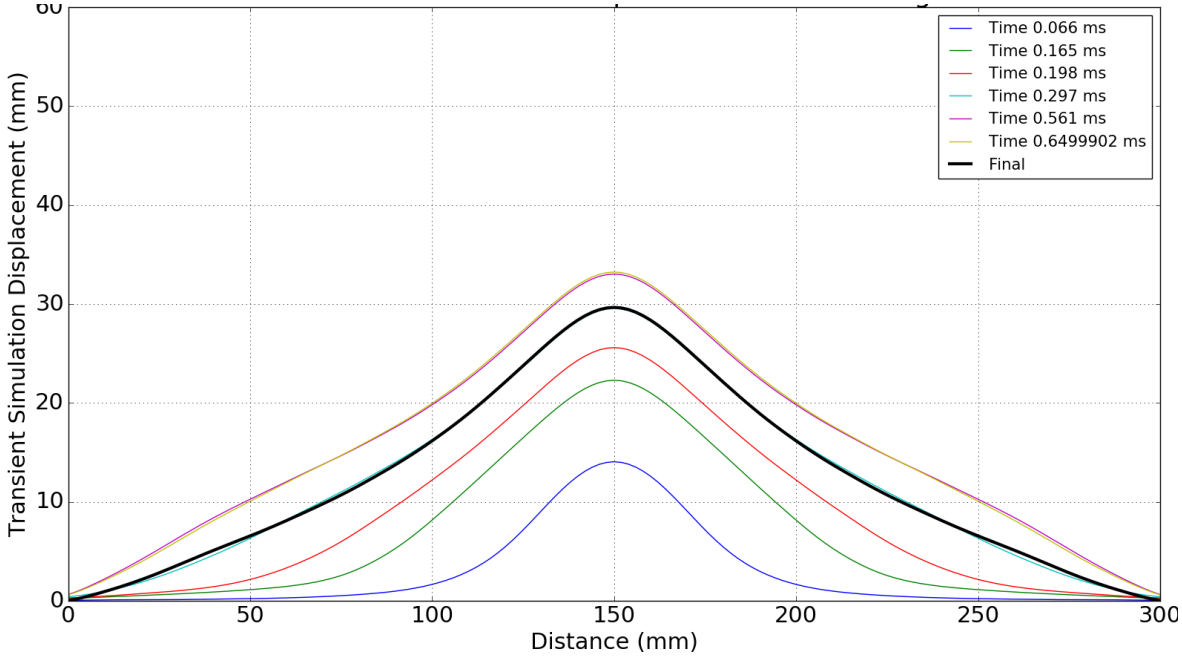

(a) 40mm Stand-off distance

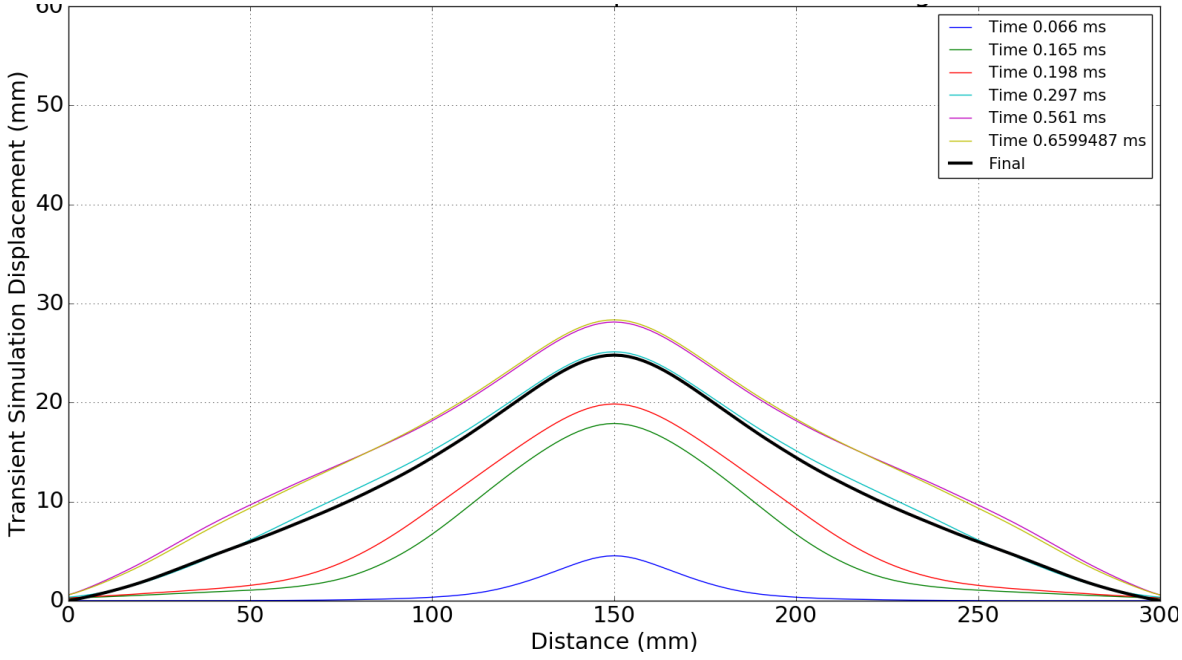

(b) 50mm Stand-off distance

Figure B.21: Transient plate deformation data from simulation for 10g VBP charge detonations

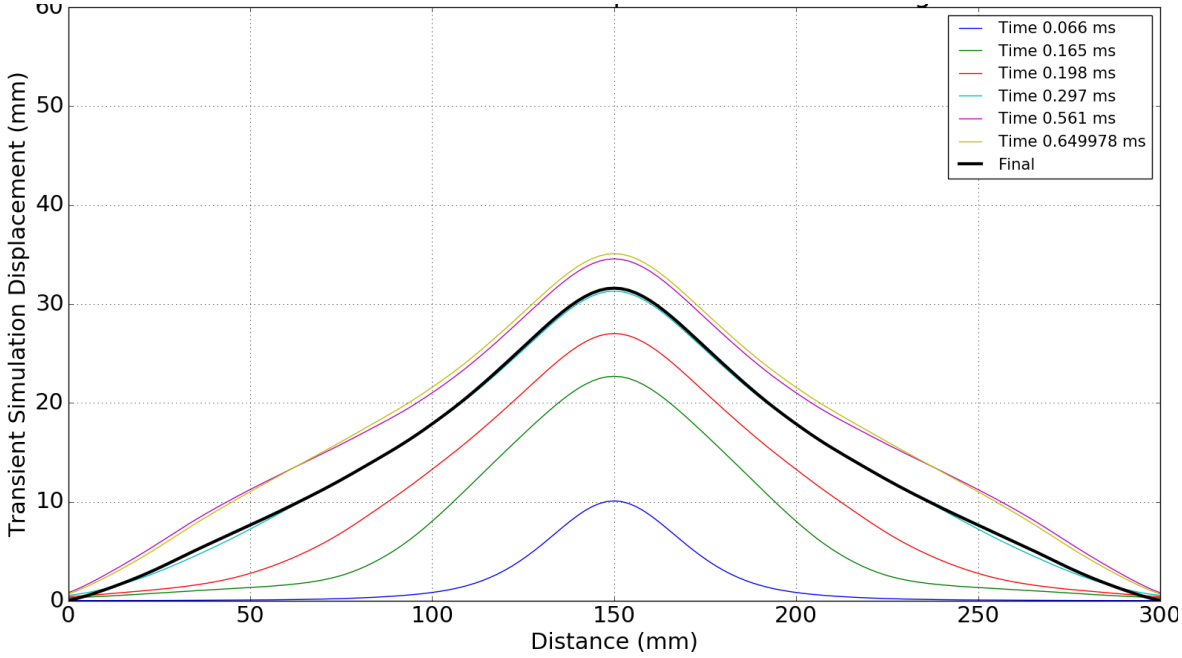

(a) 40mm Stand-off distance

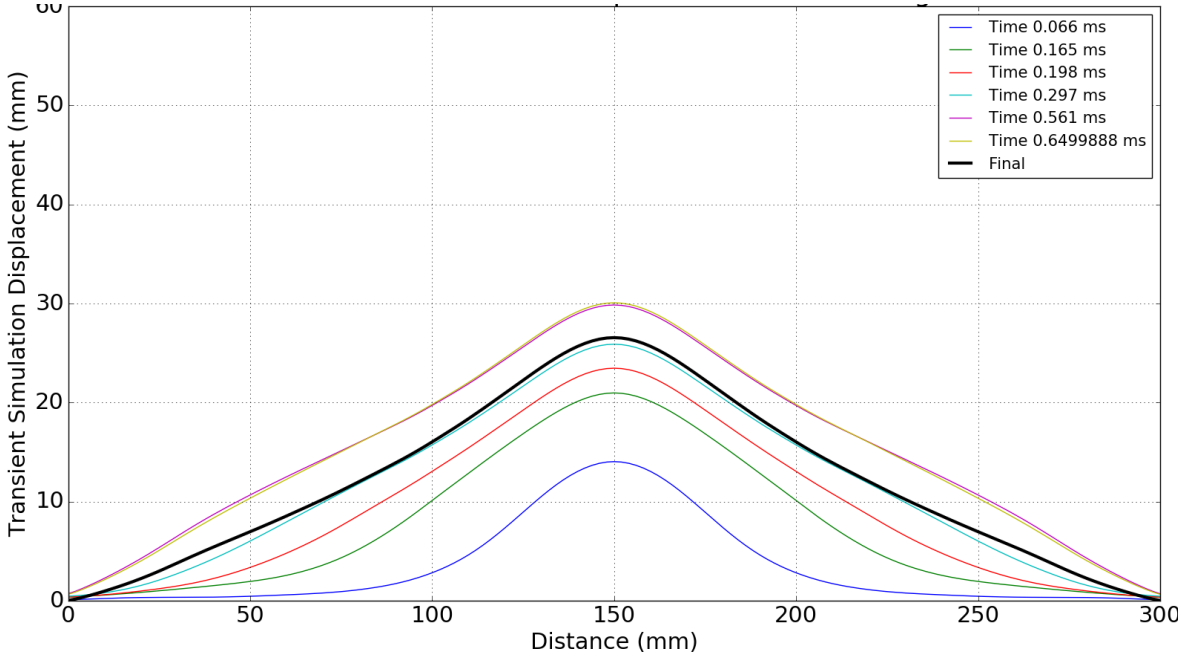

(b) 50mm Stand-off distance

Figure B.22: Transient plate deformation data from simulation for 15g VBP charge detonations

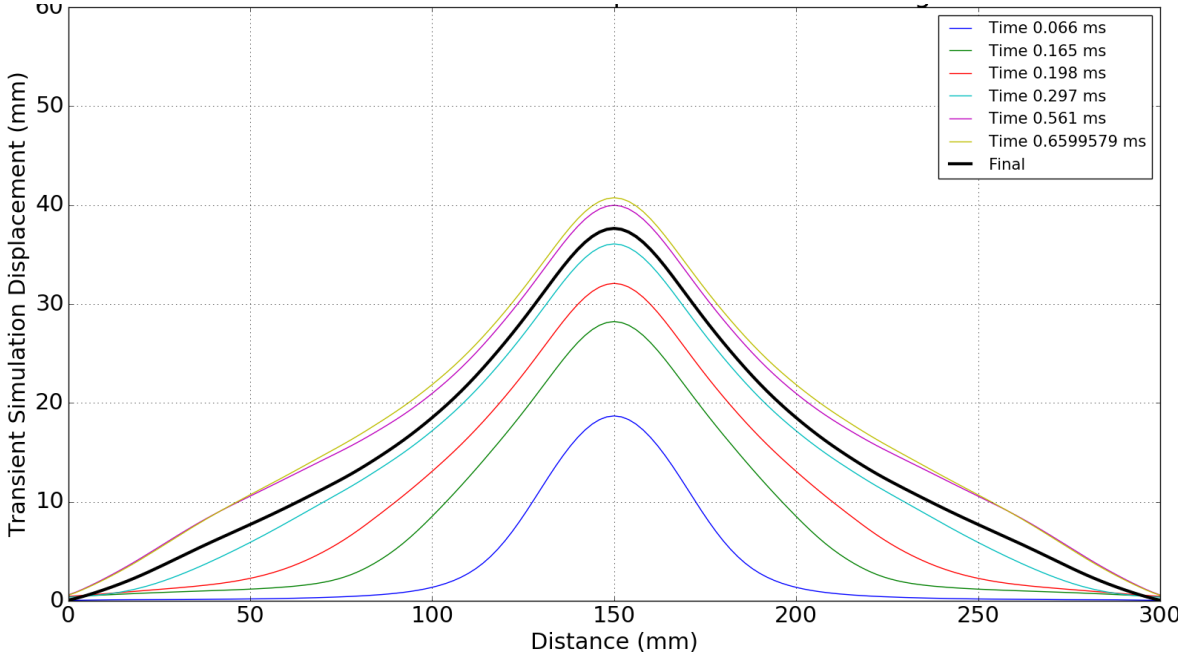

(a) 40mm Stand-off distance

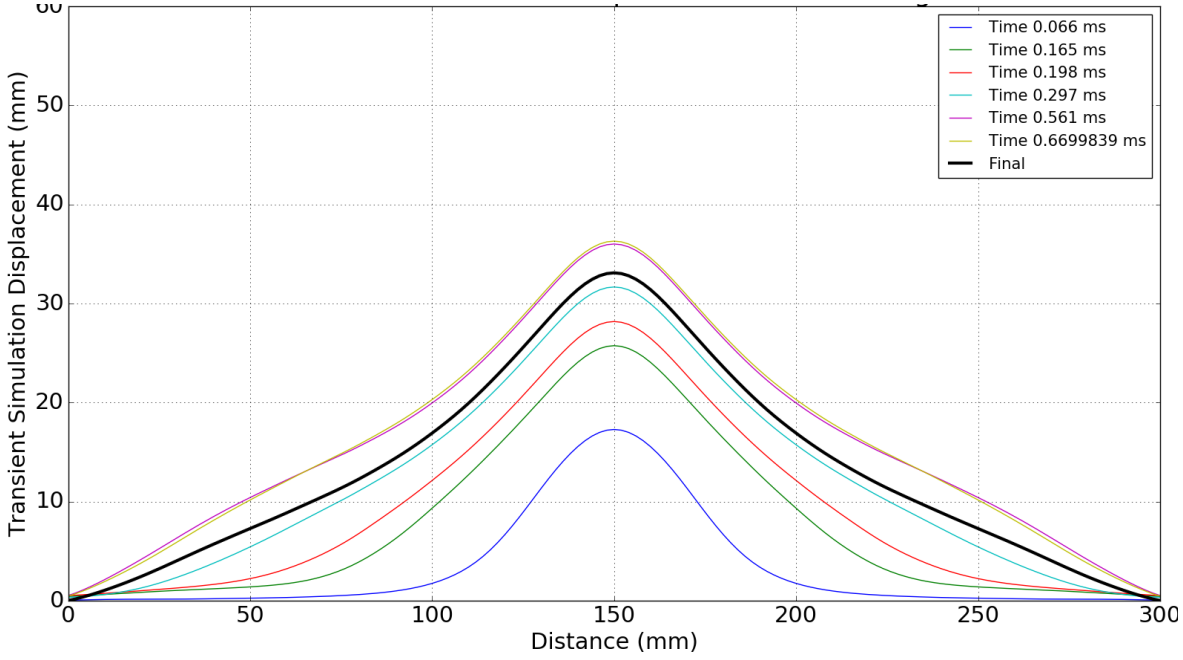

(b) 50mm Stand-off distance

Figure B.23: Transient plate deformation data from simulation for 20g VBP charge detonations

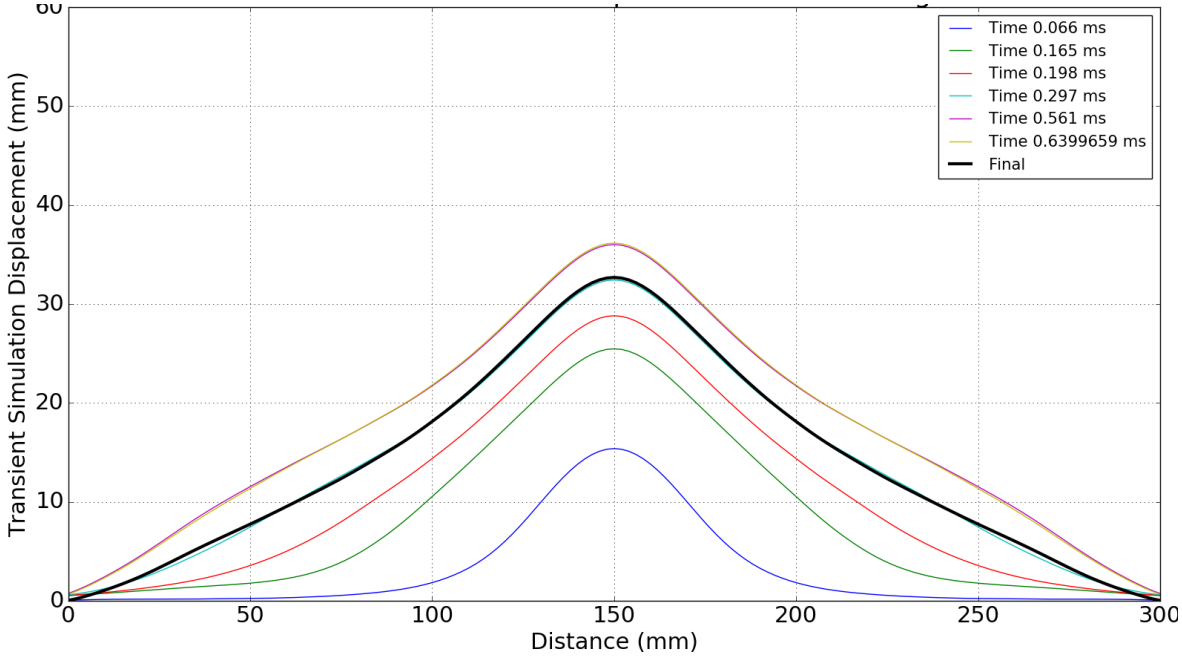

(a) 40mm Stand-off distance

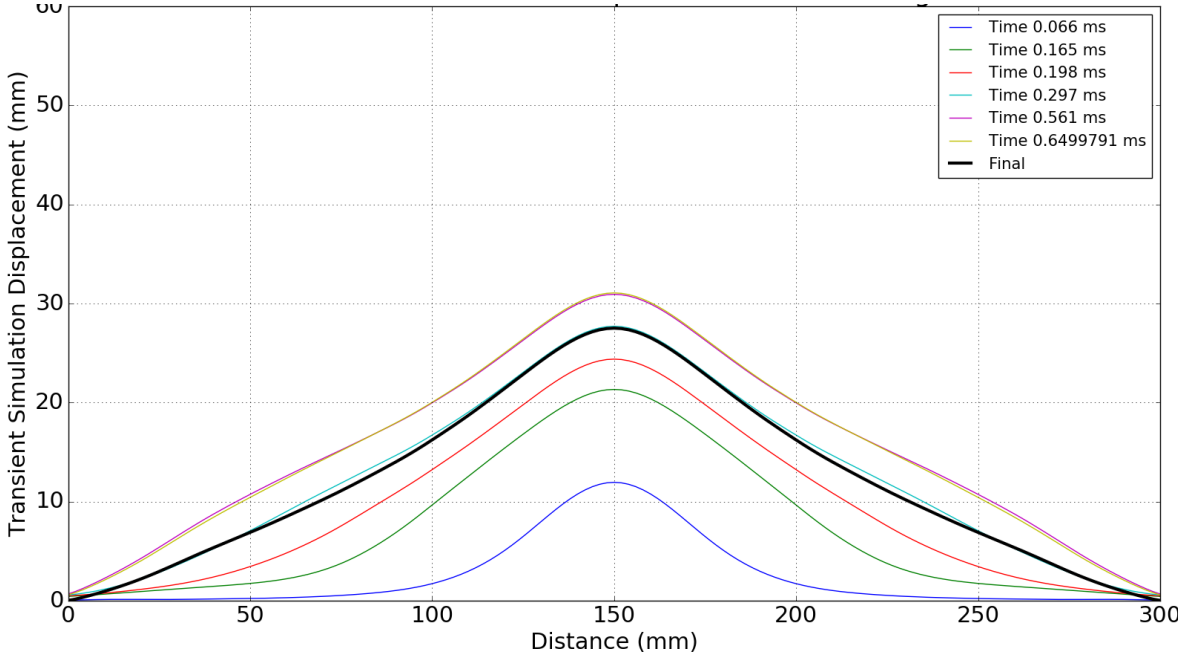

(b) 50mm Stand-off distance

Figure B.24: Transient plate deformation data from simulation for 25g VBP charge detonations

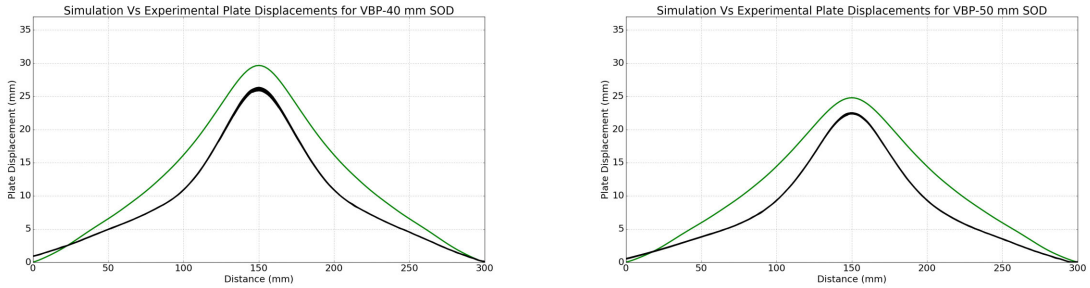

Figure B.25: Comparison of the Simulation (green) and the experimental (black) final plate deformations for VBP 10g 40 and 50mm SOD.

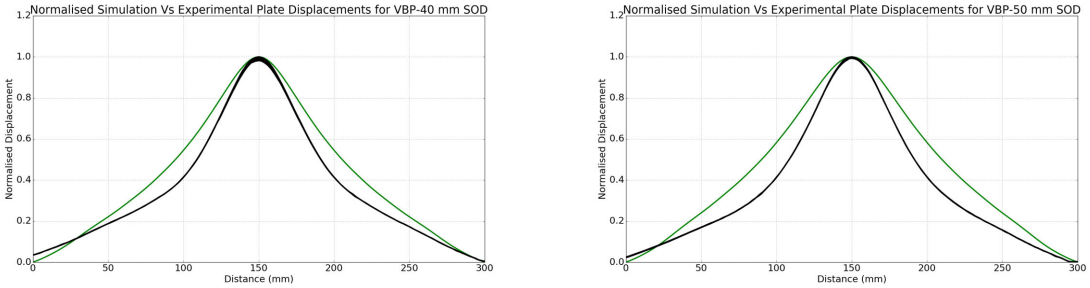

Figure B.26: Comparison of the normalised Simulation (green) and the experimental (black) final plate deformations for VBP 10g 40 and 50mm SOD.

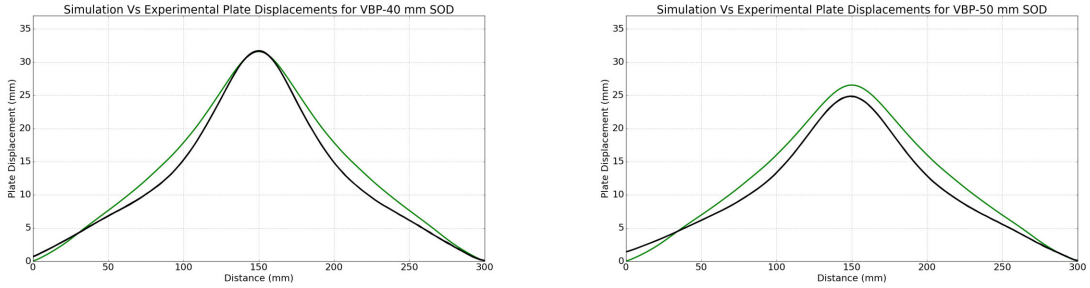

Figure B.27: Comparison of the Simulation (green) and the experimental (black) final plate deformations for VBP 15g40 and 50mm SOD.

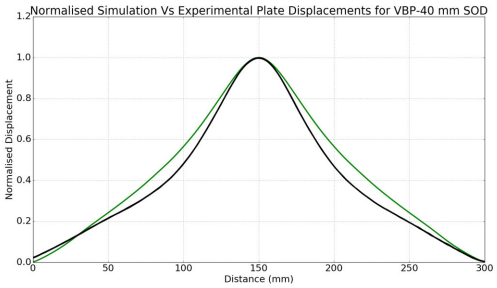

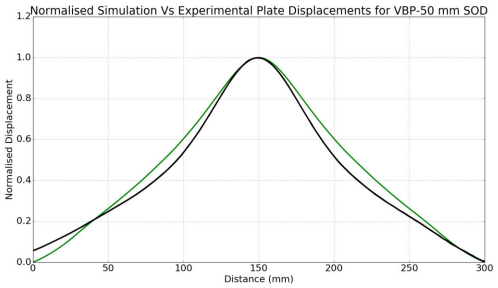

Figure B.28: Comparison of the normalised Simulation (green) and the experimental (black) final plate deformations for VBP 15g 40 and 50mm SOD.

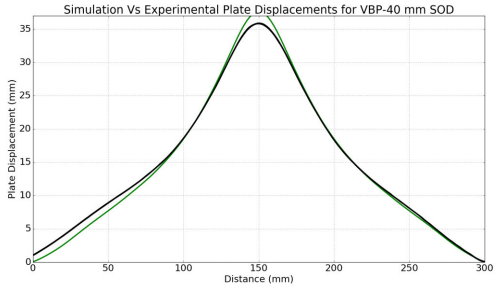

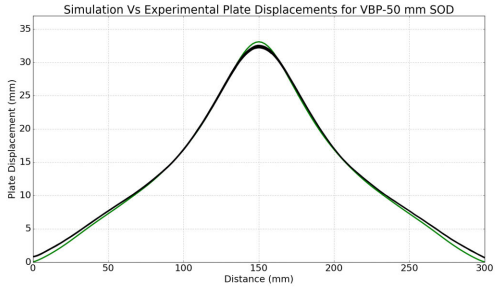

Figure B.29: Comparison of the Simulation (green) and the experimental (black) final plate deformations for VBP 20g 40 and 50mm SOD.

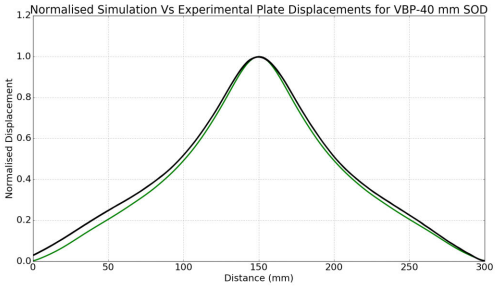

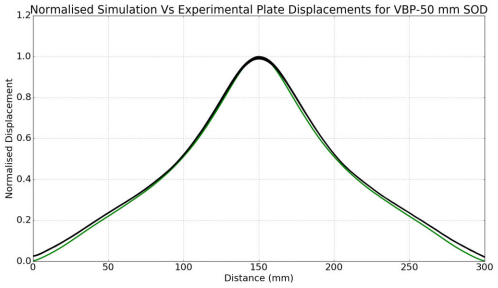

Figure B.30: Comparison of the normalised Simulation (green) and the experimental (black) final plate deformations for VBP 20g 40 and 50mm SOD.

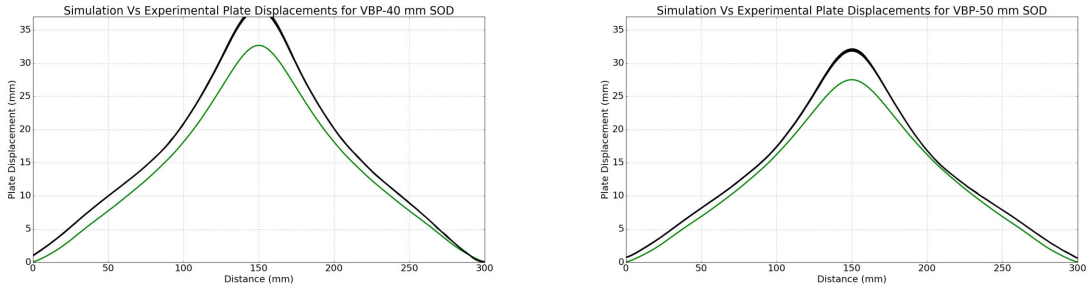

Figure B.31: Comparison of the Simulation (green) and the experimental (black) final plate deformations for VBP 25g 40 and 50mm SOD.

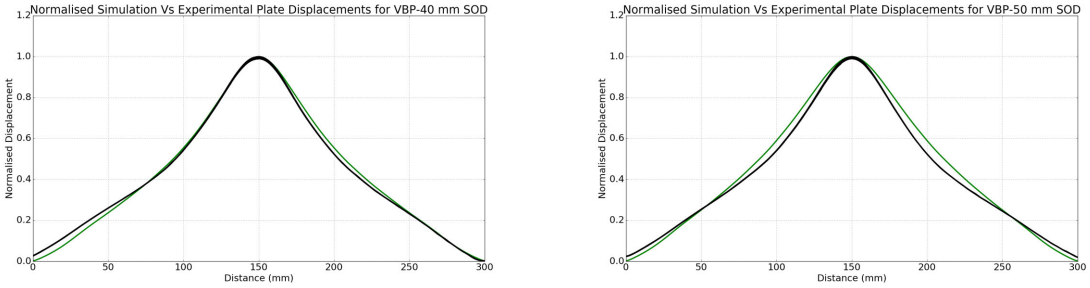

Figure B.32: Comparison of the normalised Simulation (green) and the experimental (black) final plate deformations for VBP 25g 40 and 50mm SOD.

B.3 SBP

B.3.1 SBP - Midpoint Deflection

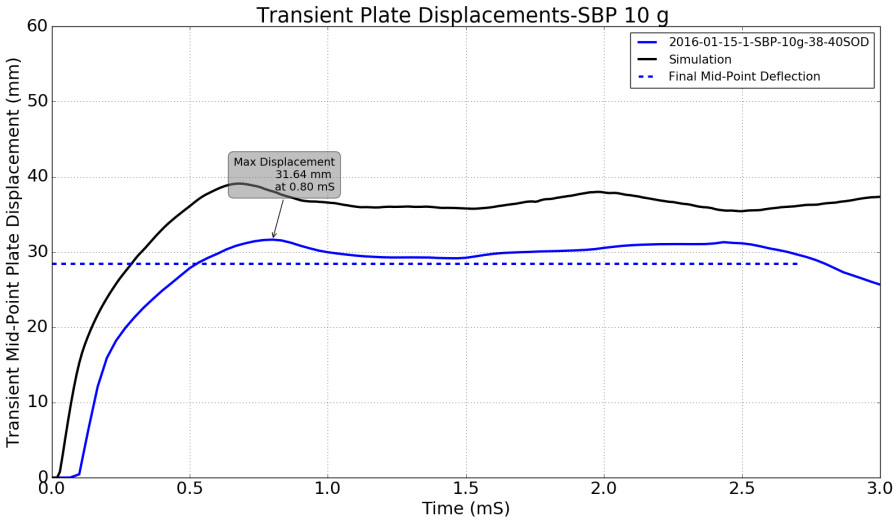

Figure B.33: Transient midpoint deflection values for the SBP 10g simulations(black) and the experimental values (blue and red)

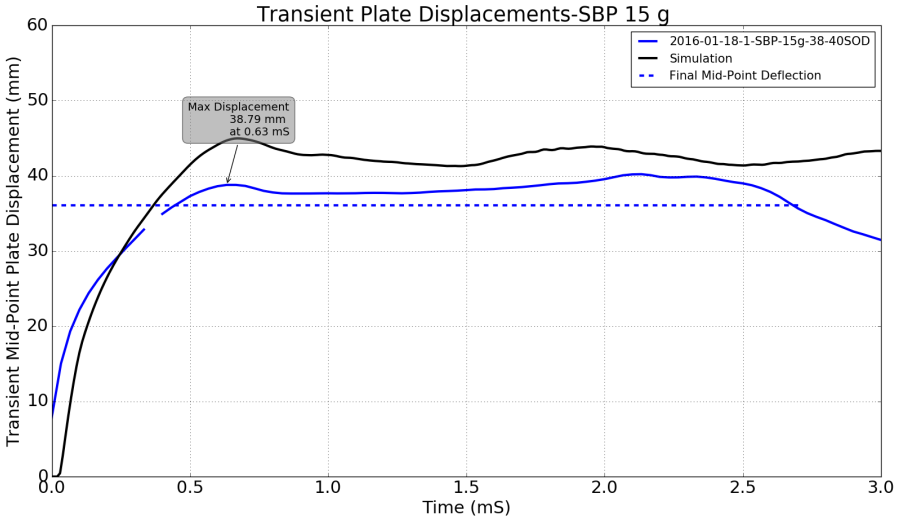

Figure B.34: Transient midpoint deflection values for the SBP 15g simulations(black) and the experimental values (blue and red)

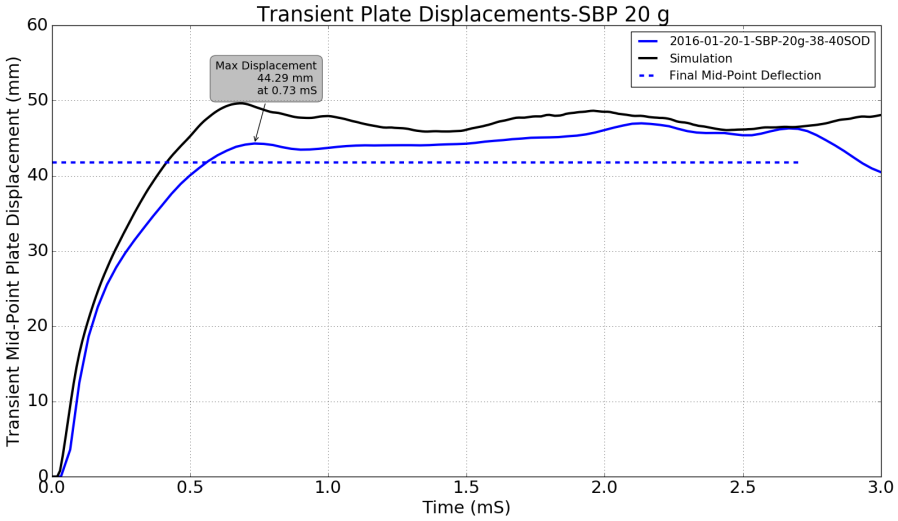

Figure B.35: Transient midpoint deflection values for the SBP 20g simulations(black) and the experimental values (blue and red)

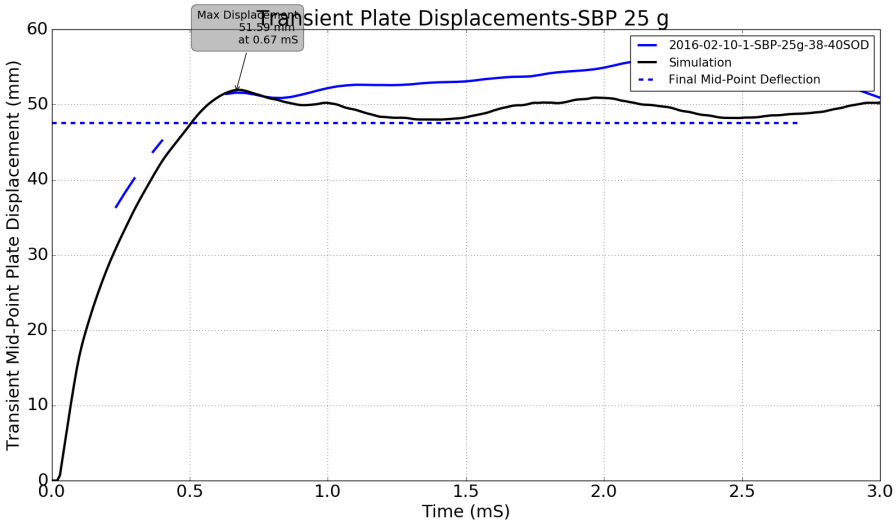

Figure B.36: Transient midpoint deflection values for the SBP 25g simulations(black) and the experimental values (blue and red)

B.3.2 SBP - Tranient Deflection Results

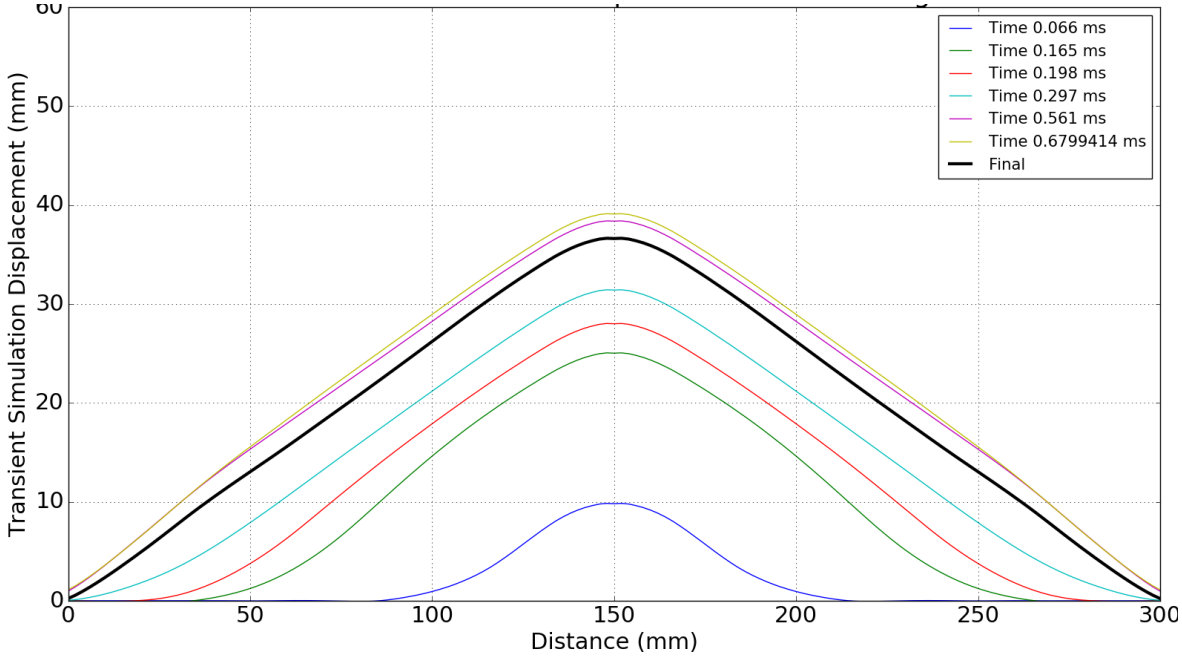

(a) SBP 10g 40 SOD 10 DOB simulation Transient Strain

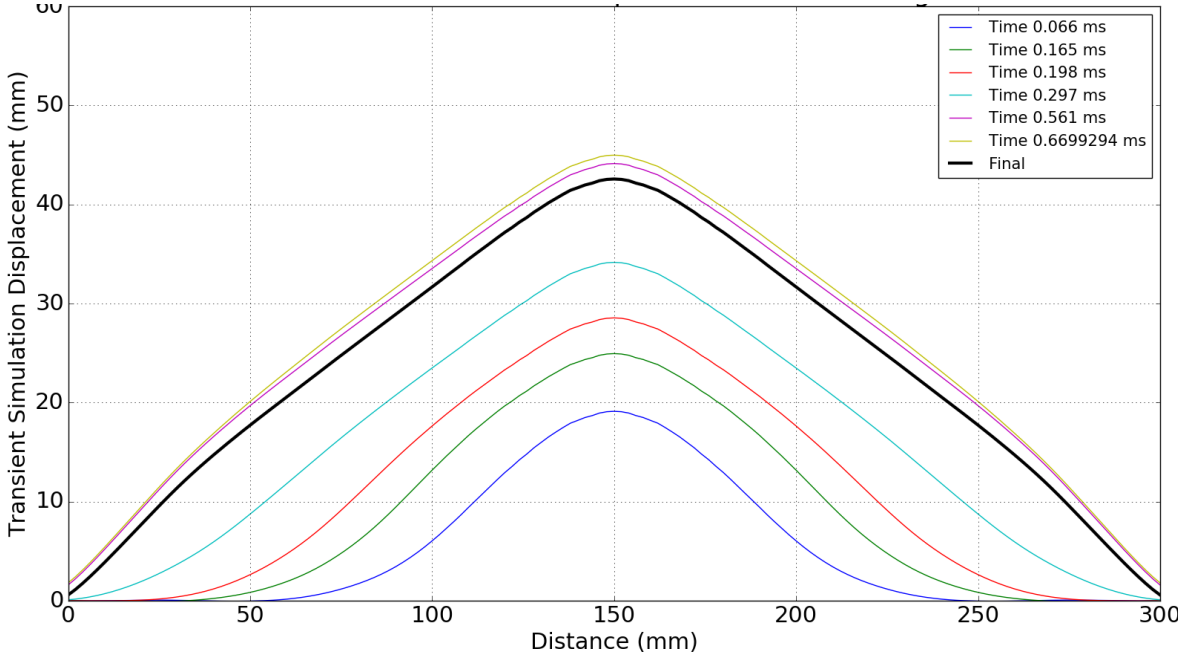

(b) SBP 15g 40 SOD 10 DOB simulation Transient Strain

Figure B.37: Transient plate deformation data from simulation for 10g and 15g SBP charge detonations

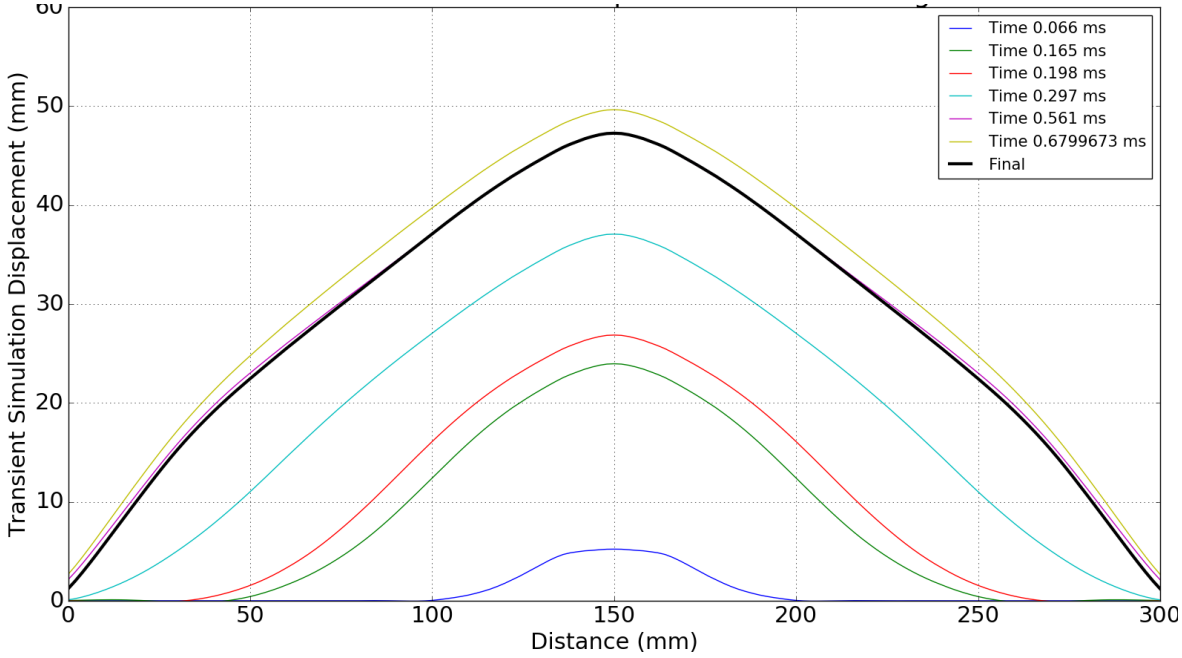

(a) SBP 20g 40 SOD 10 DOB simulation Transient Strain

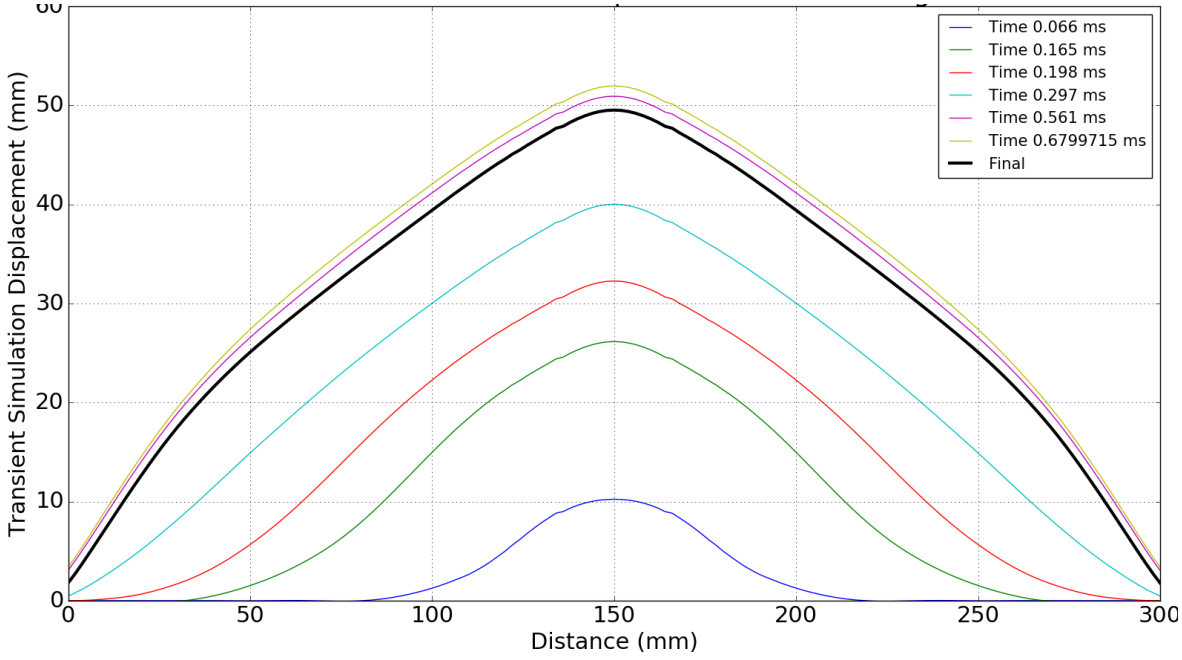

(b) SBP 25g 40 SOD 10 DOB simulation Transient Strain

Figure B.38: Transient plate deformation data from simulation for 20g and 25g SBP charge detonations

B.3.3 SBP - Final Plate Profiles

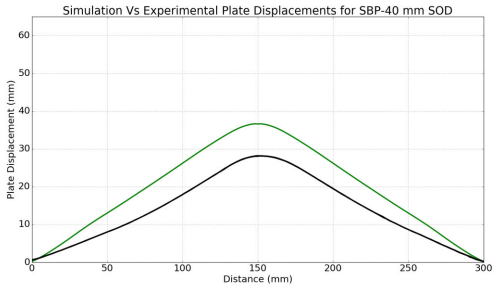

Figure B.39: Comparison of the Simulation (green) and the experimental (black) final plate deformations for SBP 10g 40 and 50mm SOD.

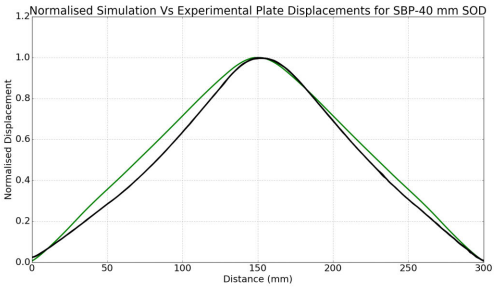

Figure B.40: Comparison of the normalised Simulation (green) and the experimental (black) final plate deformations for SBP 10g 40 and 50mm SOD.

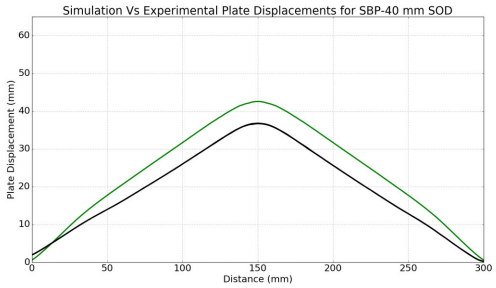

Figure B.41: Comparison of the Simulation (green) and the experimental (black) final plate deformations for SBP 15g40 and 50mm SOD.

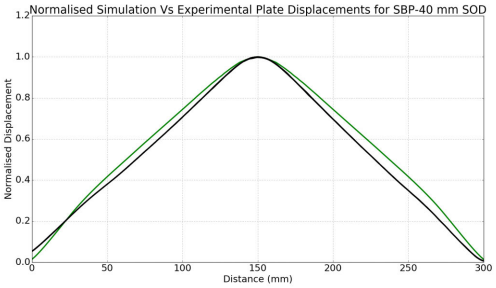

Figure B.42: Comparison of the normalised Simulation (green) and the experimental (black) final plate deformations for SBP 15g 40 and 50mm SOD.

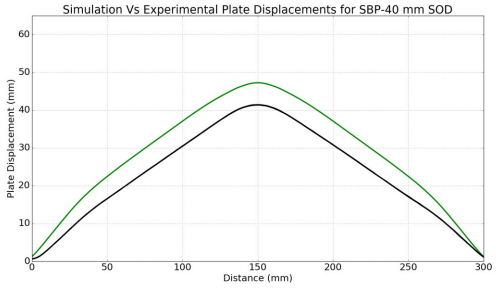

Figure B.43: Comparison of the Simulation (green) and the experimental (black) final plate deformations for SBP 20g 40 and 50mm SOD.

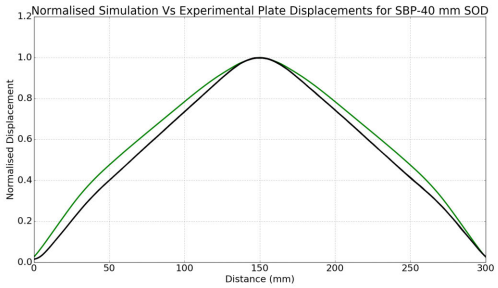

Figure B.44: Comparison of the normalised Simulation (green) and the experimental (black) final plate deformations for SBP 20g 40 and 50mm SOD.

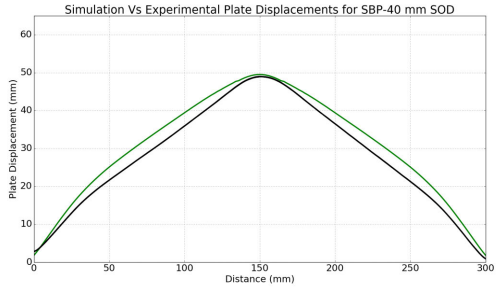

Figure B.45: Comparison of the Simulation (green) and the experimental (black) final plate deformations for SBP 25g 40 and 50mm SOD.

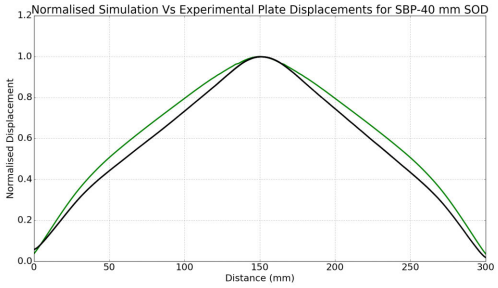

Figure B.46: Comparison of the normalised Simulation (green) and the experimental (black) final plate deformations for SBP 25g 40 and 50mm SOD.

Appendix C

Simulation Input Deck

```
 $# LS-DYNA Keyword file created by LS-PrePost(R) V4.3 (Beta) - 20Jul2014(10:00)
$# Created on Nov-23-2015 (09:35:21)
*KEYWORD MEMORY=550000000 NCPU=4
$$
*TITLE
$#                                                                         title
LS-DYNA keyword deck by LS-PrePost
$=========================================================================
$                                LS-OPT
$=========================================================================
*PARAMETER
$#   prmr1      val1     prmr2      val2     prmr3      val3     prmr4      val4
R      jca       362
R      jcb       642
R     jcq1         0
R     jcq2         0
R      jcc     0.042
R     jcc1         0
R     jcc2         0
R      jcn    0.5597
R      jcm      0.81
R      SOD        50
R   CHARGE        15
```

```
R     DIAM        19
R    THICK         3
R     Tmax      3e-5
R    EXBOT         0
*PARAMETER_EXPRESSION
RHEIGHT   (CHARGE/0.001601)/615.752
*PARAMETER_EXPRESSION
RPLATE    (HEIGHT+SOD)+THICK/2
*PARAMETER_EXPRESSION
REXTOP    EXBOT+HEIGHT
*PARAMETER_EXPRESSION
RSTOP     EXTOP+10
*PARAMETER_EXPRESSION
RDET      EXBOT+2
*PARAMETER_EXPRESSION
RCLAMP1   PLATE+1.5
*PARAMETER_EXPRESSION
RCLAMP2   CLAMP1-THICK
$#
*CONTROL_ALE
$#     dct      nadv      meth      afac      bfac      cfac      dfac      efac
        -1         1        -2      -1.0       0.0       0.0       0.0       0.0
$#   start       end     aafac     vfact      prit       ebc      pref   nsidebc
       0.0 1.00000E20       1.0 1.00000E-6         0         0    0.1013         0
$#    ncpl      nbkt    imascl    checkr
         1        50         0       0.1
*CONTROL_ENERGY
$#    hgen      rwen    slnten     rylen
         2         2         1         1
*CONTROL_SOLUTION
$#    soln       nlq     isnan     lcint
         0         0         1       100
*CONTROL_TERMINATION
$#  endtim    endcyc     dtmin    endeng    endmas
```

```
0.35000001         0       0.0       0.0      25.0
$=============================================================================
$                                   CONTROL
$=============================================================================
*CONTROL_TIMESTEP
$#  dtinit    tssfac      isdo    tslimt     dt2ms      lctm     erode     ms1st
1.00000E-7       0.5         0       0.0       0.0         0         0         0
$#  dt2msf   dt2mslc     imscl    unused    unused     rmscl
       0.0         0         0                         0.0
*DATABASE_MATSUM
$#      dt    binary      lcur     ioopt
1.00000E-5         0         0         1
*DATABASE_NODFOR
$#      dt    binary      lcur     ioopt
     0.001         3         0         1
*DATABASE_NODOUT
$#      dt    binary      lcur     ioopt   option1   option2
      16.5         3         0         1       0.0
*DATABASE_BINARY_D3DUMP
$#    cycl      lcdt      beam     npltc    psetid
       0.0         0         0         5         0
*DATABASE_BINARY_D3PLOT
$#      dt      lcdt      beam     npltc    psetid
      0.01         0         0         0         0
$#   ioopt
         0
$*DATABASE_NODAL_FORCE_GROUP
$$#    nsid       cid
$       200         0
*DATABASE_HISTORY_NODE_SET
$#     id1       id2       id3       id4       id5       id6       id7       id8
       201         0         0         0         0         0         0         0
*DATABASE_FSI
$#      dt
```

```
1.00000E-5
$#dbsfi_id       sid     stype      swid    convid
        12         1         1         0         0
        13       120         1         0         0
$$=========================================================================
$                                     Boundary
$$=========================================================================
*BOUNDARY_SPC_SET
$Air Block XZ Symmetry$$$$$$$$$$$$$$$$$
$#    nsid       cid      dofx      dofy      dofz     dofrx     dofry     dofrz
       101         0         0         1         0         1         0         1
*BOUNDARY_SPC_SET
$Air Block YZ Symmetry$$$$$$$$$$$$$$$$$
$#    nsid       cid      dofx      dofy      dofz     dofrx     dofry     dofrz
       102         0         1         0         0         0         1         1
*BOUNDARY_SPC_SET
$ Air Block Bottom of Mesh$$$$$$$$$$$$$
$#    nsid       cid      dofx      dofy      dofz     dofrx     dofry     dofrz
       103         0         1         1         1         1         1         1
$*BOUNDARY_SPC_SET
$ Plate clamped boundary$$$$$$$$$$$$$$$
$$#    nsid       cid      dofx      dofy      dofz     dofrx     dofry     dofrz
$       200         0         1         1         1         0         0         0
*BOUNDARY_SPC_SET
$ Plate XZ Symmetry    $$$$$$$$$$$$$$$$
$#    nsid       cid      dofx      dofy      dofz     dofrx     dofry     dofrz
       201         0         0         1         0         1         0         1
*BOUNDARY_SPC_SET
$ Plate YZ Symmetry    $$$$$$$$$$$$$$$$
$#    nsid       cid      dofx      dofy      dofz     dofrx     dofry     dofrz
       202         0         1         0         0         0         1         1
*BOUNDARY_SPC_SET
$ Clamp F XZ Symmetry  $$$$$$$$$$$$$$$$
$#    nsid       cid      dofx      dofy      dofz     dofrx     dofry     dofrz
```

```
       121         0         0         1         0         1         0         1
*BOUNDARY_SPC_SET
$ Clamp F YZ Symmetry  $$$$$$$$$$$$$$$$$
$#    nsid       cid      dofx      dofy      dofz     dofrx     dofry     dofrz
       122         0         1         0         0         0         1         1
*BOUNDARY_SPC_SET
$ Clamp F Ridgid Point $$$$$$$$$$$$$$$$$
$#    nsid       cid      dofx      dofy      dofz     dofrx     dofry     dofrz
       124         0         1         1         0         0         0         0
*BOUNDARY_SPC_SET
$ Clamp B XZ Symmetry$$$$$$$$$$$$$$$$$$
$#    nsid       cid      dofx      dofy      dofz     dofrx     dofry     dofrz
       131         0         0         1         0         1         0         1
*BOUNDARY_SPC_SET
$ Clamp B YZ Symmetry$$$$$$$$$$$$$$$$$$
$#    nsid       cid      dofx      dofy      dofz     dofrx     dofry     dofrz
       132         0         1         0         0         0         1         1
*BOUNDARY_SPC_SET
$ Clamp B YZ Symmetry$$$$$$$$$$$$$$$$$$
$#    nsid       cid      dofx      dofy      dofz     dofrx     dofry     dofrz
       134         0         1         1         1         0         0         0
$$==========================================================================
$                                    CONTACT
$$==========================================================================
*CONTACT_AUTOMATIC_SURFACE_TO_SURFACE_ID
$#     cid                                                           title
         1 Plate Contact Front Clamp
$#    ssid      msid     sstyp     mstyp    sboxid    mboxid       spr       mpr
        21        11         0         0         0         0         0         0
$#      fs        fd        dc        vc       vdc    penchk        bt        dt
      0.17       0.0       0.0       0.0       0.0         1       0.01.00000E20
$#     sfs       sfm       sst       mst      sfst      sfmt       fsf       vsf
       1.0       1.0       0.0       0.0       1.0       1.0       1.0       1.0
*CONTACT_AUTOMATIC_SURFACE_TO_SURFACE_ID
```

```
$#     cid                                                          title
         2 Plate Contact Back Clamp
$#    ssid      msid     sstyp     mstyp    sboxid    mboxid       spr       mpr
        31        11         0         0         0         0         0         0
$#      fs        fd        dc        vc       vdc    penchk        bt        dt
      0.17       0.0       0.0       0.0       0.0         1       0.01.00000E20
$#     sfs       sfm       sst       mst      sfst      sfmt       fsf       vsf
       1.0       1.0       0.0       0.0       1.0       1.0       1.0       1.0
$$=========================================================================
$                                    PART
$$=========================================================================
*PART
$#                                                                   title
Explosive Pe4
$#     pid     secid       mid     eosid      hgid      grav    adpopt      tmid
        10      5060      1080      1080        10         0         0         0
*PART
$#                                                                   title
New Air Block
$#     pid     secid       mid     eosid      hgid      grav    adpopt      tmid
       100      5060       100       100        10         0         0         0
*PART
$#                                                                   title
New Plate
$#     pid     secid       mid     eosid      hgid      grav    adpopt      tmid
         1        30       107         0         0         0         0         0
$*PART
$$#                                                                   title
$Mass
$$#     pid     secid       mid     eosid      hgid      grav    adpopt      tmid
$       140        40         9         0        11         0         0         0
*PART
$#                                                                   title
Clamp-F
```

```
$#     pid     secid       mid     eosid      hgid      grav    adpopt      tmid
       120        40      1200         0        11         0         0         0
*PART
$#                                                                         title
Clamp-B
$#     pid     secid       mid     eosid      hgid      grav    adpopt      tmid
       130        40      1200         0        11         0         0         0
*PART
Sand
        20      5060         4         4        10         0         0         0
$ ========================================================================
$  SECTION Cards
$ ========================================================================
*SECTION_SHELL
$#   secid    elform      shrf       nip     propt   qr/irid     icomp     setyp
        30        16  0.833000         5         1         0         0         1
$#      t1        t2        t3        t4      nloc     marea      idof    edgset
 3.0000000 3.0000000 3.0000000 3.0000000     0.000     0.000  1.000000         0
$
$
*SECTION_SOLID_TITLE
air section
$#   secid    elform       aet
      5060        11         1
$#    afac      bfac      cfac      dfac     start       end     aafac
     0.000     0.000     0.000     0.000     0.000     0.000     0.000
$
*SECTION_SOLID_TITLE
solid section
$#   secid    elform       aet
        40         1         0
$ ========================================================================
$  MAT Cards
$ ========================================================================
```

```
*MAT_HIGH_EXPLOSIVE_BURN_TITLE
Pe4
$#     mid        ro         d       pcj      beta         k         g      sigy
      1080  0.001601    8193.0   28000.0       0.0       0.0       0.0       0.0
*MAT_NULL_TITLE
Air Material
$#     mid        ro        pc        mu     terod     cerod        ym        pr
       1001.29000E-6       0.0       0.0       0.0       0.0       0.0       0.0
*MAT_MODIFIED_JOHNSON_COOK_TITLE
DOMEX355-Calibrated
$#     mid        ro         e        pr      beta       xsi        cp     alpha
       107   7.83E-3  206800.0       0.29       0.0       0.9  452.0000       0.0
$#   e0dot        tr        tm        t0     flag1     flag2
    0.0014     298.0    1800.0     298.0       0.0       0.0
$#  a/siga       b/b   n/beta0   c/beta1      m/na
      &jca      &jcb      &jcn      &jcc      &jcm
$#    q1/a      c1/n q2/alpha0 c2/alpha1
     &jcq1     &jcc1     &jcq2     &jcc2
$#   dc/dc     pd/wc     d1/na     d2/na     d3/na     d4/na     d5/na
     111.0     111.0   0.22394 6.2494001-3.0629001       0.0       0.0
$#      tc      tauc
1.00000E101.00000E10r
$
*MAT_ELASTIC_TITLE
Elastic PLate material (from Len)
$#     mid        ro         e        pr        da        db  not used
      1200   0.00785  205000.00.28999999       0.0       0.0         0
*MAT_RIGID_TITLE
Rigid plate material
$#     mid        ro         e        pr         n    couple         m     alias
         9   0.00785  205000.00.28999999       0.0       0.0       0.0
$#     cmo      con1      con2
       1.0         6         7
$#lco or a1        a2        a3        v1        v2        v3
```

```
       0.0       0.0       0.0       0.0       0.0       0.0
*MAT_ELASTIC_PLASTIC_HYDRO_SPALL_TITLE
Sand
$      MID        RO         G      SIG0        EH        PC        FS     CHARL
         4   0.00137 76.900002       0.0       0.0   -0.0069       0.0       0.0
$       A1        A2     SPALL
   1.39642       0.0       3.0
$     EPS1      EPS2      EPS3      EPS4      EPS5      EPS6      EPS7      EPS8
       0.0       0.0       0.0       0.0       0.0       0.0       0.0       0.0
       0.0       0.0       0.0       0.0       0.0       0.0       0.0       0.0
       0.0       0.0       0.0       0.0       0.0       0.0       0.0       0.0
       0.0       0.0       0.0       0.0       0.0       0.0       0.0       0.0
$ ========================================================================
$  EOS
$ ========================================================================
*EOS_JWL_TITLE
Pe4 EOS
$#   eosid         a         b        r1        r2      omeg        e0        vo
      1080    609770     12950       4.5       1.4      0.25      9000       1.0
*EOS_LINEAR_POLYNOMIAL_TITLE
LP
$#   eosid        c0        c1        c2        c3        c4        c5        c6
       100     0.000     0.000     0.000     0.000  0.400000  0.400000     0.000
$#      e0        v0
 2.5330E-1  1.000000
*EOS_TABULATED_COMPACTION_TITLE
Sand
         4       0.0       0.0       1.0
             0.0          -0.113          -0.176     -0.24699999          -0.296
          -0.352     -0.39500001          -0.433     -0.46700001           -0.47
             0.0     14.97999954     29.14999962     58.18000031     98.09999847
      179.440002      289.440002      450.200012      650.659973           800.0
             0.0             0.0             0.0             0.0             0.0
             0.0             0.0             0.0             0.0             0.0
```

```
          5.0e4           5.0e4           5.0e4           5.0e4           5.0e4
          5.0e4           5.0e4           5.0e4           5.0e4           5.0e4
$ =========================================================================================
$  HOURGLASS
$ =========================================================================================
*HOURGLASS_TITLE
Standard hour glass
$#    hgid       ihq        qm       ibq        q1        q2    qb/vdc        qw
        10         1  1.000E-4         1  0.150001      0.06       0.0       0.0
*HOURGLASS_TITLE
Houre Glass for solid
$#    hgid       ihq        qm       ibq        q1        q2    qb/vdc        qw
        11         6       0.1         0       1.5      0.06       0.1       0.1
$=========================================================================
$                              INITIAL
$=========================================================================
*INITIAL_DETONATION
$#     pid         x         y         z        lt
        10       0.0       0.0     &DET       0.0
*INITIAL_VOLUME_FRACTION_GEOMETRY
$#   fmsid   fmidtyp     bammg    ntrace
         1         0         2        10
$# conttyp   fillopt     fammg        vx        xy        xz    radvel    unused
         5         0         3       0.0       0.0       0.0         0
$#    xmin      ymin      zmin      xmax      ymax      zmax    unused    unused
       0.0       0.0    &EXBOT       200       200     &STOP         0         0
$# conttyp   fillopt     fammg        vx        xy        xz    radvel    unused
         4         0         1       0.0       0.0       0.0         0
$#    xmin      ymin      zmin      xmax      ymax      zmax    unused    unused
       0.0       0.0    &EXBOT       0.0       0.0   &EXTOP     &DIAM     &DIAM
*INITIAL_TEMPERATURE_SET
$#    nsid      temp       loc
         0     293.0         0
$=========================================================================
```

```
$                                ALE
$===============================================================================
*ALE_MULTI-MATERIAL_GROUP
$#     sid    idtype    gpname
        10         1Explosive
         1         0Air
        20         1Sand
*CONSTRAINED_LAGRANGE_IN_SOLID_TITLE
$#  coupid                                                              title
         1Lagrange in Solid for plate and air blast
$#   slave    master     sstyp     mstyp     nquad     ctype     direc     mcoup
         4         3         0         0         3         4         2       -10
$#   start       end      pfac      fric    frcmin      norm   normtyp      damp
       0.0     10e11       0.7       0.0       0.4         0         0       0.0
$#      cq      hmin      hmax     ileak     pleak   lcidpor     nvent  blockage
       0.0       0.0       0.0         1      0.20         0         0         0
$#  iboxid   ipenchk   intforc   ialesof    lagmul    pfacmm      thkf
         0         1         1         0       0.0         3         0
$ ==============================================================================
$                    TRANSFORMATION KEYWORDS
$ ==============================================================================
*DEFINE_TRANSFORMATION
$  TRANID                       Position  Plate
$#  tranid
        10
$  OPTION
$# option         a1        a2        a3        a4        a5        a6        a7
TRANSL         0.000     0.000    &plate
$
*DEFINE_TRANSFORMATION
$  TRANID                       Position  Clamp Front
$#  tranid
        20
$# option         a1        a2        a3        a4        a5        a6        a7
```

```
TRANSL         0.000     0.000   &clamp2
$
*DEFINE_TRANSFORMATION
$  TRANID                      Position  Clamp Back
$#  tranid
        30
$# option         a1        a2        a3        a4        a5        a6        a7
TRANSL         0.000     0.000   &clamp1
$$
$========1=========2=========3=========4=========5=========6=========7=========8
$                               LOAD CURVES
$========1=========2=========3=========4=========5=========6=========7=========8
$
$                    time step
*DEFINE_CURVE
200,0,0.000E+00,0.000E+00,0.000E+00,0.000E+00,0
0.0E+0, &Tmax
0.01  , 1e-5
0.06  , 1e-5
0.061 , &Tmax
1000.0, &Tmax
$
*DEFINE_CURVE_TITLE
Load Curve for PFac penetration
$#    lcid      sidr       sfa       sfo      offa      offo    dattyp
       222         0  1.000000  1.000000     0.000     0.000         0
$#               a1        o1
                0.0       0.0
               0.01       200
 0.1      2000
$=============================================================================
$                               INCLUDE
$=============================================================================
*INCLUDE
```

```
200x150-Air-block.k
*Include_Transform
Plate.k
$  INDOFF   IDEOFF   INPOFF   IDMOFF   INSOFF   IDFOFF   IDDOFF
        0,       0,       0,       0,       0,       0,       0
$  IDROFF
    0
$  FCTMAS  FCTTIM  FCTLEN  FCTTEM  INCout1
     0.0
$  TRANID
     10
$
*Include_Transform
Clamp-frame.k
$  IDNOFF   IDEOFF   IPNOFF   IDMOFF   IDSOFF   IDFOFF   IDDOFF
    20000,   20000,       0,       0,       0,       0,       0
$  IDROFF
    0
$  FCTMAS  FCTTIM  FCTLEN  FCTTEM  INCout1
     0.0
$  TRANID
     20
$
*Include_Transform
Clamp-frame-B.k
$  INDOFF   IDEOFF   INPOFF   IDMOFF   IDSOFF   IDFOFF   IDDOFF
    45000,   45000,      10,       0,      10,       0,       0
$  IDROFF
    0
$  FCTMAS  FCTTIM  FCTLEN  FCTTEM  INCout1
     0.0
$  TRANID
     30
$
```

```
$=========================================================================
$                              SPRING
$=========================================================================
*PART
$#                                                                   title
Spring
$#     pid     secid       mid     eosid      hgid      grav    adpopt      tmid
         5         3         5         0         0         0         0         0
*SECTION_DISCRETE_TITLE
Spring
$#   secid       dro        kd        v0        cl        fd
         3         0       0.0       0.0       0.0       0.0
$#     cdl       tdl
       0.0       0.0
*MAT_SPRING_ELASTIC_TITLE
Spring
$#     mid         k
         5  100000.0
*DEFINE_CURVE_TITLE
Penalty Curve
$#    lcid      sidr       sfa       sfo      offa      offo    dattyp     lcint
        10         0       1.0       1.0       0.0       0.0         0         0
$#              a1                  o1
               0.0                 0.0
            0.0125                200.0
*DEFINE_CURVE_TITLE
Clamp Displacement
$#    lcid      sidr       sfa       sfo      offa      offo    dattyp     lcint
        20         0       1.0       1.0       0.0       0.0         0         0
$#              a1                  o1
               0.0                 0.0
      2.000000e-005               0.001
               10.0               0.001
*ELEMENT_DISCRETE
```

```
$#   eid     pid      n1      n2     vid               s      pf          offset
    1900       5   26750   51750       0             0.0       0             0.5
    1901       5   26751   51751       0             0.0       0             0.5
    1902       5   28330   53330       0             0.0       0             0.5
    1903       5   28367   53367       0             0.0       0             0.5
    1904       5   29787   54787       0             0.0       0             0.5
$=========================================================================
$                              SET
$=========================================================================
*SET_PART_LIST_TITLE
Air Set
$#     sid       da1       da2       da3       da4    solver
         1       0.0       0.0       0.0       0.0MECH
$#    pid1      pid2      pid3      pid4      pid5      pid6      pid7      pid8
       100         0         0         0         0         0         0         0
*SET_PART_LIST_TITLE
Explosive
$#     sid       da1       da2       da3       da4    solver
         2       0.0       0.0       0.0       0.0MECH
$#    pid1      pid2      pid3      pid4      pid5      pid6      pid7      pid8
        10         0         0         0         0         0         0         0
*SET_PART_LIST_TITLE
All ALE
$#     sid       da1       da2       da3       da4    solver
         3       0.0       0.0       0.0       0.0MECH
$#    pid1      pid2      pid3      pid4      pid5      pid6      pid7      pid8
        10       100        20         0         0         0         0         0
*SET_PART_LIST_TITLE
All PLATES
$#     sid       da1       da2       da3       da4    solver
         4       0.0       0.0       0.0       0.0MECH
$#    pid1      pid2      pid3      pid4      pid5      pid6      pid7      pid8
         1       120       130         0         0         0         0         0
*SET_MULTI_MATERIAL_GROUP_LIST
```

```
$#  ammsid
        10
$# ammgid1   ammgid2   ammgid3   ammgid4   ammgid5   ammgid6   ammgid7   ammgid8
         1         2         0         0         0         0         0         0
*END
```

Appendix D

Tensile Testing Simulation Input Deck

```
$# LS-DYNA Keyword file created by LS-PrePost(R) V4.3 (Beta) - 20Jul2015(10:00)
$# Created on Dec-3-2016 (08:14:33)
*KEYWORD
$=============================================================================
$                                 LS-OPT
$=============================================================================
*PARAMETER
$#   prmr1      val1     prmr2      val2     prmr3      val3     prmr4      val4
R      jca       220
*PARAMETER
R      jcb       400
*PARAMETER
R     jcq1        15
*PARAMETER
R     jcq2       190
*PARAMETER
R      jcc     0.005
*PARAMETER
R     jcc1     26.13
*PARAMETER
R     jcc2     0.094
*PARAMETER
R      jcn      0.38
```

```
*PARAMETER
R      jcm      0.81
*TITLE
$#                                                                         title
LS-DYNA keyword deck by LS-PrePost
*CONTROL_IMPLICIT_AUTO
$#   iauto    iteopt    itewin     dtmin     dtmax     dtexp     kfail    kcycle
         1        11         5       0.0     100.0       0.0         0         0
*CONTROL_IMPLICIT_GENERAL
$#  imflag       dt0    imform      nsbs       igs     cnstn      form    zero_v
         1       5.0         2         1         2         0         0         0
*CONTROL_IMPLICIT_SOLUTION
$#  nsolvr    ilimit    maxref     dctol     ectol     rctol     lstol    abstol
         2        11        15     0.001      0.011.00000E100.899999981.0000E-10
$#   dnorm    diverg     istif   nlprint    nlnorm   d3itctl     cpchk
         2         1         1         0         2         0         0
$#  arcctl    arcdir    arclen    arcmth    arcdmp    arcpsi    arcalf    arctim
         0         0       0.0         1         2         0         0         0
$#   lsmtd     lsdir      irad      srad      awgt      sred
         1         2       0.0       0.0       0.0       0.0
*CONTROL_IMPLICIT_SOLVER
$#  lsolvr    lprint     negev     order      drcm    drcprm   autospc   autotol
         4         2         2         0         4       0.0         1       0.0
$#  lcpack    mtxdmp
         2         0
*CONTROL_SOLUTION
$#    soln       nlq     isnan     lcint
         0         0         0       100
$=====================================================================
$                              CONTROL
$=====================================================================
*CONTROL_TERMINATION
$#  endtim    endcyc     dtmin    endeng    endmas
  360000.0         0       0.0       0.01.000000E8
```

```
*CONTROL_TIMESTEP
$#  dtinit    tssfac      isdo    tslimt     dt2ms      lctm     erode     ms1st
       0.00.89999998         0       0.0       0.0         0         0         0
$#  dt2msf   dt2mslc     imscl    unused    unused     rmscl
       0.0         0         0                          0.0
$=========================================================================
$                            DATABASE
$=========================================================================
*DATABASE_ELOUT
$#      dt    binary      lcur     ioopt   option1   option2   option3   option4
     100.0         3         0         1         8         8         0         0
*DATABASE_NODFOR
$#      dt    binary      lcur     ioopt
     100.0         3         0         1
*DATABASE_NODOUT
$#      dt    binary      lcur     ioopt   option1   option2
     100.0         3         0         1       0.0         0
*DATABASE_BINARY_D3PLOT
$#      dt      lcdt      beam     npltc    psetid
     100.0         0         0         0         0
$#   ioopt
        0
*DATABASE_NODAL_FORCE_GROUP
$#    nsid       cid
        4         0
$=========================================================================
$                        BOUNDARY CONDITIONS
$=========================================================================
*BOUNDARY_PRESCRIBED_MOTION_SET
$#    nsid       dof       vad      lcid        sf       vid     death     birth
        4         3         2         1       1.0         01.00000E28       0.0
*BOUNDARY_TEMPERATURE_SET
$#    nsid      lcid     cmult       loc
        4         0     293.0         0
```

```
$=======================================================================
$                       Material
$=======================================================================
*PART
$#                                                                  title
staight specimen
$#     pid     secid       mid     eosid      hgid      grav    adpopt      tmid
         1         1       107         0         0         0         0         0
*SECTION_SOLID
$#   secid    elform       aet
         1         2         0
*EOS_LINEAR_POLYNOMIAL_TITLE
LP
$#   eosid        c0        c1        c2        c3        c4        c5        c6
         5     0.000     0.000     0.000     0.000  0.400000  0.400000     0.000
$#      e0        v0
 2.5330E-1  1.000000
*MAT_MODIFIED_JOHNSON_COOK_TITLE
DOMEX355
$#     mid        ro         e        pr      beta       xsi        cp     alpha
       107   7.83E-3  206800.0      0.29       0.0       0.9  452.0000       0.0
$#   e0dot        tr        tm        t0     flag1     flag2
    0.0014     298.0    1800.0     298.0       0.0       0.0
$#  a/siga       b/b   n/beta0   c/beta1      m/na
      &jca      &jcb      &jcn      &jcc      &jcm
$#    q1/a      c1/n q2/alpha0 c2/alpha1
     &jcq1     &jcc1     &jcq2     &jcc2
$#   dc/dc     pd/wc     d1/na     d2/na     d3/na     d4/na     d5/na
     111.0     111.0   0.22394 6.2494001-3.0629001       0.0       0.0
$#      tc      tauc
1.00000E101.00000E10
*MAT_THERMAL_ISOTROPIC
$#    tmid       tro     tgrlc    tgmult      tlat      hlat
         1    0.0078       0.0       0.0       0.0       0.0
```

```
$#      hc        tc
     466.0      43.0
*INITIAL_TEMPERATURE_SET
$#    nsid      temp       loc
         0     293.0         0
$=========================================================================
$                              DEFINE
$=========================================================================
*DEFINE_COORDINATE_SYSTEM
$#     cid        xo        yo        zo        xl        yl        zl
         1       1.0       0.0       0.0       0.0       1.0       0.0
$#      xp        yp        zp
       0.0       0.0       1.0
*DEFINE_CURVE
$#    lcid      sidr       sfa       sfo      offa      offo    dattyp     lcint
         1         0       1.0       1.0       0.0       0.0         0         0
$#                a1                  o1
                 0.0                 0.0
            600000.0                 3.0
$=========================================================================
$                              INCLUDE
$=========================================================================
*INCLUDE
specimen.k
*END
```